Norsk institutt for luftforskning
Norwegian Institute for Air Research

Monitoring of greenhouse gases and aerosols at Svalbard and Birkenes in 2020

Annual report

Cathrine Lund Myhre, Tove Svendby, Ove Hermansen, Chris Lunder, Stephen M. Platt, Markus Fiebig, Ann Mari Fjæraa, Georg Hansen, Norbert Schmidbauer, Terje Krognes

NILU report 22/2021

NILU report 22/2021 Norwegian Environment Agency M-2117 |2021	ISBN: 978-82-425-3060-8 ISSN: 2464-3327	CLASSIFICATION: A – Unclassified (open report)
DATE 22.10.2021	SIGNATURE OF RESPONSIBLE PERSON Ole-Anders Braathen, Deputy director (sign.)	NUMBER OF PAGES 168
TITLE Monitoring of greenhouse gases and aerosols at Svalbard and Birkenes in 2020 Annual report		PROJECT LEADER Wenche Aas NILU PROJECT NO. O-113007
AUTHOR(S) Cathrine Lund Myhre, Tove Svendby, Ove Hermansen, Chris Lunder, Stephen M. Platt, Markus Fiebig, Ann Mari Fjæraa, Georg Hansen, Norbert Schmidbauer, Terje Krognes		QUALITY CONTROLLER Kjetil Tørseth
REPORT PREPARED FOR Norwegian Environment Agency Postboks 5672 Sluppen, 7485 Trondheim		CONTRACT REF. Contract number 17078061

ABSTRACT

The report summarizes the activities and results of the greenhouse gas monitoring at the Zeppelin Observatory, situated on Svalbard in Arctic Norway, during the period 2001-2020, and the greenhouse gas monitoring and aerosol observations from Birkenes for 2009-2020.

NORWEGIAN TITLE

Overvåkning av klimagasser og partikler på Svalbard og Birkenes i 2020: Årsrapport.

KEYWORDS

Greenhouse-gases/ Drivhusgasser	Aerosols/ Partikler	Climate gases/ Klimagasser	Halocarbons/ Halokarboner

ABSTRACT (in Norwegian)

Rapporten presenterer aktiviteter og måleresultater fra klimagassovervåkingen ved Zeppelinobservatoriet på Svalbard for årene 2001-2020 og klimagassmålinger og klimarelevante partikkelmålinger fra Birkenes for 2009-2020

PUBLICATION TYPE: Digital document (pdf)	COVER PICTURE: Source: Kjetil Tørseth, NILU

Citation: Myhre, C.L., Svendby, T., Hermansen, O., Lunder, C., Platt, S.M., Fiebig, M., Fjæraa, A.M., Hansen, G., Schmidbauer, N. and Krognes, T. (2021). Monitoring of greenhouse gases and aerosols at Svalbard and Birkenes in 2020. Annual report. (NILU report 22/2021). Kjeller: NILU.

NILU's ISO Certifications: NS-EN ISO 9001 and NS-EN ISO 14001. NILU's Accreditation: NS-EN ISO/IEC 17025.

Preface

This report presents the 2020 annual results from the national monitoring of greenhouse gas concentrations and climate-relevant particle properties. The observations are done at two atmospheric observatories; one regional background site in southern Norway and one Arctic site. The observations made are part of the national monitoring programme conducted by NILU- Norsk institutt for luftforskning (NILU) on behalf of The Norwegian Environment Agency. Additionally, the report includes results from aerosol observations at Trollhaugen observatory in Antarctica. These measurements are not a part of the national monitoring programme, but receive direct support from the Norwegian Ministry of Climate and Environment.

The national monitoring programme comprises measurements of 46 greenhouse gases at the Zeppelin Observatory in the Arctic; including a long list of halocarbons, of which most are not only greenhouse gases, but also ozone depleting substances. NILU initiated measurements of methane (CH_4)-isotope ($\delta^{13}C_{CH4}$) at Zeppelin in 2012 to provide more insight into Arctic sources of CH_4, and potential changes, as part of a project funded by the Norwegian Research Council. The continuation of these measurements was implemented in the Norwegian Monitoring programme in 2019. NILU upgraded and extended the observational capabilities of the Birkenes Observatory, Agder, and from 2010, the national monitoring programme was extended to include aerosol properties relevant for understanding the effects of aerosols on radiation (particle size, number, scattering and light absorption).

The present report is the third of a series of annual reports in 2021, which cover the national monitoring of atmospheric composition in the Norwegian rural background environment. The other two reports focus on the atmospheric composition and deposition of air pollution of particulate and gas phase of inorganic constituents, particulate carbonaceous matter, ground level ozone and particulate matter (Aas et al, 2021), and the monitoring of the ozone layer and UV (Svendby et al, 2021).

Participation in international programmes is essential for quality assurance and quality control of the Norwegian measurement data and instruments. Data from this report contribute to, and benefit from, the European Research Infrastructure ACTRIS (*Aerosols, Clouds, and Trace gases Research InfraStructure*) and ICOS (*Integrated Carbon Observation System*). Additionally, data and results support and benefit from EMEP (European Monitoring and Evaluation Programme) under CLRTAP (Convention on Long-range Transboundary Air Pollution), and AGAGE (Advanced Global Atmospheric Gases Experiment).

All measurement data presented in the current report are public and can be received by contacting NILU, or they can be downloaded directly from the database: http://ebas.nilu.no.

Many people at NILU have contributed to this report, including those responsible for sampling, technical maintenance, chemical analysis and quality control and data management, in particular, Tove Svendby, Ove Hermansen, Chris Lunder, Markus Fiebig, Georg Hanssen, Stephen M. Platt, Terje Krognes, Ann Mari Fjæraa and Norbert Schmidbauer.

NILU, Kjeller, 29th September 2021
Cathrine Lund Myhre
Senior Scientist, Dep. Atmospheric and Climate Research

Contents

Sammendrag

Alle de viktigste klimagassene CO_2, CH_4 og N_2O økte til nye rekordnivåer i 2020, og det er ingen tegn til utflating for noen av disse gassene.

CH_4 fortsetter med rekordrask økning, den største vi har registrert siden målingene på Svalbard startet i 2001

N_2O har en ny sesongvariasjon i 2020 med høyere verdier om sommeren enn vi forventet.

KFK-gasser fortsetter nedgangen, mens erstatningsgassene øker raskt.

Denne årsrapporten beskriver aktivitetene og hovedresultatene fra delprogrammet "*Overvåkning av klimagasser og aerosoler på Zeppelinobservatoriet på Svalbard og Birkenesobservatoriet i Aust-Agder, Norge*". Rapporten omfatter målinger av 46 klimagasser på Zeppelinobservatoriet fram til 31. desember 2020 og inkluderer de viktigste naturlig forekommende klimagassene, syntetiske klimagasser, karbonmonoksid (CO) og ulike partikkelmålinger som har høy relevans for klimaet. Mange av gassene har også sterk ozonødeleggende effekt. Målingene på Zeppelinobservatoriet gir informasjon om utviklingen av bakgrunnsnivået av klimagasser i Arktis, og alle de 46 gassene i overvåkningsprogrammet blir målt her. Birkenesobservatoriet ligger i et område i Sør-Norge som kan være sterkt påvirket av langtransportert luftforurensning fra Europa, i tillegg til påvirkning fra lokal vegetasjon. På Birkenesobservatoriet gjøres observasjoner av karbondioksid (CO_2) og metan (CH_4), samt omfattende målinger av klimarelevante egenskaper til aerosoler (partikler). Aerosoler måles også på Zeppelin og Trollhaugen (Antarktis), men måleprogrammene er ikke like omfattende som på Birkenes.

For klimagassene er utvikling og trender for perioden 2001-2020 rapportert, i tillegg til daglige og årlige gjennomsnittsverdier. Programmet ble utvidet med 16 nye gasser på Zeppelin i 2015. I 2016 ble programmet ytterligere utvidet med seks nye gasser etter modifisering av instrumenteringen ved Zeppelinobservatoriet: tre hydrofluorkarboner (HFC), sulfurylfluorid (SO_2F_2), halon H-2402 og nitrogentrifluorid (NF_3). For de nye komponentene er data innhentet og analysert tilbake til 2010. Resultatene for alle klimagassene er oppsummert i tabell 1 på side 12.

Konsentrasjonene av alle de viktigste klimagassene har økt kraftig siden 2001, bortsett fra ozonødeleggende klorfluorkarboner (KFK-er) og noen få andre halogenerte gasser som er regulert gjennom Montrealprotokollen. De fleste av disse har blitt redusert, som vist i rapporten.

Observasjonene fra 2020 viser nye rekordhøye nivåer for de fleste klimagassene i overvåkningsprogrammet, både på Zeppelin og Birkenes. Årlig midlere CO_2 konsentrasjon i 2020 var 414,2 ppm (parts per million) på Zeppelin og 418,8 ppm på Birkenes. Dette er økninger på henholdsvis 2,3 ppm og 2,7 ppm fra 2019 og ny rekord på begge stasjoner. Den atmosfæriske konsentrasjonen av disse gassene har økt fra førindustriell tid (1750) til 2019 med henholdsvis 47,3%, 156%og 23,0%. Disse endringene er større enn endringene mellom istiden og mellomistiden i løpet av de siste 800 000 årene.

Konsentrasjonen av metan var også i 2020 rekordhøy både på Birkenes og på Zeppelin, med årlige middelverdier på 1975,2 ppb (parts per billion) på Birkenes og 1968,7 ppb på Zeppelin. I forhold til 2019-nivået er dette en økning på Zeppelin på hele 15,7 ppb, den høyeste økningen noen gang registrert på ett år og enda sterkere enn i fjor. Også på Birkenes er økningen betydelig, hele 14,0 ppb. Endringene i løpet av de siste ti årene er store i forhold til utviklingen av metan-nivået i perioden 1998-2005, da endringene var tilnærmet null både på Zeppelin og globalt. Ulike metankilder (for eksempel naturgass og våtmarker) har ulik isotop-signatur (det vil si forhold mellom isotoper). Isotopmålinger av CH_4 på Zeppelin viser en klar trend i $\delta^{13}C_{CH4}$ etter 2012 og frem til ca. 2019. En nedadgående trend i

$\delta^{13}C_{CH4}$, samtidig med en økning av metankonsentrasjonene, viser at metankildene eller opptaksprosessene har endret seg i løpet av de siste 8 årene. Endringene i $\delta^{13}C_{CH4}$ på Zeppelin tyder på økte utslipp fra biosfæren (våtmarker) og/eller jordbruk. Data fra 2019 og 2020 indikerer at denne endringen i kildesammensetning er i ferd med å flate ut, det vil si at balansen mellom kildene ser ut til å ha stabilisert seg.

Lystgass (N_2O) har både naturlige kilder og store menneskeskapte kilder som jordbruk og bergverk. N_2O nådde også nytt rekordnivå i 2020. Den årlige middelkonsentrasjonen på Zeppelin var 333,4 ppb, en økning på 1,3 ppb siden 2019. Dette er den største årlige økningen vi har observert. Vi ser en endring i årssyklusen, med høyere verdier enn forventet sommer og høst. Dette er viktig informasjon for å forstå hvilke kilder som kan ha endret seg.

Det er interessant å merke seg at CO målt på Zeppelinobservatoriet har begynt å øke igjen etter en stabil periode. En viktig kilde for CO er skogbranner og det kan virke som de store skogbrannene de siste årene i Sibir, Canada og USA kan forklare økningen vi ser, men det er for tidlig å konkludere. Dette er også i samsvar med episodene vi ser i partikkelmålinger.

De syntetiske, menneskeskapte klimagassene som inngår i overvåkningsprogrammet på Zeppelin er fire klorfluorkarboner (KFK-er), tre hydroklorfluorkarboner (HKFK-er), og 11 hydrofluorkarboner (HFK-er). De to sistnevnte gruppene er KFK-erstatninger. I tillegg inngår tre haloner, en gruppe med åtte andre halogenerte klimagasser, samt fire perfluorerte karboner (PFK-er) med svært høyt globalt oppvarmingspotensial (GWP). Videre rapporteres sulfurylfluorid, svovelhexafluorid, og nitrogentrifluorid, hvorav de to siste er meget sterke klimagasser.

Generelt avtar konsentrasjonen av KFK-gasser, mens de øvrige gassene øker da disse ofte er erstatningsgasser for KFK-ene. For et par år siden ble det oppdaget ukjente og urapporterte utslipp av KFK-11 i Asia, noe som har redusert den markante nedadgående trenden i de globale målingene av KFK-11. Utviklingen i KFK-gassene gir likevel grunn til optimisme, fordi konsentrasjonen for de fleste av disse gassene er synkende. KFK-115 er et unntak, her ser vi en liten økning fra 2019-2020. Samtidig økte konsentrasjonene av KFK-erstatningsstoffene, HKFK-er og HFK-er, i perioden 2001-2020. For HKFK-er har det riktignok vært mindre økning de siste årene, og i år ser vi en nedgang for HKFK-142b. For HKFK-142b startet nedgangen i 2017, så det er tredje året på rad med reduksjon. HKFK-141b øker igjen, etter nedgang i perioden 2017-2018. Konsentrasjonen av HFK-gassene har økt kraftig siden 2001 og med få unntak ser den økende trenden ut til å fortsette. HFK-152a viser en nedgang for første gang i 2020, men hadde særlig sterk vekst i 2019. Konsentrasjonene av disse menneskeskapte HFK-ene er fortsatt svært lave, noe som betyr at bidraget til den globale oppvarmingen per i dag er lite, men gitt den ekstremt sterke økningen og bruken av disse gassene, er det viktig å følge utviklingen nøye i fremtiden.

Konsentrasjonene av PFK-er og svovelfluorider (SF_6 og SO_2F_2) er også lave. PFK-14 er høyest, med en årlig middelverdi på 86,9 ppt (parts per trillion) i 2020, en økning på 0,79 ppt fra 2019. Konsentrasjonen av SF_6 bør også følges nøye, ettersom denne forbindelsen har en atmosfærisk levetid på 3 200 år og et GWP på hele 25 200. Denne forbindelsen har økt med hele 105% siden målingene startet på Zeppelin i 2001.

Aerosoler består av små partikler i atmosfæren. Partiklenes klimapåvirkning avhenger av mengden partikler og absorpsjonsegenskapene til enkeltpartiklene. Konsentrasjonen av partikler på Birkenes bestemmes i hovedsak av den langtransporterte luftforurensningen fra det kontinentale Europa, i tillegg til regionale og lokale vegetasjonskilder (biogene kilder).

På Birkenes ser vi i 2020 episoder med økt partikkelmengde som skyldes langtransport av vinterforurensning fra Sentral-Europa, påvirkning av naturlige utslipp fra skog, samt arktisk dis. En stor episode skyldes støv fra Sentral-Asia kombinert med utslipp fra skogbranner i Ukraina, tilsvarende en episode i august 2019. Siden oppstarten av fysiske og optiske aerosolobservasjoner på Birkenes i 2010 har vi ikke sett noen signifikant trend i aerosolegenskaper, noe som også er i samsvar med nyere trendstudier av aerosolegenskaper som dekker hele kloden.

På Zeppelin er situasjonen litt annerledes. Ved å sammenstille våre aerosolmålinger med resultater fra andre samarbeidspartnere, finner vi en nedadgående trend i aerosol-absorpsjonen, noe som viser at konsentrasjonen av sot eller såkalt svart karbon går ned. Observasjoner av den totale kolonnen av aerosoler over Ny-Ålesund (aerosol optisk dybde, AOD) viser økte konsentrasjoner om våren sammenlignet med resten av året. Dette fenomenet, som kalles arktisk dis (*Arctic haze*), skyldes transport av forurensning fra lavere breddegrader i løpet av vinteren/våren, hovedsakelig fra Europa og Russland. I 2020 ser vi transportepisoder av aerosol fra skogbrann i Ukraina og støv fra Sentral-Asia – den samme episoden som vi også ser på Birkenes.

Partiklene på Trollhaugen i Antarktis er preget av naturlige storskalaprosesser med en veldig konstant årssyklus. En episode observert vinteren 2020 skyldes luftmasser påvirket av utslipp fra en nabostasjon 360 km til øst.

Summary

All the most important greenhouse gases CO_2, CH_4 and N_2O increased to new record levels in 2020, and there are no signs of leveling off for any of these gases.

CH_4 continues with a record strong increase, the largest we have registered since the measurements on Svalbard started in 2001.

N_2O has a new seasonal variation in 2020 with higher values in the summer than we expected. CFC-gases continue to decline, while their replacement gases increase rapidly.

This annual report describes the activities and main results of the programme "*Monitoring of greenhouse gases and aerosols at the Zeppelin Observatory, Svalbard, and Birkenes Observatory, Aust-Agder, Norway*". The report presents the measurements of 46 climate gases at the Zeppelin Observatory up to 31st December 2020; including the most important naturally occurring well-mixed greenhouse gases, synthetic greenhouse gases, reactive short lived gases as volatile organic compounds (VOCs), and CO in addition to various particle properties with high relevance to climate. The measurements at Zeppelin Observatory provide the trends in background level concentrations of climate gases in the Arctic, and all the 46 climate gases in the programme are monitored at this site.

At the Birkenes Observatory in Southern Norway, carbon dioxide (CO_2) and methane (CH_4) measurements are undertaken in addition to a comprehensive aerosol measurement programme. Birkenes is highly influenced by long-range transport of pollutants from the European continent as well as local vegetation/terrestrial interactions. Aerosol measurements are also performed at Zeppelin and Trollhaugen (Antarctica), although less extensively than at Birkenes.

Many of the gases in this report also have strong ozone depleting effects. The development and trends in the measured constituents for the period 2001-2020 are reported, in addition to daily and annual means. In 2015, the programme at Zeppelin was extended to include 16 new climate gases, all with measurements starting in 2010. In 2016, the programme was further extended to include six more species after instrumentation modification at the Zeppelin Observatory: three hydrofluorocarbons (HFCs), sulphuryl fluoride (SO_2F_2), halon H-2402 and nitrogen trifluoride (NF_3). The main results for 2020 for all climate gases are summarized in Table 1.The concentrations of all main greenhouse gases measured at both Zeppelin and Birkenes have been increasing since 2001, except for the ozone-depleting chlorofluorocarbons (CFCs) and a few halogenated gases regulated through the successful Montreal Protocol.

The observations from 2020 show new record high levels for most climate gases measured. The annual average CO_2-concentration in 2019 was 414.2 ppm at Zeppelin and 418.8 ppm at Birkenes. The increases from 2019 are 2.3 ppm 2.7 ppm, respectively. The atmospheric concentration of these gases has increased from the pre-industrial time (1750) to 2019 by 47.3%, 156%, and 23.0%, respectively. These changes are larger than those between glacial and interglacial periods over the last 800,000 years.

The concentration of CH_4 also reached new record highs in 2020 at Birkenes and Zeppelin, with annual mean concentrations of 1975.2 ppb at Birkenes and 1968.7 ppb at Zeppelin. The level at Zeppelin gives a new record annual increase of 15.7 ppb, even more than last year. At Birkenes, the increase was 14.0 ppb. For the isotopic signature of CH_4, a clear trend in $\delta^{13}C_{CH4}$ is evident after 2012. The observed negative shifts in ambient $\delta^{13}C_{CH4}$, and increases in the CH_4 ambient mixing ratio at the same time, imply changes in the balance of sources and potentially sinks. The developments in $\delta^{13}C_{CH4}$ observed at

Zeppelin suggest increase in biosphere and/or agriculture (wetland or ruminant) emissions. For 2019 and 2020 the data indicate that the recent shift in the source/ sink balance may have stabilised.

The mean N_2O-concentration at Zeppelin was also at a record high in 2020, again with a record increase over 1 year. The annual mean concentration was 333.4 ppb, an increase of 1.3 ppb since 2019. This is the largest annual increase we have observed. Importantly, we see a change in the seasonal cycle, with higher values in summer and autumn than expected in 2020. This information is fundamental to understand which sources may have changed and led to the strong increase.

It is interesting to note that CO measured on Zeppelin Observatory has started to increase again, after a stable period. An important source of CO is forest fires, and it may seem that the major forest fires in recent years in Siberia, Canada and the United States explain the increase we are seeing, but it is too early to conclude. This is consistent with the episodes we see in particle measurements as well.

The synthetic manmade greenhouse gases included in the monitoring programme at Zeppelin are 4 chlorofluorocarbons (CFCs), 3 hydrochlorofluorocarbons (HCFCs), and 11 HFCs – the last two being CFC substitutes. In addition, three halons, a group of 8 halogenated gases, and 4 perfluorinated carbons (PFCs) with very high global warming potentials, are included. Furthermore, SF_6, NF_3 and SO_2F_2 were reported for the first time in 2016. SF_6 and NF_3 are extremely strong greenhouse gases.

In general, the concentration of CFC-gases has decreased, while their replacements have increased. Recently, new and previously unreported CFC-11 emission sources were discovered in Asia, which have slowed down the rate of CFC-11 decrease globally. Still, the development of the CFC-gases measured at Zeppelin is very encouraging as the concentrations of the dominating species are declining. CFC-115 is an exception and we see an increase in the concentration of this compound. Contrary to the CFCs, the CFC substitutes HCFCs and HFCs have increased over the period 2001-2020. For the HCFCs, a relaxation in the upward trend has been observed in recent years, and HCFC-142b shows a small decrease over last three years. However, for HFCs a strong increase has been observed since 2001, and the increasing trend is continuing except for HFC-152a, which declined for the first time in 2020 (but showed particularly strong growth in 2019). The contribution from these manmade gases to global warming is small today, as the concentrations of HFCs are still very low. However, given the extremely rapid increase in the use of these gases and their high global warming potentials (GWP, determined relative to CO_2), it is crucial to follow their development.

Atmospheric concentrations of PFCs, SO_2F_2 and SF_6 are also low. PFC-14 is amongst the highest, with a mixing ratio of 86.9 ppt in 2020, an increase of 0.79 ppt since 2019. SF_6 should also be followed closely, as this compound has an atmospheric life-time of 3 200 years and an extremely high GWP of 25 200. This compound has increased by 105% since 2001.

Aerosols consist of small particles in the atmosphere. They can have warming or cooling effects on climate, depending on the particle loading, their properties, and where they are located. Aerosol loads and properties at Birkenes are mainly influenced by long-range transport of air pollution from continental Europe, combined with regional sources like biogenic particle formation. Episodes visible in 2020 originate from long-range transport of winter emissions from Central Europe, natural boreal forest emissions, and Arctic haze. A major episode was caused by Central Asian dust combined with forest fire emissions in Ukraine, similar to an episode in August 2019. Since the start of physical and optical aerosol observations at Birkenes in 2010, we do not see any significant trend in aerosol properties, which is consistent with recent studies of aerosol optical property trends covering the whole globe.

At Zeppelin, the situation is different. By comparing aerosol absorption data collected at Zeppelin with data from collaborating institutes, a decreasing trend is observed, indicating a decrease of black carbon (BC, mostly soot) at Zeppelin. Observations of the total amount of aerosol particles in the atmosphere above Ny-Ålesund (aerosol optical depth) show high concentrations during springtime compared to the rest of the year. This phenomenon, called Arctic haze, is due to transport of pollution from lower latitudes accumulating in the Arctic atmosphere during winter/spring. In 2020, we can connect

observed aerosol transport episodes to forest fire events in Ukraine and dust emissions from central Asia, as for Birkenes, at the same spatial scale as the corresponding event in August 2019.

The aerosol at Trollhaugen, Antarctica, is characterised by natural, hemispheric scale processes with a very constant annual cycle. Episodes observed in Winter 2020 can be connected to emissions from a neighbouring stations 360 km east of Troll and on the Antarctic peninsula.

Table 1: Key findings; Greenhouse gases measured at Zeppelin, Ny-Ålesund; lifetimes in years[1], global warming potential (GWP over 100 years, when available[1]), annual mean concentrations for 2020 and their long term trends per year over the measurement period. CO_2 and CH_4 are also measured at Birkenes. Concentrations are in ppm (parts per million) for CO_2, ppb (part per billion) for CH_4, CO, and N_2O, and ppt (parts per trillion) for the other gases. The trend method is described in appendix II.

Component		Life-time	GWP	Annual mean 2020	Absolute change last year	Trend /yr
Carbon dioxide - Zeppelin	CO_2	**	1	414.2	2.3	2.4
Carbon dioxide - Birkenes				418.8	2.7	2.5
Methane - Zeppelin	CH_4	11.8	28	1968.7	15.7	6.4
Methane - Birkenes				1975.2	14.0	8.4
Carbon monoxide	CO	few months	-	120.3	4.8	-1.1
Nitrous oxide	N_2O	109	273	333.4	1.30	0.99
Chlorofluorocarbons						
CFC-11	CCl_3F	52	5 560	225.5	0.00	-1.77
CFC-12	CF_2Cl_2	102	11 200	501.9	-3.74	-2.57
CFC-113	CF2ClCFCl2	93	6 520	69.5	-0.52	-0.63
CFC-115	CF_3CF_2Cl	540	9 600	8.8	0.03	0.03
Hydrochlorofluorocarbons						
HCFC-22	$CHClF_2$	11.9	1 960	257.1	1.12	5.61
HCFC-141b	$C_2H_3FCl_2$	9.4	860	26.1	0.33	0.51
HCFC-142b	CH_3CF_2Cl	18	2 300	22.8	-0.37	0.50
Hydrofluorocarbons						
HFC-125	CHF_2CF_3	30	3 740	35.6	3.35	1.74
HFC-134a	CH_2FCF_3	14	1 530	120.2	5.51	5.19
HFC-152a	CH_3CHF_2	1.6	164	10.5	-0.12	0.40
HFC-23	CHF_3	228	14 600	34.5	1.25	1.07
HFC-365mfc	$CH_3CF_2CH_2CF_3$	8.9	914	1.32	0.01	0.06
HFC-227ea	CF_3CHFCF_3	36	3 600	1.90	0.15	0.12
HFC-236fa	$CF_3CH_2CF_3$	213	8 690	0.22	0.01	0.01
HFC-245fa	$CHF_2CH_2CF_3$	7.7	858	3.73	0.20	0.21
HFC-32	CH_2F_2	5.4	771	28.7	3.51	2.31
HFC-4310mee	$C_5H_2F_{10}$	17	1 600	0.31	0.01	0.01
HFC-143a	CH_3CF_3	51	5 810	27.1	1.51	1.54
Perfluorinated compounds						
PFC-14	CF_4	50 000	7 380	86.91	0.79	0.67
PFC-116	C_2F_6	10 000	12 400	4.99	0.08	0.09

* The measurements of these components have higher uncertainty. See Appendix I for more details.

[1] From Scientific Assessment of Ozone Depletion: 2010 (WMO, 2011b) and the 6th Assessment Report of the IPCC 2021a

** Carbon dioxide does not have a specific lifetime because it is continuously cycled between the atmosphere, oceans and land biosphere and its net removal from the atmosphere involves a range of processes with different time scales.

Component		Life-time	GWP	Annual mean 2020	Absolute change last year	Trend /yr
PFC-218	C_3F_8	2600	9 290	0.71	0.02	0.02
PFC-318	C_4F_8	3200	10 200	1.87	0.07	0.06
Sulphurhexafluoride	SF_6	3 200	25 200	10.44	0.31	0.29
Nitrogen trifluoride	NF_3	569	17 400	2.48	0.26	0.26
Sulphuryl fluoride	SO_2F_2	36	4 630	2.74	0.11	0.10
Halons						
H-1211	$CBrClF_2$	16	1 930	3.27	-0.10	-0.07
H-1301	$CBrF_3$	72	7 200	3.39	-0.003	0.02
H-2402	$CBrF_2CBrF_2$	28	2 170	0.40	-0.01	-0.01
Halogenated compounds						
Chloromethane	CH_3Cl	0.9	5.5	508.58	0.84	-0.46
Bromomethane	CH_3Br	0.8	2.4	6.71	-0.02	-0.15
Dichloromethane	CH_2Cl_2	0.49	11.2	62.46	3.64	1.91
Trichloromethane	$CHCl_3$	0.5	20.6	13.05	0.77	0.22
Carbon tetrachloride	CCl_4	32	2200	77.26	-0.74	-0.93
Trichloroethane	CH_3CCl_3	5	161	1.47	-0.23	-1.70
Trichloroethene	$CHClCCl_2$	0.02	0.04	0.24	-0.06	-0.01
Tetrachloroethene	CCl_2CCl_2	0.30	6.3	2.09	-0.19	-0.11
Volatile Organic Compounds (VOC)						
Ethane	C_2H_6	Ca 78 days*		1512.88	-89.53	-
Propane	C_3H_8	Ca 18 days*		337.04	-116.78	-
Butane	C_4H_{10}	Ca 8 days*		118.95	-21.04	-
Pentane	C_5H_{12}	Ca 5 days*		41.04	-2.76	-
Benzene	C_6H_6	Ca 17 days*		Not available since 2018		-
Toluene	$C_6H_5CH_3$	Ca 2 days*				-

**The lifetimes of VOCs are strongly dependent on season, sunlight, other components etc. The estimates are global averages given in C. Nicholas Hewitt (ed.): Reactive Hydrocarbons in the Atmosphere, Academic Press, 1999, p. 313. The times series for these are short and the trend is very uncertain.*

Monitoring of greenhouse gases and aerosols at Svalbard and Birkenes in 2020

Annual report

1 Introduction to monitoring of climate gases and aerosols

1.1 The monitoring programme in 2020

The purpose of the monitoring programme is to study the long-term development of climate gases and aerosols (particles). Measurements are performed at three sites and the results are Norwegian contributions to European and global observation networks.

The atmospheric monitoring programme presented in this report focuses on the concentrations of greenhouse gases and on selected particle physical and optical properties relevant for the understanding of climate change. Sampling sites are at Svalbard in the Norwegian Arctic (Zeppelin Observatory), where observations are considered to be representative for well-mixed background concentration levels, and a second site in southern Norway (Birkenes Observatory), where observations are more influenced by regional and local sources (Figure 1). A third site is in the Antarctic (Trollhaugen station).

Figure 1: Location of NILU's atmospheric supersites measuring greenhouse gases and aerosol properties.

The main objectives are to quantify the levels of the main greenhouse gases including ozone depleting substances, describe the relevant optical and physical properties of aerosols, and document their development over time. Measurements of the greenhouse gas concentrations and aerosol properties are core data for studies and assessments of climate change, and also crucial in order to evaluate mitigation strategies and their effectiveness. The Norwegian monitoring sites are located in areas where the influence of local sources is minimal, hence the sites are representative for a wider region allowing detection of long-term changes in atmospheric composition.

1.2 The measurements in relation to research and policy agreements

The Norwegian greenhouse gas and aerosol monitoring programme is set up to meet national and international obligations and needs for greenhouse gas and aerosol measurement data, both for the scientific community, national environmental authorities and global policy making.

Greenhouse gases: The Paris Agreement was negotiated and adopted by consensus at the 21st Conference of the Parties of the UNFCCC in Paris on 12th December 2015. The Paris Agreement entered into force on 4th November 2016. As of September 2021, as many as 191 of the 197 Parties to the

Convention, have ratified the Protocol[2]. The crucial aim of the Paris agreement is to keep the increase in the global average temperature to well below 2°C compared to pre-industrial levels and to pursue efforts to limit the temperature increase to 1.5°C. The EU Heads of State and Governments agreed in October 2014 on the headline targets and the architecture for the EU framework on climate and energy for 2030. As part of the European Green Deal, the Commission descded in July 2021 to raise the 2030 greenhouse gas emission reduction target, including emissions and removals, to at least 55% compared to 1990, and to be total zero in 2050. In the Norwegian "*Klimaloven*"[3] targets include a cut in greenhouse gas emissions by at least 50% and up to 55% by 2030 compared to 1990 levels[4].

Ozone depleting substances and their replacement gases: In 1987 the Montreal Protocol was signed and entered into force in 1989 in order to reduce the production, use and eventually emission of the ozone-depleting substances (ODS). The amount of most ODS in the troposphere is now declining slowly and is expected to be back to pre-1980 levels around year 2050. It is central to follow the development of the concentration of these ozone depleting substances in order to verify that the Montreal Protocol and its amendments work as expected. The development of the ozone layer above Norway is monitored closely, and the results of the national monitoring of ozone and UV is presented in "*Monitoring of the atmospheric ozone layer and natural ultraviolet radiation: Annual report 2020*" ([5]Svendby et al. 2021). The ozone depleting gases and their replacement gases are also strong greenhouse gases making it even more important to follow the development of their concentrations.

To control the new replacement gases, a historical agreement was signed on 15th October 2016 when negotiators from 197 countries agreed to reduce the production and consumption of hydrofluorocarbons (HFCs). The agreement was finalized at the United Nations (UN) meeting in Kigali, Rwanda, aiming to reduce the use of HFCs by more than 80% over the course of the twenty-first century. The agreement in Kigali represents an amendment of the 1987 Montreal Protocol. The HFCs can be up to 10 000 times as effective at trapping heat compared to carbon dioxide. Today HFCs account for a small fraction of the greenhouse gas emissions, have low concentrations and have had limited influence on the global warming up to now. However, the use of HFCs is growing rapidly and the projected HFC emissions could contribute up to 0.5°C of global warming by the end of this century if not regulated (Xu et al., 2013). The agreement in Kigali is an amendment to the Montreal Protocol and entered into force in January 2019 and is now legally binding for the countries that have ratified the amendment.

[2] https://unfccc.int/process/the-paris-agreement/status-of-ratification
[3] https://lovdata.no/dokument/NL/lov/2017-06-16-60
[4] Details here: http://ec.europa.eu/clima/policies/strategies/2030/ and here http://www.consilium.europa.eu/uedocs/cms_data/docs/pressdata/en/ec/145397.pdf
[5] Norwegian Environment Agency monitoring reports

1.3 The ongoing monitoring programme and the link to networks and research infrastructures

In response to the need to monitor greenhouse gases and ozone depleting substances, the *Norwegian Environment Agency* and *NILU – Norwegian Institute for Air Research (NILU)* first signed a contract commissioning NILU to run a programme for monitoring greenhouse gases at the Zeppelin Observatory, close to Ny-Ålesund in Svalbard in 1999. This national programme now includes monitoring of 46 greenhouse gases and trace gases at the Zeppelin Observatory in the Arctic, many of them also ozone depleting substances. In 2009, NILU upgraded and extended the observational activity at the Birkenes Observatory in Aust-Agder. From 2010, the Norwegian Environment Agency/NILU monitoring programme was extended to also include the new observations from Birkenes of the greenhouse gases CO_2 and CH_4 and selected aerosol observations particularly relevant for the understanding of climate change. Relevant components are also reported in "*Monitoring of long-range transported air pollutants in Norway, annual report 2020*" [5](Aas et al. 2021), this includes particulate and gaseous inorganic constituents, particulate carbonaceous matter, ground level ozone and particulate matter for 2020.

The locations of both sites are shown in Figure 1, and pictures of the sites are shown in Figure 3. The Zeppelin Observatory (78.90° N, 11.88° E) is located on the Zeppelin Mountain at 472 m above sea level on Spitsbergen. The unique location of the Zeppelin Observatory at Svalbard, together with the infrastructure of the scientific research community in Ny-Ålesund, makes it ideal for monitoring the global changes of concentrations of greenhouse gases and aerosols in the atmosphere. There are few local sources of emissions that can influence the observations, and the Arctic location is also important as the Arctic is a particularly vulnerable region. In relation to the 30 year anniversary of Zeppelin Observatory, NILU has written a very comprehensive paper where we detail the establishment of the Zeppelin Observatory including historical measurements of atmospheric composition in the European Arctic (Platt et al, 2021) (Figure 2). The paper presents a history of the measurements at the observatory and review the current state of the European Arctic atmosphere, including results from trends in greenhouse gases, chlorofluorocarbons (CFCs) and hydrochlorofluorocarbons (HCFCs), other traces gases, persistent organic pollutants (POPs) and heavy metals, aerosols and Arctic haze, and atmospheric transport phenomena.

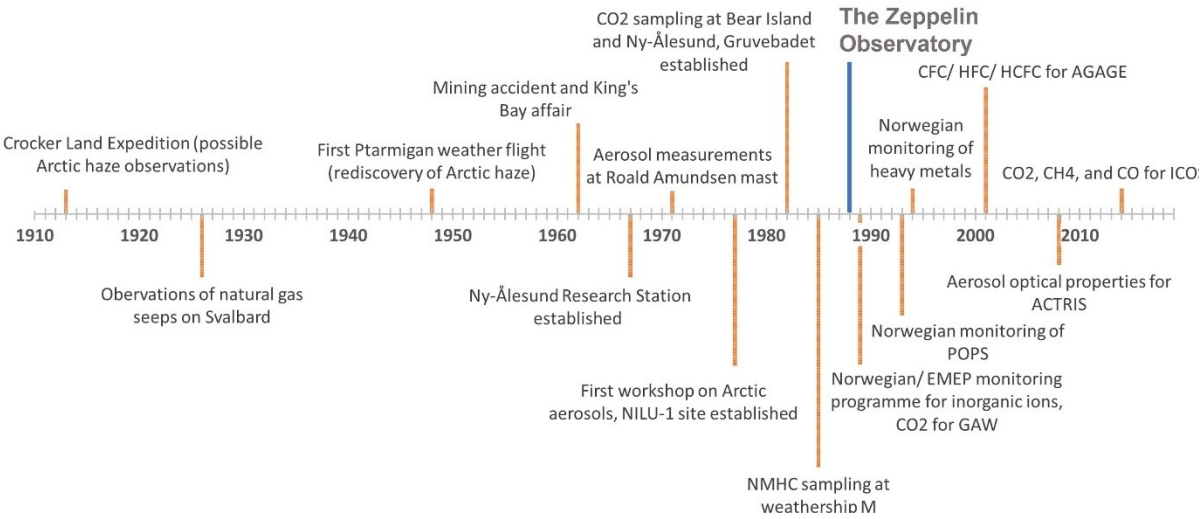

Figure 2: Timeline of various Arctic atmospheric observations, measurement sites, and later measurement programmes, see Platt et al. (2021)

The observations at the Birkenes Observatory complement the Arctic site. Birkenes Observatory is located in a forest area with few local sources. However, the Observatory often receives long-range transported pollution from Europe and the site is ideal to analyse the contribution of long range transported greenhouse gases and aerosol properties.

Figure 3: The two atmospheric observatories included in this programme, Zeppelin above and Birkenes to the left. A 75 m high mast was installed at Birkenes in 2020.

Data and results from the national monitoring programme are also included in various international programmes. Both sites contribute to EMEP (European Monitoring and Evaluation Programme) under the CLRTAP (Convention on Long-range Transboundary Air Pollution). Data from the sites are also reported to CAMP (Comprehensive Atmospheric Monitoring Programme) under OSPAR (the Convention for the Protection of the marine Environment of the North-East Atlantic, http://www.ospar.org), AMAP (Arctic Monitoring and Assessment Programme http://www.amap.no),

WMO/GAW (The World Meteorological Organization, Global Atmosphere Watch programme, http://www.wmo.int) and AGAGE (Advanced Global Atmospheric Gases Experiment).

Zeppelin and Birkenes are both included in two central European environmental research infrastructures (RI) focusing on climate forcers and air quality. International collaboration and harmonisation of these types of observations are crucial for improved processes understanding and satisfactory quality of data to assess trends. The two central RIs are ICOS (Integrated Carbon Observation System, https://www.icos-ri.eu) focusing on the understanding of carbon cycle, and ACTRIS (Aerosols, Clouds, and Trace gases Research InfraStructure, www.actris.eu) focusing on short-lived aerosol climate forcers and related reactive gases, and clouds. The participation in these RIs ensure required quality of the data with harmonised methods and measurements across Europe and also a global link to have comparable data and results on global scale. This is essential to reduce the uncertainty in trends and in the observed levels of the wide range of climate forcers. Overall, the networks EMEP and AGAGE, and the research infrastructures ACTRIS and ICOS are crucial for quality assurance and quality control of the Norwegian measurement data and instruments. All measurements included in this report follow the protocols, methodology and recommendations of these frameworks. This is a prerequisite for harmonised and comparable data on both European and global scale, see Table 2 at page 19. (Additionally, the implementation of Norwegian measurements in ICOS through the ICOS-Norway[6] project is described in the Appendix II.)

NILU hosts the data centres of the European Monitoring and Evaluation Programme (EMEP), ACTRIS and the WMO Global Atmosphere Watch (GAW) World Data Centre for Aerosol (WDCA) and GAW-World Data Centre for Reactive Gases (WDCRG), and numerous other projects and programs (e.g. AMAP, HELCOM). Data reported from these frameworks are accessible and can be downloaded directly from the EBAS data base: http://ebas.nilu.no. All data from the national monitoring programme and from these frameworks are reported to this database, and through this accessible for all types of users. It is important to highlight that NILU's work in ACTRIS and also hosting the WMO GAW World Data Centres for Aerosols and reactive trace gases, among many other synergy effects, ensures efficient dissemination of data on atmospheric aerosol properties collected within the Norwegian climate monitoring programme, to the scientific community. Among others, ACTRIS develops a primary standard for calibrating instruments measuring aerosol absorption, one of the properties of atmospheric black carbon, and developing quality standards for measuring the aerosol particle size distribution in order to further improve assessments of aerosol climate forcing. Another project relevant in this context is *ENVironmental Research Infrastructures building Fair services Accessible for society, Innovation and Research* (ENVRI-FAIR) [7] project. ENVRI-FAIR is an umbrella project for all environmental research infrastructures funded or supported by the EU under H2020. The objective is to make data FAIR, which means "*FAIR—**F**indable, **A**ccessible, **I**nteroperable, **R**eusable* (Wilkinson et al, 2016). One of its goals is to put data from the atmospheric, marine, tectonic, and biosphere domains into a common context by making the data interoperable, i.e. visible in common services. The efforts started with achieving this goal first within the atmospheric domain, and NILU is leading the implementation of FAIRness within the atmospheric domain, across all European Research Infrastructures.

Compiled key information on the national monitoring programme is listed in Table 2. From 2015 the programme was extended with 16 new greenhouse gases and reactive trace gases, mainly HFCs and non-methane hydrocarbons. For some of those, quality assured measurements were possible to retrieve from the start in 2010. From 2016 NF_3 and 4 PFCs and SO_2F_2 were also added. More detailed information on the monitoring programme and measurement frequencies are provided in Appendix II. For the measurements of aerosol properties more details are presented in chapter 3.

[6] https://no.icos-cp.eu
[7] http://envri.eu/envri-fair/

Table 2: Summary of the measurement programme, run by NILU, at Birkenes and Zeppelin Observatory. The green colour indicates the extension and components added to the program in 2016.

Component	Birkenes Start	Zeppelin Start	International network, QA programme in bold	Comment
Trace gases				
CO_2	2009	2012	**ICOS**	Measured at Zeppelin since 1988 by Univ. Stockholm. By NILU at Zeppelin since 2012, now included in the programme. Qualified as ICOS class 1 site since 2017. ICOS labelling in 2020 for Birkenes
CH_4	2009	2001	**ICOS**	ICOS labelling and implementation in 2017 for Zeppelin, 2020 for Birkenes
N_2O	-	2009	**ICOS**	ICOS labelling and implementation in 2017
CO	-	2001	**ICOS**	ICOS labelling and implementation in 2017
Ozone (surface)	1985	1989	**EMEP**	Reported in Aas et al. 2020.
CFCs		2001/ 2010 and later	**AGAGE**	*The measurements marked "*": these components are not within the required precision of AGAGE, but a part of the AGAGE quality assurance programme. This is related to the measurements in the period 2001-2010, before the installation of the Medusa instrument. After 2010, the measurements are with the same precision as the rest of the measurements in the AGAGE network. The compounds marked in green were included in the national monitoring programme from 2015, with harmonised time series and measurements back to 2010 when the Medusa instrument was installed at Zeppelin.
CFC-11*				
CFC-12*				
CFC-113*				
CFC-115*				
HCFCs				
HCFC-22				
HCFC-141b				
HCFC-142b				
HFC-125				
HFC-134a				
HFC-152a				
HFCs				
HFC-125				
HFC-134a				
HFC-152a				
HFC-23				
HFC-227ea				
HFC-236fa				
HFC-245fa				
HFC-365mfc				
HFC-32				
HFC-4310mee				
HFC-143a				
PFCs				
PFC-14				
PFC-116				
PFC-218				
PFC-318				
Halons				
H-1211				
H-1301				
H-2402				

Component	Birkenes Start	Zeppelin Start	International network, QA programme in bold	Comment
Trace gases				
Other chlorinated				
CH_3Cl				
CH_3Br				
CH_2Cl_2				
$CHCl_3$				
CCl_4				
CH_3CCl_3				
$CHClCCl_2$*				
CCl_2CCl_2*				
Other fluorinated				
SF_6		2001		
NF_3		2016		
SO_2F_2		2010		
VOCs		2010		
C_2H_6 – ethane			**ACTRIS,** EMEP	VOCs were included in the national monitoring programme from 2015, but the measurements are harmonised back to 2010.
C_3H_8 – propane				
C_4H_{10} – butane				
C_5H_{12} – pentane				
C_6H_6 – benzene				
$C_6H_5CH_3$ – toluene				
Aerosol measurements				
Absorption properties	2009	2015	**ACTRIS,** EMEP	Measured by Univ. of Stockholm at Zeppelin, New from late 2015
Scattering properties	2009	-	**ACTRIS,** EMEP	Measured by Univ. of Stockholm at Zeppelin
Number Size Distribution	2009	2010	**ACTRIS,** EMEP	Reported in Aas et al. 2019; M-1395/2019.
Cloud Condensation Nuclei	2012	-	**ACTRIS**	Zeppelin: In collaboration with Korean Polar Research Institute
Aerosol Optical depth	2010	2007	**AERONET, GAW-PFR**	Birkenes: AERONET, Ny-Ålesund: GAW-PFR
PM_{10}	2001		**EMEP**	Reported in Aas et al. 2021; M-2071.
$PM_{2.5}$	2001		**EMEP**	
Chemical composition -inorganic	1978	1979	**EMEP**	
Chemical composition - carbonaceous matter	2001		**EMEP**	

1.4 Greenhouse gases, aerosols and their climate effects

The Intergovernmental Panel on Climate Change (IPCC) is the UN body for assessing the science related to climate change. IPCC's Sixth Assessment Report (IPCC AR6) and the contribution from Working Group I "*Climate Change 2021: The Physical Science Basis*" was published in August 2021. This substantial climate assessment report presents most up-to-date physical understanding of the climate system and climate change, bringing together the latest advances in climate science, and combining evidence from paleoclimate, observations, process understanding, and global and regional climate simulations. Their conclusions are based on a variety of independent indicators, some of them are observations of atmospheric compositional change.

The first main statement in the "Summary for Policymakers" (SPM) is even clearer than in the AR5 report from 2013, and leaves no doubt about the substantial climate change and associated impact on the earth system

It is unequivocal that human influence has warmed the atmosphere, ocean and land. Widespread and rapid changes in the atmosphere, ocean, cryosphere and biosphere have occurred.
From IPCC AR6 – 2021 and the summary for policy makers

The overall conclusion with respect to the development of the concentrations of the main greenhouse gases is:

Observed increases in well-mixed greenhouse gas (GHG) concentrations since around 1750 are unequivocally caused by human activities.
Since 2011 (measurements reported in AR5), concentrations have continued to increase in the atmosphere, reaching annual averages of 410 ppm for carbon dioxide (CO_2), 20196. 1866 ppb for methane (CH_4), and 332 ppb for nitrous oxide (N_2O) in Land and ocean have taken up a near-constant proportion (globally about 56% per year) of CO_2 emissions from human activities over the past six decades, with regional differences (high confidence)
From IPCC AR6 – 2021 and the summary for policy makers

Human influence has warmed the climate at a rate that is unprecedented in at least the last 2000 years. Observed changes in global mean temperature since 1850-1900 period is slightly higher than 1 degree (IPCC 2021b, Figure 2.3). A detailed explanation of the new estimates of global warming to date is included in the Cross-Chapter Box 2.3 in IPCC, (2021a).

The observed warming is driven by emissions from human activities, with greenhouse gas warming partly masked by aerosol cooling. There is a new interesting illustrative figure showing the contribution from the changes in the various atmospheric components to the warming on the period 2010-2019, relative to the temperature in 1850-1900, see Figure 4.

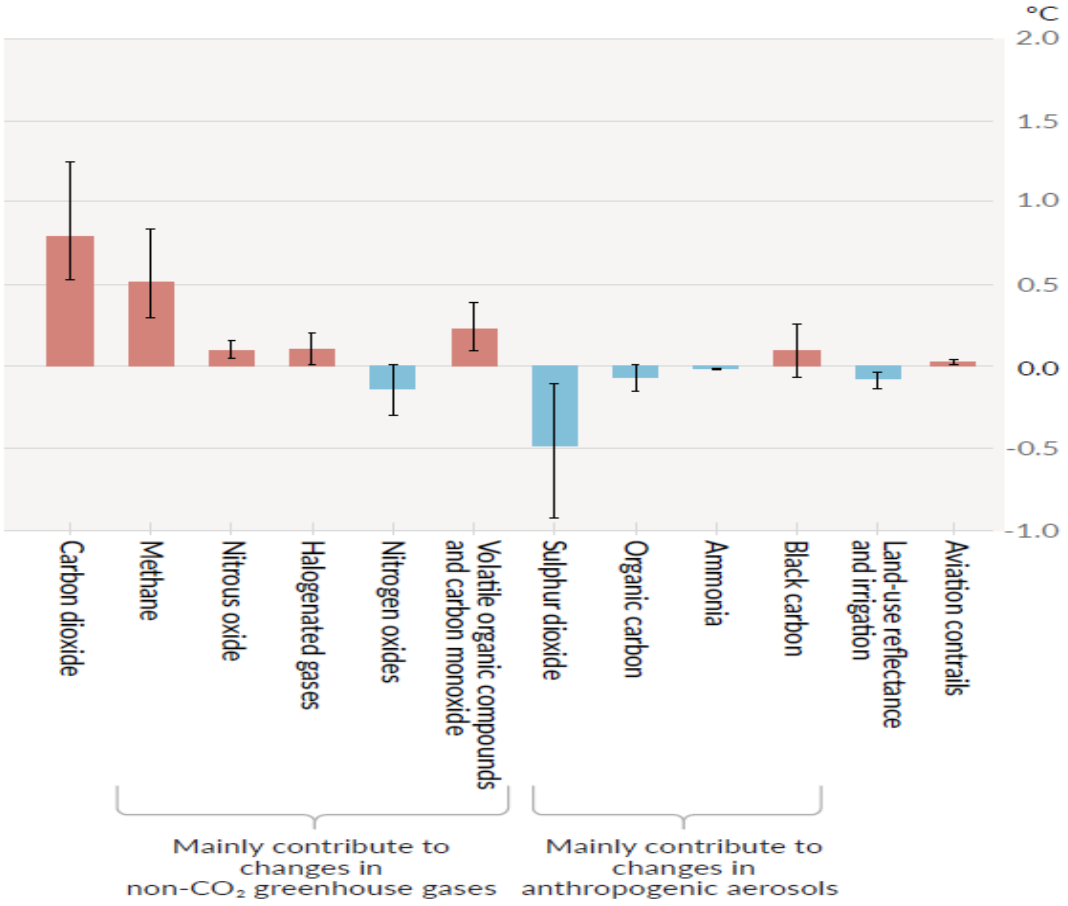

Figure 4: Assessed contributions to observed warming in 2010–2019 relative to 1850–1900. Figure from IPCC AR6, SPM – panel c of SPM.2 (IPCC, 2021b). The figure shows temperature changes from individual components of human influence, including emissions of greenhouse gases, aerosols and their precursors; land-use changes (land-use reflectance and irrigation); and aviation contrails. Whiskers show very likely ranges. Estimates account for both direct emissions into the atmosphere and their effect, if any, on other climate drivers. For aerosols, both direct (through radiation) and indirect (through interactions with clouds) effects are considered

The left part of the Figure shows the contribution from GHG gases, and the right part the impact from anthropogenic changes in aerosol components where e.g., sulfur dioxide and organic carbon is important for the cooling effect. The basic metric to compare the effect of the various climate change drivers is radiative forcing (RF). RF is the net change in the energy balance of the Earth system due to some imposed change. RF provides a quantitative basis for comparing potential climate response to different changes and Figure 4 is assessed from radiative forcing studies. Forcing is often presented as the radiative change from one time-period to another, such as pre-industrial to present-day. For many forcing agents the RF is an appropriate way to compare the relative importance of their potential climate effect. However, rapid adjustments in the troposphere can either enhance or reduce the perturbations, leading to large differences in the forcing driving long-term climate change. In the AR5 IPCC report it was also introduced a new concept, the effective radiative forcing (ERF). The ERF concept aims to take rapid adjustments into account, and is the change in net TOA (Top Of Atmosphere) downward radiative flux after allowing for atmospheric temperatures, water vapour and clouds to adjust, but with surface temperature or a portion of surface conditions unchanged. Figure 5 shows the ERF of the main components referring to a change in the atmospheric level since 1750, pre-industrial time.

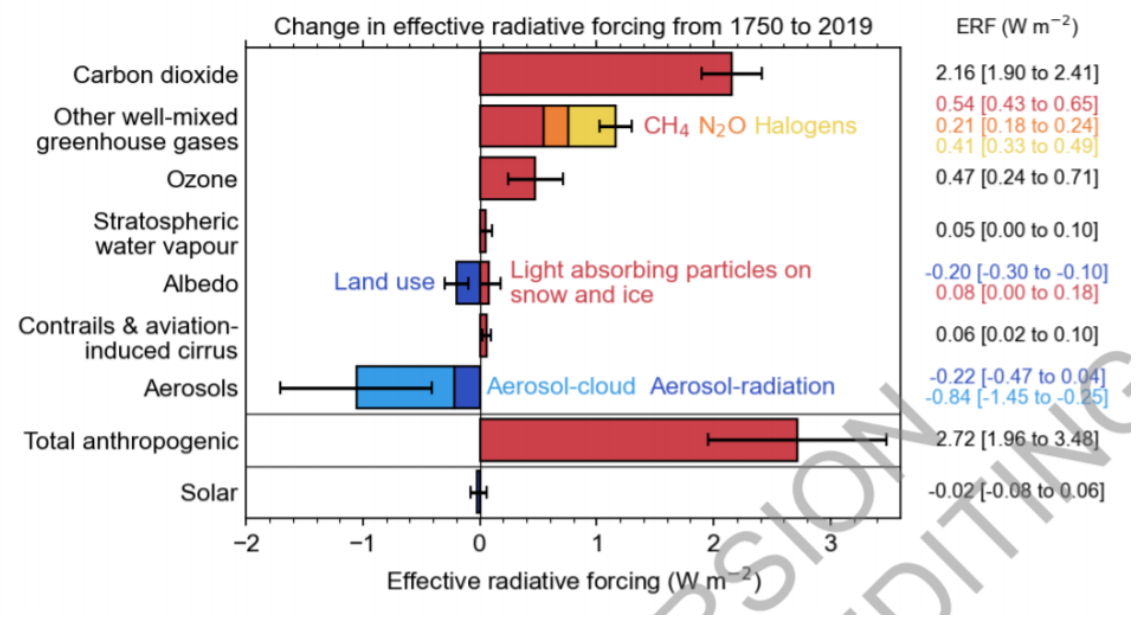

Figure 5: Radiative adjustments at top of atmosphere for seven different climate drivers as a proportion of 8 forcing. Tropospheric temperature (orange), stratospheric temperature (yellow), water vapour 9 (blue), surface albedo (green), clouds (grey) and the total adjustment (black) is shown. For the 10 greenhouse gases (carbon dioxide, methane, nitrous oxide, CFC-12) the adjustments are expressed as a 11 percentage of SARF, whereas for aerosol, solar and volcanic forcing they are expressed as a percentage of 12 IRF. Land surface temperature response (outline red bar) is shown but included in the definition of 13 forcing. (Taken from IPCC, 2021a Figure 7.6. The figure can still have some editorial changes and is not final (although the numbers are)).

Chapter 2, "Changing state of the climate system", presents all types of atmospheric and surface observations, including observations of greenhouse gases since the start of the observations in mid-1950s and changes in aerosols since the 1980s. This monitoring programme measures all relevant GHGs and optical and physical particle properties. Though the link and contribution to the international programmes EMEP, and AGAGE, the research infrastructures ACTRIS, ICOS the national program contribute to the trends and global mean data included in AR6 (see also section 2.1.1 at page 27 for details about the GHGs and in section 3.1 at page 78 for aerosols).

2 Norwegian observations of greenhouse gases

NILU measures 46 climate gases at the Zeppelin Observatory at Svalbard and 2 at Birkenes, in addition to surface ozone reported in Aas et al., 2020. The results and analyses of the climate gas measurements are presented in this chapter. Furthermore, observations of CO_2 for the time period 1988-2012 at Zeppelin performed by the Stockholm University - Department of Environmental Science and Analytical Chemistry (ACES), are included in this report.

Table 3 summarises the main results for 2020 and the trends over the period 2001-2020. The table also includes 2020 global annual mean values given in Bulletin of the American Meteorological Society (BAMS) (Lan et al., 2021).

Table 3: Greenhouse gases measured at Zeppelin and Birkenes; lifetimes in years, global warming potential (GWP) for 100 year horizon and annual mean for 2020, change last year, and trends per year over the measurement period. Red is increasing and blue is decreasing trends. Global means for 2020 taken from Bulletin of the American Meteorological Society (Lan et al., 2021) are included for comparison. All concentrations are mixing ratios in ppt, except for methane, nitrous oxide and carbon monoxide (ppb) and carbon dioxide (ppm).

Component		Lifetime	GWP-100	Global mean BAMS 2020	Annual mean 2020	Absolute change last year	Trend /yr
Carbon dioxide - Zeppelin	CO_2	-	1	-	414.1	2.3	2.4
Carbon dioxide - Birkenes					418.8	2.7	2.5
Methane - Zeppelin	CH_4	11.8	28	-	1968.7	15.7	6.4
Methane - Birkenes					1975.2	14.0	8.4
Carbon monoxide	CO	A few months	-	-	120.3	4.8	-1.1
Nitrous oxide	N_2O	109	273	-	333.4	1.30	0.99
Chlorofluorocarbons							
CFC-11	CCl_3F	52	5 560	224.5	225.5	0.00	-1.77
CFC-12	CF_2Cl_2	102	11 200	497.3	501.9	-3.74	-2.57
CFC-113	CF2ClCFCl2	93	6 520	69	69.5	-0.52	-0.63
CFC-115	CF_3CF_2Cl	540	9 600	-	8.8	0.03	0.03
Hydrochlorofluorocarbons							
HCFC-22	$CHClF_2$	11.9	1 960	246.4	257.1	1.12	5.61
HCFC-141b	$C_2H_3FCl_2$	9.4	860	24.2	26.1	0.33	0.51
HCFC-142b	CH_3CF_2Cl	18	2 300	21.6	22.8	-0.37	0.50
Hydrofluorocarbons							
HFC-125	CHF_2CF_3	30	3 740	33	35.6	3.35	1.74
HFC-134a	CH_2FCF_3	14	1 530	111.5	120.2	5.51	5.19
HFC-152a	CH_3CHF_2	1.6	164	6.2	10.5	-0.12	0.40
HFC-23	CHF_3	228	14 600	33.7	34.5	1.25	1.07
HFC-365mfc	$CH_3CF_2CH_2CF_3$	8.9	914	1.00	1.32	0.01	0.06
HFC-227ea	CF_3CHFCF_3	36	3 600	1.7	1.90	0.15	0.12
HFC-236fa	$CF_3CH_2CF_3$	213	8 690	-	0.22	0.01	0.01
HFC-245fa	$CHF_2CH_2CF_3$	7.7	858	-	3.73	0.20	0.21

Component		Lifetime	GWP-100	Global mean BAMS 2020	Annual mean 2020	Absolute change last year	Trend /yr
HFC-32	CH_2F_2	5.4	771	21.1	28.7	3.51	2.31
HFC-4310mee	$C_5H_2F_{10}$	17	1 600	-	0.31	0.01	0.01
HFC-143a	CH_3CF_3	51	5 810	24.9	27.1	1.51	1.54
Perfluorinated compounds							
PFC-14	CF_4	50 000	7 380	86.4	86.91	0.79	0.67
PFC-116	C_2F_6	10 000	12 400	4.94	4.99	0.08	0.09
PFC-218	C_3F_8	2600	9 290	0.7	0.71	0.02	0.02
PFC-318	c-C_4F_8	3200	10 200	1.82	1.87	0.07	0.06
Sulphurhexafluoride	SF_6	3 200	25 200	10.3	10.44	0.31	0.29
Nitrogen trifluoride	NF_3	569	17 400	-	2.48	0.26	0.26
Sulphuryl fluoride	SO_2F_2	36	4 630	-	2.74	0.11	0.10
Halons							
H-1211	$CBrClF_2$	16	1 930	3.11	3.27	-0.10	-0.07
H-1301	$CBrF_3$	72	7 200	3.31	3.39	-0.003	0.02
H-2402	$CBrF_2CBrF_2$	28	2 170	0.40	0.40	-0.01	-0.01
Halogenated compounds							
Chloromethane	CH_3Cl	0.9	5.5	546.6	508.58	0.84	-0.46
Bromomethane	CH_3Br	0.8	2.4	6.70	6.71	-0.02	-0.15
Dichloromethane	CH_2Cl_2	0.49	11.2	-	62.46	3.64	1.91
Trichloromethane	$CHCl_3$	0.5	20.6	-	13.05	0.77	0.22
Carbon tetrachloride	CCl_4	32	2200	77.5	77.26	-0.74	-0.93
Trichloroethane	CH_3CCl_3	5	161	1.4	1.47	-0.23	-1.70
Trichloroethene	$CHClCCl_2$	0.02	0.04	-	0.24	-0.06	-0.01
Tetrachloroethene	CCl_2CCl_2	0.30	6.3	-	2.09	-0.19	-0.11
Volatile Organic Compounds (VOC)							
Ethane	C_2H_6	Ca 78 days*		-	1512.88	-89.53	-
Propane	C_3H_8	Ca 18 days*		-	337.04	-116.78	-
Butane	C_4H_{10}	Ca 8 days*		-	118.95	-21.04	-
Pentane	C_5H_{12}	Ca 5 days*		-	41.04	-2.76	-
Benzene	C_6H_6	Ca 17 days*		-	59.23		-
Toluene	$C_6H_5CH_3$	Ca 2 days*		-	14.41		-

**The lifetimes of VOCs are strongly dependent on season, sunlight, other components etc. The estimates are global averages given in C. Nicholas Hewitt (ed.): Reactive Hydrocarbons in the Atmosphere, Academic Press, 1999, p. 313. The times series for these are short and the trend is very uncertain.*

Most greenhouse gases and other climate gases have numerous sources, both anthropogenic and natural. Trends and future changes in concentrations are determined by their sources and sinks, and in section 2.2 observations and trends of the monitored greenhouse gases with both natural and anthropogenic sources are presented in more detail. In Section 2.3 the detailed results of the ozone depleting substances with purely anthropogenic sources are presented.

For annual trend calculations we have used the method described in Appendix II. In order to estimate uncertainties, we have applied an updated method taking auto-correlated errors in the fitted model residuals into account. Appendix II also includes a description of the measurements at the Zeppelin and Birkenes Observatories in more detail. Generally, Zeppelin Observatory is a unique site for observations of changes in the background level of atmospheric components. All peak concentrations of the measured gases are significantly lower here than at other sites at the Northern hemisphere, due to the station's remote location. Birkenes is closer to the main source areas. Further, the regional vegetation is important for regulating the carbon cycle, resulting in much larger variability in the concentration level compared to the Arctic region.

2.1.1 IPCC AR6 forcing and annual mean value of the main GHG components compared to measurements at Zeppelin Observatory

This section relates the annual mean value of the main GHG components at Zeppelin to the values reported in AR6 IPCC published August 2021. The values used in AR6 refers to the 2019 year, and relates this to development since pre-industrial times, the previous report (AR5), and the year 2011. Comparison with measurements from Zeppelin Observatory is of particular interest. Zeppelin Observatory is monitoring the northern hemisphere but also global changes of concentrations of greenhouse gases and aerosols in the atmosphere.

In 2019, concentrations of CO_2, CH_4 and N_2O reached global mean levels of 409.9 ppm, 1866.3 ppb, and 332.1 ppb, respectively (IPCC, 2021a). The atmospheric concentration of these gases has increased from the pre-industrial time (1750) to 2019 by 47.3%, 156%, and 23.0%, respectively. These changes are larger than those between glacial and interglacial periods over the last 800,000 years, and illustrated in Figure 6.

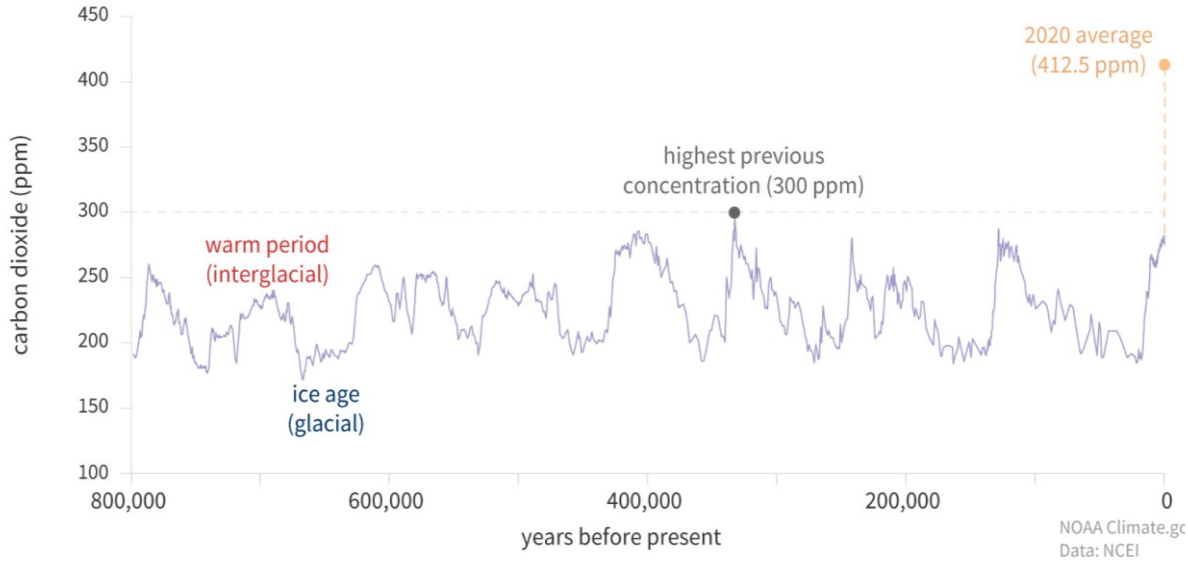

Figure 6: Global atmospheric CO_2 in parts per million (ppm) for the past 800,000 years. Graph by NOAA Climate.gov (https://www.climate.gov/news-features/understanding-climate/climate-change-atmospheric-carbon-dioxide)

The average annual CO_2 increase from 2000 through 2011 was 2.0 ppm/yr. From 2011 through 2019 it was 2.4 ppm/yr, which is higher than that of any comparable time periods since global measurements began (IPCC, 2021a).

The change in the GHG concentrations results in increase of the direct radiative forcing. The best estimate of the total radiative forcing from CO_2, CH_4, and N_2O in 2019 relative to 1750 is 2.9 W m^{-2}, an increase of 12.5% from 2011 (IPCC, 2021a). For CO_2, the forcing since 1750 is now 2.15 W m^{-2} since 1750 (compared to 1.88 Wm^{-2} in AR5) and the CH_4 forcing has increased to 0.54 Wm^{-2} since 1750 (from 0.48 Wm^{-2} in AR5). Radiative forcing from halogenated components in 2019 was 0.4 W m^{-2}, an increase of 3.5% since 2011. Table 4 summarizes the changes of CO_2, CH_4, and N_2O between 2011 and 2019 as included in AR6 (IPCC 2021a), considering measurements from the global NOAA and AGAGE networks, and from the Zeppelin Observatory.

Table 4: Comparison of atmospheric mixing ratios observed in 2011 and 2019, and relative change since 2011, estimated from the NOAA and AGAGE global networks presented in AR6 (IPCC, 2021a) and observations at the Zeppelin Observatory. Units are in ppm for CO_2 and ppb for CH_4 and N_2O.

Species	*Network/station*	*2011*	*2019*	*Change (%)*
CO_2	NOAA - *global mean*	390.5	409.9	5.0
	AGAGE - *global mean*	390.9	410.5	5.0
	Zeppelin	392.5	411.9	4.9
CH_4	NOAA - *global mean*	1803.1	1866.6	3.5
	AGAGE - *global mean*	1813	1877	3.5
	Zeppelin	1880	1953	3.9
N_2O	NOAA - *global mean*	324.2	331.9	2.4
	AGAGE - *global mean*	324.3	332.0	2.4
	Zeppelin	324.2	332.1	2.4

For CO_2 and CH_4 the annual mean values at Zeppelin are higher than the global means reported in AR6. This is due to the fact the Zeppelin is at the Northern Hemisphere, where the main emissions are. However, the percentage changes are at the same level. For CO_2, the data from NOAA and AGAGE show an increase of 5.0% from 2011 to 2019, whereas the measured change at Zeppelin is 4.9%. The CH_4 increase at Zeppelin (3.9%) is slightly higher than the global mean increases from NOAA and AGAGE (3.5%). For N_2O the measured increase from 2011 through 2019 from NOAA, AGAGE and Zeppelin are all 2.4%.

For the CFCs and other halogenated compounds there is also consistency between percentage changes measured at Zeppelin and data from AGAGE. For CFC-11, CFC-12, and CFC-113 the percentage 2011-2019 changes from AGAGE are -4.8%, -4.7%, and 6.3%, respectively. The corresponding changes at Zeppelin are -4.5%, -4.9%, and -6.2%. HFC-32 is the halogenated compound where the atmospheric concentration is growing fastest: from 2011 through 2019 AGAGE and Zeppelin reported increases of 304% and 284%, respectively. The concentration of HFC-125 has also increased dramatically from 2011 to 2019: changes of 186% and 174% are estimated from the AGAGE and Zeppelin data, respectively.

2.2 Climate gases with natural and anthropogenic sources

The annual mean concentrations for all gases included in the programme for all years are given in Appendix I, Table A 1 at page 130 All the trends, uncertainties and regression coefficients are found in Table A 2 at page 133. Section 2.2 focuses on the measured greenhouse gases that have both natural and anthropogenic sources.

2.2.1 Carbon dioxide (CO_2)

Key findings for CO_2: *CO_2 concentrations have increased in all years, in accordance with accumulation of gas in the atmosphere and the global development and increase in anthropogenic emissions. The annual CO_2 means in 2020 reached new record levels: 414.2 ppm at Zeppelin and 418.8 ppm at Birkenes. The increases from 2019 to 2020 are 2.3 ppm and 2.7 ppm, respectively. The annual atmospheric CO_2 increase continues to be high, with no sign of a reduced increase, nether at Zeppelin nor Birkenes Observatory.*

Carbon dioxide (CO_2) is the most important anthropogenic greenhouse gas, with a radiative forcing of 2.15 W m^{-2} since the year 1750 (IPCC, 2021a). This strong forcing is due to the large increase in concentration over the years. CO_2 is the end-product of the atmospheric oxidation of all main VOCs, and levels have increased by more than 50 % since preindustrial times. This is mainly due to emissions from fossil fuel combustion and land-use change.

On Emissions of CO_2

The Global Carbon Project[8] http://www.globalcarbonproject.org provides yearly updates on estimated emissions. CO_2 emissions are from fossil fuel burning (including oil, gas, coal and flaring) and cement production. Global fossil CO_2 emissions where 36.4 ± 2 $GtCO_2$ in 2019, a 61% increase compared to 1990 levels. Comparing the various periods, CO_2 emissions increased by 0.9 % per year from 1990 – 2000. Then for the next 10 years, the increase was 3.0% per year from 2000-2010, and recently from 2010-2018 it is 0.9% per year. The global growth is driven by the underlying changes at the country level, in particular the total emissions in China and India are increasing. Global fossil CO_2 emissions are projected to decline by about 7% in 2020. The main reduction is expected in USA (-12%), Europe (-11%) and a more stable development, with a small decrease in China (-1.7%.)

The global carbon project provides an estimate of the overall impact of COVID-19 on regional emissions. While China's emissions declined strongly during February 2020, emissions declines in the rest of the world reached their peaks in April. Global emissions from surface transport, especially road transport, were affected the most by the restrictions aimed at reducing infection rates. Global fossil CO_2 emissions have risen steadily over the last decades. While 2020 has witnessed an unprecedented drop, emissions will likely rebound in 2021.

The measurements

NILU started CO_2 measurements at the Zeppelin Observatory in 2012 and the results are presented in Figure 7, together with the time series provided by ITM, University of Stockholm, back to 1988. After upgrading Birkenes in 2009, there are continuous measurements of CO_2 and CH_4 from mid May 2009 also at this site.

The atmospheric daily mean CO_2 concentration measured at the Zeppelin Observatory for the period mid 1988-2020 is presented in Figure 7 (upper panel), together with the 2009-2020 time series for Birkenes in the lower panel.

[8] Used with permission of the Global Carbon Project under the Creative Commons Attribution 4.0 International license

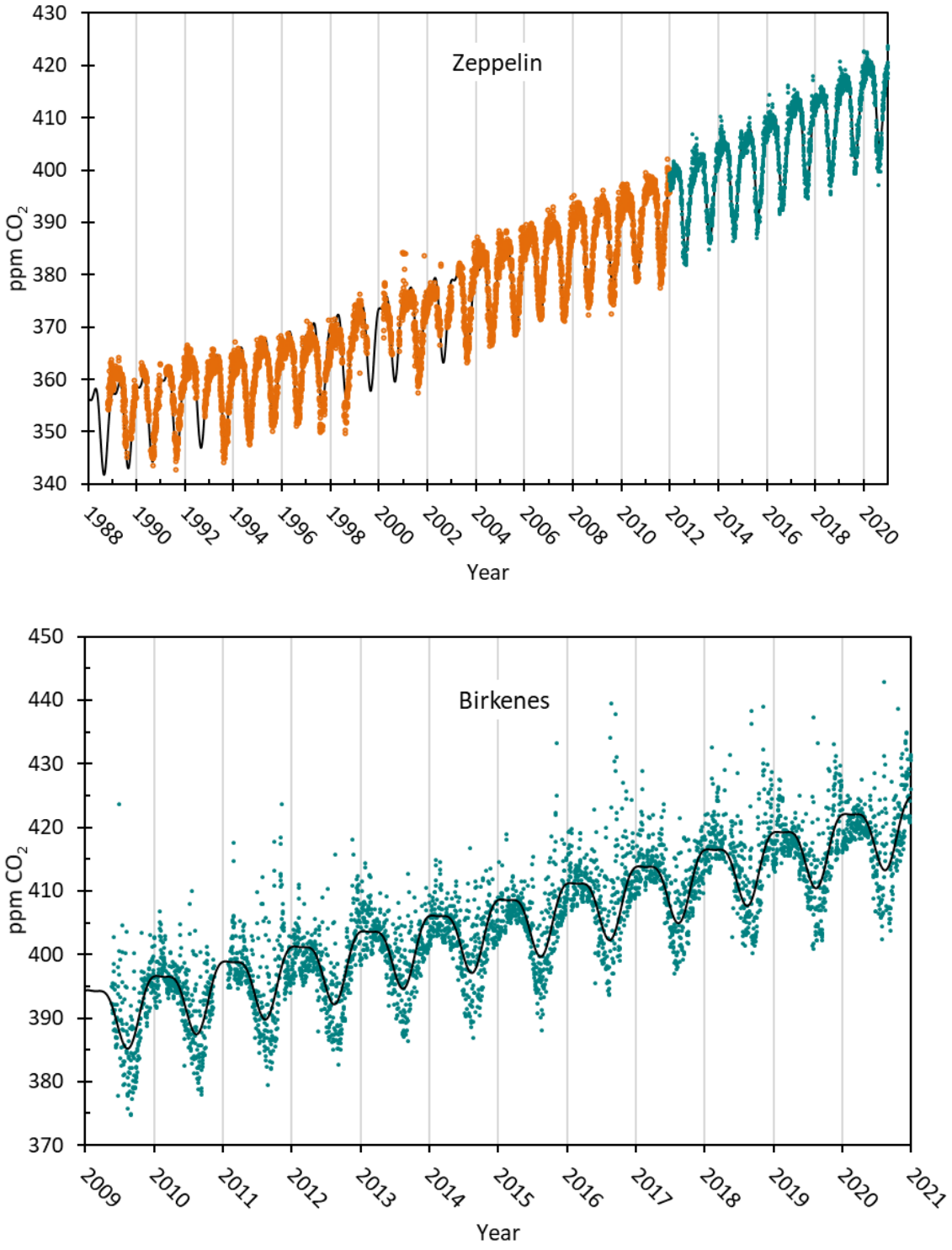

Figure 7: The atmospheric daily mean CO_2 concentrations measured at the Zeppelin Observatory for the period mid 1988-2020 are presented in the upper panel. Prior to 2012, ITM University of Stockholm provided all data, shown in orange. The green dots represent measurements from the Picarro instrument installed by NILU in 2012. CO_2 measurements at Birkenes are shown in the lower panel, the green dots are daily mean concentrations. The black solid line is empirical fitted CO_2 mixing ratio.

The results show continuous increase since the start of the observations at both sites, and as can be seen there is larger CO_2 variability at Birkenes than Zeppelin. At Zeppelin the largest variability is during winter/spring, whereas Birkenes has large variability all year around. In summer there is also a clear diurnal variation with high values during the night and lower values during daytime (not shown). This is mainly due to changes between plant photosynthesis and respiration, but also the general larger meteorological variability and diurnal change in planetary boundary layer, particularly during summer, contributes to larger variations in the concentrations. In 2020, NILU installed a 75 m mast, to also measure above the trees (see the appendix and Figure 59 included there at page 155) to limit these influences.

In addition to the diurnal variations, there are also episodes with higher CO_2 levels at both sites due to long range transport of pollution. In general, there are high levels when the meteorological situation results in transport from Central Europe or United Kingdom at Birkenes, and from central Europe or Russia at Zeppelin.

The maximum daily mean CO_2 value in 2020 at Zeppelin was 423.81 ppm, measured on 29th December. During this period the wind direction and atmospheric circulation pattern indicate that air was transported from Russia and Eastern Europe, then shifting to central part of Norway and North Europe on 30th December. At Birkenes the highest daily mean value in 2020 was as high as 442.9 ppm, measured 7th August. This day the air at Birkenes had mainly been transported from Germany, shifting from the UK and Atlantic sector the day before.

Figure 8 shows the development of the annual mean concentrations of CO_2 measured at Zeppelin for the period 1988-2020 (in orange) together with the values from Birkenes (in green) for the period 2009-2020. The global annual mean values as given by WMO (WMO, 2020) are in black. The yearly annual changes at Zeppelin and Birkenes are shown in the lower panel.

The annual mean CO_2 values at Birkenes and Zeppelin are higher than the global annual mean value as there are more anthropogenic sources and pollution at the Northern hemisphere. The mixing of air between the two hemispheres takes about 2-3 years' time. The CO_2 annual mean in 2020, shown in Figure 8 (upper panel), was 418.8 ppm and 414.2 ppm at Birkenes and Zeppelin, respectively. The annual CO_2 changes illustrated in Figure 8, lower panel, shows an increase of 2.3 ppm at Zeppelin from 2019 to 2020. At Birkenes the CO_2 increase from 2019 to 2020 was 2.6 ppm. The global mean annual CO_2 increase from 2019 to 2020 is not yet published.

Trend analyses based on method described in Appendix II show that CO_2 at Birkenes and Zeppelin increased by 2.5 and 2.4 ppm/yr, respectively, in line with the average annual increase published in AR6 IPCC, 2021a) This corresponds to an of ca 0.6 %/yr. These trend analyses are based on data from Picarro instruments, only (which were installed by NILU in 2012). If we use the entire Zeppelin time series back to 1988, the trend is less pronounced (~0.5%/yr), indicating that the CO_2 increase has intensified over the last decade.

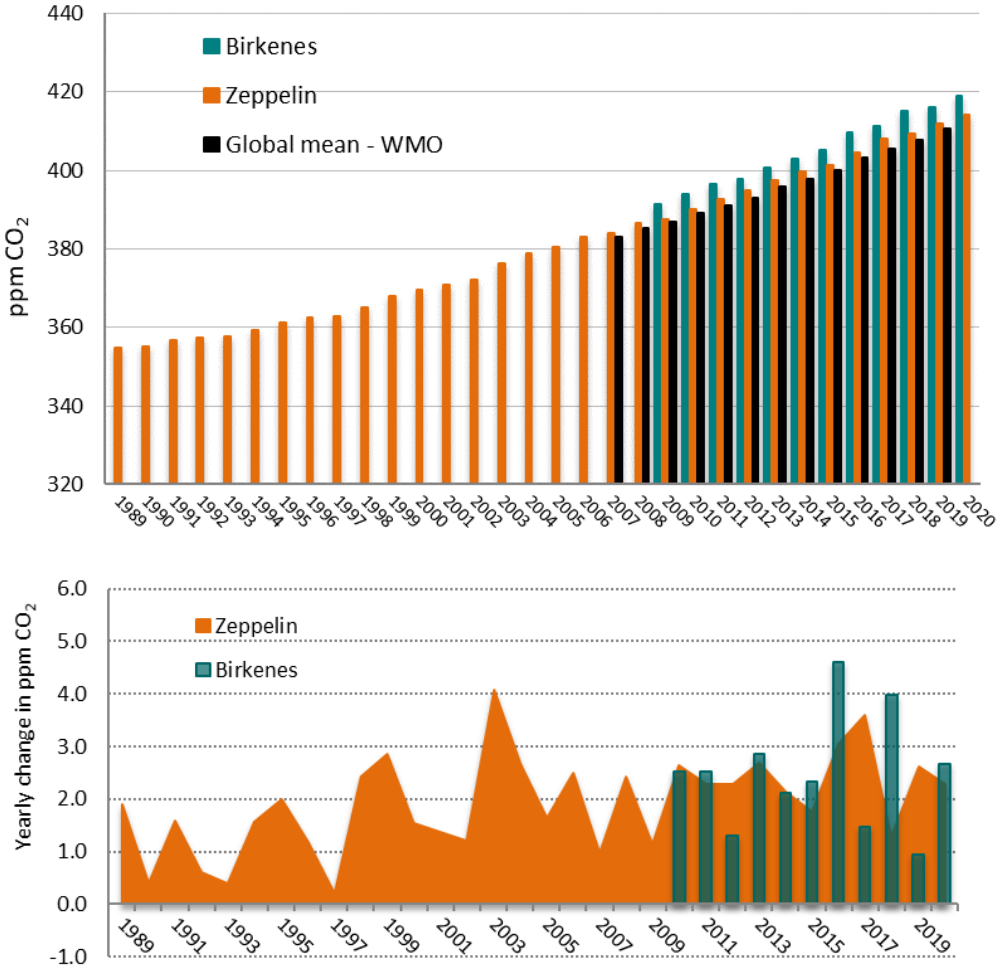

Figure 8: Upper panel: the annual mean concentrations of CO_2 measured at Zeppelin Observatory for the period 1989-2020 shown in orange. Prior to 2012, ITM University of Stockholm provides all data. The annual mean values from Birkenes are shown as green bars. The global mean values as given by WMO (2020) are included in black. The yearly annual increases are shown in the lower panel, orange for Zeppelin, green for Birkenes.

It is interesting to note that in 2018, Europe experienced one of the worst droughts of the last 20 years. The extensive heatwave and drought in 2018 had a negative impact on vegetation across Western and Northern Europe. An exceptionally long period of high temperatures and little precipitation resulted in an unprecedented browning of vegetation. It also meant that Europe's vegetation took up limited or no CO_2 from the atmosphere in that year. We are not able to see the direct sign of this in the observation time series at e.g. Birkenes, but it is well documented (Thompson et al, 2020, Ramonet et al 2020).

2.2.2 Methane (CH_4)

Key findings for Methane: *In 2020, Zeppelin saw a record year to year increase of 15.7 ppb since 2019 to reach a record level of 1968.7 ppb. At Birkenes the annual mean value in 2020 was 1975.2 ppb, 14.0 pbb higher than previous year, also a significant increase. These strong increase in methane concentrations are of great concern as the processes behind it are not well constrained and can be due to climate feedback emission processes.*

Methane (CH_4) is the second most important greenhouse gas from human activity after CO_2. The IPCC reported a radiative forcing is 0.54 W m^{-2} since 1750 and up to 2019 (IPCC, 2021a). Etminan et al. (2016) presented revised forcing estimates for all main greenhouse gases, and for CH_4 this resulted in 25% stronger forcing than given in the IPCC Fifth Assessment Report, and the updates are taken into account in AR6 (IPCC 2021a).

In addition to being a dominant greenhouse gas, methane also plays central role in atmospheric chemistry. The atmospheric lifetime[9] of methane is 11.8 years (IPCC 2021a), when indirect effects are included, as explained in section 1.4, for the direct effects ca 9-10 years.

The average CH_4 concentration in the atmosphere is determined by a balance between emission from the various sources and reaction and removal by free hydroxyl radicals (OH) to produce water and CO_2. A small fraction is also removed by surface deposition and reaction Cl. Since the reaction with OH also represents a significant loss path for the OH itself, additional CH_4 emission will consume additional OH thereby increasing its own lifetime, implying further increases in atmospheric CH_4 concentrations (and in those of all other compounds significantly removed by OH, i.e. most VOCs) (Isaksen and Hov, 1987; Prather et al., 2001).

The concentration of CH_4 was, after a strong increase during the 20th century, relatively stable over the period 1998-2006 (Dalsøren et al, 2016). The global average change was close to zero for this period, also at Zeppelin. Since 2005 a strong increase in the CH_4 levels is evident from our observations both at Zeppelin and Birkenes as well as observations at other sites, and in the global mean (WMO, 2020).

On Emissions of CH_4

The Global Carbon Project http://www.globalcarbonproject.org rereleased new and updated emission estimates and global methane budget 15th July 2020. No updates are released after this. The emission estimates are for 2017, and also compared to mean emissions for the period 2000-2006. According to the Global Carbon Project and the underlaying peer-reviewed papers (Saunois et al, 2020 and Jackson et al. 2020) the distribution between natural and anthropogenic sources CH_4 is approximately 40% natural sources, and 60% of the sources are direct result of anthropogenic emissions. The main anthropogenic sources include emissions from agriculture (e.g., rice paddies, ruminant animals), waste and extraction and combustion of fossil fuels (oil, gas and coal). CH_4 is the principal component of natural gas and leakage from pipelines and off- and on-shore installations are a known source of atmospheric CH_4. The main natural sources are tropical, boreal and Arctic wetlands, freshwater systems (lakes and rivers), and geological sources like geological sources such as terrestrial and marine seeps and volcanoes. Of natural sources there is a large unknown potential methane source under the ocean floor, so called methane hydrates and seeps.

Global Carbon Project report (Saunois et al, 2020) that the increasing anthropogenic methane emissions arise approximately equally from agricultural and fossil fuel sources. According to the estimate from this project, anthropogenic emissions dominate in the northern mid-latitudes, with the highest contribution from agriculture and waste emissions (42 % of total emissions), closely followed by fossil fuel emissions (31 % of total emissions). Boreal regions are largely dominated by wetland

[9] Time taken to decay to 1/e, 1/2.7, of original levels

emissions (60 % of total emissions). The situation is different in the polar regions, and southern hemisphere, and also forth another hemisphere there are large uncertainties (see also section 2.2.2.3.). Despite rapidly warming air temperatures (World Meteorological Organization 2019), methane emissions from northern high-latitude systems (>60°N) were virtually unchanged in 2017 relative to the average value for 2000–2006. Other regions contributed the most to greater methane emissions in 2017 compared with 2000–2006. These were Africa and the Middle East; China; and South Asia and Oceania increased their emissions. Here, agriculture and waste contributed 60% of this increase and fossil fuels the remaining 40%, with a slight decrease estimated for biomass and biofuel burning. It is worth noting that Europe is the only region with a slight decrease in CH_4 emissions in 2017 compared to the period 2000-2006.

Wetlands and freshwater systems more broadly are the largest source of methane but also the greatest source of uncertainty in the current global methane budget. Furthermore, a large unknown for the future arises due to a possible feedback via thawing permafrost which can not only release trapped CH_4 to the atmosphere directly, but more importantly increase CH_4 due to increased mobilisation of carbon and changes to hydrological conditions, i.e. wetland formation. The balance between the release of CO_2 and CH_4 from thawing permafrost, will thus also depend on the precipitation and changes in moisture.

The measurements

Figure 9 shows daily mean observations of CH_4 at Zeppelin since the start in 2001 (upper panel) and Birkenes since start in 2009 (lower panel). As can be seen from the figures there has been an increase in the concentrations of CH_4 at both sites the last years, and in general the concentrations are higher at Birkenes than at Zeppelin. The highest ambient CH_4 concentration ever detected at Zeppelin, 2036 ppb, was measured on the 29th December 2020. The transport pattern on this day indicates a strong influence from northern part of Russia/West Siberia. Fugitive emissions from Russian gas installations are normally the source of such high CH_4 values. The maximum CH_4 daily mean value recorded at Birkenes in 2020 was 2082 ppb, measured 6th December.

For both Zeppelin and Birkenes, the seasonal variations are clearly visible, although stronger at Birkenes than Zeppelin. This is due to longer distance to the sources at Zeppelin, and thus the sink through reaction with OH dominates the variation. The larger variations at Birkenes are explained by both the regional sources in Norway, as well as a stronger impact of pollution transported from central Europe or UK. For the daily mean in Figure 9, the measurements show very special characteristics in 2010 and 2011 at Zeppelin. There is remarkably lower variability in the daily mean in 2011 with fewer episodes than the typical situation in previous and subsequent years (e.g. summer/autumn 2012). This seems to be due to less impact of episodes from Northern Russia (Thompson *et al*, 2017). A similar situation is evident also in 2018 at Zeppelin, resulting in less increase than expected and reported at other sites, including Birkenes.

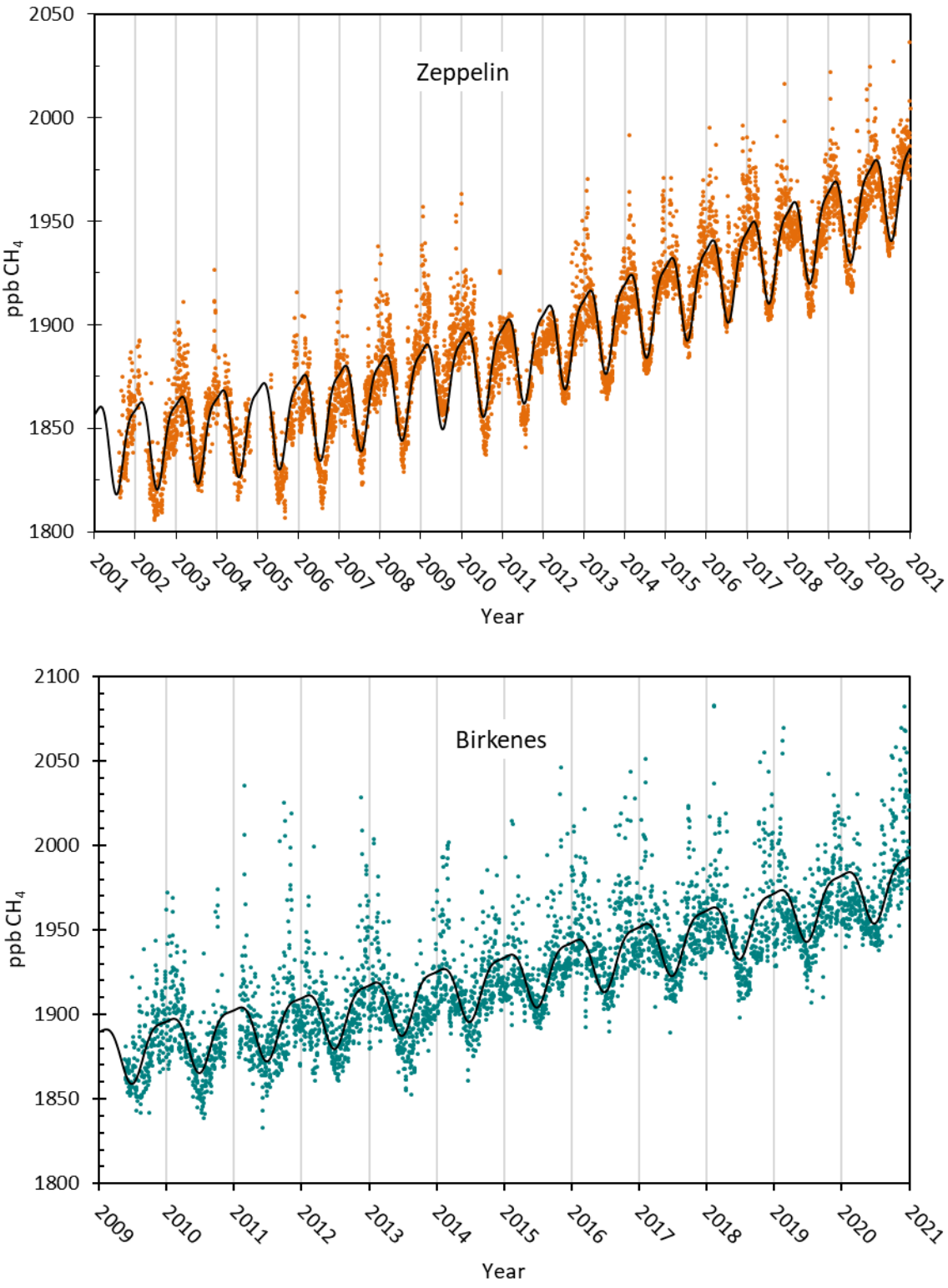

Figure 9: The upper panel shows observations of daily averaged methane mixing ratio for the period 2001-2020 at the Zeppelin Observatory. The black solid line is empirical fitted methane mixing ratio. The lower panel shows the daily mean observations for Birkenes (green dots).

At Zeppelin there are now 20 years of data for which the trend has been calculated. To retrieve the annual trend in methane for the entire period the observations have been fitted by an empirical equation, shown as the black solid line in Figure 9. This corresponds to a trend of 6.4 ppb/yr or 0.3%/yr. For Birkenes, shown in Figure 9 lower panel, the time series is shorter and the trend analysis is less accurate. The trend calculations demonstrate a CH_4 increase of 8.4 ppb/yr (0.4%/yr) for the period 2009-2020.

The annual methane increases over the last years is visualised in Figure 10, showing the CH_4 annual mean concentration at Zeppelin for the period 2001-2020 (orange) and Birkenes for the period 2009-2020 (green). The global mean values given by WMO from 2005-2019 (WMO, 2020) are included for comparison. The big difference between global mean, and the observations at Zeppelin and Birkenes is due to the fact that most emissions are in the Northern hemisphere.

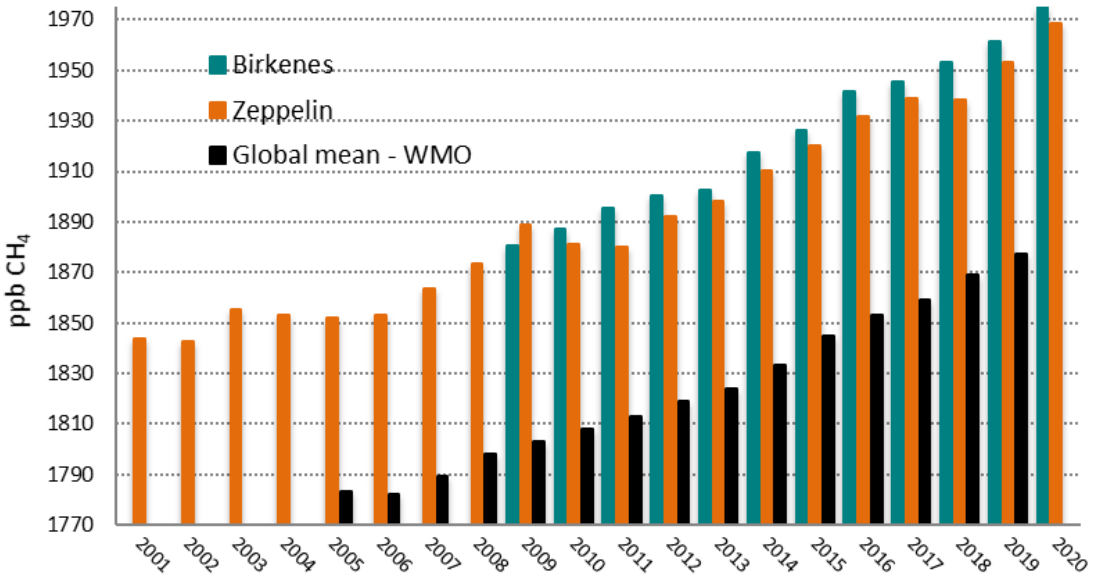

Figure 10: Development of the annual mean mixing ratio of methane in ppb measured at the Zeppelin Observatory (orange bars) for the period 2001-2020, Birkenes for the period 2010-2020 in green bars, compared to global mean provided by WMO as black bars (WMO, 2020).

The annual means are based on the measured methane values, however, model fitted values are used to fill in gaps if measurements are missing. Figure 10 demonstrates a gradual increase in the concentrations of methane at both Zeppelin and Birkenes the last decade. The annual mean concentrations in 2020 were 1975 and 1968.7 at Birkenes and Zeppelin, respectively. For Birkenes, there is an increase of 14.0 ppb since 2019. For Zeppelin, the increase is as high as 15.7 ppb since 2019. This is the highest annual increase detected at Zeppelin ever leading to a record in both concentration and change from last year.

2.2.2.1 In depth analyses of the CH_4 record year 2020 at Zeppelin Observatory

The year 2020 is a record year at Zeppelin for the levels of CO_2, and CH_4, also CO has a stronger increase than earlier years. CH_4 is in a special situation where the annual increase is stronger than ever from 2019 to 2020. The sources of CH_4 are many fold, also related to Arctic climate change and feedback see also section 2.2.2.2 and 2.2.2.3.

Figure 11 shows the observations of daily averaged methane mixing ratio for the 2020 at the Zeppelin Observatory in the upper panel. The Figure clearly shows the strong increase starting in summer, and lasting throughout almost the rest of the year. In particular, there is a period with high values in July, and then on top of that, an extreme episode 6th August. For the episode 6th August, we have explored also other components and the transport pattern. In the middle panel in Figure 11 the strong increase in CH_4 during summer is depicted to the left and the associated CO_2 and CO to the right. There is a dip in CO_2 and an increase in CO. The lower panel shows the transport of air these days, from relatively clean Arctic Air 4th August to transport form a source region is dominated by oil and gas installations, and extensive flaring episodes (Stohl et al 2013) the 8th August.

Interestingly, the concertation continues to be high thought the autumn months, until November. It seems that this is explained by transport pattern and air mass originating from Siberia, with both wetland sources, CH_4 craters at the Yamal peninsula (Moskvitch, 2014) and oil and gas installations.

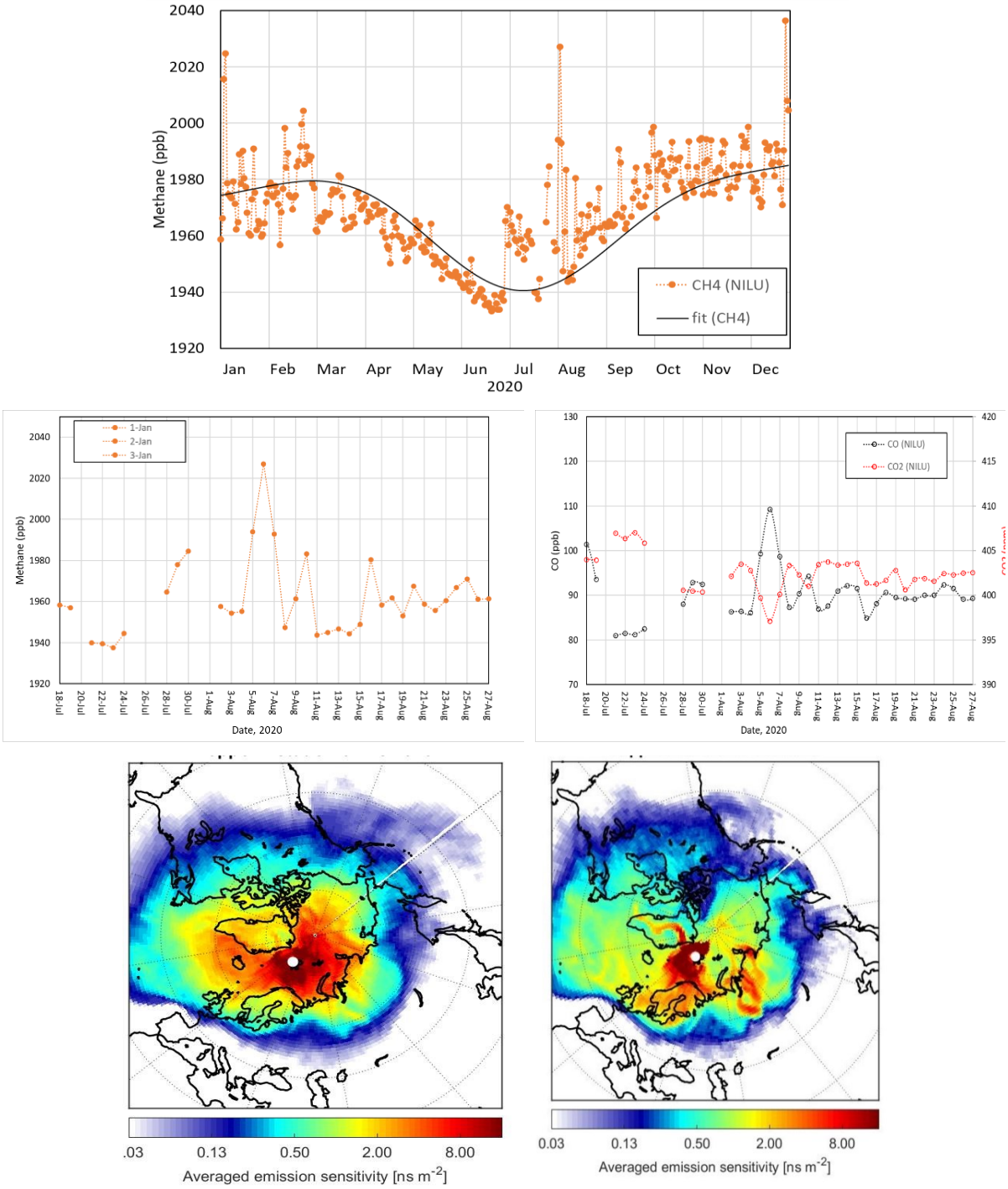

Figure 11: The upper panel shows observations of daily averaged methane mixing ratio for the 2020 at the Zeppelin Observatory. The black solid line is empirical fitted methane mixing ratio. The mid panels shows the daily mean observations over summer with a strong Ch4 episode to the left, and associated CO_2 and CO. Bottom panels show sensitivity to surface emissions by area (darker red regions more likely to influence measurement time series) for the whole month (left) and during the episode (right).

2.2.2.2 *Observations of the atmospheric $\delta^{13}C_{CH4}$ and discussion of potential change in CH_4 sources*

The isotopic signature of CH_4 (expressed as $\delta^{13}C_{CH4}$) varies by emission source (France et al., 2016, see Figure 12) and measurements of the isotopic signature provides very valuable information for the understanding of the development of CH_4 sources, complementing other measurements (e.g. CH_4, CO and ethane). As can be seen from Figure 12 the isotopic signatures of CH_4 from e.g. biomass burning is different from natural gas. Leaks from gas installations, world-wide, both onshore and offshore might be an increasing source. Hence, it is essential to find out if the increase since 2005 is due to high emissions from point sources, or if it is caused by newly initiated processes releasing methane to the atmosphere e.g. the thawing of the permafrost layer or processes in the ocean, both related to permafrost and others. As a part of a research project under Norwegian Research Council (2011-2013[10]) NILU initiated measurements of $\delta^{13}C_{CH4}$ at Zeppelin in the year 2012 to provide more insight into Arctic sources of CH_4, and potential changes. The continuation of these measurements was implemented into the Norwegian Monitoring programme in 2017. **Error! Reference source not found.** s hows the full time series of $\delta^{13}C_{CH}$ since May 2012 (red dots) to the end of 2020, together with ambient CH_4 concentrations (blue line) measured at the Zeppelin Observatory. The observations are mainly 2 times per week, performed in the morning. (For details about the measurements, see Appendix II).

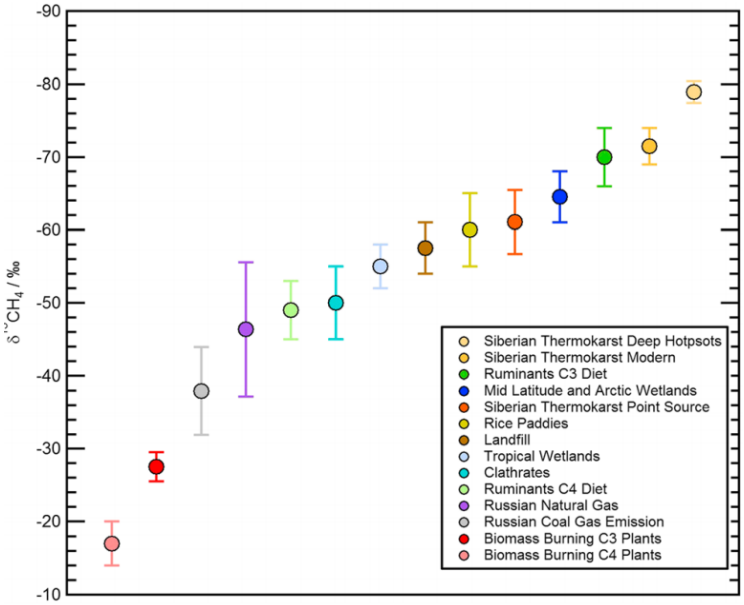

Figure 12:Isotopic ranges of $\delta^{13}C_{CH4}$ for a variety of CH4 sources as given in France et al, 2016.

A clear reduction (shift towards more negative values) in $\delta^{13}C_{CH4}$ is evident after 2012, parallel to the increase in the ambient concentration. Back in the 1980's, $\delta^{13}C_{CH4}$ shifted to more positive values, indicative of gas leaks and coal emissions (as $\delta^{13}C_{CH4}$ of fossil fuels is slightly higher than the ambient average), but it seems that increases in CH_4 concentrations since 2005 have been accompanied by a negative shift in $\delta^{13}C_{CH4}$, as illustrated in **Error! Reference source not found.** until the start of 2019. H owever, since 2019, this seems to have stopped, and the development is more stable now.

These recent negative shifts in ambient $\delta^{13}C_{CH4,}$ and increases in the CH_4 mixing ratio imply changes in the balance of sources and sinks, i.e. since changes in total fossil fuel emissions cannot account for a negative shift they also cannot entirely account for increases in the mixing ratio. Hence the development in $\delta^{13}C_{CH4}$ observed at Zeppelin suggests a role for biosphere and/or agriculture (wetland or ruminant) emissions, since these do have strongly negative $\delta^{13}C_{CH4}$ compared to ambient values and fossil sources. Changes in the sink (reaction with hydroxyl radicals, OH) is also a possibility. It is worth noting that as the major sink for almost all atmospheric Volatile Organic Compounds (VOCs), changes in OH would have profound implications for the whole atmosphere. There are a few signs of that. Ethane and methane are emitted together from fossil oil and gas sources. If fossile oil and gas is the main cause on increase, both components would experience that. Accordingly, the global decrease in ethane supports the hypothesis that wetland changes is a large contributor to the change in CH_4.

[10] https://www.forskningsradet.no/prosjektbanken/#/project/NFR/207587

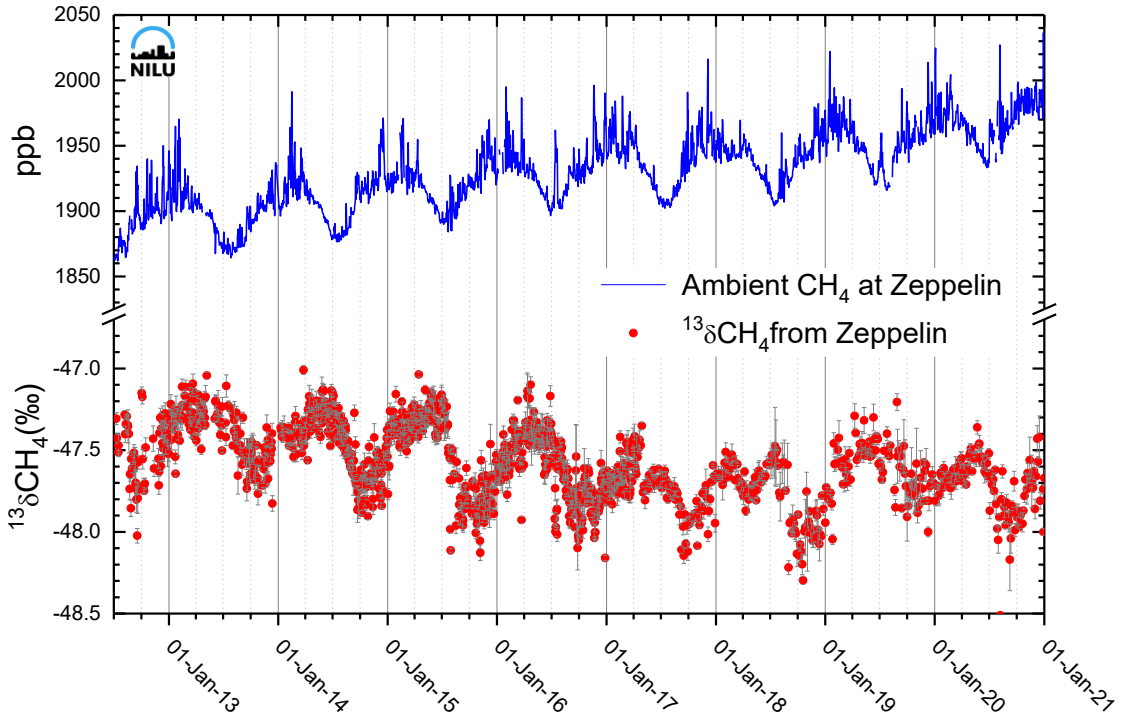

Figure 13: Long term measurements of methane (CH_4, blue) and the ^{13}C isotopic signature of CH_4 ($\delta^{13}C$-CH_4, red) at the Zeppelin Observatory, Svalbard 78°N.

Additionally, recent and ongoing scientific discussions point in the direction of increased emissions from wetlands located both in the tropical region and in the Arctic region. Thawing of permafrost, both in terrestrial regions and in marine region, might introduce new possible methane emission source initiated by the temperature increase the last years in the Arctic region, but the new revised methane budget does not support this (see section 0). Interestingly, from 2019 there is no change in the isotopic shift. This indicates that the relative change among sources has stopped, at least for this period.

Gas hydrates at the sea floor are widespread in thick sediments in this area between Spitsbergen and Greenland. These gas hydrates can decompose if temperatures increase or pressure decreases. Hence, if the sea bottom warms or sea level decreases (e.g. due to raising of the sea bed as the Greenland Ice sheet melts), this might initiate further emissions from this source. This was the core of the large polar research project *MOCA - Methane Emissions from the Arctic OCean to the Atmosphere: Present and Future Climate Effects*[11], which started at NILU in October 2013, and was finalized spring 2017. NILU is starting a new project in 2021 to further explore the global and Arctic methane budget, see section 2.2.2.3 for more information about REGAME.

To summarise, isotopic signatures provide very valuable data for understanding the development of the source of CH_4, but careful interpretation of observational data and emission inventories is required before assigning observed shifts to a particular source. The observations in 2019 and 2020 indicate that a relative change among sources have stopped, at least for this period. This further demonstrates the need for observational data on emission fluxes from the large natural reservoirs. There is most likely a combination of causes explaining the increase in methane the last years, and the dominating reason is not clear. A possible explanation is increased methane emissions from wetlands and agriculture, both in the tropics as well as in the Arctic region, in addition to increases in emission from the fossil fuel industry in some areas, but this alone cannot explain the development in the isotopic signature of CH_4 at Zeppelin.

[11] http://moca.nilu.no/

2.2.2.3 Reliable global methane emissions estimates in a changing world-REGAME

Increases in atmospheric methane (CH_4) since 2007 decrease the effectiveness of current measures undertaken to meet the Paris Agreement goal of limiting warming to 2°C. This urgently needs better assessment. Furthermore, uncertainties in sources of CH_4 under climate change limit our knowledge of future needed abatement measures. The NFR-funded REGAME project is a large-scale interdisciplinary project beginning in 2021 with the aim of providing a reliable assessment of the global atmospheric methane budget.

To better constrain the global methane budget, we will include isotopic time series, and for the first time, satellite data fields from Sentinel 5P in inversion models (in collaboration with the University of Vienna). To investigate the effects of changing atmospheric chemistry on methane sources, and particularly the main methane sink, the OH radical, we collaborate with CICERO and will use the OsloCTM model, again incorporating isotopic time series.

Furthermore, according to the latest IPCC report, the Arctic is warming at more than twice the global rate. Increases in extreme heat events, fire regimes, and permafrost thaw have accompanied this warming, all of which can contribute to increased methane (CH_4) emissions. Sub-sea CH_4 seepage (see box) is also anticipated to increase in a warmer world, while the Arctic is projected to reach practically ice-free conditions in summer at least once before 2050, with unclear effects on ocean emissions and weather patterns. Hence, following up on the successful MOCA project, in REGAME we will also investigate the role of polar regions and potential tipping points (e.g., thawing permafrost and subsea gas hydrates, see box) with a dedicated high-resolution, regional Arctic inversion, informed by oceanographic observations to elucidate the location of subsea-seeps and other potential emissions sources as well as their temporal variability, in collaboration with the center for Arctic gas hydrates (CAGE). Assessment of the role of changing ice cover will be done during the REGAME project by including a new atmospheric laboratory on the ice-breaking vessel RV Kronprins Haakon (including online monitoring of methane and flask sampling, as currently performed on the RV Helmer Hanssen).

What are gas hydrates?

Large amounts of natural gas, mainly methane, are stored in the form of hydrates in continental margins worldwide, particularly, in the Arctic. Gas hydrate consists of ice-like crystalline solids of water molecules encaging gas molecules, and is often referred to as 'the ice that burns'.

What are seeps?

Cold seeps are locations where hydrocarbons are emitted from sub-seabed gas reservoirs into the ocean. This can be both from petroleum reservoirs and methane hydrates. The illustration is gas bubbles rising 800 m up from Vestnesa Ridge, offshore Svalbard (Smith et al. 2014).

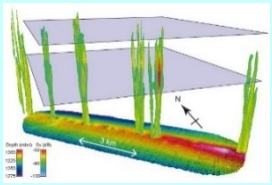

http://cage.uit.no

The outcomes of this project will be summarized in a report for policy makers, enabling society to evaluate our current climate change strategies and provide knowledge essential to future stewardship of the Earth's climate.

The **primary objective** of *REGAME* is to constrain the global CH_4 budget
Secondary objectives are to: 1. Assess the status of CH_4 reservoirs such as wetlands and ocean 2. Survey ocean CH_4 seeps in the Arctic and assess temporal variability and dynamics of seep fluxes 3. Incorporate isotopic tracers in models (FLEXPART/ OsloCTM) 4. Develop the use of the Ensemble Kalman Filter method to use S5P CH_4 in inversions with FLEXPART 5. Investigate the added value of satellite data in inversions 6. Determine implications of improved CH_4 budget and state of CH_4 reservoirs for the Paris Agreement and produce a report for policy makers

2.2.3 Nitrous Oxide (N_2O)

Key findings Nitrous Oxide: *N_2O is a strong greenhouse gas and contributes ~6% to the total forcing of well-mixed greenhouse gases since 1750. N_2O is also the major source of the ozone-depleting NO and NO_2, thus the component influences the stratospheric ozone layer. The global mean level of N_2O has increased from around 270 ppb prior to industrialization. At Zeppelin, the annual mean N_2O level was 333.4 ppb in 2020, with a stronger increase than earlier years due to less seasonal variation with less pronounced minimum during summer, than normal.*

Nitrous Oxide (N_2O) is a greenhouse gas with both natural and anthropogenic sources. The sources include oceans, tropical forests, soil, biomass burning, cultivated soil, animal manure, use of particular synthetic fertilizers, and various industrial processes. There are high uncertainties in the major soil, agricultural, combustion and oceanic sources of N_2O. Anthropogenic sources contribute approximately to 45% of total global N2O, according to Global Carbon Project.

Also, frozen peat soils in Arctic tundra is reported as a potential source (Repo et al., 2009), but studies identify tropical and sub-tropical regions as the largest source regions (Thompson et al, 2013). N_2O is an important greenhouse gas with a radiative forcing of 0.21 W m^{-2} since 1750 (IPCC, 2021a). N_2O is also the major source of the ozone-depleting nitric oxide (NO) and nitrogen dioxide (NO_2) in the stratosphere, thus the component is also influencing the stratospheric ozone layer (WMO, 2018).

N_2O has increased from around 270 ppb prior to industrialization and up to an average global mean of 331.1 ppb in 2019 (WMO, 2020). In 2009, NILU installed a new instrument at Zeppelin measuring N_2O with high time resolution of 15 minutes. The instrument was in full operation in April 2010 and has later been upgraded to comply with ICOS. The results for 2010-2020 are presented in Figure 14. As seen from Figure 14 there has been a gradual increase in N_2O at Zeppelin since the measurements started in 2010. For the period 2010-2020 the overall trend is 0.9 ppb/yr, an increase of 0.3%/yr. In particular we see from the 2020 data set that the summer seasonal minimum is almost lacking. It will be very interesting to follow this and for the moment the reason for the lacking summer minimum is uncertain.

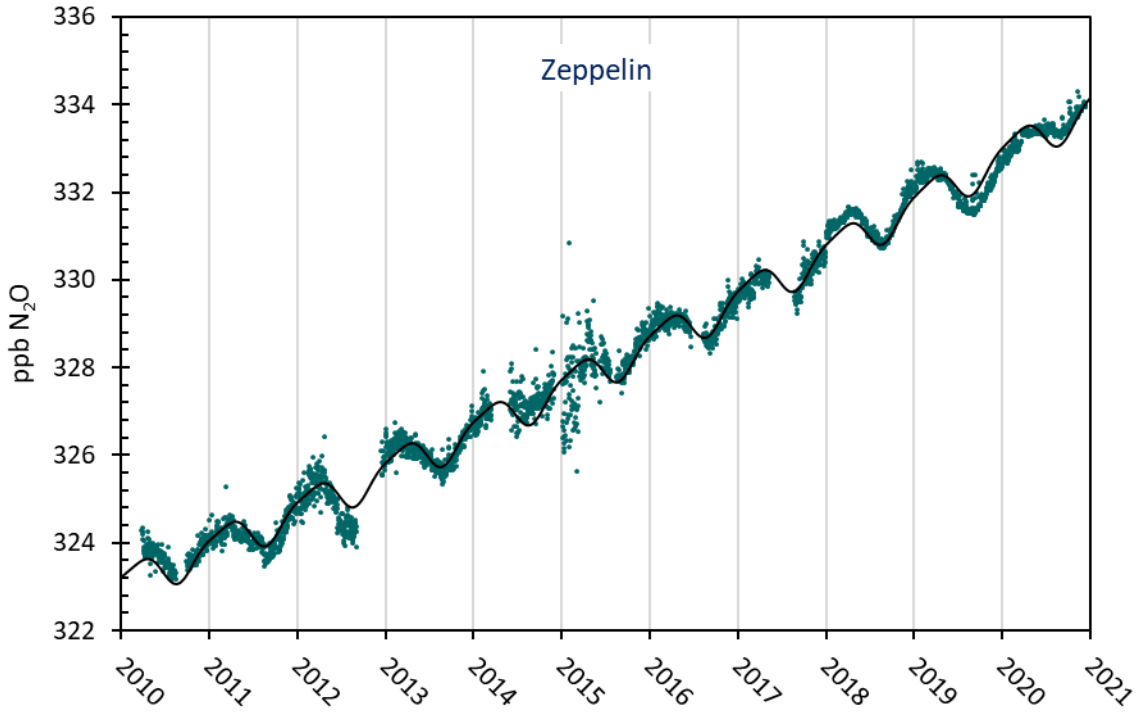

Figure 14: Measurements of N_2O at the Zeppelin Observatory for 2010-2020.The black line is empirical modelled N_2O mixing ratio.

Figure 15 shows annual average concentrations of N_2O measured at Zeppelin for the periods 2010-2020. The global annual means of N_2O (WMO, 2020) are included as a black bars for comparison. The concentrations at Zeppelin are slightly higher than the global means. The annual mean N_2O value at Zeppelin was 333.4 ppb in 2020, an increase of 1.3 ppb from the 2019 annual mean value. This is the second highest annual increase recorded since 2010, explained by the lack of the summer minimum.

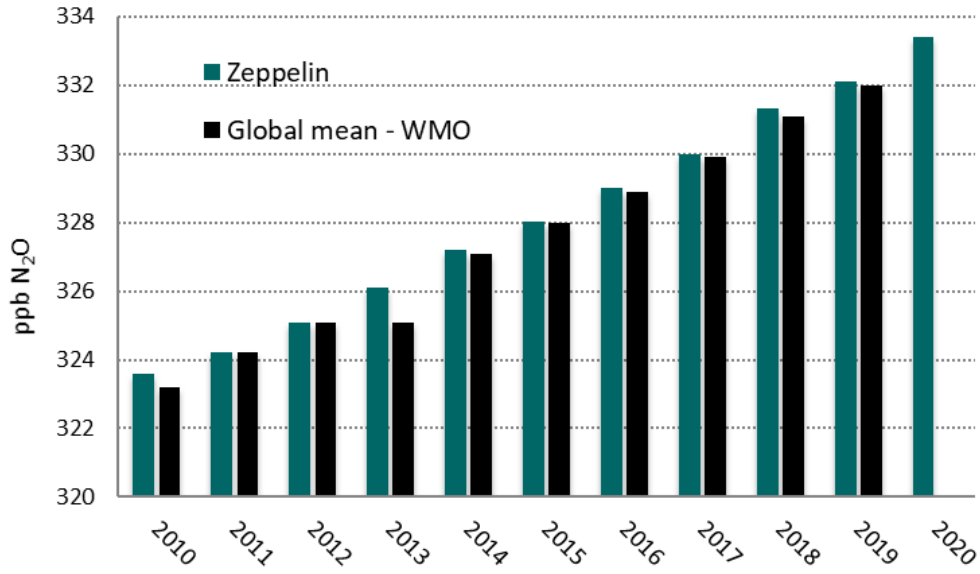

Figure 15: Annual mean concentration of N_2O at the Zeppelin Observatory for 2010-2020.

2.2.4 Volatile organic compounds (VOC)

Key findings – VOCs: *The VOCs are short lived greenhouse gases with low direct greenhouse gas effects. However, they have an indirect climate effect as they influence the levels of e.g. aerosols, ozone, and CO. Furthermore, they are important for surface ozone. Six different VOCs have been measured at Zeppelin since September 2010. The annual mean concentrations vary from one year to another and for most compounds it is not possible to draw any conclusions about developments and trends at this early stage.*

Volatile Organic Compounds (VOCs) represent a large group of carbon-based compounds that have a high vapour pressure and easily evaporate at room temperature. VOC oxidation contributes to the production of tropospheric ozone and influences photochemical processes, both impacting climate and air quality. Sources of VOCs (here ethane, propane, butane, pentane, benzene and toluene) are both natural (mostly geological but also from wildfires) and anthropogenic (fossil fuels). CH_4 and VOCs are co-emitted from oil and natural gas sources, for CH_4 to ethane the mass ratio varies from 7 to 14 (Helmig et al, 2016). The atmospheric ethane budget is not fully understood, and state-of-the-art atmospheric models underestimate ethane-mixing ratios, implying that current emission inventories require additional sources to balance the global atmospheric ethane budget.

Helmig *et al*. (2016) showed, from long-term observations of ethane from a global network that concentrations are increasing (since circa 2010), and that there is a strong latitudinal gradient, with the highest abundances observed in the Arctic, and a steep decline towards the south. They concluded that emissions from North American oil and natural gas development are the primary cause of increasing concentrations in recent years. However, there might be other factors. Another study by Nicewonger et al. (2016) used analysis of polar ice cores to estimate the pre-industrial emissions and concluded that natural ethane emissions from geologic seeps contributed significantly to the preindustrial ethane budget, and Etiope and Ciccioli (2009) suggested that a substantial part of the missing ethane source can be attributed to gas seepage (classified as geologic seeps), but they did not include the Arctic in their study.

A study in Nature Geoscience performed under the MOCA project unveils a need of revising previous ethane and propane emissions studies, as these emissions have been underestimated by more than 50%. Such a revision could in turn improve our understanding of the forceful and related methane emissions (Dalsøren et al, 2018).

There has been large progress recently in the access to quality assured measurements of VOC under ACTRIS, with high time resolution. In a study by Dalsøren et al (2018) recent atmospheric measurement data from a number of sites are compared with the simulations from an atmospheric chemistry transport model, and found that a substantial increase of the emissions is needed to match the model predictions. Dalsøren et al (2018) showed that substantial geologic emissions are necessary to reproduce observations of preindustrial ethane concentrations. This provides an important constraint on both preindustrial and current natural emission budgets, reducing the relative contribution of fossil sources.

In 2010 a Medusa-GCMS instrument was installed at Zeppelin, which made it possible to perform online VOC measurements. Figure 16 shows the daily mean observations of the four non-methane hydrocarbons included in the programme in 2010: ethane, propane, butane and pentane.

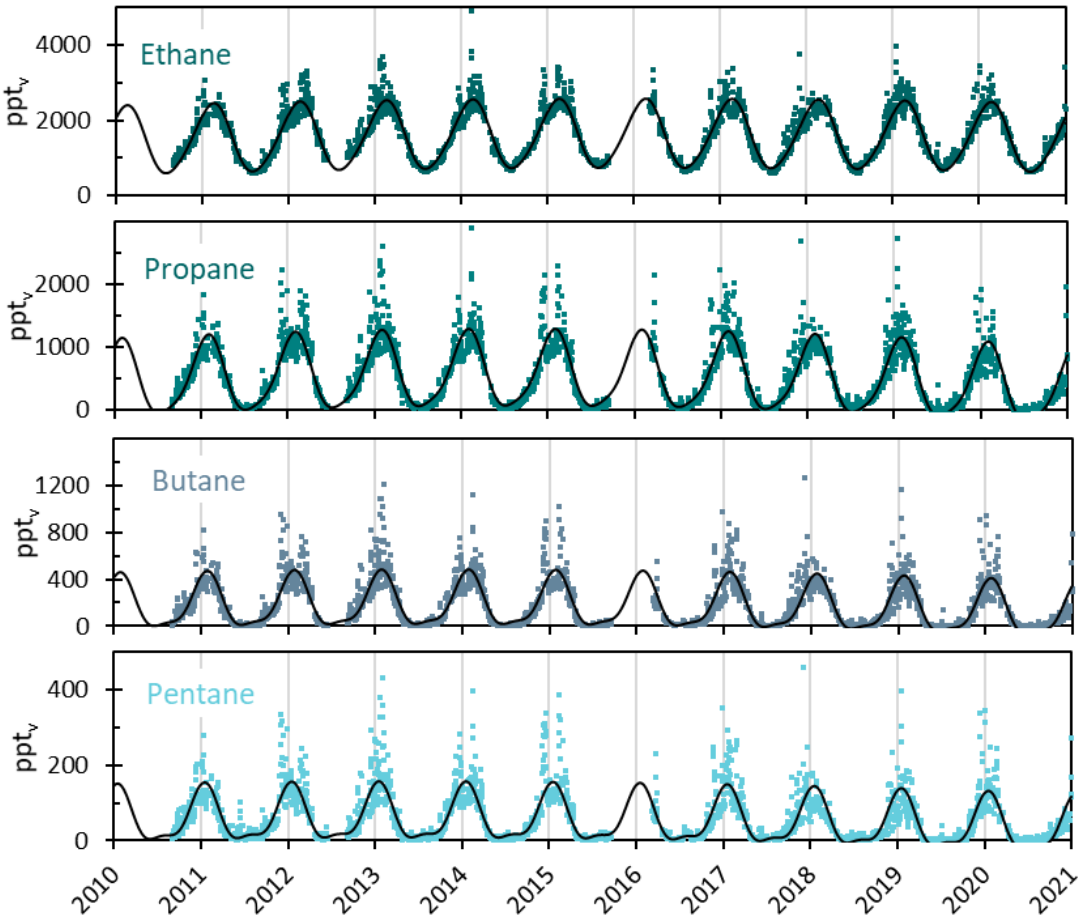

Figure 16: Observations of daily averaged mixing ratios of ethane, propane, butane, and pentane for the period September 2010 – 2020 at the Zeppelin Observatory. The black line is empirical modelled mixing ratio.

Due to the short lifetimes, ranging from a few days for pentane to 2-3 months for ethane, the annual cycles are very strong and are regulated by OH reactions. The annual mean from 2011 to 2019 are shown in Figure 17.

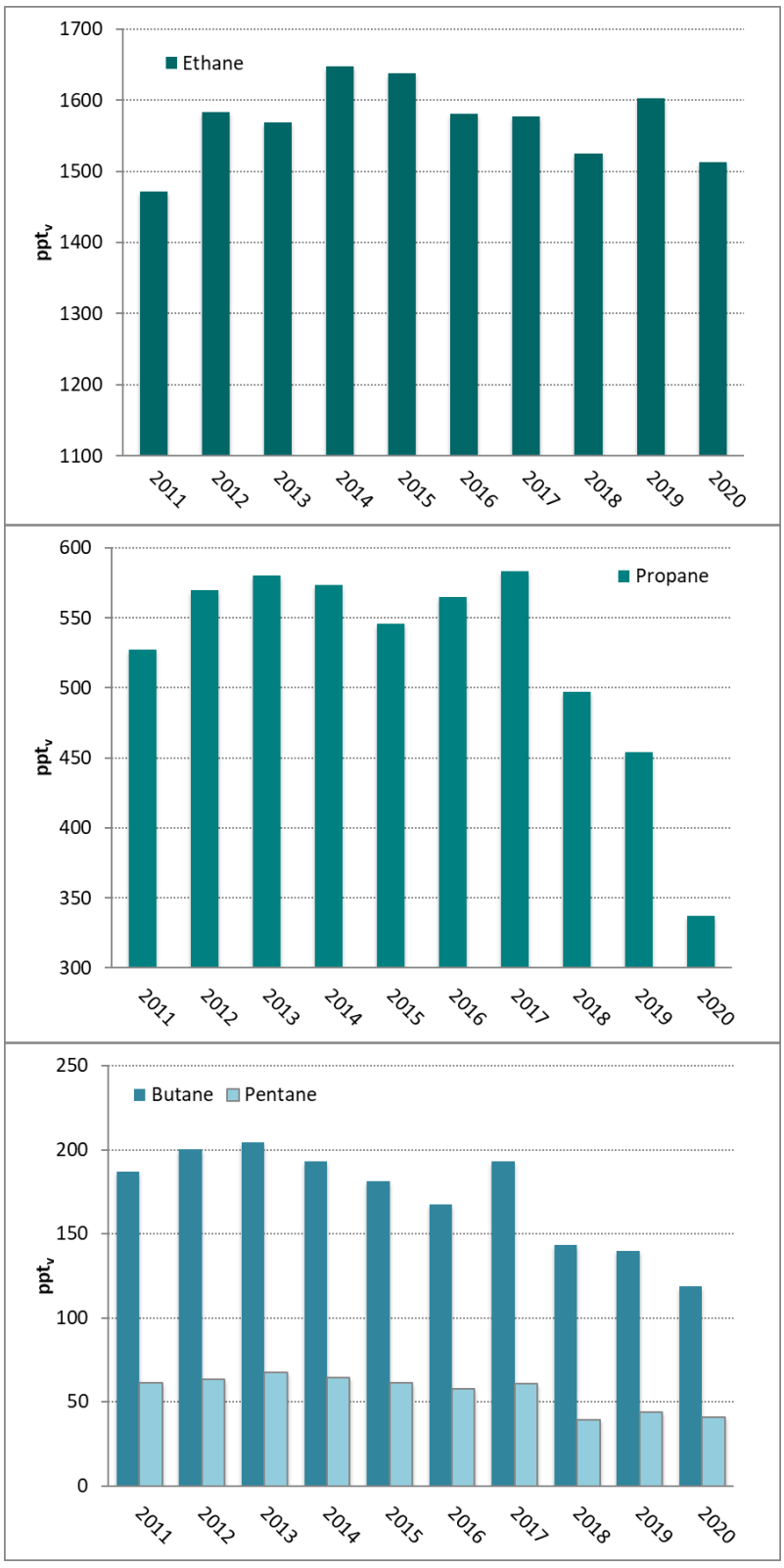

Figure 17: Development of the annual means of the measured non-methane hydrocarbons at the Zeppelin Observatory for the period 2011-2020. Upper panel in dark green: ethane, mid-panel propane, and lower panel butane and pentane. All concentrations are in ppt.

As seen from the figure the annual mean concentrations vary from one year to another and for most compounds it is not possible to draw any conclusions about development and trend. However, for all these compounds, there is a decrease from 2017-2018, but then an increase in ethane from 2018-2019. The decrease from 2017-2018 should be interpreted in light of the drought, and fewer transport episodes from Central-Europe during wintertime.

At Zeppelin we aim to measure two other aromatic VOCs, benzene and toluene, which belong to a group of VOCs found in petroleum hydrocarbons, such as gasoline. These compounds have attracted much attention since benzene are considered carcinogens, but they are also relevant for climate. The VOCs have relatively short atmospheric lifetimes and small direct impact on radiative forcing. However, anthropogenic secondary organic aerosols (SOA) are formed from photo oxidation of benzene and toluene (Ng et al., 2007), which indirectly impacts the climate (negative forcing). The SOA formation from these VOCs is most effective under low-NO_x conditions and when ambient concentration of organic aerosols is high. Thus, benzene and toluene influence climate through their production of secondary organic aerosols and their involvement in photochemistry, i.e., production of O_3 in the presence of light.

Figure 18 shows the daily mean observations of benzene and toluene at Zeppelin for the period 2010-2018. After an upgrade of the Medusa-GCMS in fall 2017, the benzene and toluene values became unrealistically low. The upgrade was required to measure the low concentrations of the halogenated gases. Thus, the measurements performed after 4th October 2017 are flagged as “missing”.

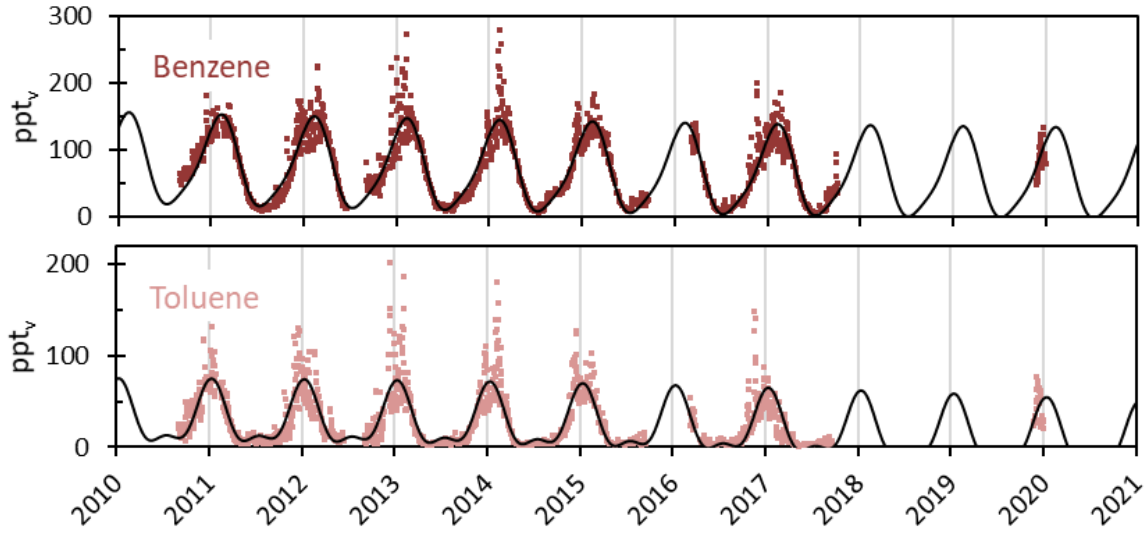

Figure 18: Observations of daily averaged mixing ratio of benzene (upper panel) and toluene (lower panel) for the period September 2010 – 2020 at the Zeppelin Observatory. The black line is empirical modelled mixing ratio.

As can be seen from the figure there are strong annual variations, mainly explained by the reactions induced by sunlight. The annual means of benzene and toluene for the period 2011-2019 are presented in Figure 19. The figure shows a declining tendency for both compounds, but unfortunately no annual mean values are calculated from the measurements in 2018. The shaded bars in Figure 19 indicates that the annual means in 2018 and 2019 are based on model values only (i.e. the black curve in Figure 18).

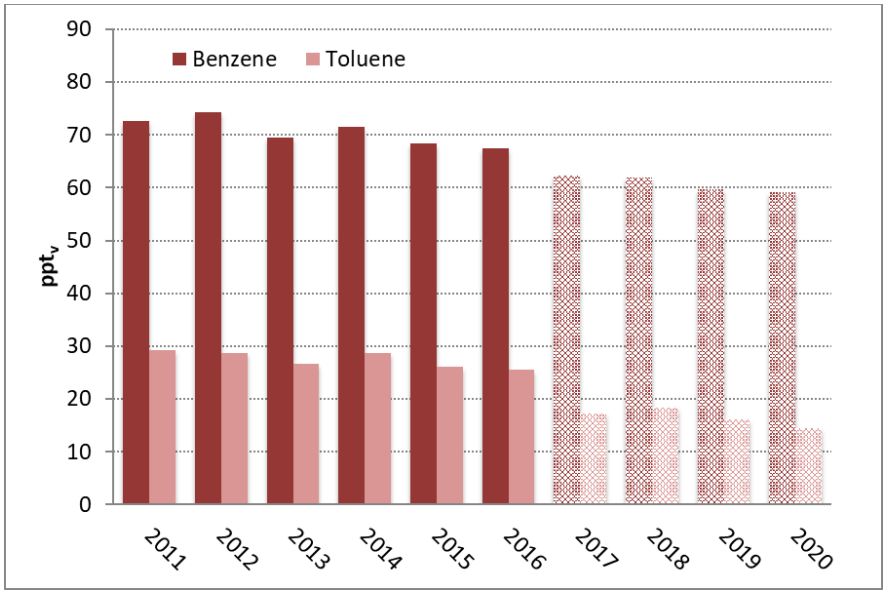

Figure 19: Development of the annual means of benzene (brown) and toluene (light red) for the period 2011 – 2020 at the Zeppelin Observatory. All concentrations are in ppt. Note that benzene and toluene in 2017-2020 mainly are based on model data.

2.2.5 Carbon monoxide (CO)

Key findings CO: *CO is not a greenhouse gas, but considered as a climate gas as it regulates the levels of methane and ozone. CO is also an excellent tracer for long-range transport of smoke from fires. CO has been measured at Zeppelin since 2001. For the period 2001-2020 a decreasing trend of -1.04 ppb/yr is recorded. In 2019 and 2020 there were strong CO transport episodes registered at Zeppelin traced back to fires, at the same time we also see an annual mean increase in the CO level at Zeppelin.*

Atmospheric carbon monoxide (CO) has both natural and anthropogenic sources. CO is produced when various organic gases are oxidized, such as methane, VOCs emitted from fossil fuel, and gases from biomass burning. Additionally, emissions from plants and ocean are important sources. CO is not considered as a direct greenhouse gas, as it does not absorb terrestrial thermal IR energy strongly enough. However, CO modulates the level of methane and production of tropospheric ozone, which are both very important greenhouse gases. Hence, CO is considered as a climate gas although not a greenhouse gas. CO is closely linked to the cycles of methane and ozone and it also plays a key role in the control of OH radicals.

CO at Zeppelin is included in the current monitoring programme and for ICOS and the observed CO mixing ratios for the period September 2001-2020 are shown in Figure 20.

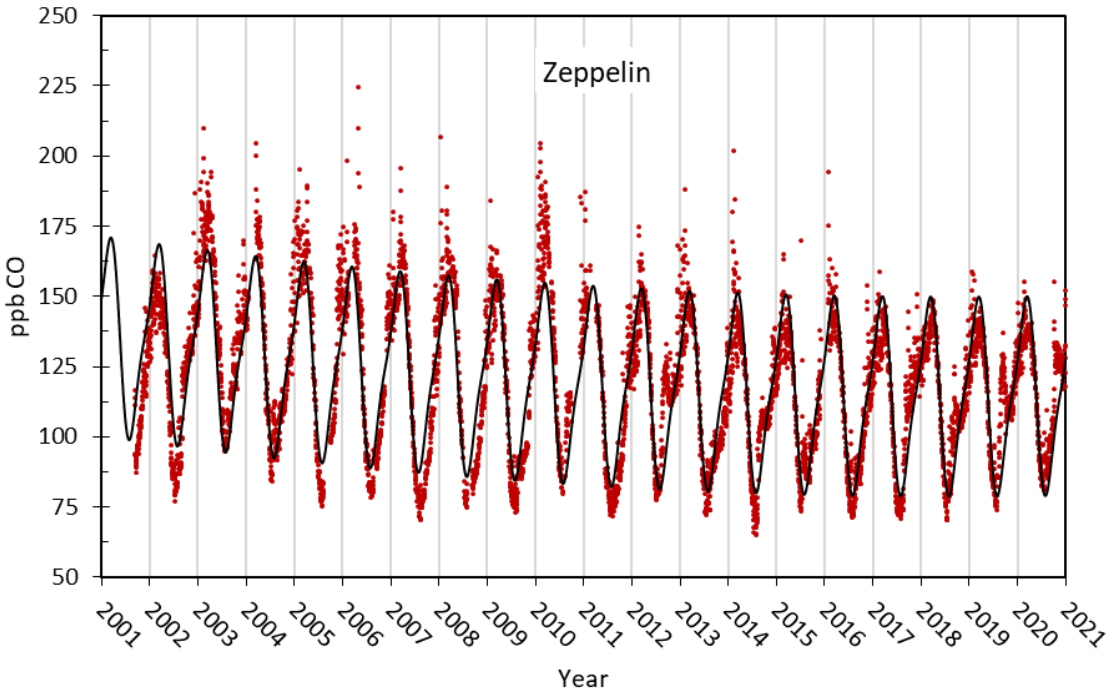

Figure 20: Observations of carbon monoxide (CO) from September 2001 to 2020 at the Zeppelin observatory. Red dots: daily averaged observed mixing ratios. The solid line is the empirical fitted mixing ratio.

The concentrations of CO show characteristic seasonal variations with a clear annual cycle with a late winter (February/March) maximum and a late summer (August) minimum. This seasonal cycle is driven by variations in OH concentration as a sink, emission by industries and biomass burning, and transport of air on a large scale. As seen from the figure there are also peak values which are due to long-range transport of polluted air to Zeppelin and the Arctic. The highest mixing ratio of CO ever observed at Zeppelin is 225 ppb, measured on the 2nd of May 2006. This peak value was due to agricultural fires in

Eastern Europe. In general, CO is an excellent tracer for transport of smoke from fires (biomass burning, agricultural- or forest fires). Notable the seasonal variations are getting smaller the last years and the annual mean is increasing (Figure 21). For the period 2001-2020 a trend of -1.06 ppb/yr is calculated.

The development of the annual CO means at Zeppelin for the period 2001-2020 is presented in Figure 21. Overall, the CO concentration at Zeppelin shows a decrease during the period 2003 to 2009, and stable levels the last years with a small peak in 2010. Last 2 years, there is an increase evident.

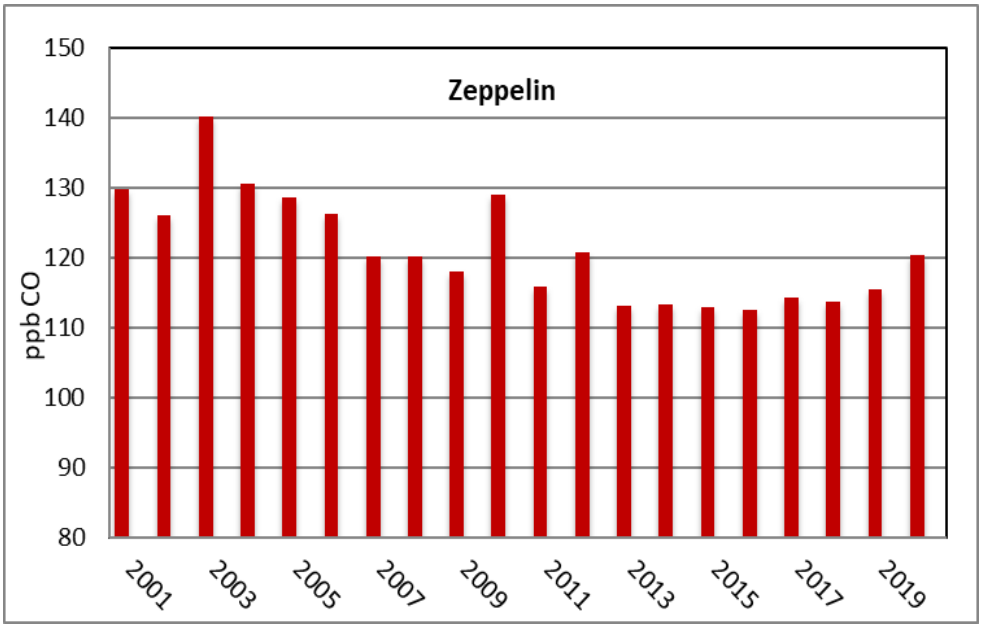

Figure 21: Development of the annual means of CO measured at the Zeppelin Observatory for the period 2001-2020. The concentrations are in ppb.

An unprecedented amount of wildfires have been raging in various regions of the Arctic, including Greenland and Alaska in the US the last 2 years. They have been caused by record-breaking temperatures and lightning, fuelled by strong winds. These fires emit significant smoke and particulates harmful pollutants and toxic gases into the atmosphere, which make their way across the Bering Sea to the U.S. and Canada. According to the WMO, fires in the Arctic in 2019 released around 50 mega tonnes of carbon dioxide in June alone – equivalent to Sweden's total annual emissions. There was an extreme CO episode in the year 2019 is as there were heavy fires in Siberia, in particular. There was also a large increase in fires in Amazonas in 2019 and elsewhere in the southern hemisphere, and this might influence even the observations at Zeppelin. The increase we now see at Zeppelin can possibly be explained by the large fires the last year in Canada, US and Siberia.

In summer 2019, Siberia saw wildfires on a massive scale across the countryside. We can also see the high CO concentration during summertime at Zeppelin in Figure 20, better shown in the next figure. The image shown is captured from space on 28th July 2019 (European Space agency (ESA)). According to ESA almost three million hectares of land are estimated to have been affected. This Copernicus Sentinel-3 image shows a number of fires, producing plumes of smoke.

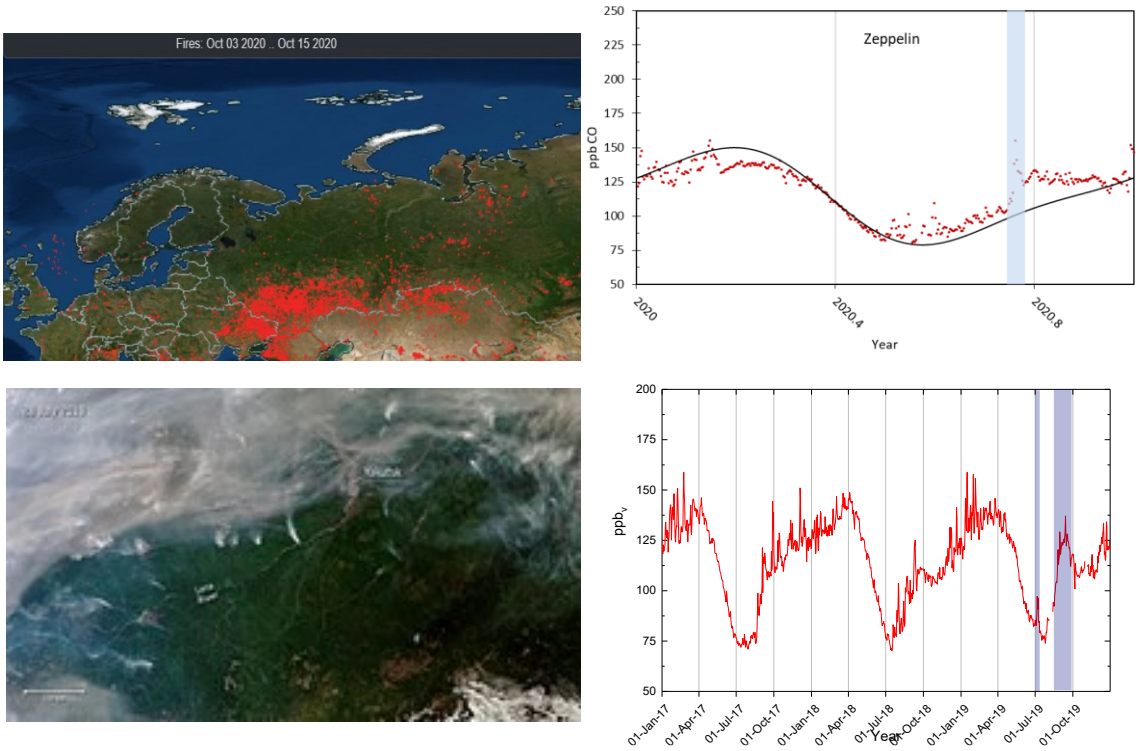

Figure 22: An unprecedented amount of wildfires have been raging in various regions of the Arctic, including Greenland and Alaska in the US last 2 years. Upper panel: Episode in 2020; Fires in Siberia and southwest Russia, with transport of air from these regions. The map is from NASA, FIRMS[12] Lower panel: episode in 2019. The picture to the left is from Sentinel-3, the plot to the right is CO at Zeppelin for 2017-2019. The blue bars show when there are high CO concentration for the season, highly impacted by the fires.

[12] *NASA FIRMS uses satellite observations from the MODIS and VIIRS instruments to detect active fires and thermal anomalies and deliver this information in near real-time to decision makers through email alerts, analysis ready data, online maps and web services.* https://firms.modaps.eosdis.nasa.gov

2.2.6 Chloromethane at the Zeppelin Observatory

***Key findings - Chloromethane**: The atmospheric concentration of chloromethane is relatively stable. The gas has a dominating natural origin and is not regulated through the Kyoto or Montreal protocols. The annual mean CH_3Cl concentration at Zeppelin has decreased by ~-1.3% since 2001.*

Chloromethane (also called methyl chloride, CH_3Cl) is the most abundant chlorine containing organic gas in the atmosphere. It contributes approximately 16% to the total chlorine from the well-mixed gases in the troposphere (WMO, 2014b), and through this a strong contributor to ozone depletion. The main sources of chloromethane are natural, and the dominating sources include ocean, biomass burning, fungi, wetlands, rice paddies, and tropical forests. Due to the dominating natural sources, this compound is not regulated through the Montreal or the Kyoto protocols. To reach the stratosphere, the lifetime in general needs to be above the order of 2-4 years, but this is also dependent on the source strength and the regional distribution of the gas. Chloromethane has a relatively high mixing ratio and contributes to the stratospheric chlorine burden.

The result of the measurements of this gas for the period 2001-2019 is shown in Figure 23. The lifetime of chloromethane is only one year, resulting in large seasonal fluctuations due to rapid changes in emission, as shown in Figure 23.

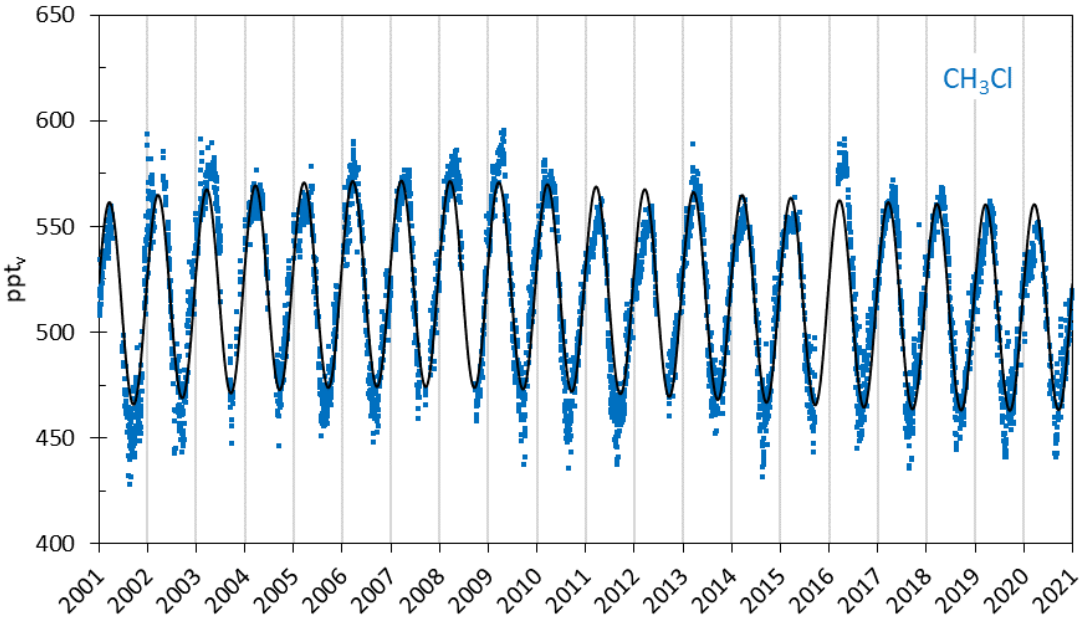

Figure 23: Observations of chloromethane, CH_3Cl, for the period 2001-2020 at the Zeppelin Observatory. Blue dots: daily averaged concentrations from the observations, solid line: empirical fitted mixing ratios.

The annual means of chloromethane for the period 2001-2019 are shown in Figure 24. Days with missing observations are filled with empirical fitted data. Only small changes have been observed since the measurements started in 2001. The trend for the period 2001-2019 is -0.37 ppt/yr (-1.3% for the entire period). From 2002 to 2009 the annual mean chloromethane concentrations were relatively stable at a level around 520 ppt, but since 2009 there has been larger variability and a decreasing tendency, except from 2016 where the annual mean value was 10 ppt higher than previous year. The black bars in Figure 24 shows that the global annual means in 2016-2019 (Hall et al., 2017 and 2020; Dlugokencky et al., 2018 and 2019) were 30-40 ppt (6-7%) higher than the annual mean values at the Zeppelin Observatory. This is likely explained by strong emission sources in the tropics, resulting in

increased CH_3Cl mixing ratios towards lower latitudes (Umezawa et al., 2014). Zeppelin is less affected by this, due to the short lifetime.

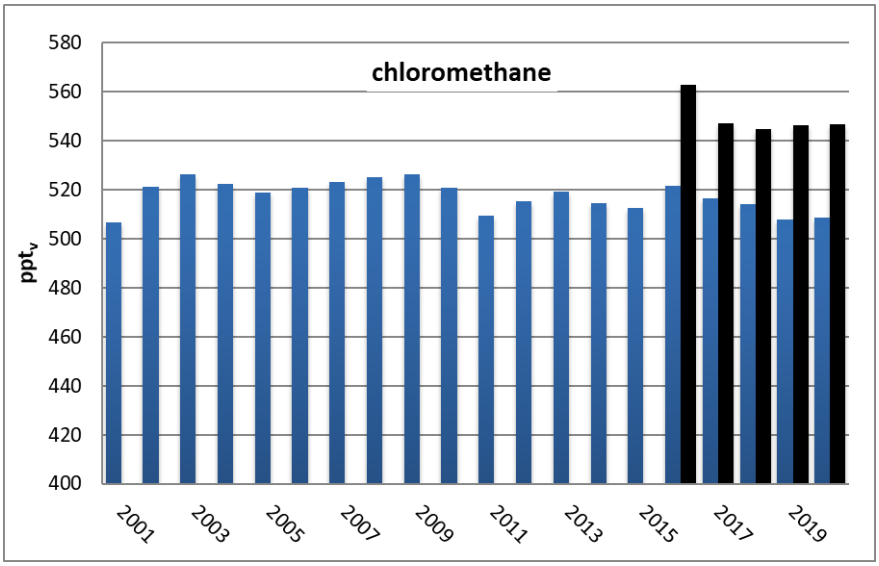

Figure 24: Development of Chloromethane annual means measured at the Zeppelin Observatory for the period 2001-2020. Global annual means for 2016-2020 are included as black bars. All units are in ppt.

2.2.7 Bromomethane at the Zeppelin Observatory

Key findings - Bromomethane: *The atmospheric concentration of CH_3Br at Zeppelin has decreased by ~25% since the observations started in 2001. The decrease is a result of the implementation of the Montreal Protocol. However, CH_3Br has many natural sources with uncontrolled fluctuations from one year to another.*

Bromomethane (also called Methyl bromide, CH_3Br) is an important reservoir for atmospheric bromine, which reacts with ozone to deplete the ozone layer. CH_3Br has both natural and anthropogenic sources. The natural sources such as the ocean, plants, and soil, can also be a sink for this gas. The primary anthropogenic source of bromomethane has been from its use as a fumigant, e.g. for pest control and pesticide in the control of weeds. Other anthropogenic sources of CH_3Br include the combustion of leaded gasoline, biomass burning, and emissions from certain crop species. Even though bromomethane is a natural substance, the additional contribution from anthropogenic sources contributes to the man-made depletion of the ozone layer. Total organic bromine from halons and bromomethane peaked in the mid-1990s, but the tropospheric concentration has decreased by ~25% over the past 20 years. Also, the stratospheric abundance of bromide has started to decrease (WMO, 2018).

The result of the daily averaged observations of bromomethane for the period 2001-2019 is shown in Figure 25. Bromomethane is a greenhouse gas which is twice as strong as CO_2 and has a lifetime of 0.8 years (Myhre et al, 2013b). The short lifetime explains the strong annual and seasonal variations of this compound.

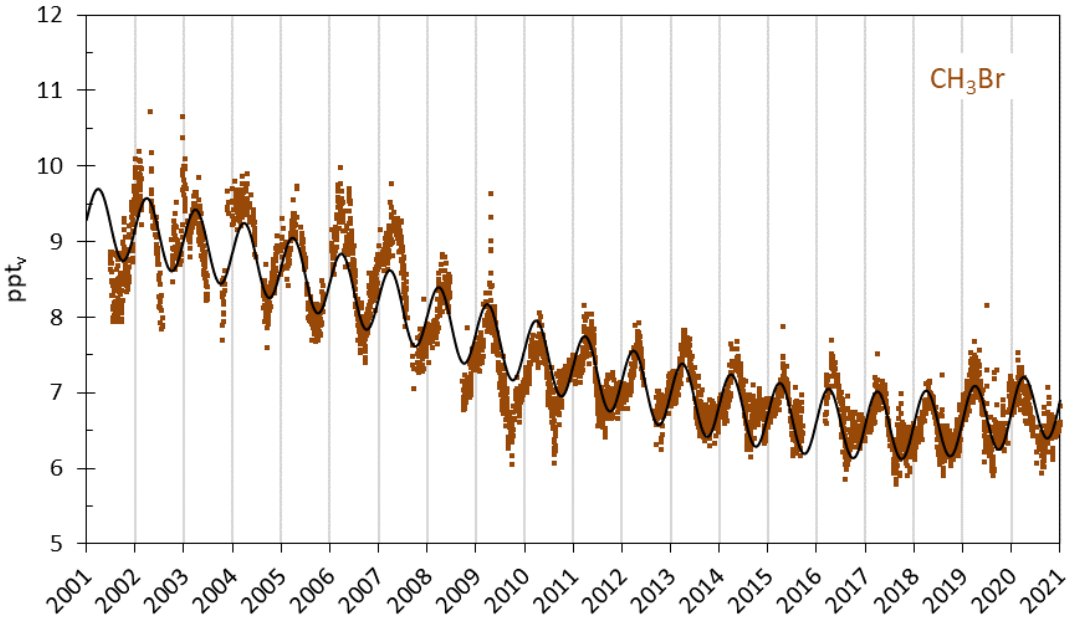

Figure 25: Observations of Bromomethane, CH_3Br, for the period 2001-2020 at the Zeppelin Observatory. Brown dots: daily averages mixing ratios from the observations, solid line empirical fitted mixing ratios.

The development of the annual means for the period 2001-2019 is presented in Figure 26. For this period there is a trend in the mixing ratio of -0.16 ppt/yr. The overall observed change since 2001 is -2.3 ppt, i.e. -25%. In 2019 the annual mean CH_3Br concentration was 6.8 ppt, which is slightly higher than the mean values from the previous two years. In general, the decline in bromomethane is explained by considerable reduction in emissions; The uses of CH_3Br has decreased steadily as a result of the implementation of the Montreal Protocol, from over 50 000 tonnes/yr in the late 1990s to about 4 000 tonnes/yr in 2012 (WMO, 2014b).

The global mean mixing ratios published by BAMS in “State of the Climate” (Dlugokencky et al., 2018 and 2019; Hall et al., 2017 and 2020; Lan et al.. 2021), presented by the black bars in Figure 26, were ~6.6 ppt in both 2017, 2018 and 2019. This is close to the annual mean values observed at the Zeppelin Observatory.

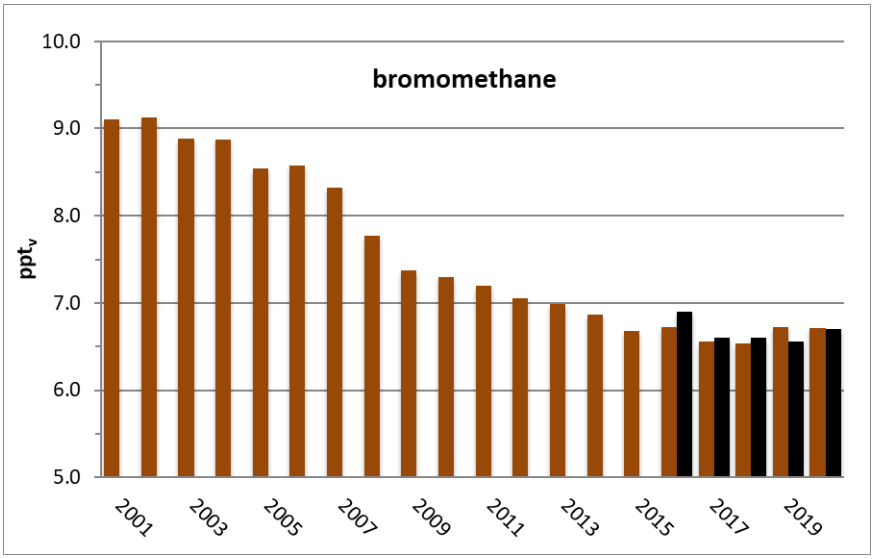

Figure 26: Development of the annual means of bromomethane measured at the Zeppelin Observatory for the period 2001-2020. The global annual mean for 2016-2020 are included as black bars.

2.3 Greenhouse gases with solely anthropogenic sources

The gases presented in this chapter have solely anthropogenic sources. These man-made greenhouse gases include CFCs, HCFCs, HFCs, SF_6, NF_3, SO_2F_2 and halons, and most of these gases did not exist in the atmosphere before the 20th century. Although the gases have much lower concentration levels than most of the natural gases mentioned in the previous section, they are strong infrared absorbers, many of them with extremely long atmospheric lifetimes resulting in high global warming potentials (see Table 3). As a group, the gases contribute to around 12% to the overall global radiative forcing since 1750 in according to the AR5 IPCC report (Myhre et al, 2013b). The annual mean concentrations for all years and all gases included in the monitoring programme are given in Appendix I (Table A 1, page 130), whereas trends, uncertainties and regression coefficients are found in Table A 2.

Some of these gases are ozone depleting, and consequently regulated through the Montreal protocol. Especially chlorine and bromine from CFCs, HCFCs and halons contribute to the depletion of the ozone layer, allowing increased UV radiation to reach the earth's surface, with potential impact not only on human health and the environment, but on agricultural crops as well. In 1987 the Montreal Protocol was signed in order to reduce the production and use of these ozone-depleting substances (ODSs) and the amount of ODSs in the troposphere reached a maximum around 1995. The amount of most ODSs in the troposphere is now declining slowly and the concentrations are expected to be back to pre-1980 levels around year 2050. In the stratosphere the peak ODS level was reached around year 2000. According to WMO (2018) the amount of Equivalent Effective Stratospheric Chlorine (EESC) declined by about 9% in the Polar regions and 13-17% in Mid-latitude regions from mid 1990s to 2016.

There are two generations of substitutes for the CFCs. The first generation is included in the Montreal protocol as they also deplete the ozone layer. This comprises the HCFCs listed in Table 2. The second-generation substitutes, the HFCs, are included in the Kyoto protocol and in the amendment to the Montreal Protocol agreed in Kigali in 2016. The general situation now is that the CFCs are declining, while their substitutes are increasing, and some of them are increasing rapidly.

2.3.1 Chlorofluorocarbons (CFCs) at Zeppelin Observatory

Key findings - CFCs: *The development of the CFC levels at Zeppelin is promising and in good accordance with the compliance of the Montreal protocol. The concentrations of CFC-11, CFC-12 and CFC-113 are all declining, and the mixing ratios of these gases are reduced with approximately 13.0%, 8.9% and 14.8% since 2001, respectively. Studies have shown that the rate of decline in CFC-11 slowed down by ~50% after 2012, both globally and at Zeppelin due to unreported emissions in China. However, the Chinese emission has been back to a pre-2013 level after 2019. Also, CFC-115 has increased by 5.9% since 2001 and the increase has intensified after 2013. This might be related to Chinese emissions.*

In total, four chlorofluorocarbons (CFCs) are measured and analysed at the Zeppelin observatory: CFC-11, CFC-12, CFC-113, and CFC-115. These are the main ozone depleting gases. The anthropogenic emissions started around the 1930s, and all these compounds were restricted in the Montreal protocol from 1987. The main sources of these compounds were foam blowing, aerosol propellant, temperature control (refrigerators), solvents, and the electronics industry. The highest production of the CFCs took place around 1985, with maximum emissions around 1987. The lifetimes of these compounds are long, from 45 to over one thousand years (see Table 3), and combined with strong infrared absorption properties their GWPs are high.

Figure 27 shows the daily averaged observed mixing ratios of the four CFCs. Before 2010/2011 the instrumentation for measurements of CFCs at Zeppelin was not in accordance with recommendations and criteria of AGAGE, and consequently there are relatively high uncertainties in the observations of these compounds, see also Appendix I. From September 2010, new and improved instrumentation was installed at Zeppelin, providing more accurate observations of CFCs. The higher precision is clearly

visualised in Figure 27, but due to several severe instrumental problems in 2013/14, 2015/16 and 2019 there are some periods without CFC measurements[13].

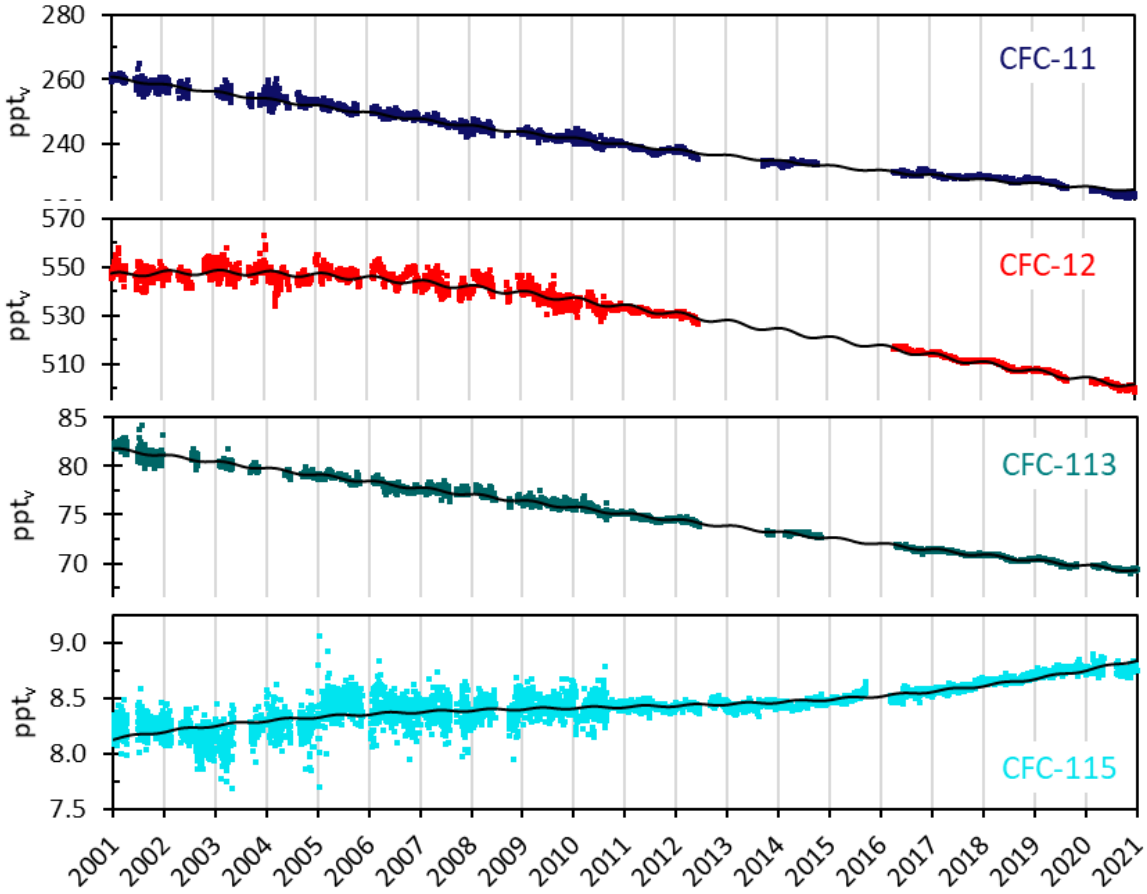

Figure 27: Daily averaged mixing ratios of the monitored CFCs at the Zeppelin observatory for the period 2001-2020: CFC-11 (dark blue), CFC-12 (red), CFC-113 (green) and CFC-115 (light blue). The solid lines are empirical fitted mixing ratios.

The trends per year for CFC-11, CFC-12 and CFC-113, given in Table 2, are all negative. The decreases are -1.8, -2.6, and -0.6 ppt/yr for CFC-11, CFC-12 and CFC-113, respectively. For the compound CFC-115 the trend is still slightly positive, +0.025 ppt/yr, and there has also been a small increase the last few years, after a stable period. It should be noted that the ambient concentration of CFC-115 is relatively low compared to CFC-11 and CFC-12, but it has a very long lifetime of 540 years, which limits our ability to reduce the abundance in the atmosphere. In total, the development of the CFC levels at the global background site Zeppelin is promising and in accordance with the compliance of the Montreal protocol.

Studies from Rigby et al. (2019) showed that the rate of decline of atmospheric CFC-11 concentrations slowed down by about 50% after 2012, caused by new production and unreported CFC-11 emissions in China, strongly inconsistent with the Montreal Protocol agreement. Also, studies from Vollmer et al. (2018) conclude that a large fraction of the current global emissions of CFC-115 originate from the Chinese mainland. However, a recent publication from Park et al. (2021) indicates that the CFC-11 emissions in eastern China returned to pre-2013 levels in 2019. This demonstrates the importance of

[13] *The instrumentation is not in accordance with recommendations and criteria of AGAGE for measurements of the CFCs and there are larger uncertainties in the observations of this compound, see also Appendix I. This is also why these compounds are particularly sensitive to instrumental problems.*

maintaining good monitoring networks, both to detect possible changes in ODSs, but also to detect possible effects of climate change on the ozone layer.

The 2001-2020 annual means for all the observed CFCs at Zeppelin are shown in Figure 28. Also, the global annual means in 2016 – 2020 as reported in "State of the Climate", BAMS (Dlugokencky et al., 2018 and 2019; Hall et al., 2017 and 2020; Lan et al., 2021) are included as black bars for comparison. As can be seen, the observed concentrations at Zeppelin are close to the global mean for these compounds, as the lifetimes are long and there are hardly any present-day emissions.

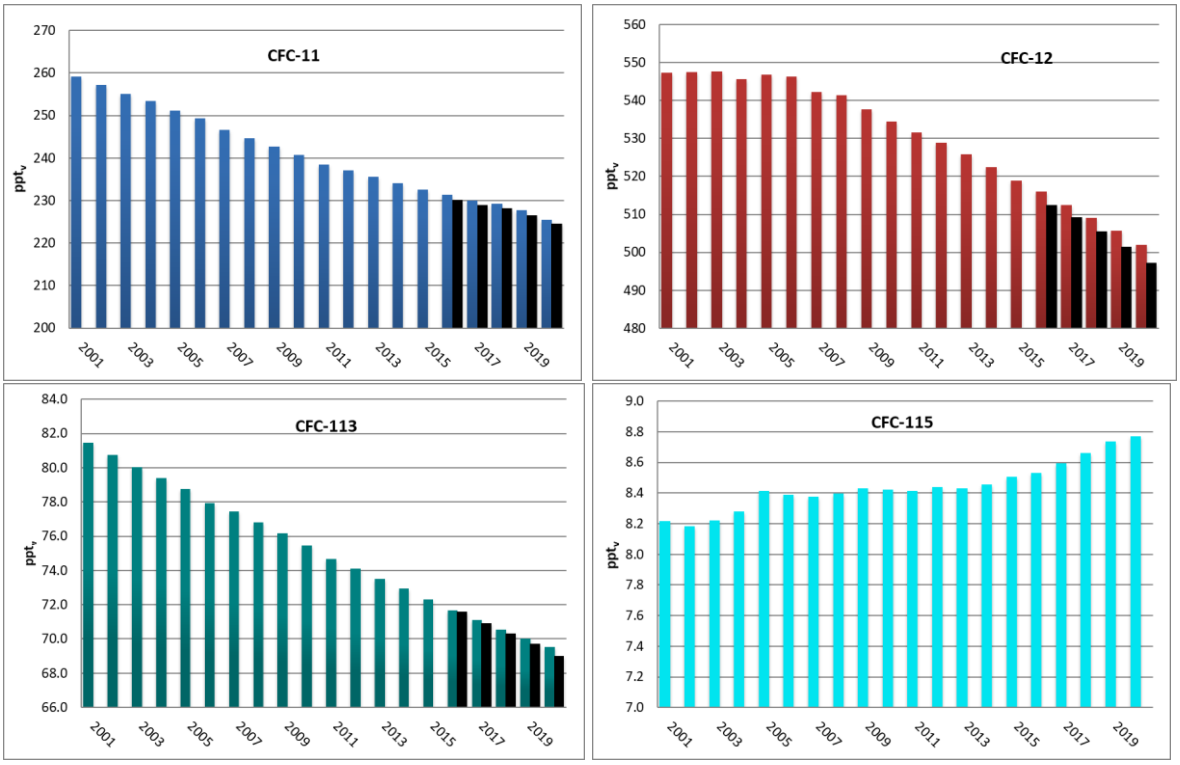

Figure 28: Development of CFC annual means at the Zeppelin Observatory for the period 2001-2020. Upper left panel: CFC-11, upper right panel: CFC-12, lower left panel: CFC-113, lower right panel: CFC-115. See Appendix I for data quality and uncertainty. The global annual means for 2016-2020 are included as black bars. All units are in ppt.

According to WMO (2018) the global mean mixing ratio of CFC-11 (from the AGAGE network) decreased with approximately 1.3 ppt/yr from 2015 to 2016. This is in accordance with the measurements at Zeppelin. As mentioned above, the rate of atmospheric CFC-11 decline slowed down after 2012. At Zeppelin, the average rate was -2.1 ppt/yr prior to 2012 and -1.5 ppt/yr after 2012. CFC-12 (the red diagram) has a very high GWP, 11 200, and it is also the most abundant CFC. This makes CFC-12 a very potent greenhouse gas. The global mean estimates from the AGAGE network, show that the atmospheric mixing ratio of CFC-12 decreased at a rate of -0.7%/yr from 2015 to 2016 (WMO, 2018). This fits well with our observations at Zeppelin the last years. CFC-12 had a maximum around 2003-2005, but there has been a clear reduction over the last years: 45 ppt since 2005.

2.3.2 Hydrochlorofluorocarbons (HCFCs) at Zeppelin Observatory

Key findings - HCFCs: *The CFC substitutes HCFC-22, HCFC-141b and HCFC-142b have increased significantly since the measurements started at Zeppelin in 2001. HCFC-22 has a growth rate of 5.6 ppt/yr, whereas HCFC-141b and HCFC-142b have average growth rates of 0.5 ppt/yr. From 2001 to 2020 HCFC-22, HCFC-141b and HCFC-142b increased by 67%, 59% and 66%, respectively. HCFC-22 is still increasing, but the rate has slowed down. The situation is even more positive for HCFC-141b and HCFC-1412b, where concentrations have stabilized or declined the last five years.*

Hydrochlorofluorocarbons, HCFCs, represent the first generation of replacement gases for CFCs. Their lifetimes are rather long, see Table 3, and although not as stable and persistent in the atmosphere as CFCs, they can still reach the stratosphere where they can destroy the ozone layer. Consequently, these gases are regulated through the Montreal protocol. The Norwegian monitoring programme includes three HCFC species: HCFC-22, HCFC-141b and HCFC-142b. These compounds are mainly used as refrigerants, foam blowing agents and solvents. The use of the gases worldwide is now frozen, but they are yet not completely phased out. All these gases potentially have a strong warming effect due to their high GWPs, e.g. (see Table 3) HCFC-142b has the highest GWP, with a warming potential 2 300 times stronger than CO_2, per kg gas emitted.

The daily averaged observations of the three HCFCs are shown in Figure 29 for the period 2001-2020.

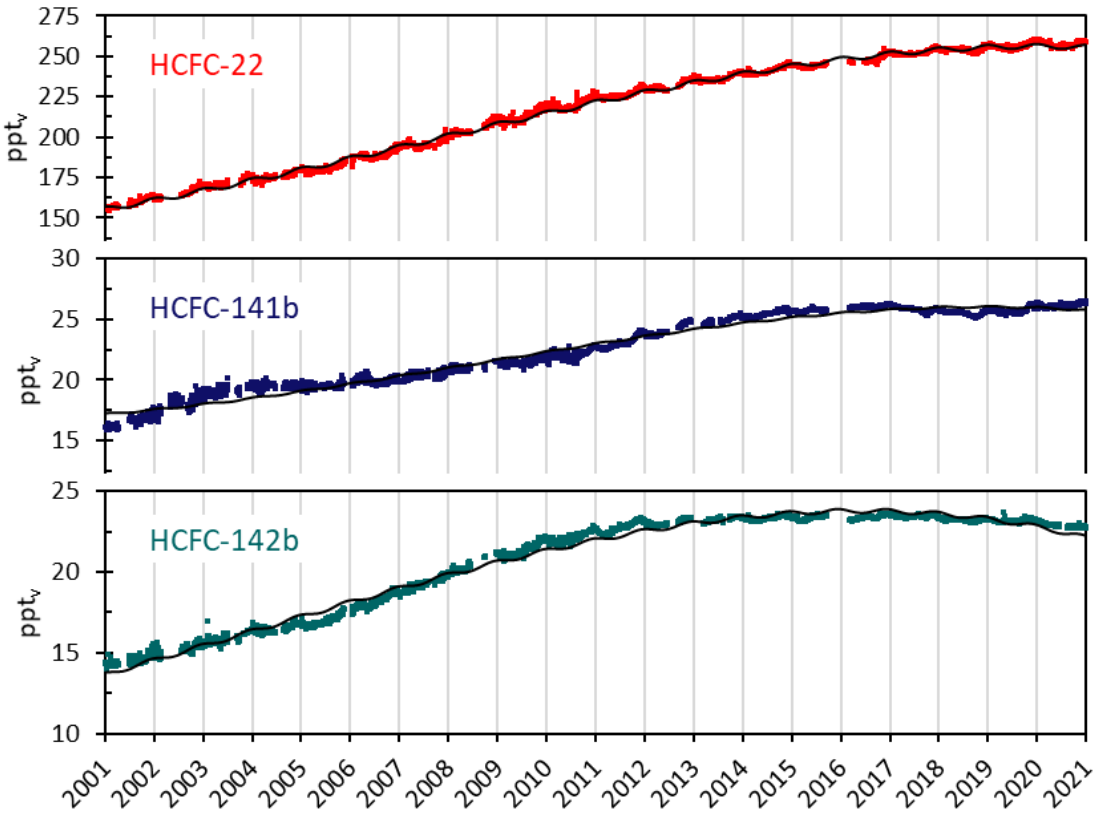

Figure 29: Daily averaged mixing ratios of the monitored HCFCs for the period 2001-2020 at the Zeppelin observatory: HCFC-22 (red), HCFC-141b (dark blue), and HCFC-142b (green). The solid lines are empirical fitted mixing ratios. All units are in ppt.

HCFC-22, HCFC-141b and HCFC-142b have all increased over the period 2001-2020. HCFC-22 is the most abundant HCFC species and has been increasing at a rate of 5.6 ppt/yr over the period 2001-2020. The concentration of the two other compounds, HCFC-141b and HCFC-142b, are a factor of ten

lower than HCFC-22, and the increase in absolute annual means are also a factor of ten lower; HCFC-141b and HCFC-142b both increased by 0.5 ppt/yr over the period 2001-2020. However, the development is encouraging for HCFC-141b and HCFC-142b, which have stabilized or even decreased after 2017. This is best illustrated in Figure 28, which shows the annual means for the full period. The rate of increase for HCFC-22 has also slowed down the last 4-5 years. Ten years ago, HCFC-22 increased by ~8 ppt/yr. From 2019 to 2020 the increase was reduced to 1.9 ppt/yr. With lifetimes in the order of 10-20 years, it is important to continue monitoring the development of the HCFCs for many years to come, as they have a significant influence on the ozone layer and are also strong greenhouse gases. The global annual means for 2016-2020 are included in Figure 28 as black bars (Hall et al. 2017 and 2020; Dlugokencky et al. 2018 and 2019; Lan et al., 2021). The observed concentrations at Zeppelin are 4-6% higher than the global means.

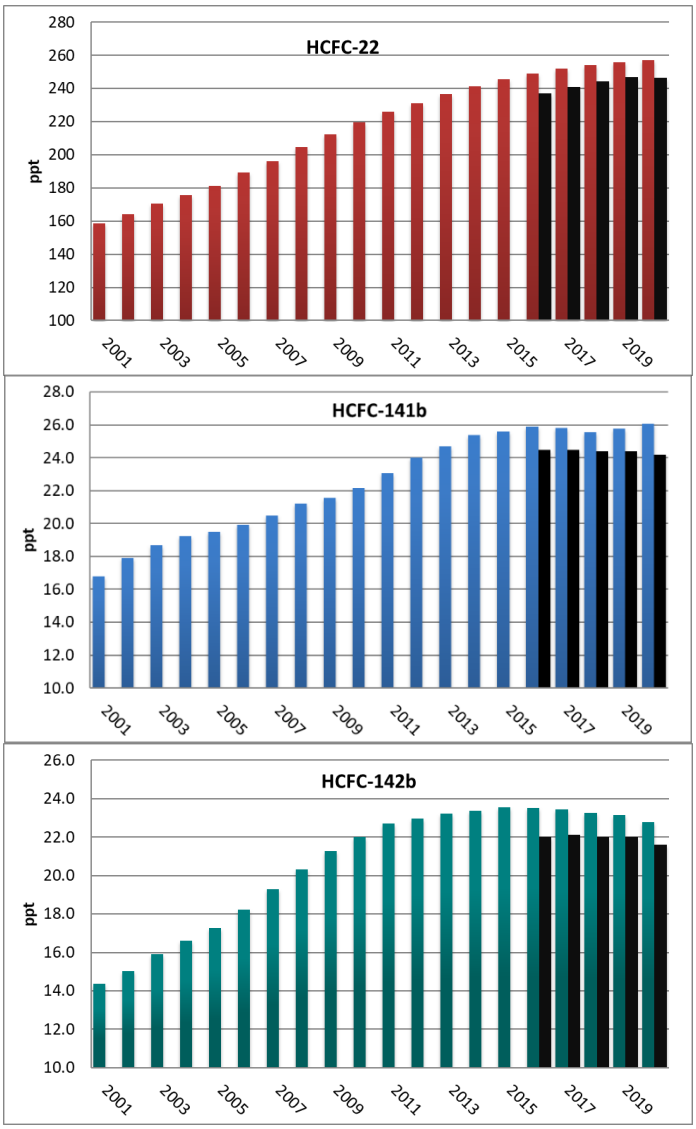

Figure 30: Development of the annual means of observed HCFCs at the Zeppelin Observatory for the period 2001-2020. HCFC-22 (red), HCFC-141b (blue), and HCFC-142b (green). The global annual means in 2016 to 2020 are included as black bars. All units are in ppt.

2.3.3 Hydrofluorocarbons (HFCs) at Zeppelin Observatory

Key findings - HFCs: *The hydrofluorocarbons (HFCs) were introduced as replacements for the ozone depleting CFCs and HCFCs. They are not harmful to the ozone layer since they do not contain chlorine, but they are strong greenhouse gases. The mixing ratios of HFC-125, HFC-134a, and HFC-152a have been measured at the Zeppelin observatory since 2001, and for the period 2001-2020 the concentrations have increased by 1510%, 471% and 303% since 2001, respectively. Eight new HFCs were introduced to the monitoring programme in 2015 and 2016: HFC-23, HFC-365mfc, HFC-227ea, HFC-236fa, HFC-245fa, HFC-32, HFC-143a, and HFC-4310mee. The mixing ratios of these gases are analysed back to 2010, showing an increase of 4-16%/yr, except for HFC-32 which increase by as much as 40%/yr. HFC-152a is the only HFC which has levelled off and stabilized the last years, but for HFC-365mfc the growth rate has also declined the last 4-5 years. For all the other HFCs the steep growth rate continued in 2020. The contribution from the HFCs to the global warming is still relatively small but given the rapid atmospheric increase it is crucial to follow the development of these gases. The phase-down of HFCs under the Montreal Protocol, agreed in Kigali in 2016, is important in curbing the growth in these gases.*

HFCs are the so-called second-generation replacements of CFCs, which means that they are considered as better alternatives to the CFCs with respect to the ozone layer than HCFCs, as they do not contain chlorine or bromine. However, many of these compounds are strong greenhouse gases. 1 kg of HFC-23 is as much as 12 400 times more powerful greenhouse gas than CO_2 (see Table 3). The phase-out of HFCs under the Montreal Protocol was under negotiation for many years and the successful agreement in Kigali, October 2016, represented an important progress. Presently, the contribution to global warming posed by HFCs is very limited. However, most of the compounds are increasing rapidly. The compounds are strong infrared absorbers with high GWP hence it is crucial to reduce future emissions.

For the period 2001-2020 three compounds have been measured at the Zeppelin Observatory: HFC-125, HFC-134a, and HFC-152a. HFC-125 is mainly used as a refrigerant and fire suppression agent. HFC-134a is used as a temperature control for domestic refrigeration and automobile air conditioners, whereas HFC-152a is used as a refrigerant and propellant for aerosol sprays and in gas duster products. Since 1990, when HFC-134a was almost undetectable in the atmosphere, the concentration of this gas has risen massively, and HFC-134a is currently the HFC with highest atmospheric concentration.

In 2015 five new HFCs were included in the Norwegian monitoring programme: HFC-23, HFC-365mfc, HFC-227ea, HFC-236fa, and HFC-245fa. In 2016 three additional HFCs were introduced to the programme: HFC-32, HFC-143a, and HFC-4310mee. All these species have been measured at Zeppelin since 2010, but they have not been analysed or reported to an international data base until 2016. The development of HFC-23 should be followed carefully since this gas has a relatively high concentration and an extremely high GWP. HFC-23 is a by-product of the production of HCFC-22 and is also used in the semiconductor industry. In addition, it is a useful refrigerant and fire suppressant.

Generally, the new HFCs are used for refrigeration and air conditioning, foam blowing, and fire extinguishing. Both HFC-245fa and HFC-365mfc are substitutes for HCFC-141b in foam blowing applications. HFC-236fa is also a foaming agent, in addition to a fire suppression agent and a refrigerant. HFC-227ea is mainly used to suppress fire in data equipment and telecommunication facilities, and in protection of flammable liquids and gases. HFC-227ea is also used as an aerosol propellant in pharmaceutical dose inhalers for e.g. asthma medication.

The three new HFCs introduced to the monitoring programme in 2016, are mainly used for refrigeration (HFC-32 and HFC-143a). In addition, HFC-143a is applied as propellant in canned air products for cleaning electronic equipment. HFC-4310mee is mainly used as a cleaning solvent in the electronics industry.

The seasonal cycles in HFC mixing ratios are closely linked to the lifetimes and variations in the incoming solar radiation. HFC-152a has the shortest lifetime (1.6 year), and as seen in Figure 31 HFC-152a has the most distinct seasonal cycle. The gas is mainly destroyed in the lowest part of the atmosphere by photolysis and reactions with OH.

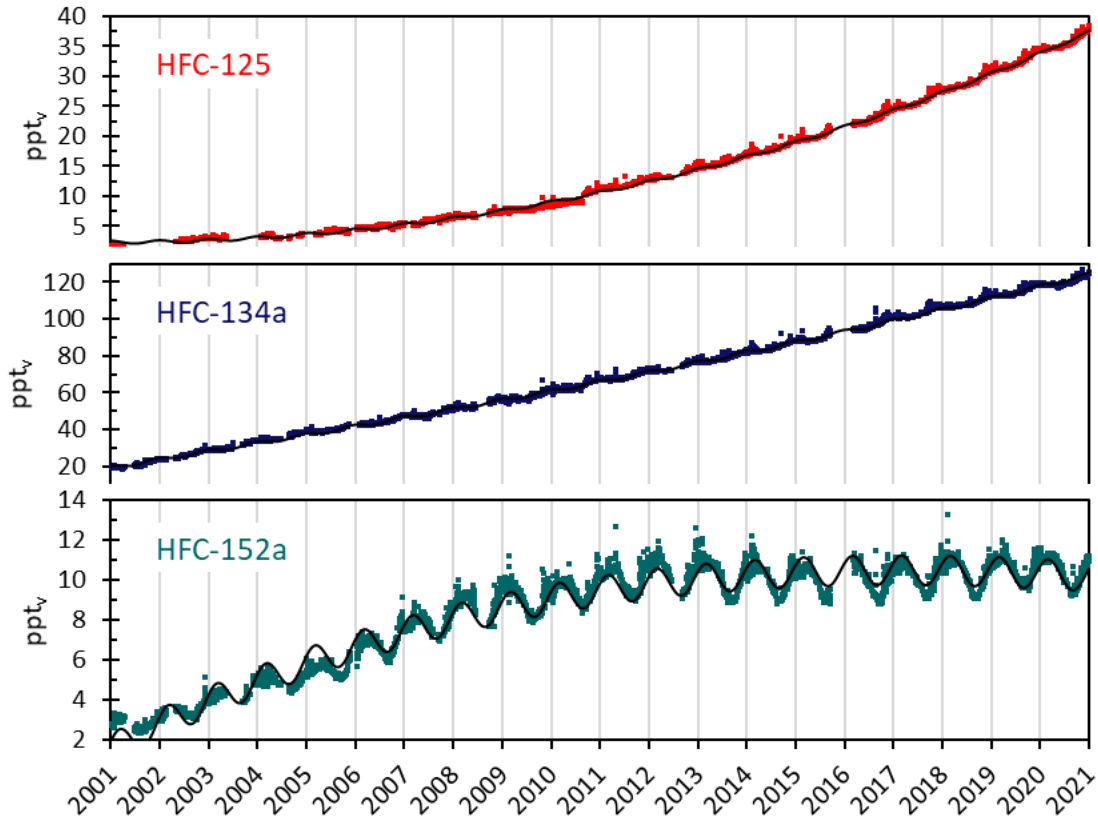

Figure 31: Daily averaged concentrations of the monitored HFCs for the period 2001-2020 at the Zeppelin observatory: HFC-125 (red), HFC-134a (dark blue), and HFC-152a (green). The solid lines are empirical fitted mixing ratios.

For the period 2001-2020 all HFCs shown in Figure 31 have increased significantly. HFC-134a has an increasing trend of 5.2 ppt/yr, which leaves this compound as the one with highest change per year of the all the halocarbons measured at Zeppelin the last decade. The mixing ratios of HFC-125, HFC-134a and HFC-152a have increased by as much as 1510%, 471% and 303% since 2001, respectively. For HFC-125 we can even see an accelerating trend. HFC-152a, however, is the only HFC where the rapid increase has levelled off and stabilized after 2012. This is partly due to the shorter lifetime and rapid response to emission changes. This is clearly illustrated in Figure 31 and Figure 33. For HFC-365mfc the growth rate has also declined the last 4-5 years.

The eight new HFCs included in the programme in 2015 and 2016 are shown in Figure 32, which clearly demonstrates that the concentrations of all HFCs have increased steadily since 2010. The compounds generally increase by 4-16%/yr, except from HFC-32 which increases by as much as 40%/yr.

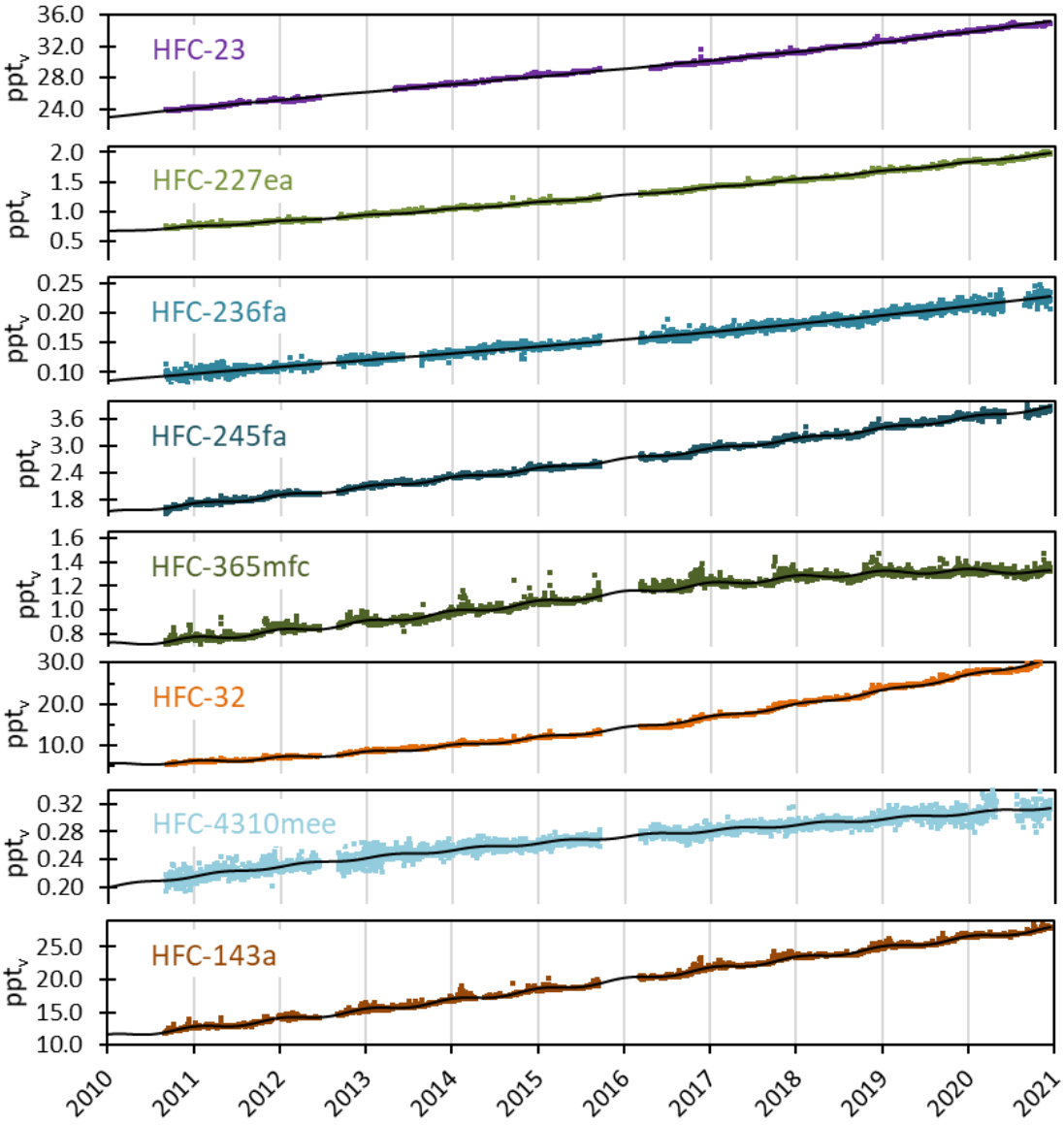

Figure 32: Daily averaged concentrations of monitored HFCs at the Zeppelin observatory for the period 2010-2020: HFC-23 (violet), HFC-227ea (light green), HFC-236fa (blue), HFC-245fa (dark blue), HFC-365mfc (dark green), HFC-32 (orange), HFC-4310mee (light blue), and HFC-143a (brown). The solid lines are empirical fitted mixing ratios.

The development of annual means of all reported HFCs are shown in Figure 33. The global annual means of 2016 - 2020 as given in Hall et al. (2017; 2020), Dlugokencky et al. (2018; 2019), and Lan et al. (2021) are included as black bars for comparison. As for HCFCs the concentrations at Zeppelin are slightly higher than the global means. Also, the increasing tendency for most HFCs is clear, even if the concentrations are still very low, particularly for the new HFC-365mfc, HFC-245fa, HFC-236fa, HFC-227ea, and HFC-4310mee, with 3.7 ppt as maximum for HFC-245fa.

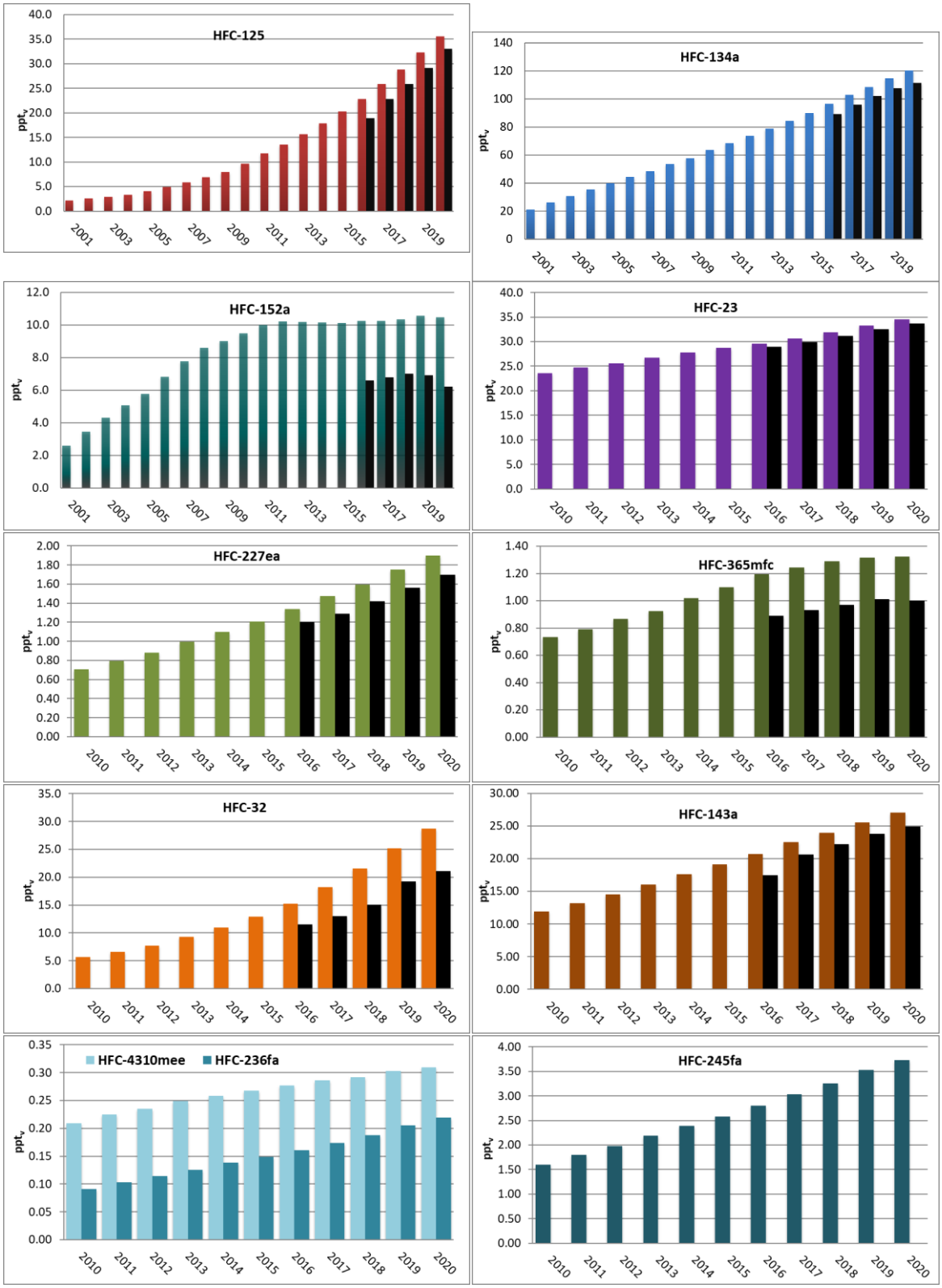

Figure 33: Development of the annual means of observed HFCs at the Zeppelin Observatory. For the period 2001-2020: HFC-125 (red), HFC-134a (blue), and HFC-152a (dark green). For the period 2010-2020: HFC-23 (violet), HFC-227ea (light green), HFC-365mfc (dark green), HFC-32 (orange), HFC-143 (brown), and light to dark blue: HFC-4310mee, HFC-236fa, and HFC-245fa. The global annual means in 2016-2020 are included as black bars, when available.

2.3.4 Halons measured at Zeppelin Observatory

***Key findings - Halons**: Halons are bromine containing halocarbons that contribute both to the depletion of the ozone layer and to global warming. Three halons are measured at Zeppelin: H-1211, H-1301, and H-2402. For H-1211 a maximum was observed in 2004, followed by a gradual decline. The concentration of H-1211 is ~25% lower today than when the measurements started in 2001. H-2402 has deceased by ~15% during the same period. H-1301, however, has increased by ~13% from 2001 to 2020, but no increase has been measured the last 5-6 years. According to the last Ozone Assessment (WMO, 2018) the stratospheric bromine concentration has now started to decrease.*

Halons are greenhouse gases containing bromine. Thus, regulations of halons are also important to protect the ozone layer. Actually, bromine, if it reaches the stratosphere (high atmosphere), is even more effective in destroying ozone than chlorine. The halons are regulated through the Montreal protocol and the concentration of most of these substances are decreasing. The main source of halons has been fire extinguishers.

Previously, two halons were measured at the Zeppelin observatory: H-1301 and H-1211. In 2016 H-2402 was also included in the monitoring programme. H-2402 was used primarily in the former USSR and was the main halon fire suppressant in that region.

The ambient concentrations of the three halons are fairly low, below 4 ppt. Figure 34 shows the daily average concentrations of the monitored halons at Zeppelin. The halon trend analyses, listed in Table 2 and visualized in Figure 34, show an increase for H-1301 during the period 2001-2020 and a decrease for H-1211. The concentration of H-1211 is ~25% lower today than when the measurements started in 2001, whereas H-1301 has increased by ~13%. However, the concentration of H-1301 has stabilized and no increase has been measured the last 5-6 years. The new compound, H-2402, shows a relaxation of ~15% from 2010 to 2020. The development of the annual means for all three compounds are shown in Figure 35.

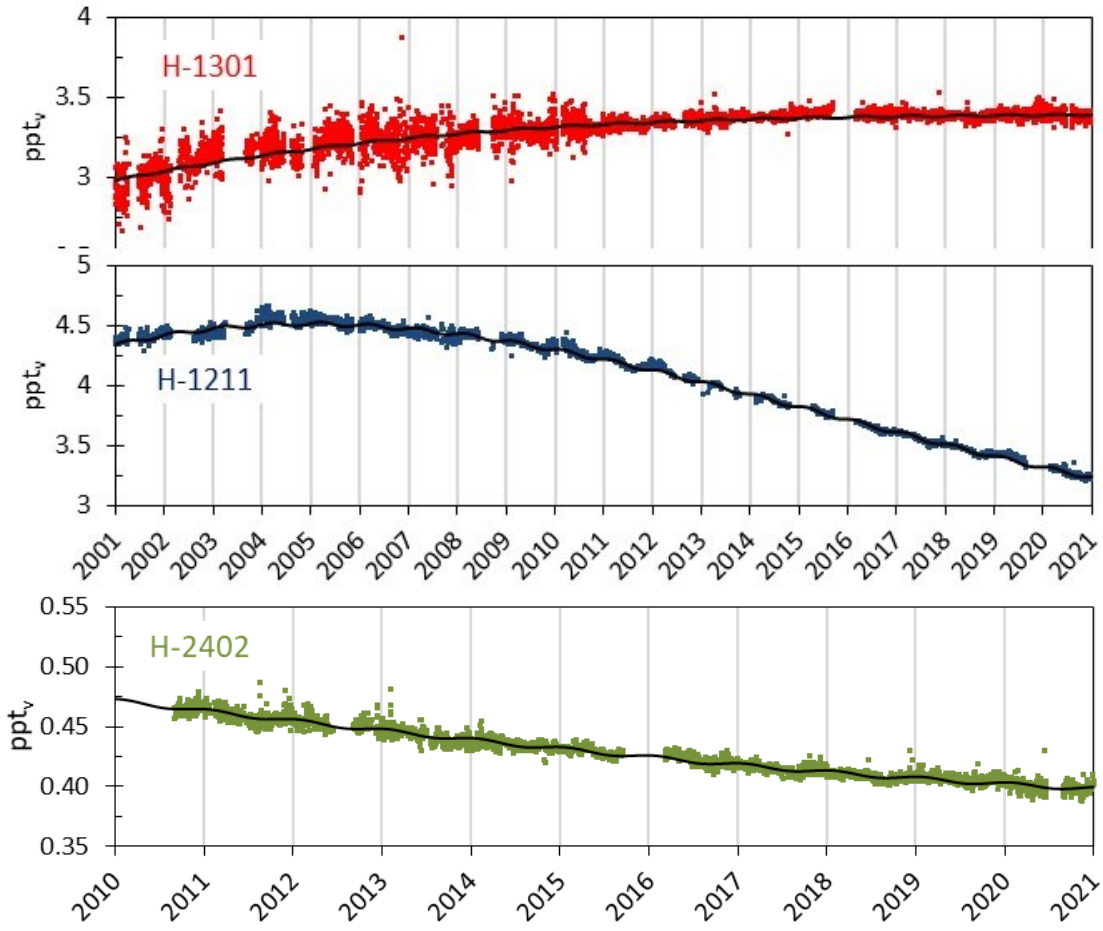

Figure 34: Daily averaged concentrations of the monitored halons at the Zeppelin Observatory. For the period 2001-2020: H-1301 (red) and H-1211 (blue). For the period 2010-2020: H-2402 (green). The solid lines are empirical fitted mixing ratios.

The annual means have not changed dramatically over the measured period, which is explained by low emissions and relatively long lifetimes (16 years for H-1211, 72 years for H-1301, and 28 years for H-2402). However, clear declines are evident for H-1211 and H-2402, which have the shortest lifetimes. According to the last Ozone Assessment report (WMO, 2018) the total stratospheric bromine concentration decreased by ~0.15 ppt/yr from 2012 to 2016.

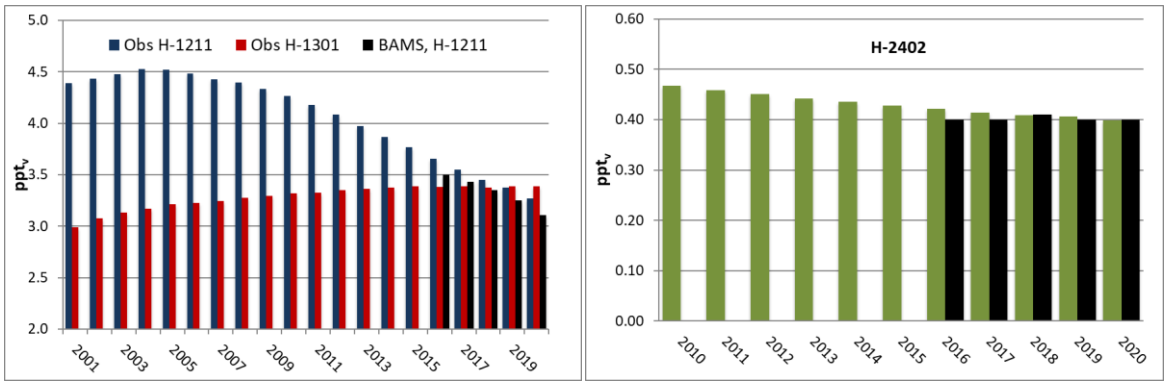

Figure 35: Development of the annual means of the observed halons at the Zeppelin Observatory. Red: H-1301, blue: H-1211, and green: H-2402. The global annual means in 2016 to 2020 are included as black bars. All units are in ppt.

2.3.5 Other chlorinated hydrocarbons at Zeppelin Observatory

***Key findings - Other chlorinated greenhouse gases**. In addition to chloromethane and bromomethane described in section 2.2.6 and 2.2.7, the following six chlorinated gases are measured at the Zeppelin Observatory: Trichloroethane (CH_3CCl_3), dichloromethane (CH_2Cl_2), trichloromethane ($CHCl_3$), trichloroethene ($CHClCCl_2$), tetrachloroethene (CCl_2CCl_2), and carbon tetrachloride (CCl_4). The concentration of most of these gases are decreasing. Possible exceptions are trichloromethane and dichloromethane, which increased significantly from 2007 to 2017. However, the last three years the annual mean concentrations of trichloromethane at Zeppelin has decreased and dichloromethane seems to have stabilized*.

This section describes the following components measured at the Zeppelin Observatory: Trichloroethane (also called methyl chloroform, CH_3CCl_3), dichloromethane (CH_2Cl_2), trichloromethane (also called chloroform, $CHCl_3$), trichloroethene (TCE, $CHClCCl_2$), and tetrachloroethene (PCE, CCl_2CCl_2). The daily average concentrations are shown in Figure 37. Additionally, a new compound was added to the monitoring programme in 2015; Carbon tetrachloride (CCl_4). The main sources of all these substances are solvents.

The global fraction of trichloroethane (CH_3CCl_3), which is controlled under the Montreal Protocol, has been declining steadily since the peak values in the early 1990s. In 2016 the global amount of CH_3CCl_3 reaching the stratosphere was reduced by 98% of its maximum value (WMO, 2018). The measurements at Zeppelin show that the concentration has decreased to 1.5 ppt in 2020, a reduction of 96% since the measurements started in 2001. Today trichloroethane contributes negligible to the atmospheric chlorine burden.

It is worth noting the strong increase in dichloromethane (violet) and trichloromethane (light blue) from 2007 to 2017, seen in Figure 36 and Figure 37. Dichloromethane has a lifetime of less than 6 months and responds rapidly to emissions changes, where about 90% has industrial origin. Its main applications are from paint strippers, degreasers, and solvents, in foam production and blowing applications or as an agricultural fumigant (WMO, 2011). The natural sources of dichloromethane, which account for ~10% of the total emission, is mainly from biomass burning and marine sources. At Zeppelin dichloromethane has increased by ~97% since 2001. However, the growth rate has decreased the last years and the annual mean concentration in 2020 was close to the 2017 value.

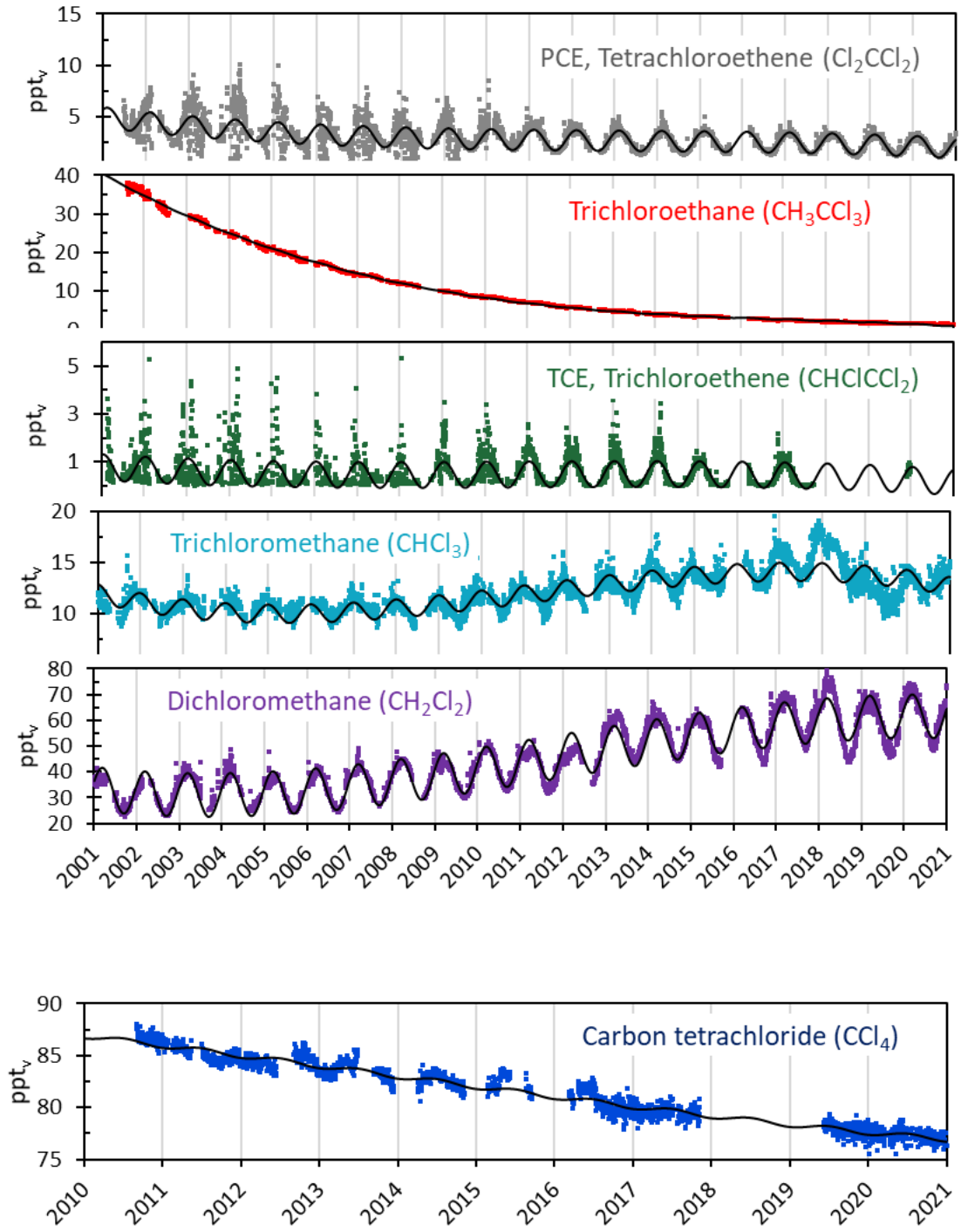

Figure 36: Daily averaged concentrations of chlorinated hydrocarbons at the Zeppelin observatory: For the period 2001-2020: Tetrachloroethene (grey), trichloroethane (red), trichloroethene (green), trichloromethane (light blue), and dichloromethane (violet). For the period 2010-2020: carbon tetrachloride (dark blue). Solid lines are empirical fitted mixing ratios.

Trichloromethane (light blue) has a lifetime of ~0.5 year, thus the response to emission changes is also relatively rapid. The annual mean value of trichloromethane at Zeppelin increased by 37% from 2001 to 2017 and similar increases were observed at other sites (e.g. Mauna Loa at Hawaii and Barrow in Alaska). However, there has been a clear decrease in trichloromethane at Zeppelin the last three years,

and the annual mean concentration in 2020 was 2.3 ppt below the 2017 peak value. The reason for these rapid changes is not yet clear, but they might be explained by natural sources.

Even if trichloromethane and dichloromethane have relatively short lifetimes, modelling studies imply that chlorine from these compounds can reach the lower stratosphere and potentially destroy stratospheric ozone (Hossaini et al., 2017). Thus, sustained growth in these compounds might offset some of the gains achieved by the Montreal Protocol, further delaying recovery of Earth's ozone layer.

The atmospheric concentrations of trichloroethene (TCE; green) and tetrachloroethene (PCE; grey) are low, and the annual variabilities are quite high, especially before 2011 due to instrumental limitations (see appendix 2). This makes it difficult to draw conclusions about trends and development of these species. In 2020 the annual average concentration of PCE was 2.1 ppt, a reduction of 0.2 ppt from 2019.

The concentration of carbon tetrachloride (CCl_4) has been measured at Zeppelin since 2010. This compound was once a popular solvent in organic chemistry, but because of its adverse health effects it is rarely used any more. Today CCl_4 is sometimes applied as a solvent for infrared spectroscopy. For the period 2010-2020 the annual mean values have decreased by 1.1%/yr, i.e. from 86.6 ppt in 2010 to 77.3 ppt in 2020.

It should be noted that no annual mean values of TCE are calculated from the measurements in 2018 to 2020. This is related to the upgrade of the Medusa-GCMS in 2017 (see Appendix II), which caused problems for this compound. Thus, most of the TCE measured performed after October 2017 are flagged as "absent".

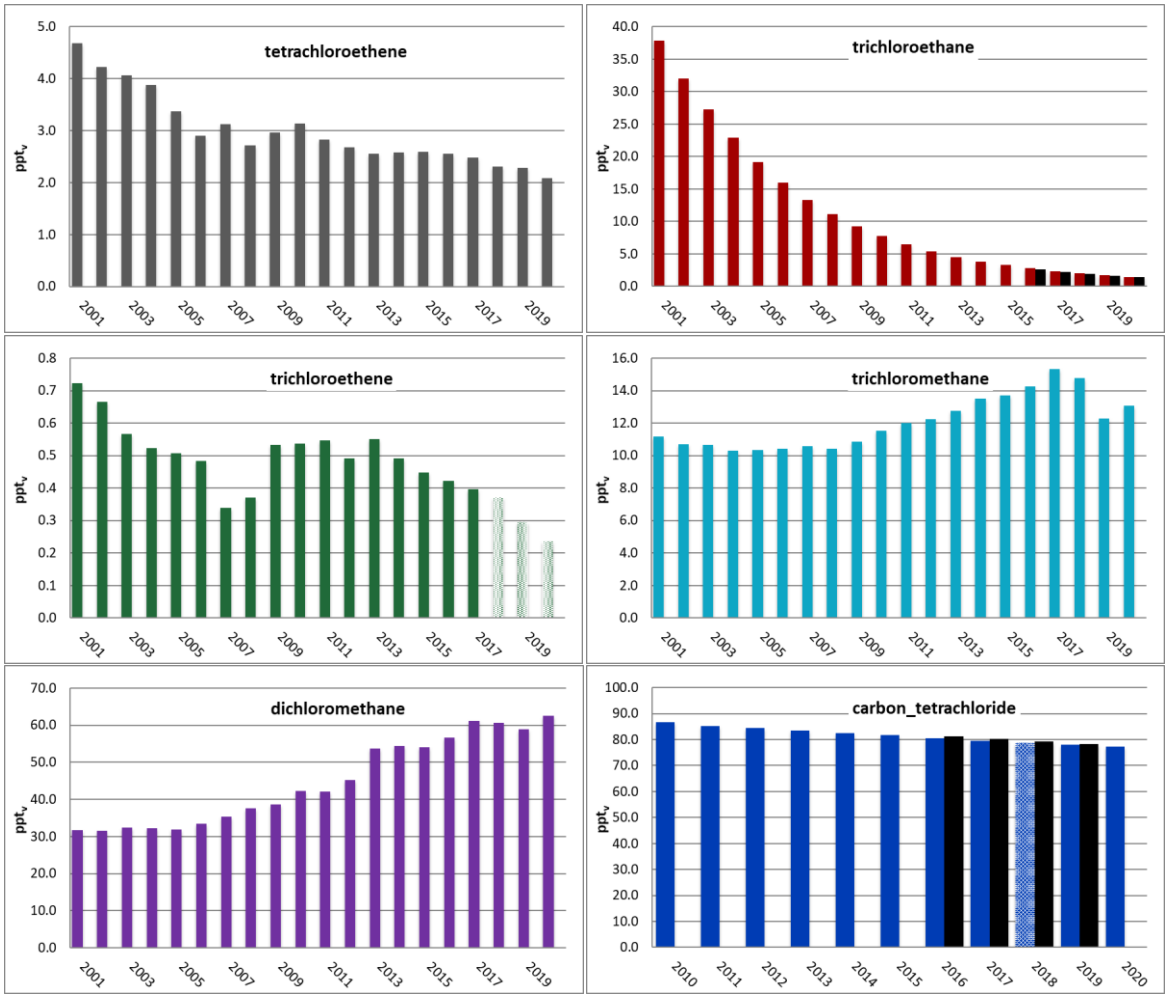

Figure 37: Annual means of the chlorinated hydrocarbons. Upper panel: tetrachloroethane (grey) and trichloroethane (red). Mid panel: trichloroethene (TCE, green) and trichloromethane (light blue). Lower panel: dichloromethane (violet) and carbon tetrachloride (CCl_4, dark blue). The global annual means for CH_3CCl_3 and CCl_4 in 2016-2020 are included as black bars, when available. All units are in ppt. Note that TCE data from 2018-2020 are based on model data.

2.3.6 Perfluorinated compounds at Zeppelin Observatory

Key findings – Perfluorinated compounds. *This group of compounds include SF_6, SO_2F_2, NF_3, PFC-14, PFC-116, PFC-218, and PFC-318. Generally, these compounds are extremely potent greenhouse gases, but their concentrations are still low. An exception is PFC-14, which had a mixing ratio of 86.9 ppt in 2020, an increase of 0.8 ppt since 2019. SF_6 should also be followed closely, as this compound has an atmospheric lifetime of 3 200 years and an extremely high GWP of 25 200. This compound has increased by 111% since 2001.*

Perfluorinated compounds belong to a group of long-lived greenhouse gases, and their contribution to the Earth's radiative forcing has increased over the past several decades. The impact of these highly fluorinated compounds on climate change is a concern because of their exceptionally long atmospheric lifetimes, as well as their strong absorption in the infrared "window" region (Baasandorj et al., 2012).

Up to 2015, the Norwegian national monitoring programme only included measurements of one perfluorinated compound, SF_6. However, other perfluorinated compounds are also very powerful

greenhouse gases with atmospheric lifetimes up to 50 000 years (See Table 3) and with increasing concentrations in the atmosphere. From 2010 NILU extended the monitoring of perfluorinated compounds at Zeppelin, after new and improved instrumentation was installed. Several of these compounds, so-called perfluorocarbons (PFCs), were included in the current monitoring programme in 2015, with analysis back in time to September 2010. Two additional compounds were included in the 2016 monitoring programme: Nitrogen trifluoride (NF_3) and Sulphuryl fluoride (SO_2F_2). For the latter compound data was analysed back to 2010. The instrument at Zeppelin was re-built and optimised in 2015 and 2016, which made it possible to measure NF_3. Thus, NF_3 data are only available from 2016 and onwards.

2.3.6.1 Sulphurhexafluoride (SF6), Sulphuryl fluoride (SO_2F_2), Nitrogen trifluoride (NF_3)

Sulphurhexafluoride, SF_6, is an extremely strong greenhouse gas emitted to the atmosphere mainly from the production of magnesium and in the electrical industry for high-voltage circuit breakers, switch gears and other electrical equipment. This component has been a part of the monitoring programme since 2001. The atmospheric lifetime of this compound is 3 200 years, and the global warming potential is 25 200, which means that the emission of 1 kg of SF_6 has a warming potential which is 25 200 times stronger than 1 kg emitted CO_2 (Myhre et al, 2013b).

Sulphuryl fluoride, SO_2F_2, has a lifetime of 36 years and a GWP of 4 630. SO_2F_2 is normally used as a pesticide fumigant for dried fruits, nuts, and other agricultural commodities that must be kept pest-free during storage. It is one of the most common replacements for bromomethane, an ozone-depleting substance whose use is being phased out.

Nitrogen trifluoride, NF_3, has a lifetime of 569 years and a GWP as high as 17 400, meaning that it also is an extremely strong greenhouse gas. NF_3 is used in the manufacturing of new generation solar panels, flat-screen televisions, touch-sensitive screens, and electronic processors. The use of NF_3 has widely increased in the past because of the rising demand in flat-screen televisions and microelectronics.

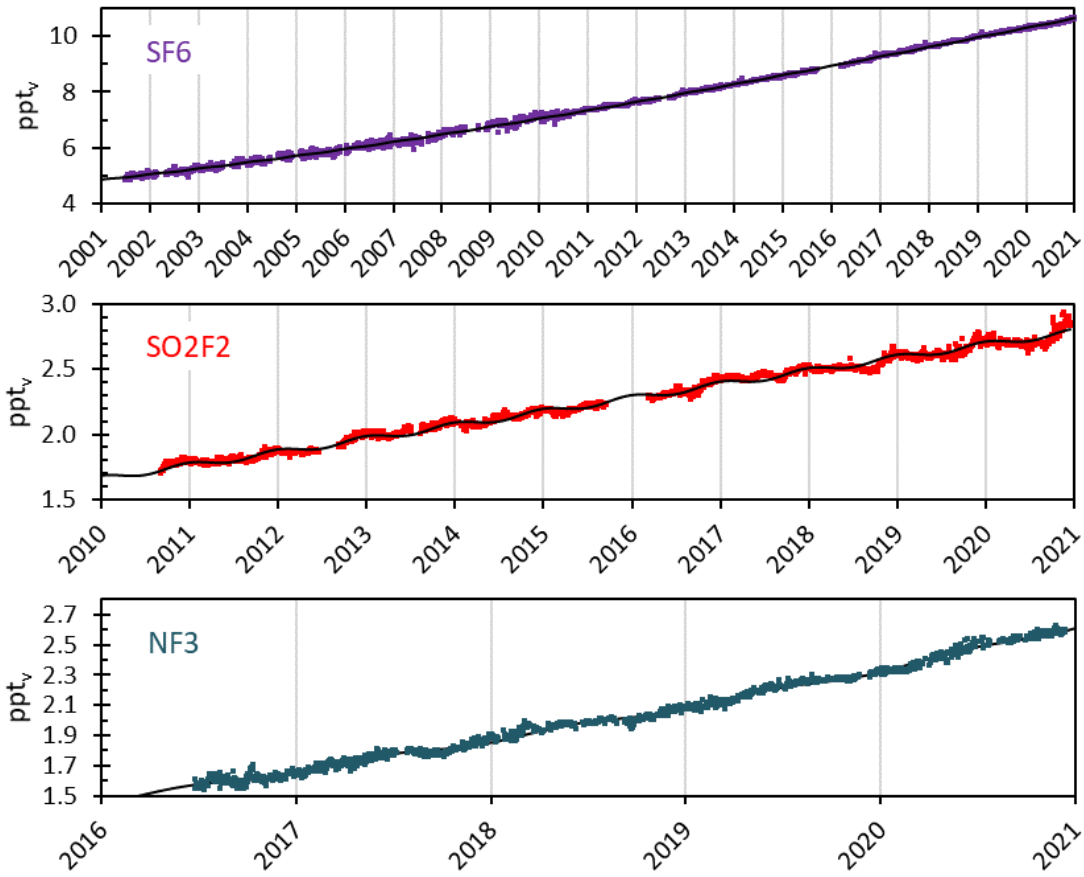

Figure 38: Daily averaged concentrations at the Zeppelin Observatory. Upper panel: SF_6 for the period 2001-2020. Middle panel: SO_2F_2 for the period 2010-2020. Lower panel: NF_3 from mid 2016 to 2020. Solid lines are statistical fitted mixing ratios.

The daily averaged concentrations of SF_6, SO_2F_2 and NF_3 are presented in Figure 38. SF_6 is increasing with a rate of 0.29 ppt/yr and has increased as much as 111% since the start of our measurements in 2001. The instrumentation before 2010 was not optimal for measurements of SF_6, thus there are higher uncertainties for this compound's mixing ratios than for most of the other compounds reported from 2001 to 2010 (see Appendix I).

The concentration of SO_2F_2 has also increased significantly the last years (see Figure 38). The total increase for the period 2010-2020 is 1.02 ppt (59%). Daily average observations of NF_3 are visualized in Figure 38, lower panel, and the figure clearly demonstrates a continued increase since the measurements started in June 2016. The annual average NF_3 concentration in 2020 was 2.48 ppt, an increase of 0.87 ppt (54%) from 2017.

Figure 39 shows annual average concentrations of SF_6 (left panel) and SO_2F_2 (right panel) measured at Zeppelin for the periods 2001-2020 and 2010-2020, respectively. The global annual means of SF_6 in 2016 - 2020 (Hall et al., 2017 and 2020; Dlugokencky et al., 2018 and 2019; Lan et al., 2021) are included as black bars for comparison. Again, the concentrations at Zeppelin are slightly higher than the global means.

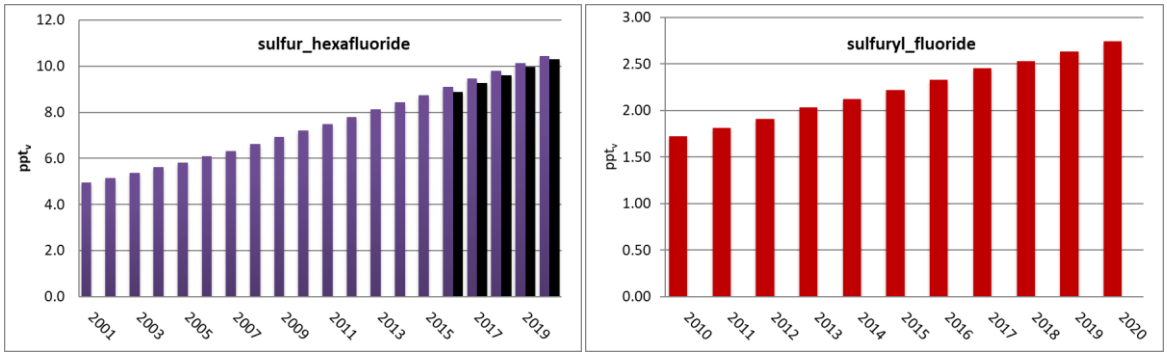

Figure 39: Annual means of SF_6 for the period 2001-2020 (left) and SO_2F_2 for the period 2010-2020 (right) at the Zeppelin observatory. The global annual means for SF_6 in 2016 to 2020 are included as black bars.

2.3.6.2 Perfluorocarbons or PFC's: PFC-14, PFC-116, PFC-218, PFC-318

Perfluorocarbons or PFCs are compounds that contain only carbon and fluorine. Four of these compounds are currently measured and reported at Zeppelin: PFC-14, PFC-116, PFC-218, and PFC-318. PFC-14, also called tetrafluoromethane or CF_4, is the most persistent PFC greenhouse gas with an atmospheric lifetime of 50 000 years and a greenhouse warming potential of 7 380. It is used as a low temperature refrigerant, in electronics microfabrication, and in neutron detectors. Another potent greenhouse gas is hexafluoroethane, PFC-116, which has an atmospheric lifetime of 10 000 years and a GWP of 12 400. The gas is used as an etchant in e.g. semiconductor manufacturing, and aluminium and semiconductor manufacturing industries are the major emitters of PFC-116. Fraser et al. (2013) showed that the release of PFC-14 at Hydro's aluminium plant in Australia was 10 times greater than the release of PFC-116. Octafluoropropane, PFC-218, which has an atmospheric lifetime of 2 600 years and a GWP of 9 290, is also used in the electronics industry as a plasma etching material. In medicine, PFC-218 microbubbles reflect sound waves well and is used to improve the ultrasound signal backscatter. Octafluorocyclobutane, PFC-318, with an atmospheric lifetime of 3 200 years and a GWP of 10 200, is the third most abundant PFC in the atmosphere (Oram et al, 2012). Although a number of potential sources of PFC-318 have been reported, including electronic and semi-conductor industries, there remains a large discrepancy in the atmospheric budget. *A study from Mühle et al. (2019) suggests that production of Teflon and other fluorochemicals in China, India, and Russia is a likely source of PFC-318, as pyrolysis of HCFC-22 produces PFC-318 as a by-product*

The daily averaged concentrations of the PFCs measured at Zeppelin are shown in Figure 40. For the period 2010-2020 PFC-116, PFC-218 and PFC-318 increased by 2.1%/yr, 2.8%/yr and 4.5%/yr, respectively. For PFC-14 no data exist until October 2014, but the measurements in 2015 to 2020 indicate that the concentration of PFC-14 increases by ~1.1%/yr.

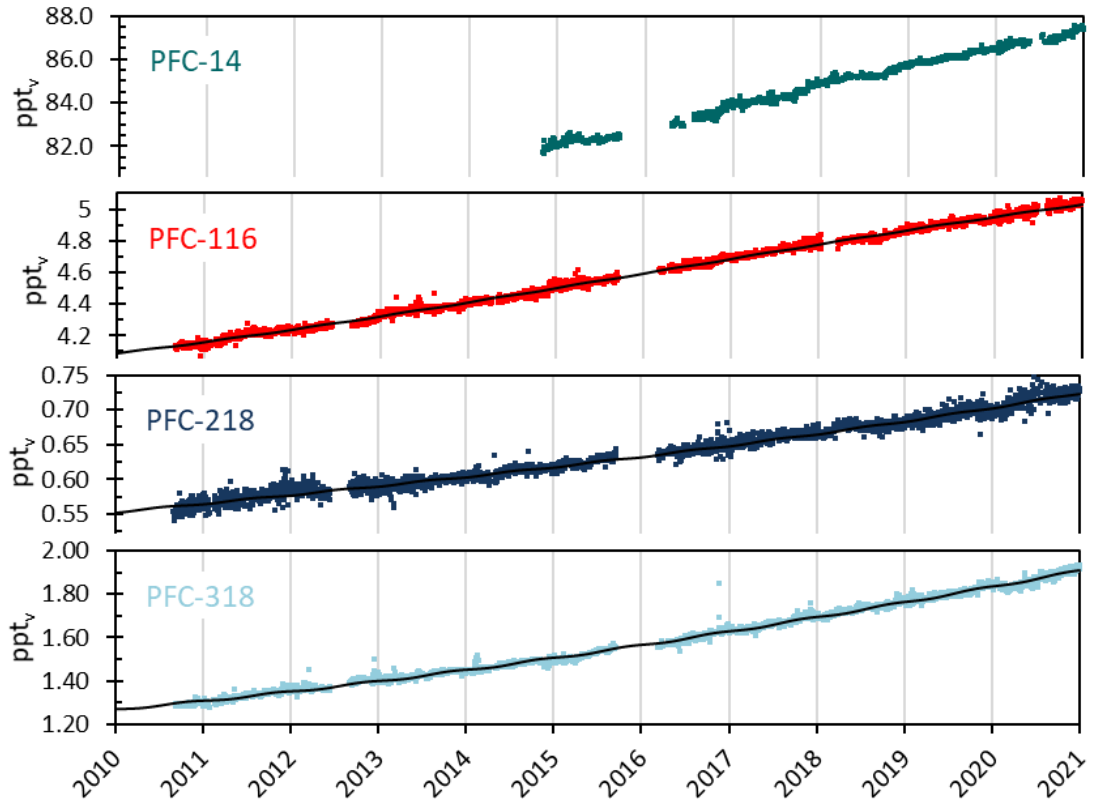

Figure 40: Daily averaged concentrations of perfluorocarbons at the Zeppelin observatory for the period 2010-2020: PFC-14 (green), PFC-116 (red), PFC-218 (dark blue), and PFC-316 (light blue). PFC-14 is only ranging back to autumn 2014. The solid lines are statistical fitted mixing ratios.

The development of the annual means of the PFCs are shown in Figure 41. For PFC-116 the global annual mean in 2016 to 2020 (Hall et al., 2017 and 2020; Dlugokencky et al., 2018 and 2019; Lan et al., 2021) are shown as black bars for comparison. The concentrations of most PFCs are relatively low. However, PFC-14 is an exception. With an annual mean concentration of 86.9 ppt in 2020, a lifetime of 50 000 years and GWP of 7 380, this is an important greenhouse gas that should be followed carefully.

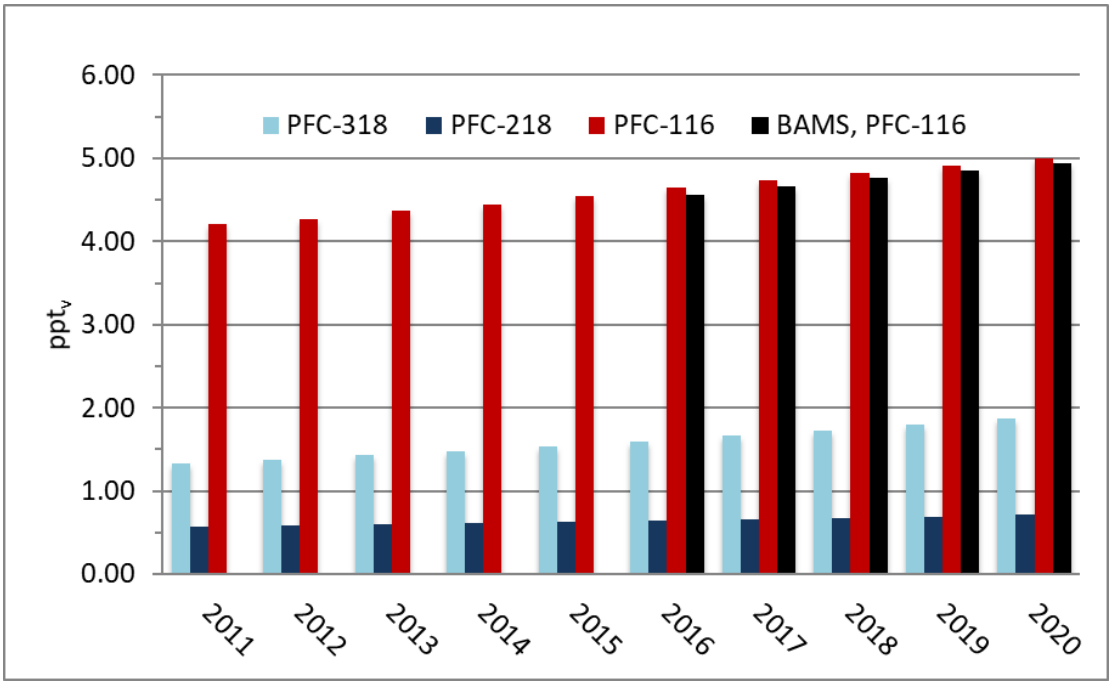

Figure 41: Annual mean concentrations of perfluorocarbons for the period 2010-2020 at the Zeppelin observatory: PFC-116 (red), PFC-218 (dark blue), and PFC-318 (light blue). The global annual means for PFC-116 in 2016 to 2020 are included as black bars.

3 Aerosols and climate

Atmospheric aerosol influences climate by scattering incoming solar radiation back into space or absorbing the radiation. This so-called direct aerosol climate forcing results mostly in cooling, but can be moderated if the aerosol itself absorbs solar radiation, e.g. if it consists partly of light absorbing carbon or light absorbing minerals. In this case, the aerosol warms the surrounding atmosphere. Atmospheric aerosol influences climate as outlined in section 1.4. Atmospheric aerosol particles also affect the reflectivity and lifetime of clouds, which is termed the indirect aerosol climate effect. The effect can be cooling as well as warming for climate, but in most cases, the cloud reflectivity and lifetime are increased, leading again to a cooling effect (see Figure 5). Figure 42 gives an overview of the main natural and anthropogenic sources of atmospheric aerosols, also described in detail the annual report of Aas et al. 2020 on long range transport of air pollution.

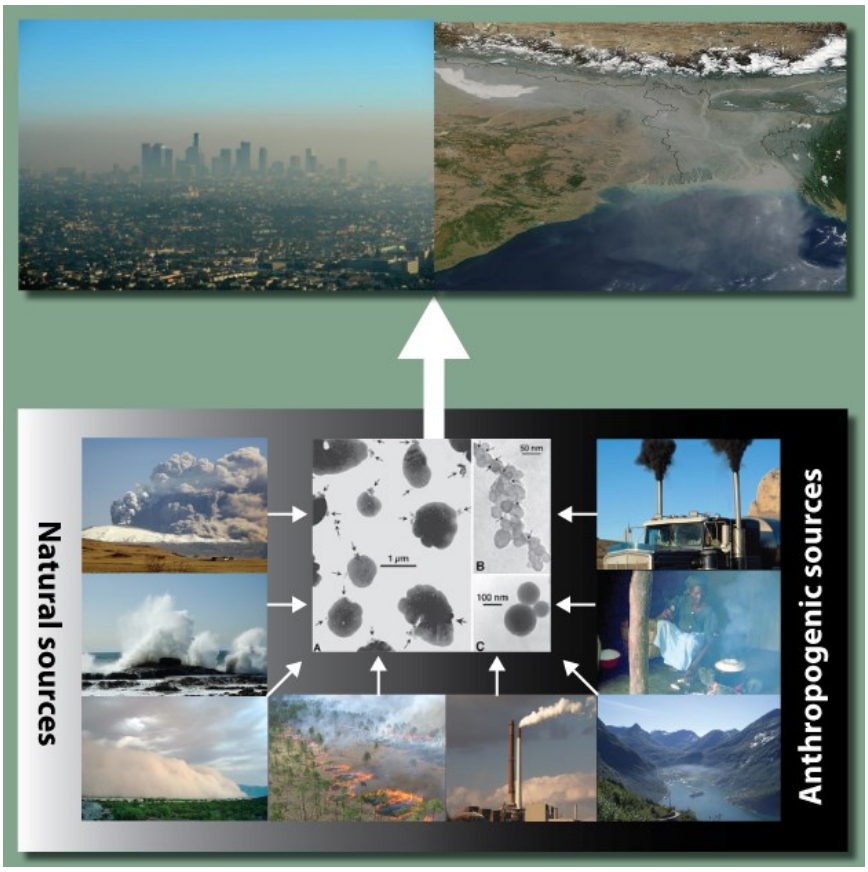

Figure 42: Illustration of the main natural and anthropogenic sources of atmospheric aerosols taken from Myhre et al (2013b). Top: local and large scale air pollution. Sources include (bottom, counter clockwise) volcanic eruptions (producing volcanic ash and sulphate), sea spray (sea salt and sulphate aerosols), desert storms (mineral dust), savannah biomass burning (BC and OC), coal power plants (fossil fuel BC and OC, sulphate, nitrate), ships (BC, OC, sulphates, nitrate), cooking (domestic BC and OC), road transport (sulphate, BC, VOCs yielding OC). Additionally, Biogenic VOC to SOA and primary biological (e.g. pollen) from vegetation is crucial. Center: Electron microscope images of (A) sulfates, (B) soot, (C) fly ash, a product of coal combustion (Posfai et al., 1999).

With respect to monitoring climate change and the atmospheric constituents exerting an effect on climate, this year marks the publication of the 6th IPCC assessment report (AR6). Putting the data on atmospheric aerosol properties documented in this report into the context of AR6, a few relevant findings of AR6 are summarised below:

- Aerosol loadings across Northern Hemisphere mid-latitudes increased between 1700 and the late 20th century before declining after 2000 due to air quality measures, while increases over South Asia and East Africa are still ongoing due to industrialisation (Gulev et al., 2021).
- Atmospheric aerosol led to a negative radiative forcing throughout the industrial period, ERF = –1.3 [–2.0 to –0.6] W m^{-2}. To this, aerosol-cloud interactions (indirect aerosol climate effect) contributed –1.0 [–1.7 to –0.3] W m^{-2}, whereas direct aerosol-radiation interaction (direct aerosol climate effect) contributed–0.3 [–0.6 to 0.0] W m^{-2} (IPCC 2021a, Forster et al., 2021).
- The negative aerosol ERF is offset a significant part of the positive (warming) ERF due to greenhouse gases (IPCC 2021a, Chap7)
- The cooling aerosol climate effect (negative ERF) also increased between 1750- late 20th century before declining after 2000.
- It is now less important compared to other climate forcing agents, e.g. well-mixed greenhouse gases. This recent decrease of negative aerosol radiative forcing has thus led to a positive ERF (warming) last years.
- Due to the decreasing relative contribution of aerosol climate forcing, the induced uncertainty on climate projections is decreasing as well. Nevertheless, the aerosol effect remains the largest uncertainty in ERF between 1750- 2019.
- Smaller absolute and relative negative aerosol climate forcing and an induced net warming climate effect, are projected to continue into the future (IPCC 2021a, Gulev et al., 2021).
- Carbonaceous aerosol loads have decreased over several regions of the Northern Hemisphere (IPCC 2021a, Chap6).
- COVID-19 lockdowns led to a discernible temporary improvement of air quality in most regions, but changes to global and regional climate are undetectable above internal variability (IPCC 2021a, Naik et al., 2021).
- AR6 states it as virtually certain that hot extremes and heatwaves are more frequent and more intense across most land regions since the 1950s, with high confidence that human-induced climate change is the main driver of these changes (IPCC 2021b). Heatwaves in the Arctic are strongly linked with increased atmospheric transport/ exchange at high latitudes. Increased high latitude air mass exchange also implies increased poleward transport of aerosol pollution. This should be carefully monitored due to the potential for rapid, large-scale changes in relative pollution levels considering the clean starting conditions, alongside the potential for feedbacks.

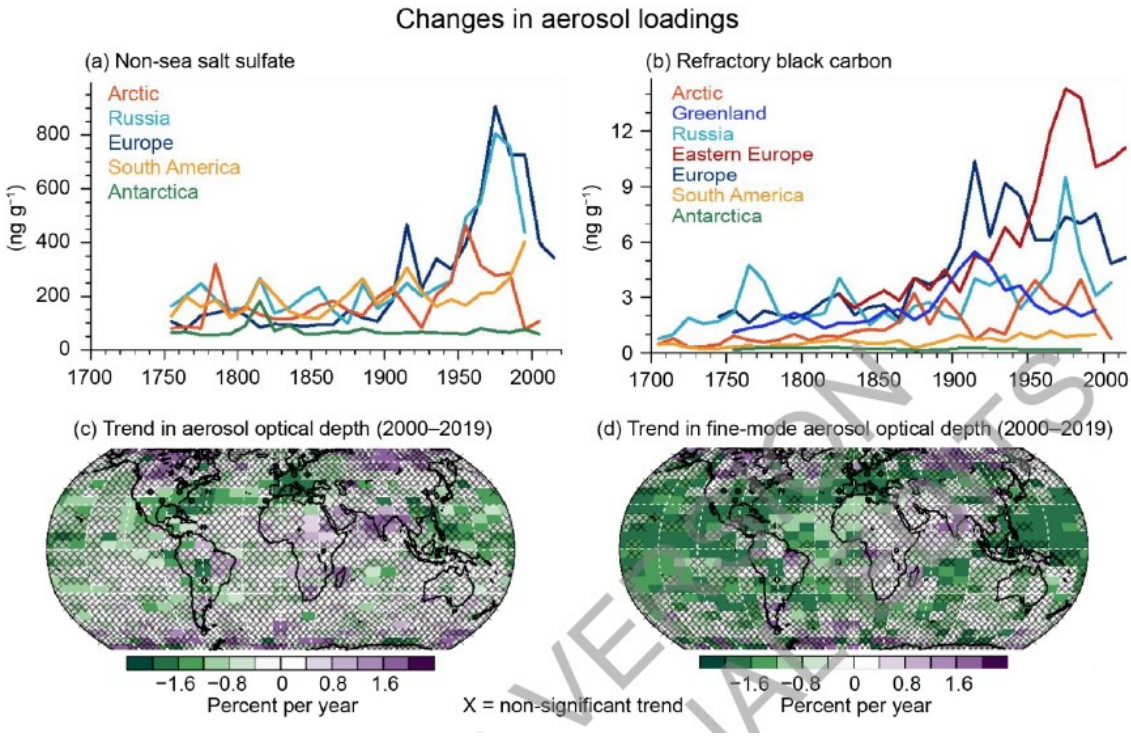

Figure 43: The temporal and regional development of atmospheric loads of relevant aerosol component loadings or properties (Gulev et al., 2021): a) concentration of particulate non-sea salt sulphate in regions of the globe; b) concentration of particulate refractory black carbon in regions of the globe; c) regional trend of aerosol optical depth for the years 2000-2019; d) regional trend of fine-mode aerosol optical depth for the years 2000-2019. The trends illustrate the increase of aerosol loading throughout the industrialised period until the late 20th century, and the decrease since then due to measures for improving air quality.

3.1 Analysis of in situ aerosol radiative properties around the world

In preparation of IPCC AR6, several studies have presented the global status and trends in aerosol properties using, among others, data and results from the Norwegian national monitoring programme. Among these articles are several initiated by the WMO Global Atmosphere Watch (GAW) programme and ACTRIS, in which the observations of aerosol properties at Zeppelin, Birkenes, and Trollhaugen are used directly or indirectly in AR6:

1. Laj et al. 2020, entitled "*A global analysis of climate-relevant aerosol properties retrieved from the network of Global Atmosphere Watch (GAW) near-surface observatories*". This article gives an overview over the GAW station network measuring climate relevant aerosol particle properties at surface stations, with link to ACTRIS as quality assurance and quality control framework (see section 1.3 on page 16). The properties observed comprise particle light scattering and absorption coefficient, particle number concentration and size distribution.

2. Collaud Coen et al. (2020), entitled "*Multidecadal trend analysis of in situ aerosol radiative properties around the world*". A subset of Laj et al., data from 52 stations worldwide is used in Collaud Coen et al., to provide a robust analysis of the long-term (>10 yr) trends of aerosol optical properties. This study contains a detailed discussion of trends in climate relevant optical aerosol properties, namely particle scattering, backscattering, and absorption coefficient, but also the derived properties single scattering albedo, scattering and absorption

Ångström coefficient (see section 3.3 for a definition of these terms). Also, the evolution of trends and their causes are evaluated.

3. Gliß et al. (2020), entitled "*Multi-model evaluation of aerosol optical properties in the AeroCom phase III Control experiment, using ground and space based columnar observations from AERONET, MODIS, AATSR and a merged satellite product as well as surface in-situ observations from GAW sites*". The authors use synthetic observations generated by those climate models feeding into IPCC AR6, and compare them to corresponding real-world observations. Comparisons include aerosol optical depth by space and surface based remote sensing, as well as observations of aerosol optical properties from the GAW network.
4. Mortier et al. (2020), entitled "*Evaluation of climate model aerosol trends with ground-based observations over the last two decades - an AeroCom and CMIP6 analysis*". The authors take the trends discovered in atmospheric aerosol observations (aerosol optical depth from surface remote sensing, aerosol optical properties and mass of particulate matter from surface in situ stations), and investigate whether climate models can reproduce these. Since observations aren't representative for the whole globe, they use the climate models to extrapolate the trends in the observations to the global level.
5. Pandolfi et al. (2018), entitled "*A European aerosol phenomenology – 6: scattering properties of atmospheric aerosol particles from 28 ACTRIS sites*". Looks at the spatial distribution of the aerosol particle scattering coefficient σ_{sp} across Europe, as well as diurnal and annual patterns. Find a gradient of increasing values from northern / western stations towards the centre of Europe.
6. Zanatta et al. (2016), entitled "*A European aerosol phenomenology-5: Climatology of black carbon optical properties at 9 regional background sites across Europe*". Major findings: 1) Both σap and mEC in southern Scandinavia and Central Europe have a distinct seasonality with maxima during the cold season and minima during summer, opposite trend at Mediterranean sites; 2) mass absorption cross-section of black carbon is homogeneous over Europe; 3) presence of non-absorbing matter induces an enhancement of black carbon absorption.
7. Putaud et al. (2010), entitled "*A European aerosol phenomenology – 3: Physical and chemical characteristics of particulate matter from 60 rural, urban, and kerbside sites across Europe*". Synthesizes data on aerosol (particulate matter, PM) physical and chemical characteristics (PM_{10} and/or $PM_{2.5}$ mass, aerosol particle number concentrations, PM chemistry), which were obtained over the past decade in aerosol research and monitoring activities at more than 60 natural background, rural, near-city, urban, and kerbside sites across Europe. Find, among others: 1) organic matter, sulfate and nitrate as main constituents of both PM10 and PM2.5; 2) total carbon/PM10 ratio increases from rural to kerbside sites.

This series of publications demonstrates how time series of high-quality observations of atmospheric aerosol properties can feed into IPCCs Assessment Reports, contributing to improved understanding of ongoing climate change , and predictions. The value chain leads from data management and quality control by network participation, via trend assessment at the network level, to validation and improvement of model produced climate predictions.

These studies provide an in-depth analysis of trends in surface in situ observations of atmospheric aerosol properties, to which the observations covered by this report contribute. They also investigate how well these trends are captured by climate models feeding into IPCC AR6. While such in-depth studies usually coincide with these assessment reports, there now exist services which quantify such trends in observations, as well as the agreement with climate models, on a continuous basis. One such is operated by the Norwegian Meteorological Institute as part of the ACTRIS research infrastructure.[14]

[14] https://actris.nilu.no/Content/trends

3.2 Overview of aerosol observations at Zeppelin, Birkenes and Troll Observatory

This monitoring programme includes measurements of aerosol properties relevant for quantifying the direct and indirect aerosol climate effect from 3 NILU operated/ partly operated observatories : 1) Zeppelin Observatory (in collaboration with the Norwegian Polar Institute and Stockholm University); 2) Birkenes Atmospheric Observatory, Aust-Agder, Southern Norway; 3) Trollhaugen Atmospheric Observatory, Antarctica (observatory operated by NILU, main station operated by Norwegian Polar Institute). The observations cover the particle concentration as a function of particle size as physical aerosol property, as well as particle light scattering and absorption as a function of light wavelength, both optical aerosol properties (Table 5).

Table 5: Aerosol observations at Zeppelin, Birkenes and Troll Observatory. Observations contributing to ACTRIS follow ACTRIS recommendations. Parameters in green are funded by the Norwegian Environment Agency and Ministry of Climate and Environment and the rest is funded by NILU and other institutes. *Parameters included in this report, are printed in green.*

	Zeppelin	Birkenes	Trollhaugen
Particle Number Size Distribution (PNSD) (fundamental to all aerosol processes)	fine and coarse mode (0.01 µm < D_p < 10 µm), coarse mode since autumn 2020, NILU	fine and coarse mode (0.01 µm < D_p < 10 µm)	fine mode (0.01 µm < D_p < 0.8 µm)
Number Size Distribution of Refractory Particles (proxy for BC PNSD)	fine mode (0.01 µm < D_p < 0.8 µm), NILU	---	---
Aerosol Scattering Coefficient (addressing direct climate effect)	spectral at 450, 550, 700 nm, in collaboration with Stockholm University	spectral at 450, 550, 700 nm	spectral at 450, 550, 700 nm
Aerosol Absorption Coefficient (addressing direct climate effect)	single wavelength at 525 nm, (Stockholm University); single wavelength at 670 nm (Stockholm University); 7-wavelength (Demokritos Athens); 7-wavelength (NILU)	spectral at 470, 522, 660 nm wavelength.; 7-wavelength (NILU)	spectral at 470, 522, 660 nm wavelength. 7-wavelength installed 2020
Aerosol Optical Depth (addressing direct climate effect)	spectral at 368, 412, 500, 862 nm in collaboration with WORCC (in Ny-Ålesund)	spectral at 340, 380, 440, 500, 675, 870, 1020, 1640 nm, in collaboration with Univ. Valladolid	spectral at 368, 412, 500, 862 nm
Aerosol Chemical Composition (addressing direct + indirect climate effect)	inorganic ions (ion chromato-graphy), heavy metals (inductively-coupled-plasma mass-spectrometry)	main components (daily resolution, offline filter-based, ion chromatography), heavy metals (inductively-coupled-plasma mass-spectrometry)	inorganic ions and POPs (ion chromato-graphy), discontinued from 2011 due to local contamination.
Aerosol Chemical Speciation (direct + indirect climate effect, source attribution, transport)	Particle main chemical species (hourly resolution, online mass spectrometry)	Particle main chemical species (hourly resolution, online mass spectrometry)	---
Particle Mass Concentration	---	$PM_{2.5}$, PM_{10}	PM_{10}
Cloud Condensation Nuclei (addressing indirect climate effect)	size integrated number concentration at variable supersaturation in collaboration with Korean Polar Research Institute	---	---

3.3 Observed optical properties of aerosols

Aerosol particle absorption and scattering are decisive for the cooling or warming effect of aerosol in climate. All types of particles are scattering solar radiation, but the higher the fraction of particle absorption, the more warming the aerosol becomes. The absorption depends on the particle composition; black carbon (e.g. soot) and some minerals absorb radiation.

3.3.1 Optical aerosol properties measured at the Birkenes Observatory

Key findings aerosol optical properties Birkenes: *There are no statistically significant trends in aerosol optical properties observed at Birkenes, agreeing with findings at other European stations and recent trend analyses (e.g. Collaud Coen et al., 2020). Aerosol scattering shows a stronger presence of smaller particles in summer than in winter. The reason for these seasonal differences lies in summer aerosol being influenced by biogenic emissions which tends to give large amounts of newly formed small particles. In contrast, aerosol absorption shows a higher contribution of smaller (newer) particles in winter than in summer, reflecting the winter contribution of wood burning for domestic heating. In 2020, a major transport event of Central Asian dust combined with Ukrainian forest fire emissions influenced Southern Norway and other regions in Northern Europe.*

A comprehensive suite of instruments observing in situ optical aerosol properties relevant to direct climate effects has been in operation at Birkenes since 2010, hereunder including the scattering coefficient σ_{sp} and the absorption coefficient σ_{ap} at various wavelengths. Figure 44 summarises these observations for 2010 – 2020 in time series of the observations themselves and relevant directly derived parameters. All properties are measured for particles with aerodynamic diameter $D_{p,aero} < 10$ µm and at relative humidity < 40%, thus avoiding water uptake by particles. This protocol follows the recommendations provided by ACTRIS. This is crucial to have comparable data at Zeppelin, Trollhaugen and Birkenes, and with other sites on European and global scale. For more details concerning measurement principles and quality assurance routines, please see Appendix II and Laj et al (2020). The data gap in 2019 is caused by a failure of the integrating nephelometer, measuring the particle scattering coefficient σ_{sp}, which also affected the particle absorption measurements since these depend on the nephelometer for bias corrections.

Panel a) of Figure 44 displays the time series of the scattering coefficient σ_{sp} at 450, 550, and 700 nm wavelength. Thin lines represent daily average values for the respective wavelength, whereas the heavy green line represents the running 8-week median for easier visibility of seasonal averages (green wavelength at 550 nm only for clarity). The σ_{sp} time series exhibits significant variability on the time scale of days, illustrating that particle load in an air mass varies significantly with air mass type and thus air mass origin, i.e. with the synoptic weather situation on a time scale of 1 – 3 days. When focussing on the graph of the running median, a slight seasonal variation can be detected, with values higher in summer than winter.

For optical aerosol properties, information is contained both in the absolute level and in the values at different wavelengths relative to each other. In order to make this spectral information accessible, the Ångström coefficient has been defined, that can be calculated for optical aerosol properties, both for scattering and for absorption. Higher values of the scattering Ångström coefficient correlate with higher concentration ratios of particles in the fine size range ($D_p < 1$ µm) as compared to the coarse size range ($D_p > 1$ µm). Moreover, the relative size of particles determining an optical aerosol property decreases with wavelength, i.e. smaller wavelengths “see” smaller particles in relative terms, larger wavelengths “see” larger particles. Already with these simple qualitative rules, many features exhibited by spectral aerosol optical property data in general and Ångström coefficient data in particular can be interpreted meaningfully.

Panel b) of Figure 44 shows the time series of the scattering Ångström coefficient $å_{sp}$, calculated from $\sigma_{sp}(\lambda)$, again as daily averages (thin line) and running 8-week median (heavy line). As with σ_{sp}, the strongest variability is associated to a time scale of 1-3 days, indicative of changes associated with air mass type, origin, and synoptic weather situation. Looking at the running median however, the seasonal cycle is more pronounced for $å_{sp}$ than for σ_{sp}, with $å_{sp}$ values around 1.1 in winter and 1.8 in summer. This indicates a stronger contribution of smaller particles, i.e. particles with D_p smaller than about 120 nm, to σ_{sp} in summer than in winter. This is consistent with number concentrations of particles in this size range exhibiting a similar seasonal cycle, as will be discussed below. The time series of σ_{sp} and $å_{sp}$ don't show any trend, which is consistent with the findings for other European continental background stations at Jungfraujoch (Switzerland, mountain top), Hohenpeissenberg (Southern Germany, elevated boundary layer), and Pallas (Northern Finland, boreal background) (Collaud Coen et al., 2013, 2020). Also the range of σ_{sp} values encountered, 3 - 50 Mm^{-1} with an annual average of about 12.5 Mm^{-1}, is consistent with findings at comparable stations (Delene & Ogren, 2002).

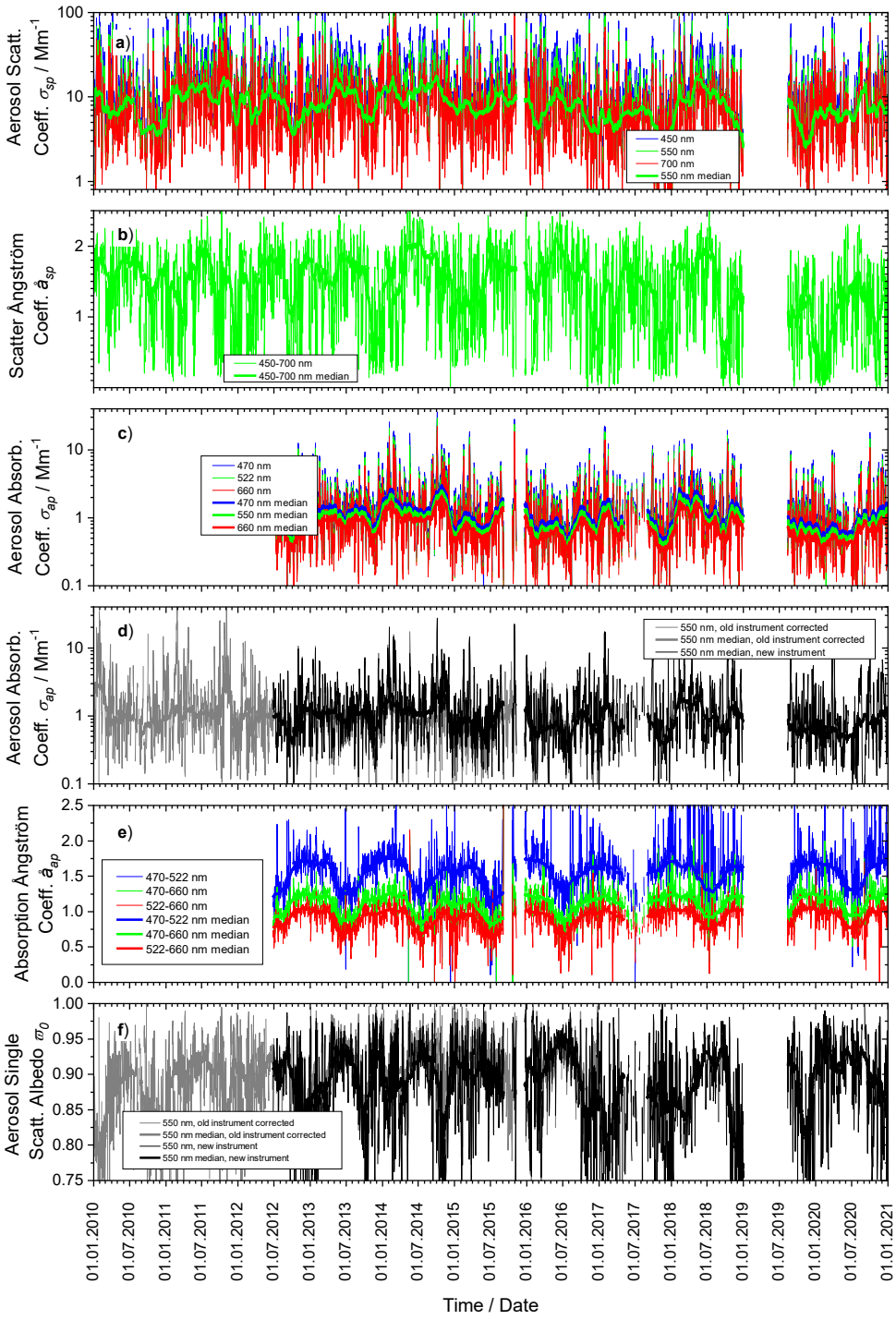

Figure 44: Time series of aerosol particle optical property daily means measured for 2010 - 2020 at Birkenes. Panel a) shows the aerosol scattering coefficient σ_{sp} at 450, 550, and 700 nm wavelength measured by integrating nephelometer. Panel c) the aerosol absorption coefficient σ_{ap} at 470, 522, and 660 nm wavelength measured by the newer filter absorption photometer, Panel d) the aerosol absorption coefficient σ_{ap} at 550 nm of the older filter absorption photometer, shifted from the instrument wavelength at 525 nm for consistent comparison assuming an absorption Ångström coefficient of -1. Panels b) and e) show the derived properties scattering and absorption Ångström coefficient $å_{sp}$ and $å_{ap}$, respectively, while Panel f) depicts the single scattering albedo ϖ_0. All plots also depict the running 8-week medians of the respective properties as heavy lines to visualize seasonal variations. To demonstrate consistency between old and new filter absorption photometer, respective comparison lines are displayed.

The observations of the particle absorption coefficient σ_{ap} at Birkenes were upgraded in 2012 and in November 2017. All 3 concerned instruments use the same physical principle, tracking the change of attenuation of light that passes through a filter while the filter is loaded with sampled particles. The 2012 instrument measures σ_{ap} at 3 wavelengths (470, 522, 660 nm) with considerably less electronic noise and significantly better long-term stability than the previous instrument of 2010 with one wavelength (522 nm). The 2017 instrument extends the spectral range to 7 wavelengths (370, 470, 520, 590, 660, 880, 950 nm). Panel c) of Figure 44 displays the σ_{ap} time series of the 2012, 3-wavelength filter absorption photometer, Panel d) the data of the 2010 one wavelength instrument. For the 2010 instrument, the wavelength has been recalculated to the same green wavelength as observed by the nephelometer (550 nm) assuming an absorption Ångström coefficient of 1. Both panels use thin lines for daily averages, heavy lines for the running 8-week medians. The data of the 2017 instrument have been evaluated for consistency with the 2012 instrument over a whole year (see Appendix II). The data of the 2 instruments show a correlation coefficient R^2 of 0.97, i.e. 97% of the variation in one instrument is explained by the variation in the other instrument. This ensures that the 2017 instrument will continue the σ_{ap} time series consistently. The data of the 2017 instrument are displayed separately in Figure 45 below to prevent excessive information density in Figure 44.

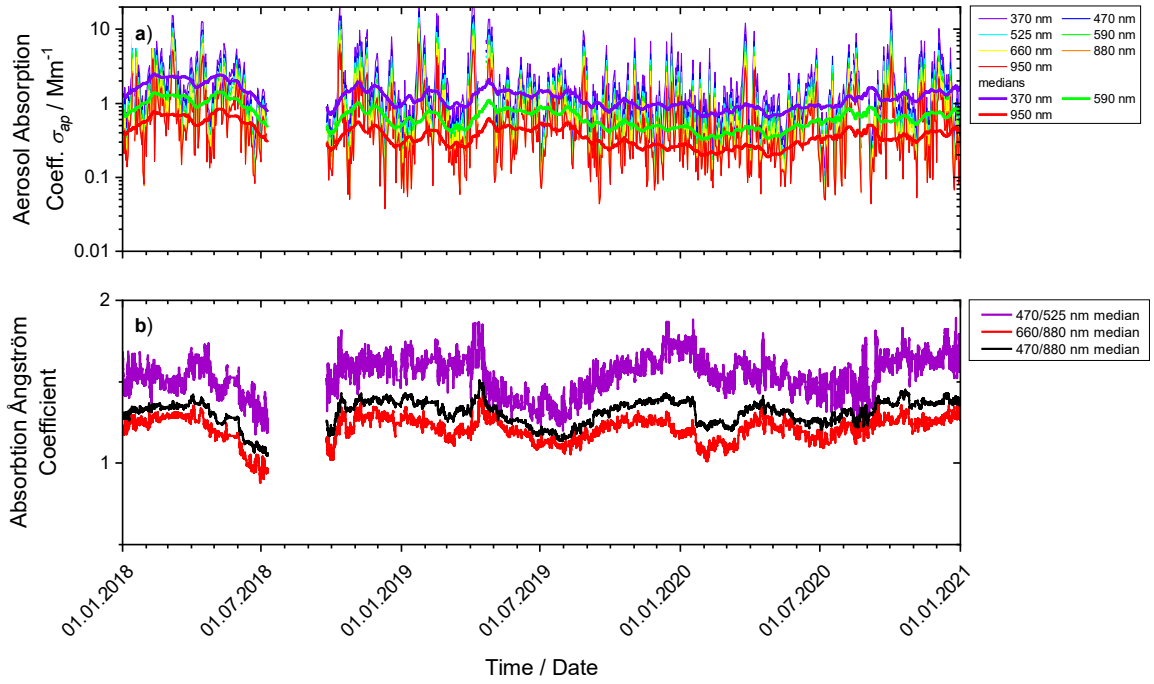

Figure 45: Time series of aerosol particle absorption coefficient σ_{ap} (top) and the absorption Ångström coefficient $å_{ap}$ (bottom), both daily means, measured by the filter absorption photometer deployed at Birkenes in November 2017. The time series covers the years 2018 - 2020.

Turning back to Figure 44, Panel d) also displays the σ_{ap} running median time series of the 2012 filter absorption photometer (also recalculated to 550 nm wavelength) together with the data of the 2010 instrument as an indicator for the goodness of overlap between the 2 instruments measuring the same property (see appendix II page 161 for more details).

Apart from the variation with synoptic transport and air mass origin, σ_{ap} does not seem to exhibit significant seasonal variation. The values of σ_{ap} are in the range of 0.3 – 4 Mm^{-1} with annual means around 1 Mm^{-1}.

In order to cover the largest possible time period, panel f) of Figure 44 shows the time series of the aerosol particle single scattering albedo ϖ_0 based on the time series of the older filter absorption photometer (grey lines), again daily averages (thin line) and 8-week running median (heavy line), together with the respective time series of the new instrument (black lines). The single scattering albedo ϖ_0 quantifies the fraction of light scattered by the particles rather than absorbed. It thus quantifies how absorbing the average aerosol particle is, with ϖ_0 values decreasing with increasing absorption of the average particle. For a purely scattering aerosol, ϖ_0 is 1, and decreases with increasing fraction of light absorbing components in the aerosol particle phase. The most prominent feature in the ϖ_0 time series is the pronounced annual cycle, varying between 0.86 – 0.96, with lower ϖ_0 values and higher particle absorption in winter. The annual cycle in ϖ_0 has been discussed in previous reports of the Birkenes aerosol dataset, and has been connected to the combustion of biomass in wood stoves for domestic heating in the winter season.

Panel e) of Figure 44 is based on data of the 2012 filter absorption photometer, measuring σ_{ap} at 3 wavelengths, as opposed to 1 wavelength with the 2010 instrument. Panel e) depicts the time series of the absorption Ångström coefficient $å_{ap}$ for all 3 wavelength pairs provided by the new instrument. Similar, Figure 45 (bottom) shows $å_{ap}$ for 3 wavelength pairs of the newest instrument. For $å_{ap}$, the information on relative particle size concerns not the overall aerosol particle phase, but the fraction of absorbing particles. Thus, considering $å_{ap}$ data allows to investigate changes in source and transport of the absorbing particle fraction in the aerosol. When looking at the $å_{ap}$ data, an annual cycle is apparent that is opposite of the annual cycles seen in scattering Ångström coefficient $å_{sp}$ and single scattering albedo ϖ_0. Both $å_{sp}$ and ϖ_0 increase in summer as compared to winter, $å_{sp}$ because of a summer increase in small particles due to particle formation from biogenic precursors, ϖ_0 because of fewer combustion emissions in summer than in winter. For $å_{ap}$, values increase in winter as compared to summer, indicating, in relative terms, higher abundance of smaller absorbing particles in winter than in summer. This observation is consistent with assuming emissions from domestic heating by wood stoves to contribute to the Birkenes winter aerosol, which is the explanation for the decreased winter values of ϖ_0. The size of the absorbing aerosol particles increases with aerosol age. Consequently, a smaller size of the absorbing particles indicates a younger combustion aerosol and a closer combustion source, which is consistent with a scattered distribution of houses using wood stoves for heating, i.e. typical for Southern Norway. The previous instrument upgrade of aerosol absorption measurements in Birkenes has thus provided another indication for the contribution of wood stove emissions to the Birkenes winter aerosol.

3.3.2 Optical aerosol properties measured at the Zeppelin Observatory

Key findings aerosol optical properties Zeppelin: *The aerosol absorption measurements at Zeppelin station are conducted in collaboration with the Greek Demokritos-Athens research institute, and continue a time series that has been in started 2001. The decreasing trend in aerosol absorption observed since 2001 by Eleftheriadis et al. (2009) has continued, and fits with the trend observed at other surface in situ stations in the Arctic (Coen et al., 2013; Collaud Coen et al., 2020). The spectral dependence of particle light absorption at Zeppelin indicates a contribution of absorbing components with spectral dependence due to chemical composition, e.g. brown carbon or mineral dust.*

The in situ optical properties of the particles at Zeppelin Observatory covered in this report are more limited as compared to Birkenes and Trollhaugen. NILU operates only one filter absorption

photometer, an AE33 aethalometer, at Zeppelin measuring the absorption coefficient $\sigma_{ap}(\lambda)$ between 370-950 nm wavelength. A nephelometer providing the spectral scattering coefficient $\sigma_{sp}(\lambda)$ is also deployed at Zeppelin, but operated by Stockholm University, and data are therefore not available for this report. This excludes calculation and discussion of the particle single scattering albedo.

Figure 46 summarises the 2015 – 2020 time series, i.e. 5.5 years, of spectral aerosol particle absorption coefficient $\sigma_{ap}(\lambda)$ data collected at Zeppelin Observatory since deployment of the aethalometer in June 2015. The top panel displays daily averaged $\sigma_{ap}(\lambda)$ data for all 7 wavelengths (thin lines), as well as running 8-week medians (bold lines), here only for 3 wavelengths to improve readability of the graph. The bottom panel shows graphs of the absorption Ångström coefficient $\mathring{a}_{ap}$ for 3 wavelength pairs representing short wave end, long wave end, and full range of the measured wavelength spectrum. The $\mathring{a}_{ap}$ data are plotted as 8-week median only, since daily averages are too noisy due to the low particle load commonly observed at Zeppelin.

The time series of σ_{ap} (top panel of Figure 46) exhibits the same annual cycle as described already in the data of the other aethalometer instrument at Zeppelin collected in earlier years (Eleftheriadis et al., 2009), with lower values in summer and higher ones in winter. These variations have been attributed to changes in combustion aerosol sources caused by emissions from domestic heating in the relevant source regions, e.g. Northern and Central Russia (Law & Stohl, 2007). This pattern is moderated by incidents of emissions from large forest fires reaching the Arctic, which can increase aerosol particle absorption in episodes also in summer (e.g. Stohl et al., 2007). Absolute values of σ_{ap} vary in the range of 0.02 – 2 Mm^{-1}at Arctic Zeppelin station, with median values roughly a factor of 5 lower than at boreal Birkenes, but a factor of 4 larger than at Antarctic Trollhaugen station.

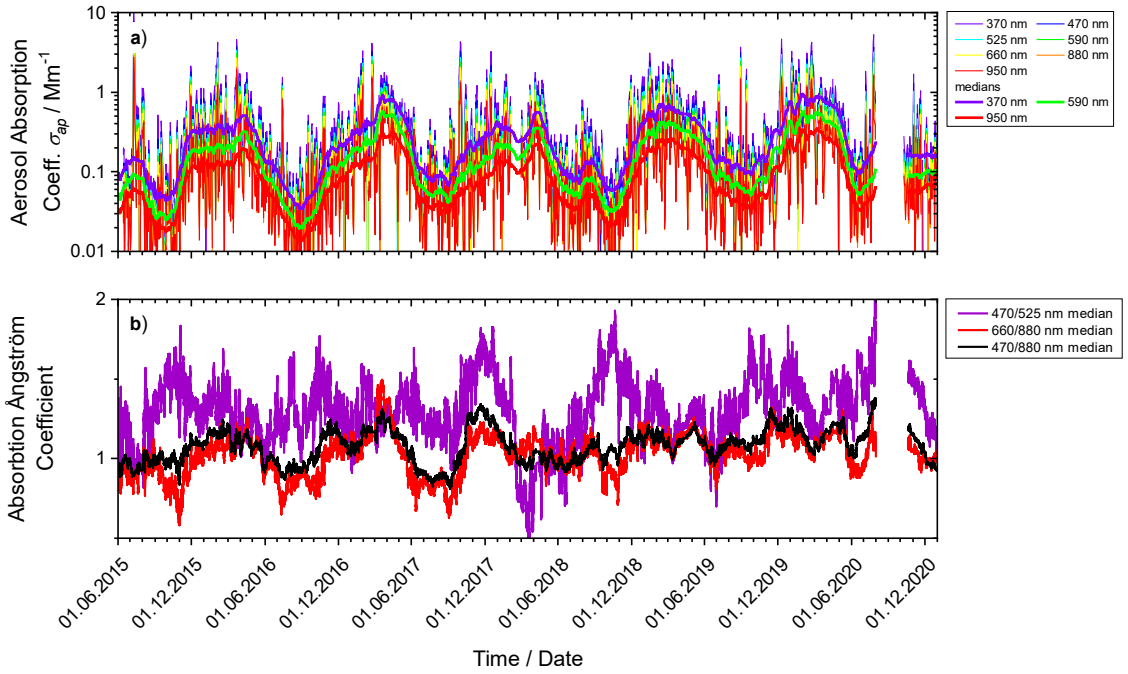

Figure 46: 2015 – 2020 time series graphs of data collected by the filter absorption photometer at Zeppelin Observatory since deployment in June 2015. Top: daily means of absorption coefficient at all 7 measured wavelengths (thin lines), and 8-week running medians for top, middle and bottom of observed spectral range (heavy lines). Bottom: 8-month running medians of absorption Ångström coefficient, top, bottom, and whole observed spectral range.

Also interesting in the data provided by the filter absorption photometer is the aerosol absorption Ångström coefficient $å_{ap}$. The $å_{ap}$ values exhibit a distinct spectral dependence on wavelength, with $å_{ap}$ for shorter wavelengths deviating to higher values as compared to $å_{ap}$ at larger wavelengths for periods of lower aerosol absorption, i.e. in summer. Such a behaviour can be caused by absorbing aerosol components that exhibit a spectral dependence in absorption, e.g. brown carbon or dust. For black carbon in contrast, $å_{ap}$ at shorter and larger wavelength agree at values around 1.

3.3.3 Optical aerosol properties measured at the Trollhaugen Observatory

Key findings aerosol optical properties Trollhaugen: *The length of the time series of data on optical aerosol properties at Trollhaugen is still too short for drawing conclusions on trends. The annual cycle of the aerosol optical properties at Trollhaugen has been studied in detail, and is associated with a natural, hemispheric-scale atmospheric pattern. The same annual cycle with higher particle loads and larger particles in summer is observed also at other stations on the central Antarctic continent.*

This section covers the aerosol optical properties collected at the station after the relocation in January 2014 from the Troll main base to Trollhaugen located above and upwind of the previous location. At the location of the old station, up to 80% of the collected data were contaminated by diffuse (unavoidable) emissions from the main buildings, making the scientific value and interpretation of the data from the old location difficult.

At Trollhaugen station, the same comprehensive set of instruments for observing optical aerosol properties as used in Birkenes is deployed. These cover the spectral scattering coefficient $\sigma_{sp}(\lambda)$, the spectral absorption coefficient $\sigma_{ap}(\lambda)$, as well as the derived properties scattering and absorption Ångström coefficient $\mathring{a}_{sp}$ and $\mathring{a}_{ap}$, parameterising the wavelength dependence of σ_{sp} and σ_{ap}, as well as the single scattering albedo ϖ_0. Figure 47 summarises the corresponding data collected at Trollhaugen for the years 2014 – 2020.

Starting with the time series of $\sigma_{sp}(\lambda)$ in panel a) of Figure 47, a slight annual cycle can be observed, with superimposed peaks throughout the year. The peaks are associated with intrusions of marine air during storm episodes, while the annual cycle is caused by an annual cycle of the particle number size distribution (PNSD) in Antarctic background air, with higher particle loads and larger particles in summer. The same annual cycle in the PNSD also explains the annual cycle in the scattering Ångström coefficient $\mathring{a}_{sp}$ plotted in panel b). The scattering Ångström coefficient increases as the PNSD receives a relative peak at smaller particle sizes, which is the case in Antarctic background summer air.

An annual cycle can also be detected in the $\sigma_{ap}(\lambda)$ time series depicted in panel c) of Figure 47, even though the filter absorption photometer operates constantly around the detection limit. The minimum in the cycle occurs in Southern hemisphere winter when the Antarctic vortex decreases transport from lower latitudes through the lower and mid-troposphere. In the absorption Ångström coefficient $\mathring{a}_{ap}$ time series shown in panel d), the annual cycle is rather weakly pronounced, with the lowest values also occurring in winter.

The time series of the single scattering albedo ϖ_0 (panel e) of Figure 47) shows the highest values close to 1, i.e. almost no particle absorption at all, in Antarctic winter, coincident and consistent with the minimum in particle absorption. Lower ϖ_0 values, i.e. higher average particle absorption, occur towards summer when the Antarctic continent is subject to stronger transport from mid-latitude sources through the lower part of the troposphere.

Optical aerosol properties are tightly connected to the physical aerosol properties, which is why they are ideally interpreted together. The annual cycle in the optical aerosol properties observed at Trollhaugen is caused by a corresponding annual cycle in the physical properties, which will be discussed in section 3.4.3.

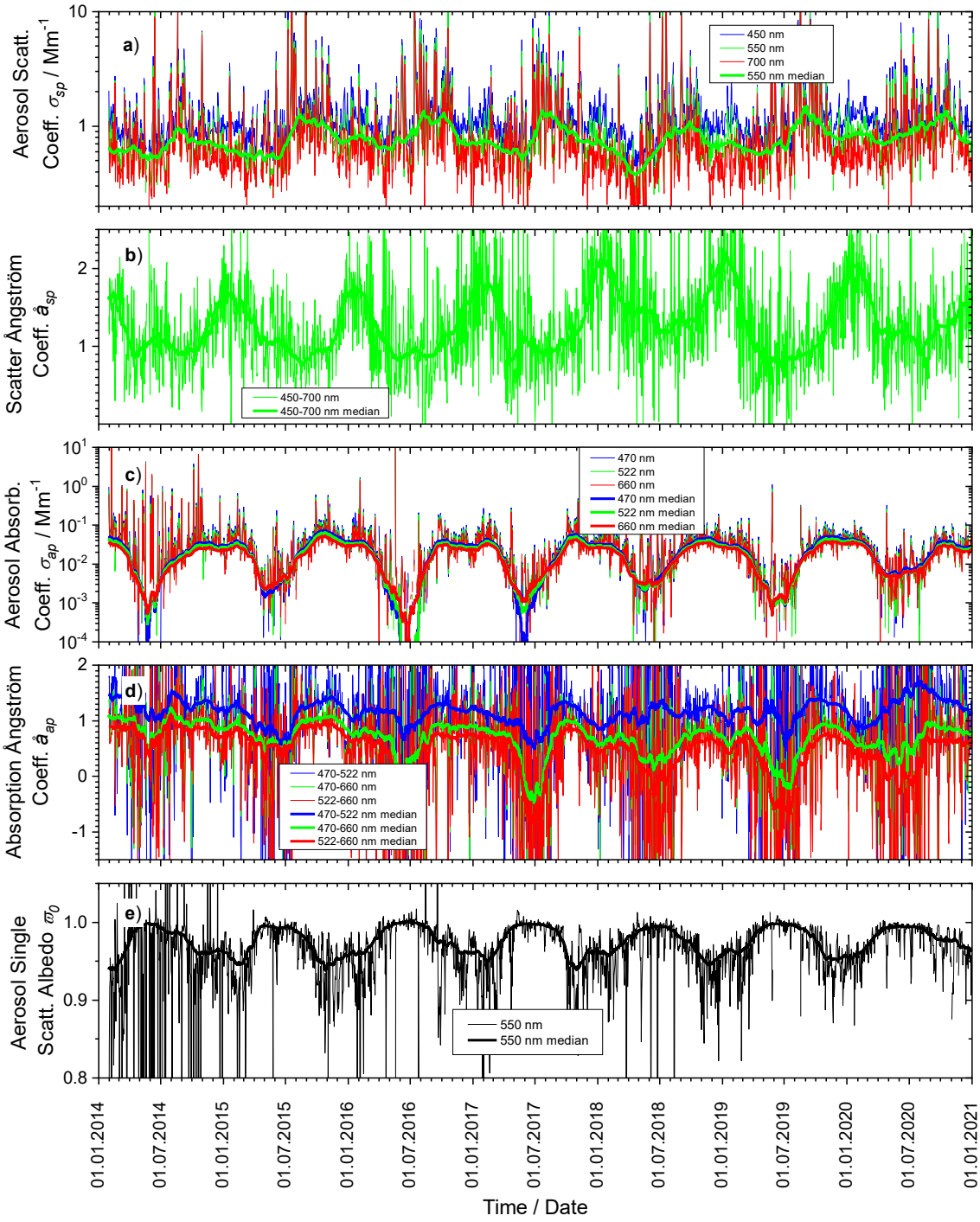

Figure 47: Time series of aerosol particle optical property daily means measured for 2014 - 2020 at Trollhaugen station. Panel a) shows the aerosol scattering coefficient σ_{sp} at 450, 550, and 700 nm wavelength measured by integrating nephelometer. Panel c) the aerosol absorption coefficient σ_{ap} at 470, 522, and 660 nm wavelength measured by filter absorption photometer. Panels b) and d) show the derived properties scattering and absorption Ångström coefficient $\mathring{a}_{sp}$ and $\mathring{a}_{ap}$, respectively, while Panel e) depicts the single scattering albedo ϖ_0. All plots also depict the running 8-week medians of the respective properties as heavy lines to visualize seasonal variations.

3.4 Measurements of particle number and size

3.4.1 Physical aerosol properties measured at the Birkenes Observatory

Key findings aerosol physical properties Birkenes: *Size segregated aerosol particle concentrations at Birkenes do not exhibit any obvious trend. This corresponds to findings obtained at other Nordic stations within ACTRIS and EMEP. The particle size distribution at Birkenes is governed by 5 major sources: 1) clean Arctic background aerosol; 2) Central and Eastern European aerosol; 3) Arctic haze; 4) fine fraction biogenic aerosol; 5) wood combustion aerosol from domestic heating. A major transport episode observed in early October 2020 can be traced to sources of dust in central Asia, combined with forest fire emissions from Ukraine. Other observed episodes concern Central European winter pollution, and boreal forest summer emissions.*

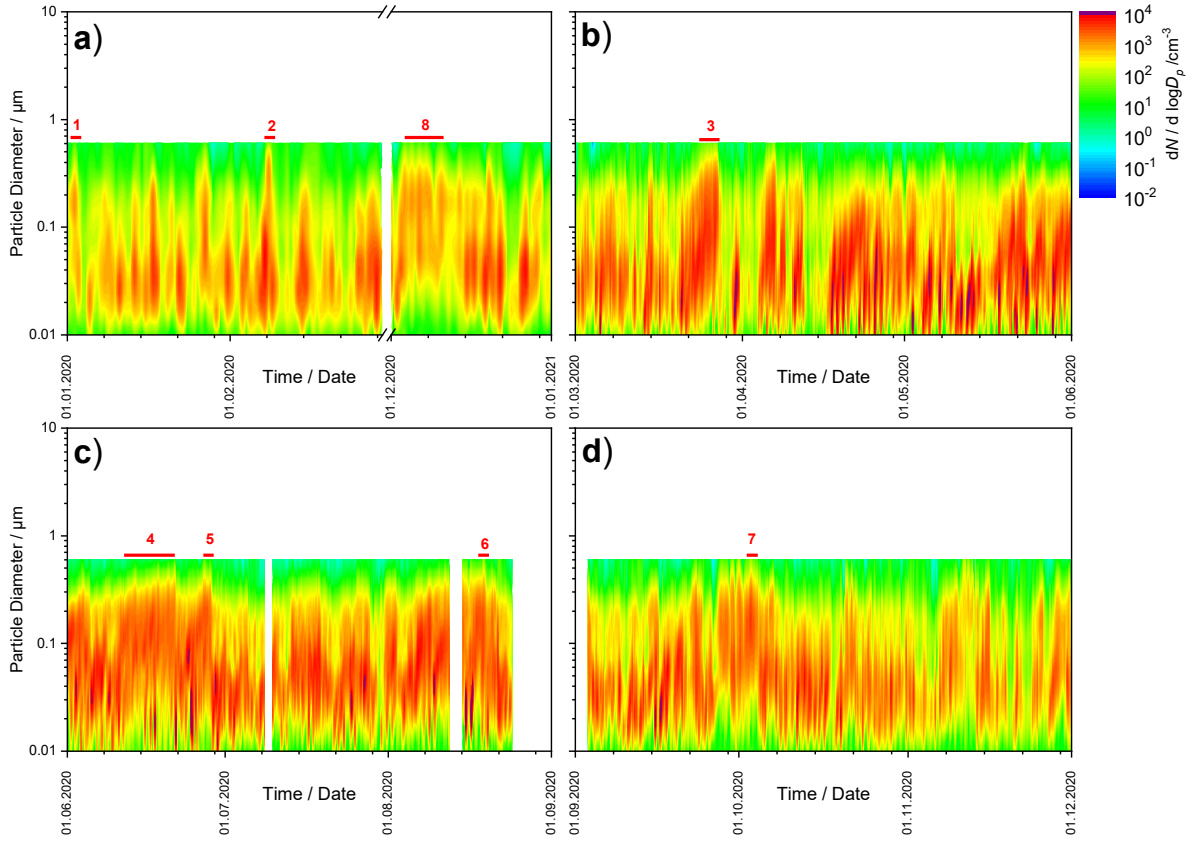

Figure 48: 2020 time series of particle number size distribution at Birkenes, panel a) winter, panel b) spring, panel c) summer, panel d) autumn. Episodes are marked by numbered red bars, with episode numbers referring to Table 6.

Figure 48 shows the time series of the particle number size distribution (PNSD) measured at Birkenes in 2020, separated into 4 different panels by season. In this plot type, the x-axis shows the time of the observation, whereas the y-axis shows the particle diameter D_p on a logarithmic scale. The logarithmic colour scale is the particle concentration, normalised to the logarithmic size interval, dN / dlog D_p. The use of logarithmic axis is common when displaying particle size information since both, particle diameter and particle concentration, tend to span several orders of magnitude while containing relevant information over the whole scale. In this report, the PNSD reported for Birkenes is intended to cover the whole size range between 0.01 – 10 µm by combining the information of 2 instruments, one each focussing on the fine (D_p < 1 µm) and coarse (D_p > 1 µm) size ranges, into a common PNSD product (see Appendix II for details). For the common PNSD product, both instruments need to agree in their overlap size range. At observation times when this criterion isn't met, the resulting PNSD is

rejected, which can lead to gaps in the PNSD time series. This normally occurs predominantly in winter when the aerosol particles are absorbing, which affects the instrument covering the coarse size rage, an Optical Particle Size Spectrometer (OPSS). Existing operating procedures and quality standards defined by the European research infrastructure ACTRIS have been used (Wiedensohler et al., 2012), but cover only the fine particle size range.

The OPSS follows a schedule of manufacturer calibrations, which is traceable only to a master unit, but not to an independent SI standard. This limits options for in-the-field QA and calibration measures using portable SI standards. In 2019, the OPSS experienced calibration issues, which were addressed by a major manufacturer overhaul. After repair, the instrument did not operate normally, which first in 2021 could be traced to a faulty firmware installed during the 2019 overhaul. Today, the instrument is back in normal operation, but a replacement is still pursued. These incidents highlight the need for manufacturer independent, SI traceable calibration options and operation procedures. In this context, the role of station networks such as ACTRIS and WMO GAW cannot be overstated.

Table 6: Selected transport events observed at Birkenes in 2020, together with characteristics and air mass origin determined by trajectory analysis.

#	Time Begin	Time End	Comment	Air mass origin (backwards order)	Air mass type
1	01.01.2020 12:00	03.01.2020 08:00	single mode around 0.15 µm, Arctic haze?	Britain, Greenland East coast, Arctic ocean	Arctic haze
2	08.02.2020 03:00	08.02.2020 13:00	mode around 0.25 µm	Germany, Scotland, North Atlantic	continental winter pollution
3	24.03.2020 12:00	27.03.2020 08:00	large scale episode, significant acc. mode, peak in absorption	Benelux, Germany, Poland, Baltic states / Belarus	continental winter pollution
4	11.06.2020 06:00	21.06.2020 08:00	longer episode with significant accumulation mode	Southern Sweden, Southern Finland, Karelia, Kola peninsula	Boreal forest emissions
5	26.06.2020 14:00	28.06.2020 08:00	longer episode with significant coarse mode	Southern Sweden, Southern Finland, Karelia, Kola peninsula	Boreal forest emissions
6	17.08.2020 13:00	18.08.2020 13:00	narrow acc. mode only, at 0.18 µm	Poland, Baltic states	continental air
7	02.10.2020 22:00	03.10.2020 09:00	narrow acc. mode only, at 0.18 µm	Ukraine, Central Asia	central Asian dust, forest fires Ukraine
8	04.12.2020 09:00	12.12.2020 18:00	pronounced accumulation mode, SSA = 0.82	Benelux , Germany	central European pollution

There doesn't exist any unique connection between the PNSD and air mass type, but the PNSD still is rather characteristic for the air mass, and can serve, together with the single scattering albedo ϖ_0, and the scattering Ångström coefficient $å_{sp}$, as valuable indication of air mass origin, which at Birkenes shifts with the synoptic weather situation. Consequently, the information content of a PNSD time series plot is too high to be discussed in detail in this overview-type annual report. The PNSD and ϖ_0

observations reconfirm findings from earlier years on the dominant air mass types at Birkenes, which consist of: 1) clean Arctic background aerosol; 2) Central and Eastern European aerosol; 3) biogenic aerosol, i.e. vegetation emitted precursor gases condensing to the particle phase by photooxidation; 4) wood combustion aerosol from domestic heating. Selected transport events observed at Birkenes are listed in Table 6 together with characteristics and air mass origin determined by trajectory analysis.

Of particular interest in 2020 is a transport episode occurring in late September and early October, which is most visible in the data discussed here between 2nd – 3rd October 2020 (episode 7 in Table 6). An in depth analysis including backwards plume calculations conducted by Groot Zwaaftink et al. (2021) revealed that this episode was caused by a combination of Central Asian dust and emissions from biomass burning in Ukraine, which influenced not only Southern Norway, but also Southern Sweden, Poland and the Baltic states. Below, we will see that this episode was also observed at Svalbard. This episode is significant as it character differs from most other transport episodes of biomass burning emissions. Usually, biomass burning plumes have an effective emission height in the free troposphere or higher, are transported at the same altitude, and don't descend to the surface before reaching polar latitudes (Keywood et al., 2013). In the present case, the plume was transported close to the surface, influencing air quality over a large area. In a changing climate, heatwaves are projected to increase in frequency and intensity (IPCC 2021b, SPM), where heatwaves are associated with strong poleward transport. It needs to be observed further whether these heatwaves are associated with the observed type of long-range, surface-level transport of dust and biomass burning pollution that influences air quality over large areas.

In order to condense the information in the PNSD time series, Figure 49 shows the time series of selected PNSD integrals, i.e. the concentration of particles falling into selected size intervals. The size intervals are chosen to represent characteristic processes governing the atmospheric aerosol (see Appendix II for more details): 1) the Aitken-mode size range, 0.02 – 0.1 µm; 2) the accumulation mode size range, 0.1 – 1 µm; 3) the coarse mode size range, 1 – 10 µm. The time series in Figure 49 represent daily averages over these PNSD integrals for the whole period since the Birkenes station upgrade in 2010, as well as the corresponding running 8-week medians to highlight seasonal variations. The respective size range integral particle concentrations are denoted N_{ait} for the Aitken mode, N_{acc} for the accumulation mode, and N_{coa} for the coarse mode.

As to be expected, the particle concentration in the Birkenes aerosol in absolute terms is dominated by the Aitken mode particles, followed by the accumulation mode. Also the most prominent feature in Figure 49 is exhibited by the particle concentrations in these 2 modes, a clear annual cycle caused by the same underlying physical process. In summer, the vegetation emits gaseous aerosol precursors, which are photo-oxidised and condense onto Aitken-mode particles or form those directly. These particles coagulate, increasing the concentration of accumulation mode particles. These same processes increasing N_{ait} and N_{acc} in summer are also responsible for increasing the scattering Ångström coefficient $\mathring{a}_{sp}$ in summer. The processes controlling N_{coa} are decoupled from those controlling N_{ait} and N_{acc}. Coarse mode particles are formed from bulk material, their concentration is affected by wind speed (levitating dust, spores, pollen), snow cover, and rain (both inhibiting dust levitation).

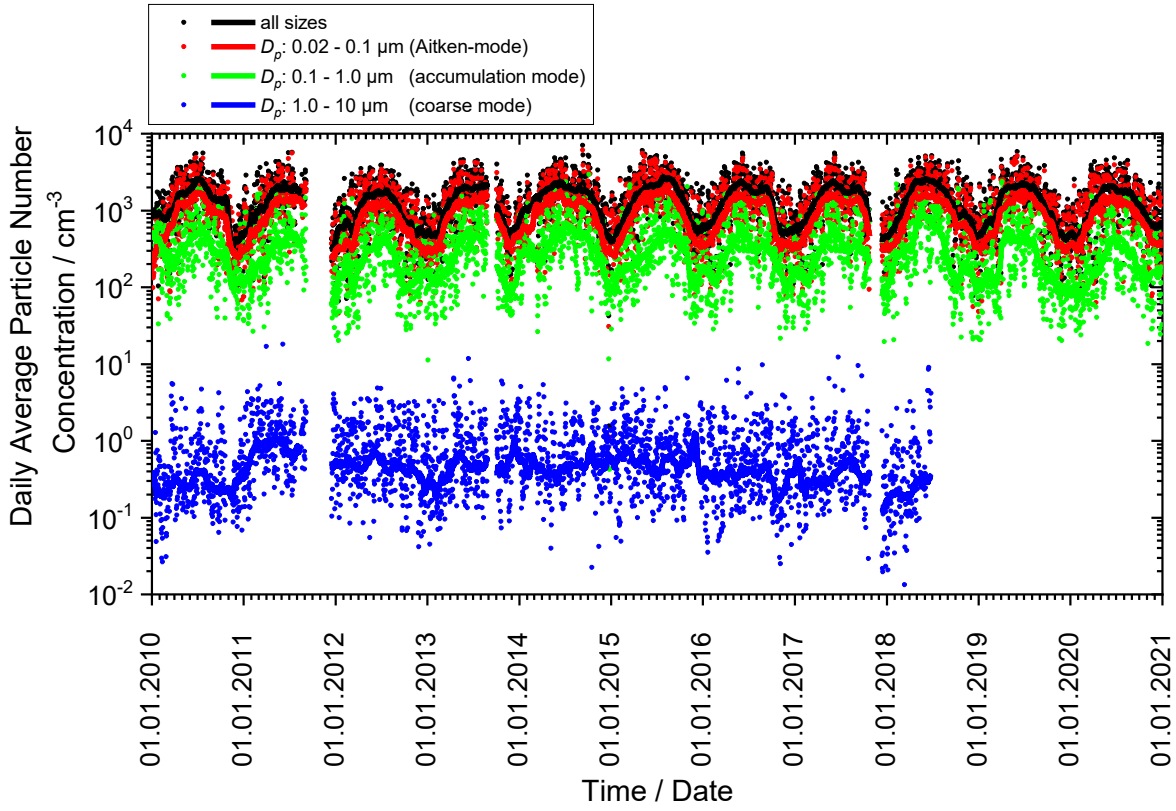

Figure 49: Birkenes 2010-2020 time series of particle number concentration integrated over selected size ranges representing the different physical processes governing the atmospheric aerosol. The dotted graphs represent daily averages of the respective size range, the lines the 8-week running median. The period where the OPSS, measuring the concentration of coarse size range particles, experienced calibration issues, is marked by a red box.

3.4.2 Physical aerosol properties measured in situ at the Zeppelin Observatory

Key findings aerosol physical properties Zeppelin: *Zeppelin particle size distribution data exhibit the well-known Arctic haze pattern. Trends in this pattern cannot be studied yet due to too short the time series. Observations of the particle size distribution in the refractory particle fraction can serve as indicator of aerosol processing time. An episode occurring at Zeppelin in early October 2020 can be traced back to Central Asian dust and forest fires in Ukraine, the same plume observed at Birkenes a few days before Zeppelin.*

A Differential Mobility Particle Sizer (DMPS) instrument, measuring the particle number size distribution, was installed at Zeppelin in 2016 primarily to calibrate the ACSM instrument, but included continuous monitoring as an additional benefit. The same instrument type, operated in a different mode, is used to *measure* the particle number size distribution (PNSD) in the particle diameter range 0.01 µm – 0.8 µm at Birkenes and Trollhaugen stations. It was therefore decided to deploy the Zeppelin DMPS in the same way when not needed for calibrating the ACSM instrument.

As an additional feature, the Zeppelin DMPS has been upgraded late 2017 to also provide the PNSD of refractory (non-volatile) particles. The refractory particle fraction is often used as a proxy for the absorbing aerosol particle fraction, which will allow to study changes in particle absorption on a

microphysical basis in the Arctic environment routinely. The corresponding data [are available in real-real-time](#) with only 1 hour delay.

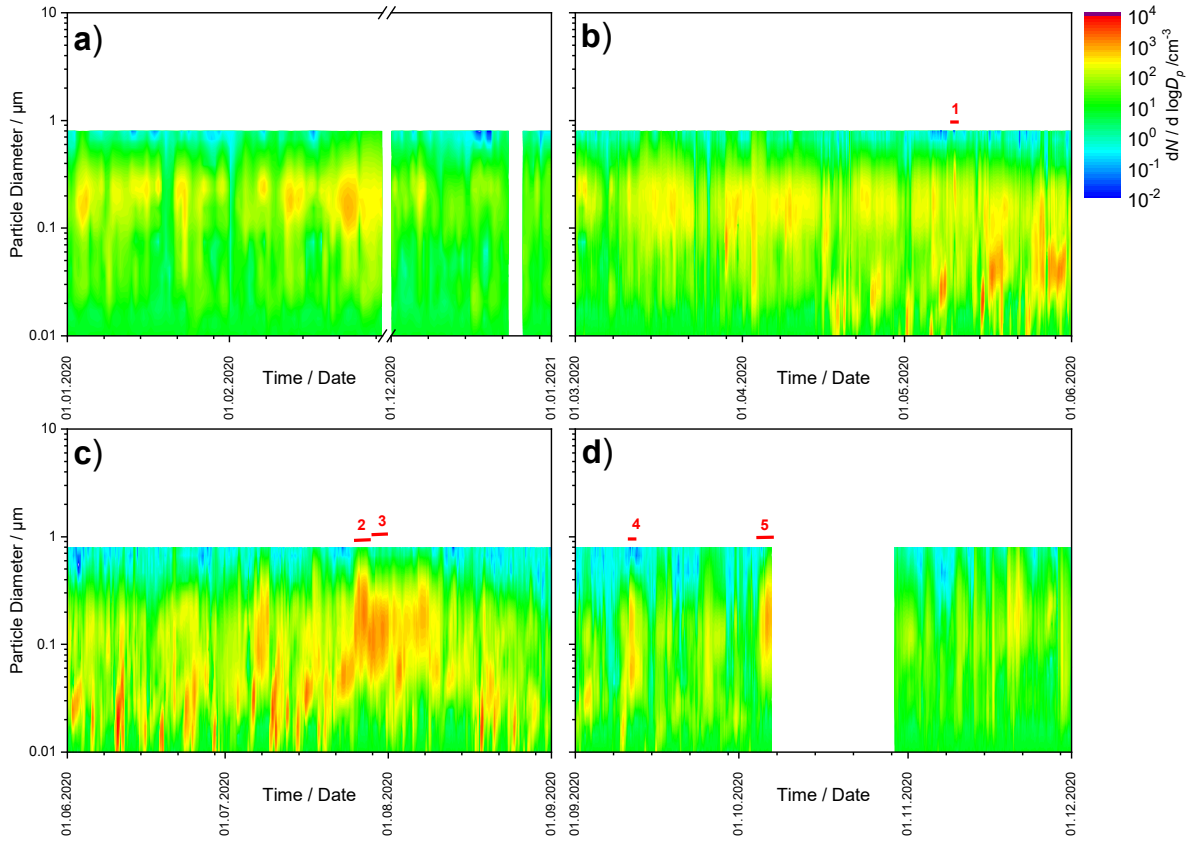

Figure 50: 2020 time series of particle number size distribution at Zeppelin, panel a) winter, panel b) spring, panel c) summer, panel d) autumn. Episodes are marked by numbered red bars, with episode numbers referring to Table 7.

At Zeppelin, the DMPS has recently been combined with an instrument covering the coarse particle size range larger 1 µm. The Aerodynamic Particle Sizer (APS) measures the PNSD up to 10 µm particle diameter using acceleration of particles in an air stream. The data of the APS will be included in next year's report when the time series has grown sufficiently. Figure 50 presents the Zeppelin PNSD data available for this report for 2020 in the same way as for Birkenes and Trollhaugen, with one PNSD time series panel per season.

In contrast to mid-latitudes, air masses don't shift quite as rapidly at polar latitudes due to a smaller influence of frontal systems, making weather patterns more persistent at least in parts of the year. This allows to interpret the information on air mass types contained in PNSD data in more detail. Focussing in on Panel a) of Figure 50 displaying the PNSD data of winter 2018, periods with a uni-modal size distribution are visible. This means the PNSD is dominated by a single mode, in this case the accumulation mode with a peak around 0.25 µm particle diameter. Such a PNSD is typical of early-phase Arctic haze (Heintzenberg, 1980), which is also detectable in late autumn (Panel d) and early spring (Panel b) of Figure 50. Arctic haze is formed by auto-processing of aerosol particles trapped under the winter Arctic vortex while the particle mass increases from industrial emissions under the vortex (e.g. Law & Stohl, 2007).

Table 7: Selected transport events observed at Zeppelin in 2020, together with characteristics and air mass origin determined by trajectory analysis.

#	Time Begin	Time End	Comment	Air mass origin (backwards order)	Air mass type
1	09.05.2020 06:00	09.05.2020 12:00	single accumulation mode, 0.22 µm, stronger than normal Arcyic haze, still Arctic haze?	Arctic ocean, Yamal peninsula, Northern Siberia	Arctic, industrially influenced
2	24.07.2020 17:00	26.07.2020 14:00	single accumulation mode, 0.19 µm	Kola / Kanin peninsula	Arctic, industrially influenced
3	27.07.2020 18:30	30.07.2020 17:30	single accumulation mode, 0.13 µm	Kola peninsula	Arctic, industrially influenced
4	10.09.2020 00:00	10.09.2020 14:30	bi-modal episode, 0.063 and 0.15 µm	Kola peninsula	Arctic, industrially influenced
5	05.10.2020 00:00	06.10.2020 00:00	single accumulation mode, 0.15 µm	Northern Sweden, Finland, Baltic States, Belarus, Ukraine, Central Asia	central Asian dust, forest fires Ukraine

The late spring and summer PNSD at Zeppelin (Figure 50 panels c) and d) is somewhat more variable than in winter due to less stable atmospheric conditions. Particle formation events can be observed, with peak in the PNSD at particle diameters between 0.01 –0.02 µm. These are triggered by photo-chemical production of chemical species that condense into the particle phase, and don't find enough existing particle surface to condense on, thus forming new particles.

There are several transport events visible in the 2020 PNSD data, where a selection has been marked and numbered in Figure 50. The same events are listed in Table 7 summarising the time, the characteristics, air mass origin determined by trajectories, and air mass type. The transport events are characterised by dominant modes in the accumulation mode size range, occasionally accompanied by a detached Aitken-mode. Most of the investigated events originate from industrial emissions in the Russian Arctic (Kola / Yamal / Kanin peninsula). The exception is the transport event in early October 2020, the same as observed at Birkenes a few days earlier, originating from central Asian dust and forest fires in Ukraine. The origin, forest fires in Ukraine, is partly similar to events observed at Zeppelin in 2019 in July – September. Also in 2019, parts of the plume were observed at Birkenes as well. It needs to be monitored whether climate change will affect transport patterns, frequency and magnitude of such long-range transport events from lower to high latitudes, including possible effects for surface air quality under transport. Such a connection is thinkable since the amplitude of mid-latitude circulation patterns ("Rossby-waves") is projected to increase in a warming climate due to a decreasing temperature difference between polar and subtropical latitudes. This in turn leads to increased meridional transport. This type of transport has been investigated on a cases basis (e.g. Groot Zwaaftink et al., 2021) or for certain pollutants (Hansen et al., 2015), but a dedicated study focussing on Norway seems to be lacking.

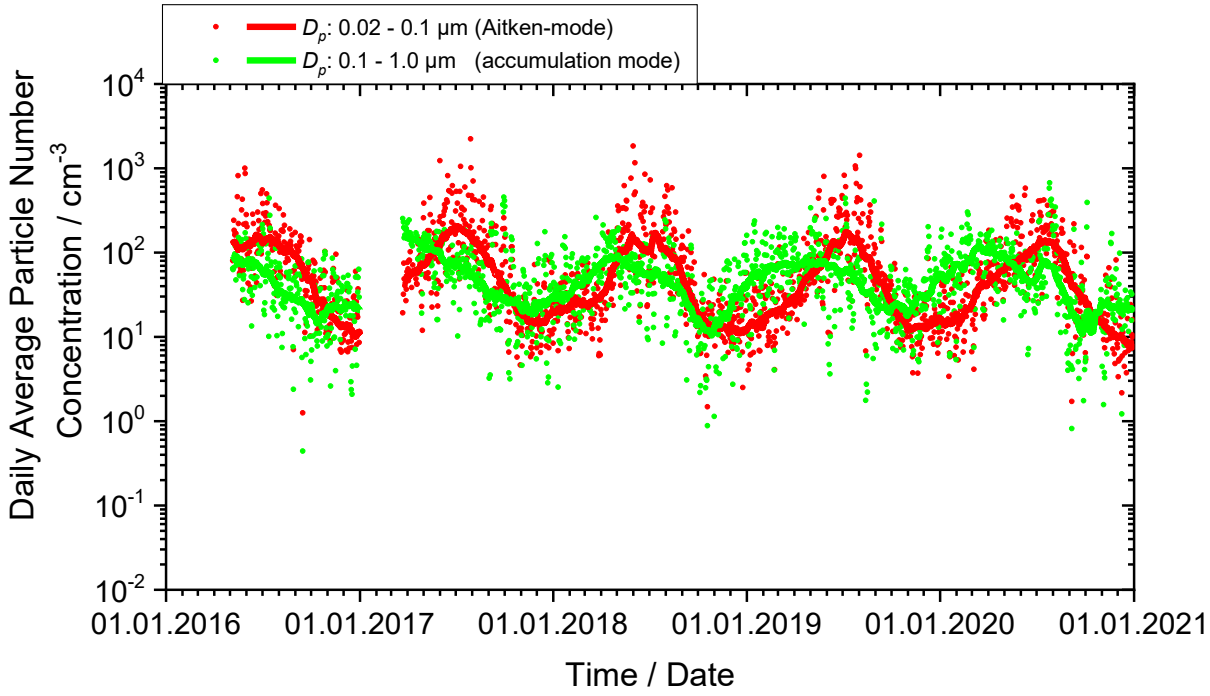

Figure 51: Zeppelin 2016-2020 time series of particle number concentration integrated over selected size ranges representing the different physical processes governing the atmospheric aerosol. The dotted graphs represent daily averages of the respective size range, the lines the 8-week running median.

Figure 51 summarises the 2016-2020 Zeppelin PNSD data by displaying time series of the PNSD size integrals for the Aitken mode N_{ait} (0.02 µm< D_p < 0.1 µm) and N_{acc} (0.1 µm< D_p < 0.8 µm). Apart from particle concentrations an order of magnitude lower than at boreal Birkenes, the most prominent feature of the graph is the point in early November where the N_{acc} running median becomes consistently larger than N_{ait} running median. This behaviour is typical for auto-processed aerosols, and occurs normally only for shorter events. At Zeppelin, this point marks the onset of the Arctic haze period. The Zeppelin DMPS experienced an outage in 2017 caused by a diaphragm failure in the sheath air pump. Though unfortunate, such failures can occur despite preventive maintenance.

Figure 52 displays the annual time series of the PNSD measured at Zeppelin in the non-volatile (refractory) particle fraction in 2019, again with one panel per season. The refractory particle fraction is measured by heating the aerosol sample to 250°C prior to measuring the PNSD. It can be considered as proxy for the BC particle fraction, but contains also mineral dust and condensed species which become non-volatile by charring or oligomerisation while the sample is heated.

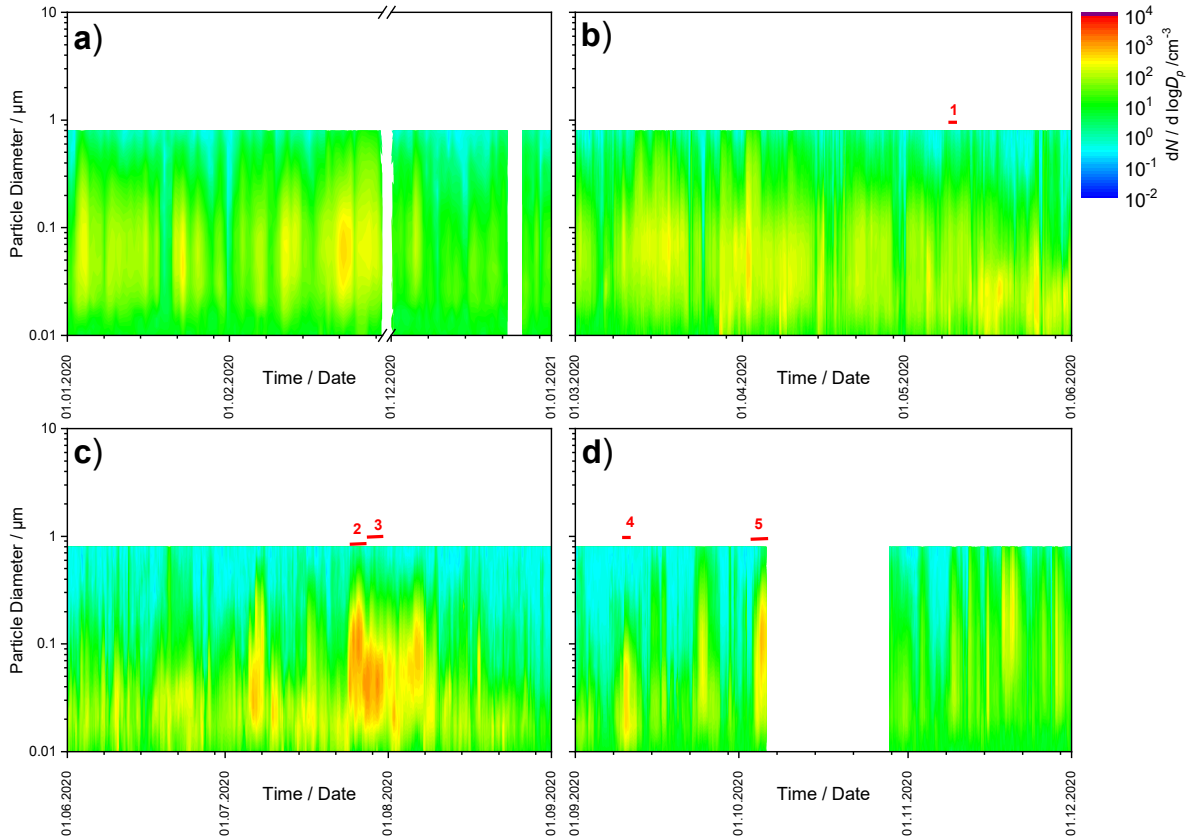

Figure 52: 2020 time series of particle number size distribution of the non-volatile particle fraction at Zeppelin, panel a) winter, panel b) spring, panel c) summer, panel d) autumn. Episodes are marked by numbered red bars, with episode numbers referring to Table 7.

As most obvious distinction between the PNSD of the ambient aerosol (Figure 50) and the PNSD of the non-volatile aerosol fraction (Figure 52), the particle number concentration levels are around half-a-magnitude lower in the non-volatile as compared to the ambient aerosol. The PNSD is almost exclusively mono-modal, with the single mode peaking in the Aitken-size range between 0.25-0.5 µm particle diameter. The peak diameter increases with the auto-processing and lifetime of the aerosol. The refractory particle component increases in size due to coagulation, and not modulated by volatile particle components. The refractory particle fraction can even reveal aerosol age which would not be visible otherwise, as exemplified by episode 5 around in early October 2020, but also for the industrial emissions in episode 2. The fire episode, 5, is marked by a pronounced mode in the refractory particle PNSD. The peaks correspond to the episodes visible in the ambient aerosol PNSD (Figure 50).

Similar as before, Figure 53 summarises the 2020 Zeppelin PNSD data for the refractory particle fraction by displaying time series of the PNSD size integrals for the Aitken mode N_{ait} (0.02 µm< D_p < 0.1 µm) and accumulation mode N_{acc} (0.1 µm< D_p < 0.8 µm). As mentioned before, the overall level of N_{ait} and N_{acc} for the refractory particle fraction is roughly half an order of magnitude lower than for the respective counterparts in the ambient aerosol. An annual cycle might be visible, now confirmed by 3 years of data.

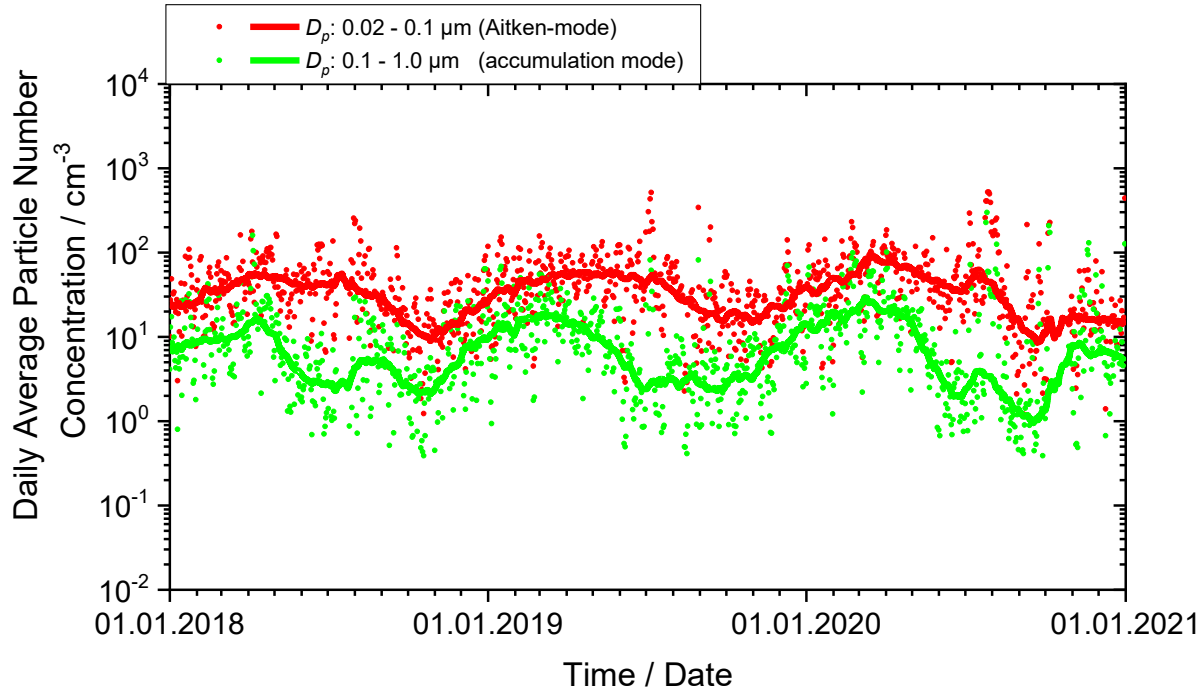

Figure 53: Zeppelin 2020 time series of number concentration in the refractory particle fraction integrated over selected size ranges representing the different physical processes governing the atmospheric aerosol. The dotted graphs represent daily averages of the respective size range, the lines the 8-week running median.

3.4.3 Physical aerosol properties measured in situ at the Trollhaugen Observatory

Key findings aerosol physical properties Trollhaugen: *The length of the time series of reliable data on the aerosol particle number size distribution at Trollhaugen is too short for drawing conclusions on trends. The annual cycle of the PNSD at Trollhaugen has been studied in detail, and is associated to a natural, hemispheric-scale atmospheric pattern. Antarctic background air descends over the Central continent from the upper troposphere / lower stratosphere. At that altitude, it has been transported to the pole after being uplifted (and cleaned by wet removal) at mid- or tropical latitudes. Episodes of mono-modal aerosol intrusions during winter can be connected to emissions form research stations 360 km east of Trollhaugen.*

In contrast to mid-latitudes, polar latitudes exhibit more stable atmospheric conditions with less influence of frontal systems. This is especially true for the Antarctic continent due to colder inland temperatures and the absence of land masses in the mid- to high-latitude Southern hemisphere that could disturb the atmospheric air flow, as compared to the Northern hemisphere. This makes air masses well-defined in these regions, and their associated aerosol properties easier to interpret than under shifting Northern mid-latitude conditions.

This section only covers data collected at the station after the relocation in January 2014 from the Troll main base to Trollhaugen located above and upwind of the previous location. At the old station location, up to 80% of the collected data were locally contaminated by diffuse (unavoidable) emissions

from the main station buildings, making a statistically meaningful interpretation of the data from the old location difficult.

The DMPS system measuring the PNSD at Trollhaugen station has been re-built on–site during the station maintenance visit of January / February 2016, causing a gap in the PNSD time series in January 2016. After the re-built, the system conforms to the quality standards of the ACTRIS research infrastructure, and the observed size range has been extended from 0.03 – 0.8 µm to 0.01 – 0.8 µm, making it now suitable to study formation of new particles. As a consequence, absolute particle concentrations measured by the system before and after remodelling are not directly comparable. This disadvantage has been accepted in favour of a wider range of applications for the DMPS system.
Figure 54 plots the 2020 Trollhaugen PNSD data in the same way as for Birkenes. Due to the rather well-defined atmospheric conditions over the Antarctic continent, 2020 is again rather representative also for previous years. Please observe that the times for the panels are the same as for the Northern hemisphere stations, but that seasons in the Southern hemisphere are shifted by 6 months.

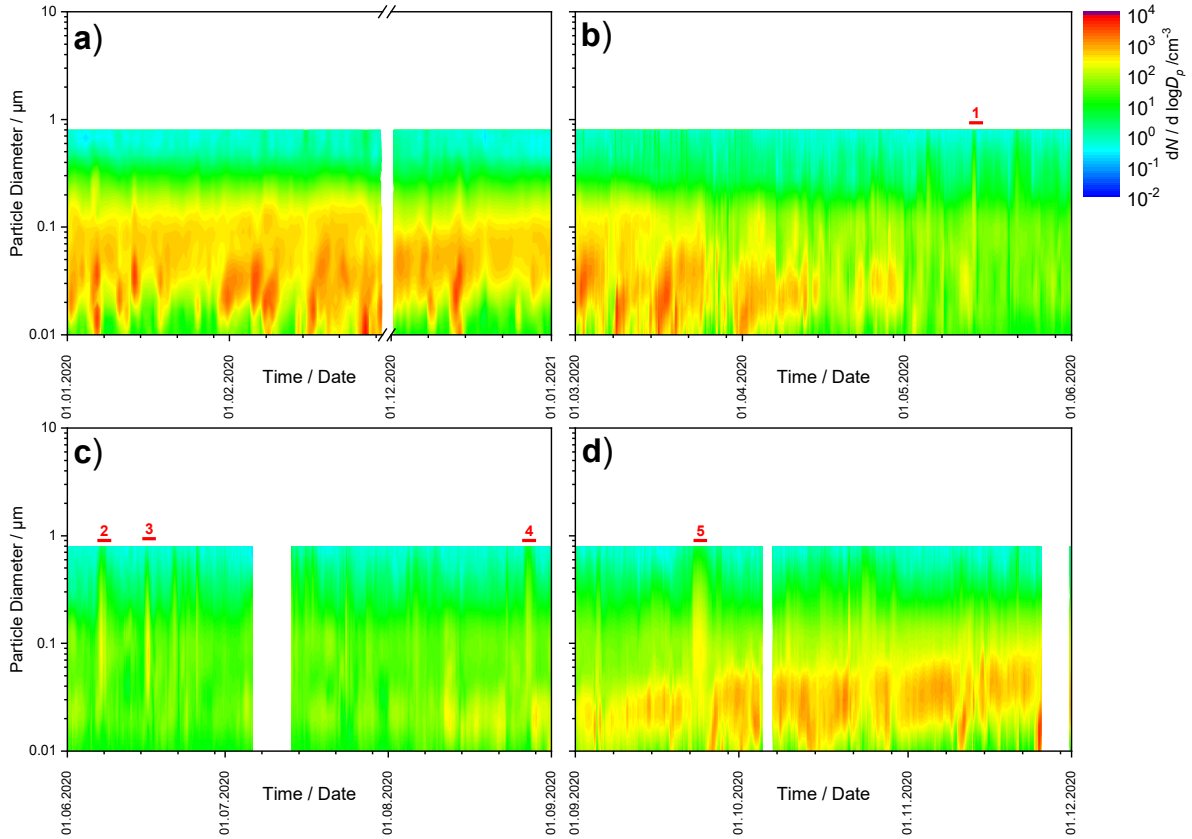

Figure 54: 2020 time series of particle number size distribution at Trollhaugen, panel a) Southern Hemisphere summer, panel b) autumn, panel c) winter, panel d) spring.

Even though the Antarctic continent is among the most pristine regions on the globe, new particle formation events triggered by photo-chemical oxidation of precursor substances can be observed in Antarctic summer. Formation of new particles is not a function of available condensable vapour alone, but also of the available particle surface. If the available particle surface becomes too small to accept the condensing vapour, new particles occur. This ratio doesn't depend on the absolute amount of aerosol particles. Thus, formation of new particles can occur anywhere on the globe.

A year-round feature observed at Trollhaugen is the intrusion of marine air associated with marine storms. These have been observed even at South Pole, and are visible in the PNSD when the particle concentration at the upper end of the particle size range increases.

The probably most prominent feature in the Trollhaugen annual PNSD time series data is the annual cycle visible in the background aerosol. Particle concentrations are low in winter over the whole observed PNSD size range, and nucleation events lacking. In spring, particle concentrations in the diameter range 0.01 – 0.03 µm increase, and the central particle diameter of this peak increases throughout spring until reaching values around 0.09 µm in summer. Towards autumn and winter, the cycle reverses.

Table 8: Selected transport events observed at Trollhaugen in 2020, together with characteristics and air mass origin determined by Lagrangian backward plume analysis.

#	Time Begin	Time End	Comment	Air mass origin (backwards order)	Air mass type
1	13.05.2020 14:00	14.05.2020 06:00	single accumulation mode, 0.1 µm	straight from the East	likely emissions from neighboring station
2	07.06.2020 08:00	07.06.2020 16:00	single accumulation mode, 0.1 µm	strong footprint at Antarctic peninsula	possibly emissions from stations on Antarctic peninsula
3	16.06.2020 00:00	16.06.2020 14:15	single accumulation mode, 0.1 µm	straight from the East	likely emissions from neighboring station
4	27.08.2020 04:00	27.08.2020 11:00	single accumulation mode, 0.09 µm	straight from the East	likely emissions from neighboring station
5	22.09.2020 15:00	24.09.2020 14:00	single accumulation mode, 0.09 µm	straight from the East	likely emissions from neighboring station

Despite the uniform character of the air mass cycle at Trollhaugen, transport episodes occur also here, some of which are marked in Figure 54 and explained in Table 8. In Antarctica, transport episodes remain visible also for very long transport times due to pristine background particle concentrations. These long transport time require use of Lagrangian backward plume modelling in order to determine air mass origin instead of “simple” trajectory modelling. In 2020, most distinct episodes observed at Trollhaugen were caused by emissions of the neighbouring station in the East, with one exception in early July originating from the Antarctic peninsula.

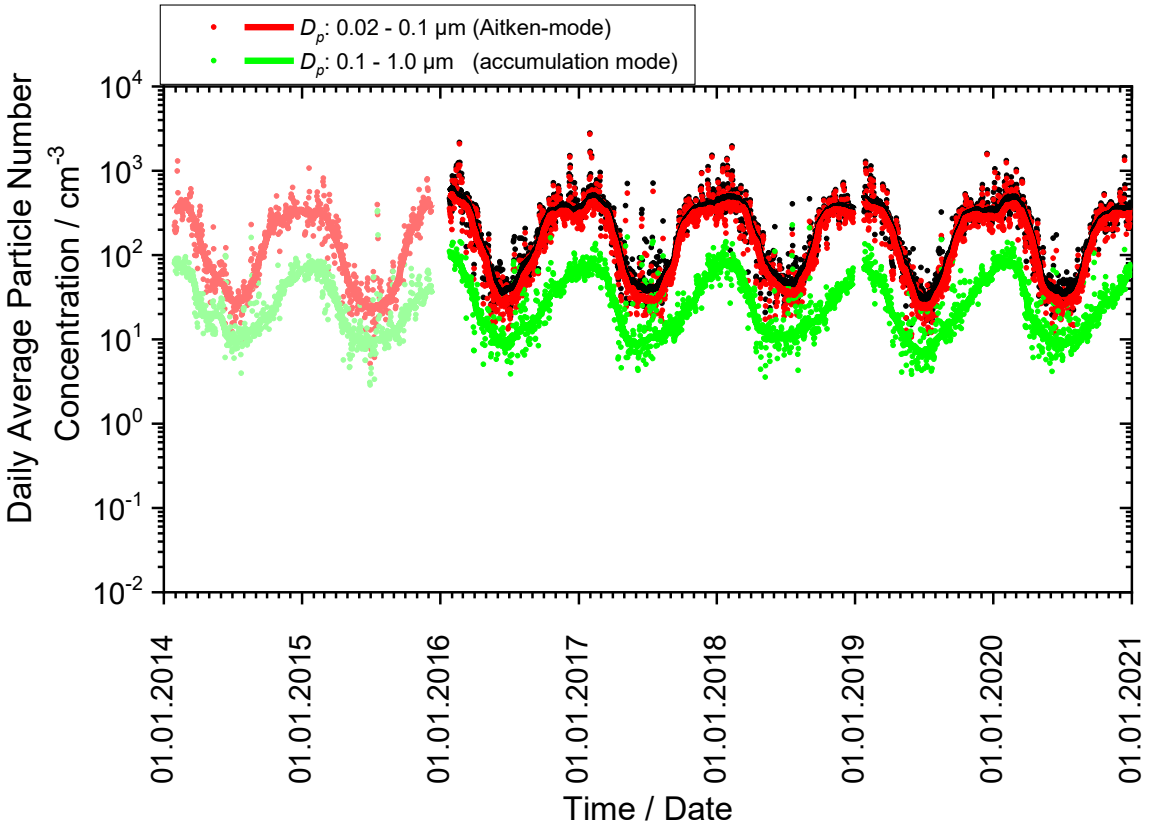

Figure 55: 2014-2020 time series of particle number concentration integrated over selected size ranges representing the different physical processes governing the atmospheric aerosol. The dotted graphs represent daily averages of the respective size range, the lines the 8-week running median. Data of the DMPS instrument prior to its upgrade are plotted in lighter colour as reminder that data before and after remodelling aren't directly comparable due to extension of the particle size range observed by the instrument.

The annual cycle in the Antarctic background PNSD is reflected by the PNSD size integrals for the Aitken mode N_{ait} (0.02 µm< D_p < 0.1 µm) and N_{acc} (0.1 µm< D_p < 0.8 µm) plotted in Figure 55, with higher particle concentrations in summer than in winter. A study based on data collected at Troll (Fiebig et al., 2014) connects the annual cycle to transport patterns seen by Antarctic background air. Antarctic background air descends over the central continent from the upper troposphere / lower stratosphere region, where it has been transported from mid-latitudes or even the tropics at the same altitude. At these lower latitudes, it had been uplifted by frontal conveyers (mid-latitudes) or tropical anvil clouds. The uplift process, associated with extensive wet removal of particles in the frontal or anvil cloud system, explains the cleanliness of the air.

Fiebig et al. (2014) raise the hypothesis that the annual cycle of the Antarctic background aerosol is caused by the annual variation of solar insolation seen by the air during this transport pattern. The hard UV radiation in the upper troposphere would oxidise water-insoluble vapours that survived wet removal during uplift of the air. The oxidation products would subsequently condense into the particle phase, causing the observed annual cycle in the Antarctic background PNSD.

3.5 Summary of physical and optical aerosol properties

Aerosol particle absorption and scattering are decisive for the cooling or warming effect of aerosols on climate. All types of aerosols are scattering solar radiation, but the higher fraction of aerosol absorption, the more warming is the aerosol. The absorption depends on the composition; black carbon (e.g. soot), certain organic compounds (brown carbon), and some minerals absorb radiation. The number size distribution of the aerosol particles also determines the scattering properties. In order to summarise the measurements of physical and optical aerosol properties observed at Birkenes, Trollhaugen, and Zeppelin stations, annual and seasonal means of the main parameters are collected in Table A 3 for the physical parameters, and in Table A 4 for the optical parameters (see Appendix I)

Focussing first on the columns for Birkenes, Aitken-mode particle concentrations N_{ait} for the summer and winter show surprisingly little variation over the years. Relative to previous years, particle concentrations in 2020 for winter are close to the multi-year range, which applies also to summer concentrations. Similarly, spring N_{ait} concentrations are close to those for many previous years, whereas those for autumn are lower, but all still within the range seen in previous years. Variations of this kind are not unusual, and depend on the actual transition from winter to summer weather and vice versa. Late onset of summer weather in spring and early onset of winter weather in autumn will decrease the N_{ait} particle concentrations for these seasons. Also for the accumulation mode seasonal average particle concentrations N_{acc}, spring values are in the middle of the variability range, autumn values at the lower end, whereas summer and winter values don't show exceptional deviations.

At Birkenes, N_{ait} values for winter are typically around 33% of their summer values due to lack of biogenic particle production from the gas-phase. They depend on emissions from domestic heating, with higher values for colder winters. With spring and autumn as transition periods between the winter and summer extreme values, the variability of N_{ait} in these seasons depends on the pace of transition between summer and winter. The same tendencies apply to the accumulation mode particle concentration N_{acc}.

Coarse mode particle concentrations at Birkenes have a tendency to be up to a factor of 2 smaller in winter than in summer due to less crustal particle production with a snow-covered ground. Particle concentrations at Birkenes don't exhibit any obvious trend over time.

Aitken and accumulation mode particle concentrations at Trollhaugen are an order of magnitude lower than at Birkenes, reflecting the pristine conditions in Antarctica. Their pronounced annual cycle and its cause has been discussed in section 3.4.3. Both concentrations show little variability over the years, reflecting the fact that atmospheric composition in Antarctica is still mostly governed by natural processes whose large scale pattern changes slowly.

Zeppelin particle size distribution data exhibit the well-known Arctic haze pattern. Trends in this pattern cannot be studied in this context due to the short time series. Newly established observations of the particle size distribution in the refractory particle fraction can serve as indicator of aerosol atmospheric processing time. The spectral dependence of particle light absorption at Zeppelin indicates a contribution of absorbing components with spectral dependence due to chemical composition, e.g. brown carbon or mineral dust.

The conclusion of no obvious trends applies also to the optical aerosol properties observed at Birkenes, and Trollhaugen, and is confirmed by the trend study of Collaud Coen et al. (2020), whereas Zeppelin aerosol absorption continues to show a decreasing trend (Eleftheriadis et al., 2009). At Birkenes, the annual and inter-annual variability is governed by the same processes mentioned when discussing the particle concentrations. More specifically, the aerosol is more absorbing in winter, and hence more warming, due to emissions from wood burning for domestic heating, which come on top of a baseline

of absorbing aerosol emitted from traffic. This is reflected in higher particle absorption coefficient values in winter, and even more significantly in lower winter values of the single scattering albedo (lower meaning higher average particle absorption).

Episodes of long-range transport are visible at Birkenes and Zeppelin stations 2020, with sources of Central European winter emissions in Birkenes, and Ukrainian summer fires, mixed with Central Asian dust in both Birkenes and Zeppelin. At Trollhaugen, transport episodes are traces back to emissions from neighbouring stations.

3.6 Column optical aerosol properties measured by ground-based remote sensing

Ground-based remote sensing of the optical characteristics of aerosols in the atmospheric total column is conducted with multi-wavelength sun-photometers. A sun-photometer is oriented towards the sun to detect the solar radiation attenuated along the slant path from the top-of-atmosphere to the ground. The atmospheric aerosol load leads to a decrease in the solar radiation transmitted through the atmosphere. This decrease depends on the aerosol optical depth (AOD), which is given by the integral of the volume aerosol extinction coefficient along the vertical path of the atmosphere. The wavelength dependence of AOD, described by the Ångström exponent (AE) is a qualitative indicator of the particle size and contains information about the aerosol type. The larger the Ångström exponent, the smaller the size of the particles measured.

Photos of instruments used for monitoring of spectral resolved AOD at Birkenes and Ny-Ålesund, their main characteristics are given in Appendix II, and detailed tables with monthly data for all years are given in Appendix I.

3.6.1 Column optical aerosol properties measured by ground-based remote sensing at Birkenes Observatory

Key findings column-integrated optical aerosol properties Birkenes: *There is no statistically significant trend, neither in AOD nor in AE, in the eleven years of AOD observations at Birkenes. While AOD monthly means in most months of 2020 are close to or lower than the multi-year average, the summer and autumn values (except July) show large variations, though not necessarily high mean values, due to pronounced short episodes of polluted air masses, probably caused by biomass burning. AE means are very close to the long-term mean in all months covered except April.*

AOD measurements started at the Birkenes Observatory in spring 2009, utilizing an automatic sun and sky radiometer (CIMEL type CE-318, instrument #513). The retrieval method is that of the AERONET version 3 direct sun algorithm (for details: http://aeronet.gsfc.nasa.gov).

A second Cimel instrument (#1163) was purchased in summer 2018 and subsequently calibrated at the University of Valladolid in October 2018; it was for the first time installed at Birkenes in November 2018. Regular measurements started on 7th January 2019, and continued until 5th May 2020 when it was replaced by the instrument #513. The instruments were again swapped in early March 2021, but until present (3rd September, 2021) the calibration of instrument #1163 has not been finalized, so that data from 5th May to 31st December 2020, only are available in a preliminary version (level 1.5). However, experience with the Aeronet analysis algorithm version 3 in recent years has shown that level 1.5 data are very close to the final version.

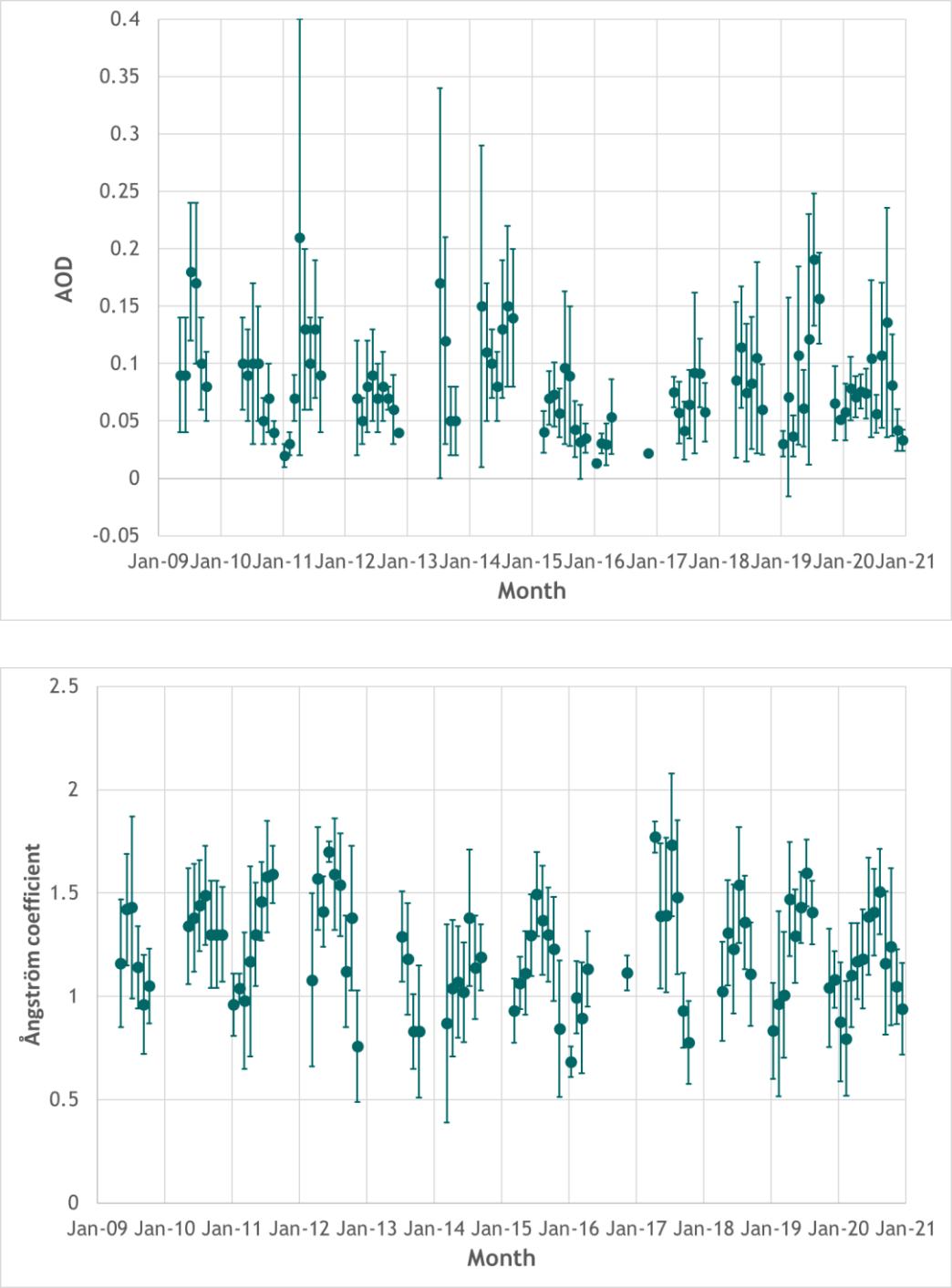

Figure 56: 2009 - 2020 time series of aerosol optical depth (AOD) at 500 nm wavelength in the atmospheric column above Birkenes (upper panel) and (470 nm, 800 nm) Ångström exponent describing the AOD wavelength dependence (lower panel). Mean values and standard deviations are given.

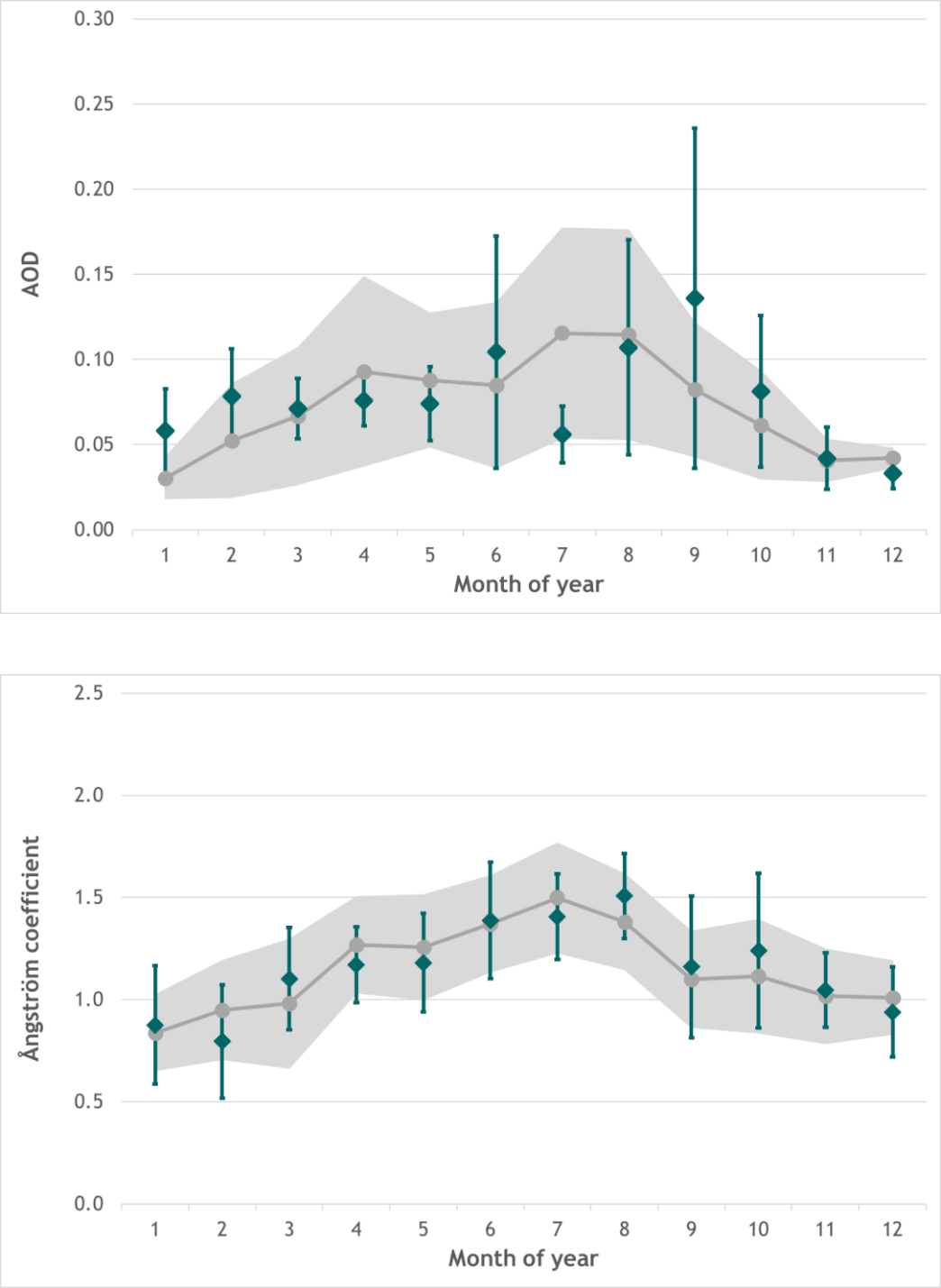

Figure 57: 2020 monthly mean aerosol optical depth (AOD) at 500 nm wavelength in the atmospheric column above Birkenes (upper panel) and (470, 800 nm) Ångström coefficient describing the AOD wavelength dependence (lower panel). Mean values and standard deviations are given. Values marked in grey are the mean and standard deviations for the 2009-2020.

The AOD and Ångström coefficient time series and seasonal variations for 2020 are shown in *Figure 56* and Figure 57. The 2020 monthly mean and mean values for all years are given in

Table 9, while data for all years can be found in Appendix I. The low number of accepted measurements in March and April were not due to weather conditions or technical problems, but repeated establishment of thin spider webs in the collimator tube (!). AERONET calculates daily averages in case of more than 3 single measurements, but we have used a minimum of 10 single measurements. In the monthly means we include all approved single measurements from the respective month instead of daily averages weighted with the number of single measurements included in the respective daily means. This yielded 107 daily means. There are no obvious (and statistically significant) trends visible in the 12-year series of AOD and AE monthly means.

Compared to central European observations, e.g. the Cabauw station in the Netherlands with AOD monthly means well above 1.0 for large parts of the year, the aerosol load at Birkenes is relatively low, but episodes with advected airmasses rich in pollution/aerosol load occur. As one can see in figure 60, in 2020, such episodes occurred in summer and autumn, while the first five months of the year were characterized by AOD (500 nm) values around or below 0.1 . The elevated episodes were typically 10-20 days long, with single days of AOD values up to 0.4 embedded. The monthly means of June, August and September are clearly influenced by these episodes, with a large scattering of single measurements included, while the July mean, in absence of such events, is very low. From the second half of October, values again dropped below 0.1. The highest monthly average AOD of 0.14 occurred in September, mainly due to an extended high-AOD episode with a maximum daily average of 0.33 , while the lowest monthly means were observed in November and December with a value of 0.04 and 0.03, respectively (few days).

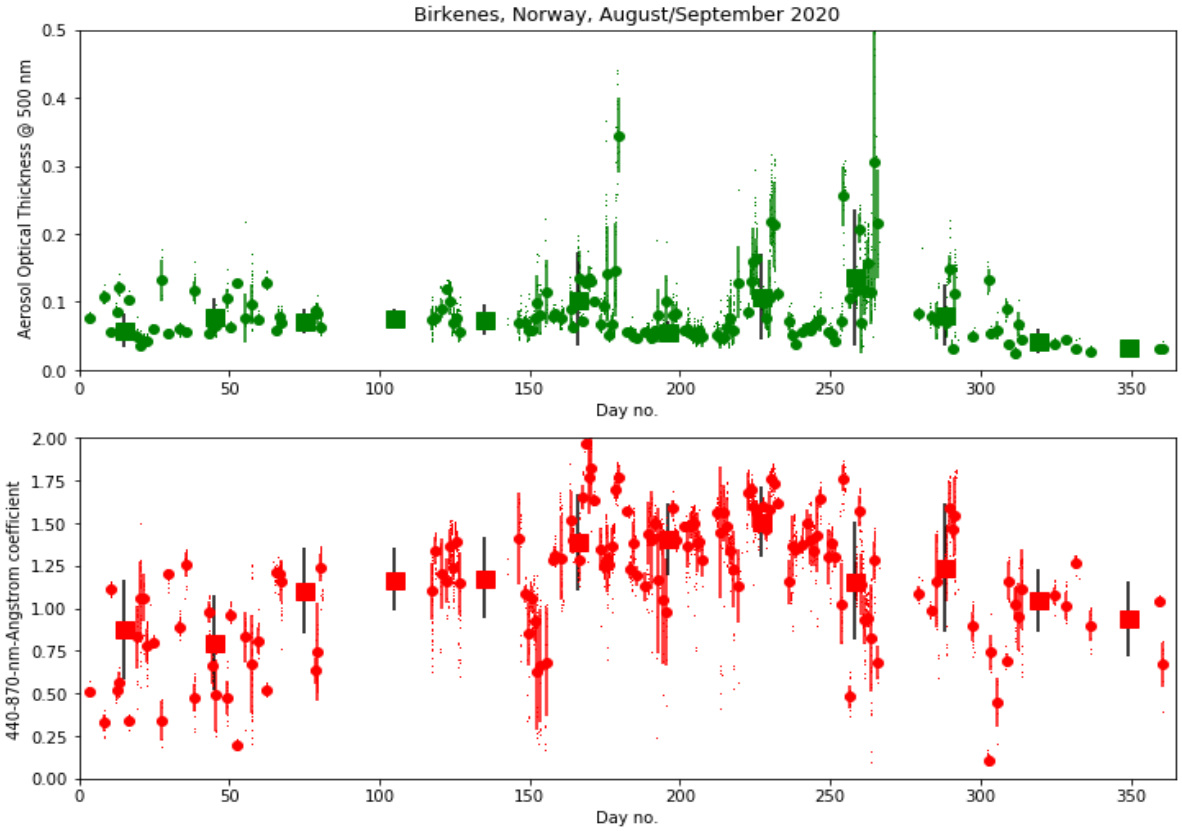

Figure 60: 2020 single (small dots), daily mean (filled circles, with "error" bars), and monthly mean (filled squares, with "error" bars) aerosol optical depth (AOD) at 500 nm wavelength in the atmospheric column above Birkenes (upper panel) and (470, 800 nm) Ångström coefficient describing the AOD wavelength dependence (lower panel). Error bars denote standard deviation of single measurements included in means.

The Ångström exponent monthly means varied much less than AOD means and were all within the standard deviations of the 12-year series throughout the year. In some months (September, October), the standard deviation of the monthly means was relatively large, though.

Table 9: Monthly mean values for 2020 and mean for the time period 2009-2020, plus standard deviations, for aerosol optical depth (AOD) and Ångström exponent observed in Birkenes. In addition, the number of days with cloud free and quality assured observations are given.

Month/Year	Jan	Feb	Mar	Apr	May	Jun	Jul	Aug	Sep	Oct	Nov	Dec
Aerosol optical depth (AOD)												
2020	**0.06 ±0.02**	**0.08 ±0.07**	**0.07 ±0.02**	**0.08 ±0.01**	**0.07 ±0.02**	**0.10 ±0.07**	**0.06 ±0.02**	**0.11 ±0.06**	**0.14 ±0.10**	**0.08 ±0.04**	**0.04 ±0.02**	**0.03 ±0.01**
Mean 09-20	**0.03 0.01**	**0.05 ±0.03**	**0.07 ±0.04**	**0.09 ±0.06**	**0.09 ±0.04**	**0.08 ±0.05**	**0.12 ±0.06**	**0.11 ±0.06**	**0.08 ±0.04**	**0.06 ±0.03**	**0.04 ±0.01**	**0.04 ±0.01**
Ångström coefficient (Å)												
2020	**0.88 ±0.29**	**0.80 ±0.28**	**1.10 ±0.25**	**1.17 ± 0.18**	**1.18 ± 0.24**	**1.39 ± 0.28**	**1.41 ± 0.21**	**1.51 ± 0.21**	**1.16 ±0.35**	**1.24 ±0.38**	**1.05 ±0.18**	**0.94 ±0.22**
Mean 09-20	**0.84 ±0.15**	**0.95 ±0.24**	**0.98 ±0.33**	**1.27 ±0.24**	**1.26 ±0.26**	**1.37 ±0.24**	**1.50 ±0.27**	**1.38 ±0.23**	**1.10 ±0.24**	**1.12 ±0.28**	**1.02 ±0.23**	**1.01 ±0.18**
Number of days with cloud-free and quality assured observations (AERONET level 2)												
2020	**8**	**10**	**7**	**3**	**11**	**21**	**22**	**22**	**16**	**11**	**8**	**3**
Total 09-20	**22**	**30**	**81**	**98**	**171**	**181**	**193**	**165**	**101**	**71**	**23**	**6**

3.6.2 Column optical aerosol properties measured by ground-based remote sensing at Ny-Ålesund

Key findings column-integrated optical aerosol properties Ny-Ålesund: In 2020, technical problems prohibited an extensive observation series with the PFR instrument. Measurements with the co-located Cimel instrument at the AWIPEV station indicate a limited number of high-AOD episodes in April, May and July/August, which probably all were caused by biomass burning events in the boreal zone.

In 2002, Physikalisch-Meteorologisches Observatorium Davos/World Radiation Center (PMOD/WRC), in collaboration with NILU, started AOD observations in Ny-Ålesund (at the Sverdrup station, 46 m a.s.l.) as part of the global AOD network on behalf of the WMO GAW program. A precision filter radiometer (PFR) measures the extinction in four narrow spectral bands.

In Ny-Ålesund, the solar elevation is less than 5° before 4th March and after 10th October, limiting the period with suitable sun-photometer observations to the spring-summer-early autumn period. In 2020, technical problems occurred throughout the measurement period, except a 3-week period in late April and early May, resulting in only 13 days with sufficient numbers of single measurements to allow the calculation of daily means. The AOD and Ångström coefficients time series of monthly means and standard deviation since the start of measurements in 2002 are shown in 1, while the 2020 values on the background of the average data and their standard deviation from the whole 19-year period (including 2020) are shown in 2. The 2020 monthly mean values and standard deviations for all years are given in Table 10. Data for all years are given in Appendix I.In order to fill the long data gap during the Arctic winter, a PFR version making use of the moonlight around full moon (Lunar PFR) has been developed and tested by PMOD/WRC since 2015. In 2018, the Lunar PFR was integrated in the Svalbard Integrated Arctic Earth Observing Network (SIOS), and data are made available also for monitoring purposes. In principle, reliable measurements are possible from rising half-moon to waxing half-moon, but in Ny-Ålesund the period is further limited by the rapidly changing maximum elevation during the lunar cycle. In 2020, lunar observations were performed in February and March, while bad weather conditions prohibited observations in the autumn. These data are included in Figure 6 and Figure 62, as well as in the data tables.

In 2020, an SSF strategic grant coordinated by NILU was started with the aim to collect, harmonize and store all available AOD/AE measurements from Svalbard and surrounding marine areas since their start in 2002. These involve observations with the sun and lunar PFR, the SP1A sun photometers at the AWIPEV station and at Zeppelin Observatory, Cimel observations at AWIPEV, all these in Ny-Ålesund, Cimel observations at the Polish Polar Station in Hornsund, and various marine observations on research vessels (Oceania, Polarstern, Oden) since 2007. In 2020, the Cimel instrument at AWIPEV station measured throughout the period when solar observations are possible; these observations are considered in the scientific conclusions below. As in the case of the Birkenes data, final data with after-calibration of the instrument header are not yet available due to challenging calibration conditions at the instrument calibration site in Valladolid in Spain, this summer. The preliminary Cimel data, together with the lunar and sun PFR data are shown in Figure 63.

While the few PFR observations do not reveal episodes with high AOD values in winter and spring, the Cimel observations at the same site show several such episodes both in spring and in late summer. However, the duration of these episodes was limited to 2 days (in July) or less, and most of the summer and autumn measurements reveal typical low summer values (< 0.1 at 500 nm). The lunar PFR measurements are in good agreement with later spring measurements except the high-aerosol-load episodes.

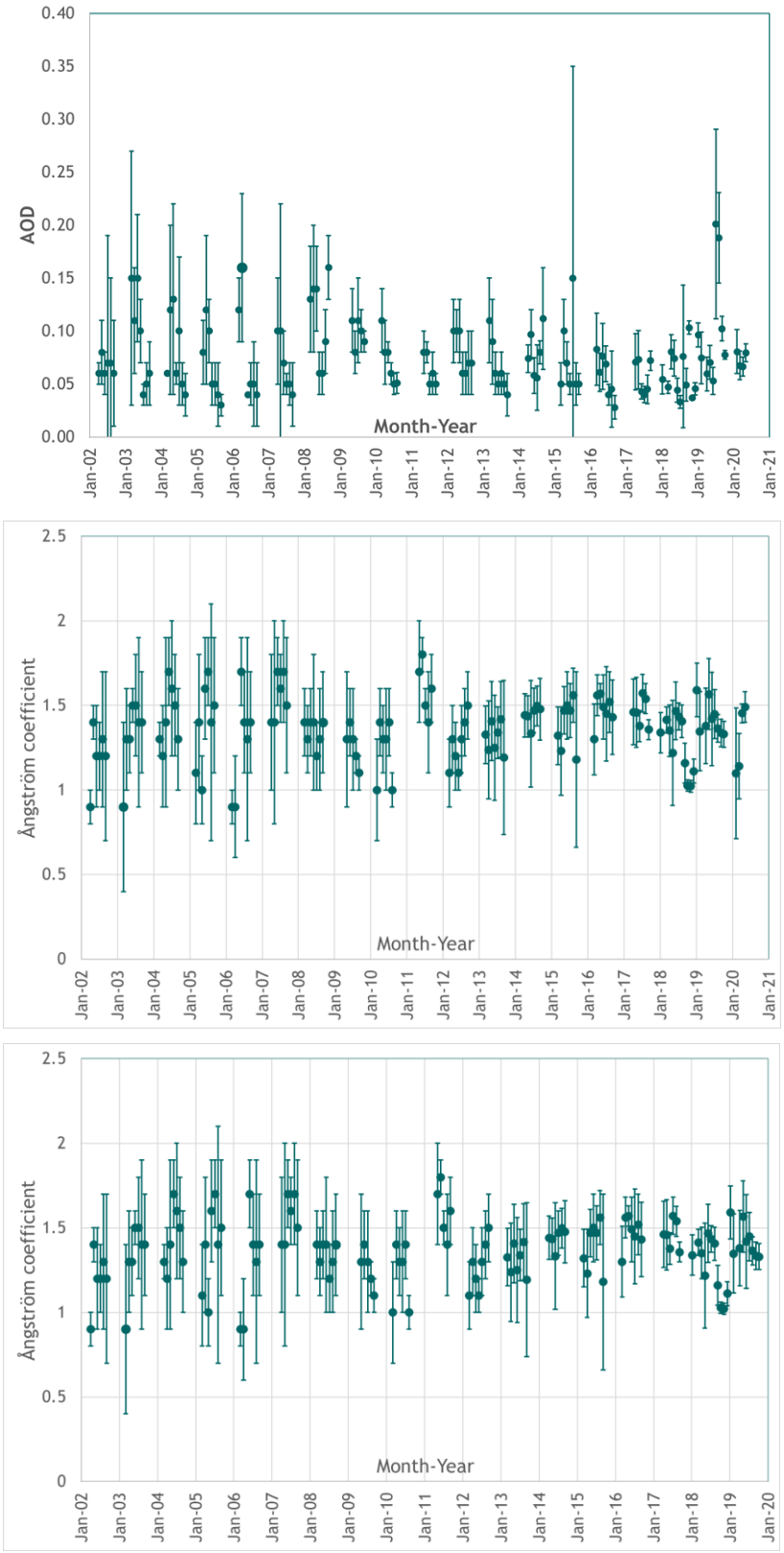

Figure 61: 2002 - 2020 time series of aerosol optical depth (AOD) at 500.5 nm wavelength in the atmospheric column above Ny-Ålesund (upper panel) and Ångström coefficient (lower panel). Monthly mean values and standard deviations are given.

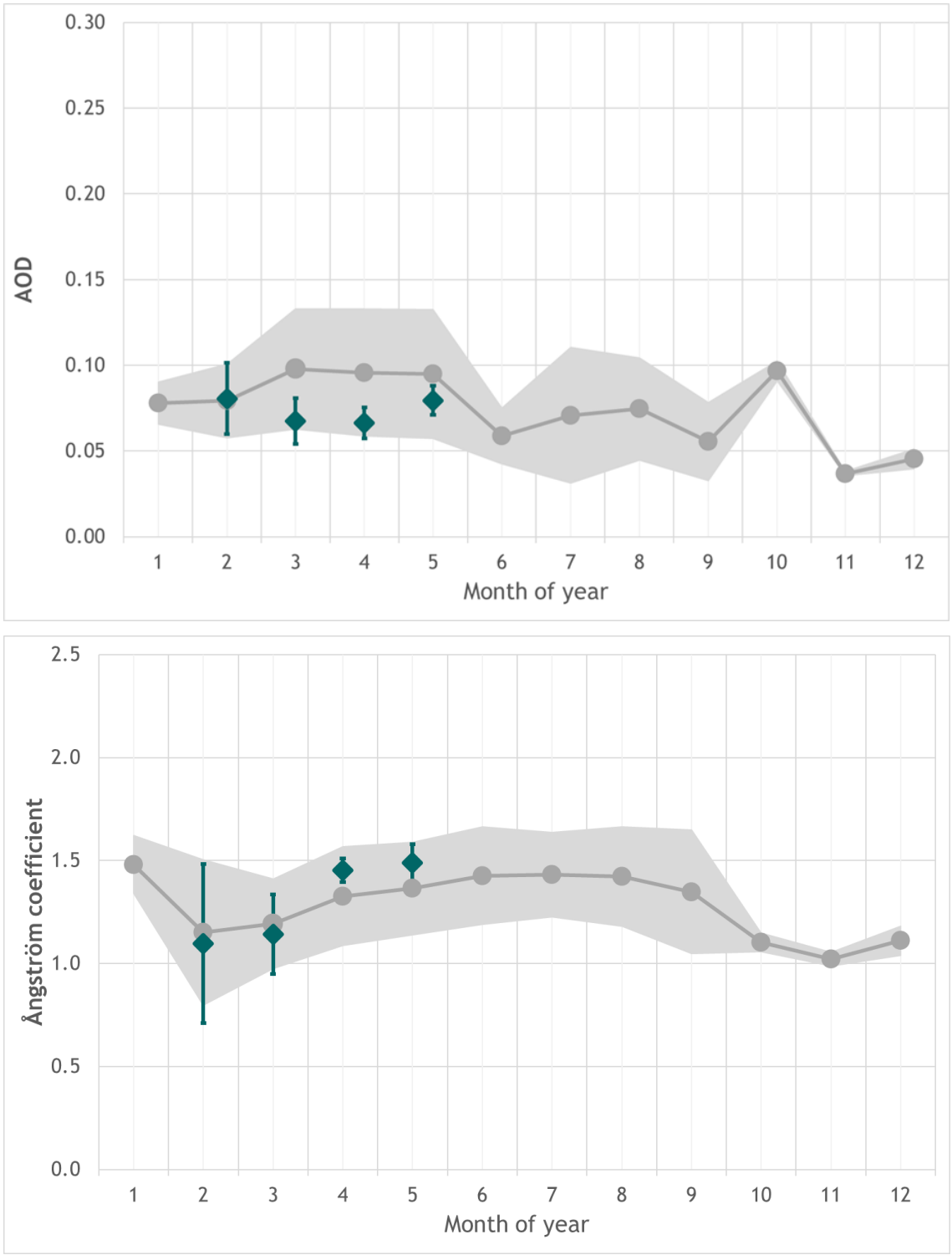

Figure 62: Seasonal variation of the aerosol optical depth (AOD) (upper panel) and Ångström coefficient (lower panel) observed in Ny-Ålesund in 2020. Values marked in grey are the mean and standard deviations for the time period 2002-2020; the 2020 monthly mean and standard deviations are shown in green.

Table 10: Monthly mean values for 2020 and mean for the time period 2002-2020, plus standard deviations, for aerosol optical depth (AOD) and Ångström coefficient observed in Ny-Ålesund. In addition, the number of days with cloud free and quality assured observations are given. Values in February and March are derived from lunar PFR observations.

	Jan	Feb	Mar	Apr	May	Jun	Jul	Aug	Sep	Oct	Nov	Dec
Aerosol optical depth (AOD)												
2020		**0.08 ±0.02**	**0.07 ±0.04**	**0.07 ±0.01**	**0.08 ±0.01**							
Mean 02-20	**0.08 0.01**	**0.08 ±0.02**	**0.10 ±0.04**	**0.10 ±0.04**	**0.10 ±0.04**	**0.06 ±0.02**	**0.07 ±0.04**	**0.07 ±0.03**	**0.06 ±0.02**	**0.10 ±0.01**	**0.04 ±0.00**	**0.05 ±0.01**
Ångström coefficient (Å)												
2020		**1.10 ± 0.39**	**1.14 ±0.19**	**1.45 ± 0.06**	**1.49 ± 0.09**							
Mean 02-20	**1.48 ±0.14**	**1.15 ±0.35**	**1.19 ±0.22**	**1.33 ±0.24**	**1.36 ±0.23**	**1.43 ±0.24**	**1.43 ±0.21**	**1.42 ±0.24**	**1.35 ±0.30**	**1.10 ±0.04**	**1.02 ±0.03**	**1.11 ± 0.07**
Number of days with cloud-free and quality assured observations (AERONET level 2)												
2020		**11**	**5**	**6**	**7**							
Total 02-20	**16**	**14**	**75**	**213**	**211**	**193**	**209**	**168**	**133**	**3**	**2**	**2**

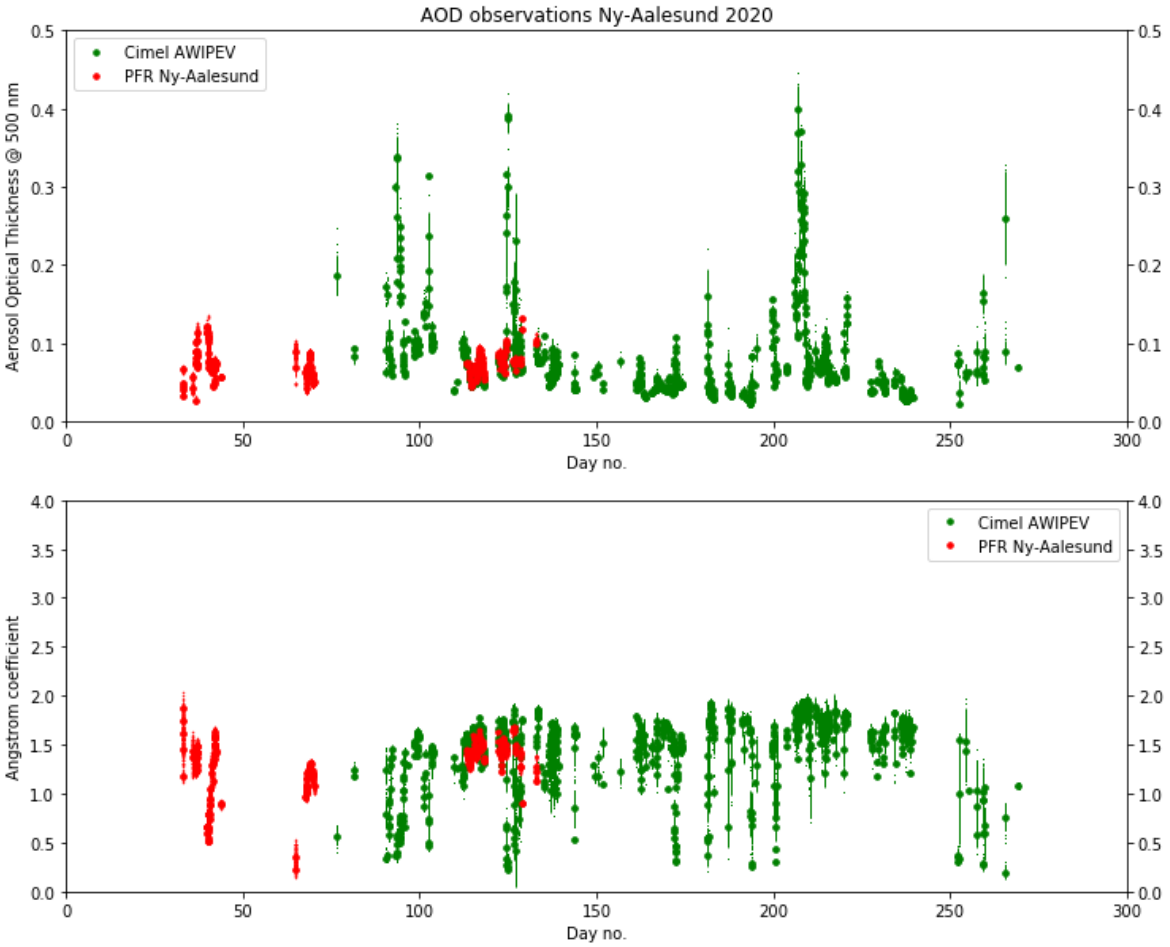

Figure 63: AOD and AE data from Ny-Ålesund, combining PFR (red; lunar and solar) and Cimel (green) observations. Single measurements are marked by dots and daily averages by filled circles. Standard deviations of single measurements used for means calculations are marked by error bars.

3.6.3 Column optical aerosol properties measured by ground-based remote sensing at Troll Station, Antarctica

In austral summer 2006/2007, NILU established an atmospheric observatory at the Norwegian Troll Station (72°01'S, 2°32'E, 1270 m a.s.l.). During the first years of operation, the observatory was located close to the main building of Troll, which caused frequent episodes of local pollution inhibiting aerosol and pollution measurements focusing on long-range transport. For this reason, in January 2014, the atmospheric monitoring station was moved to Trollhaugen, which is more than 2 km away from the main station and at an elevation of more than 280 m above the station. The original instrumentation included a sun PFR instrument from PMOD/WRC (instrument #513); it has been operated quasi-continuously since, but with largely improved measurement statistics after the move of the atmospheric observatory to Trollhaugen.

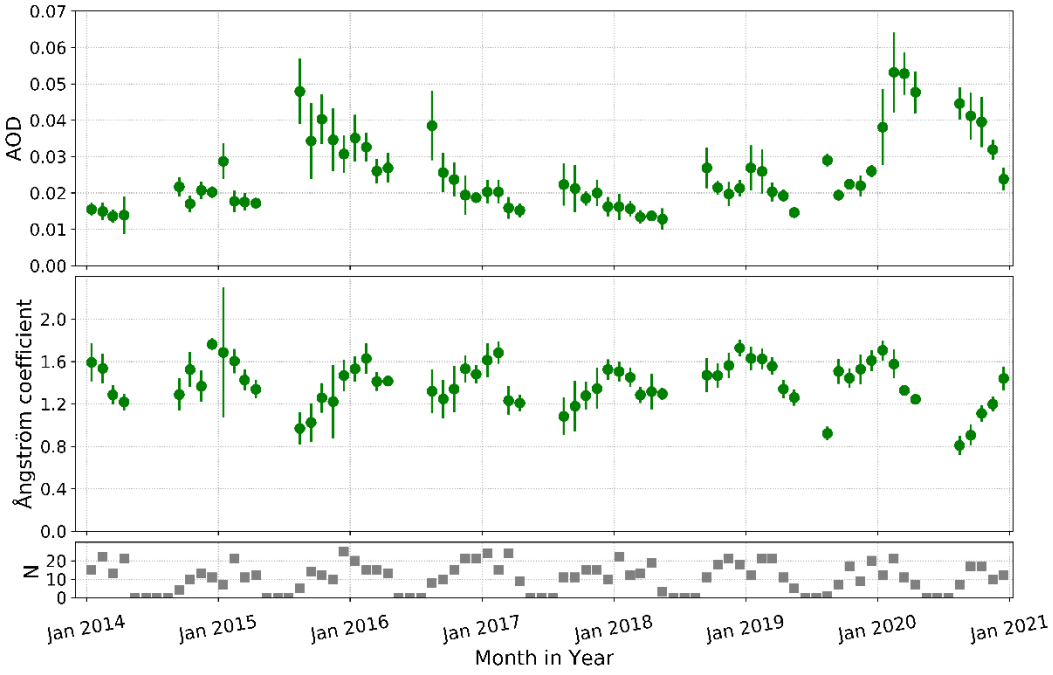

Figure 64: 2014 - 2020 time series of aerosol optical depth (AOD) at 500.5 nm wavelength in the atmospheric column above Trollhaugen Observatory, Antarctica (upper panel), Ångström coefficient (centre panel), and number of days per month with measurements. Monthly mean values and standard deviations are given

Here we present the measurements collected since the move, i.e., from the years 2014 to 2020. 64shows the series of monthly means of both AOD at 500.5 nm, the multi-wavelength Ångström coefficient, and the number of days with usable observations. While the AOD values usually are significantly lower than at high Northern latitudes with monthly mean values between 0.013 and 0.023, 2020 clearly did not match this pattern and showed much higher values, especially during the first months of the year, but also after the austral winter break; only in November and December the monthly means reached typical values of previous years. Regarding the Ångström exponents, the annual cycle with lowest values in austral winter is reinforced; the minimum value of about 0.8 was found for August.

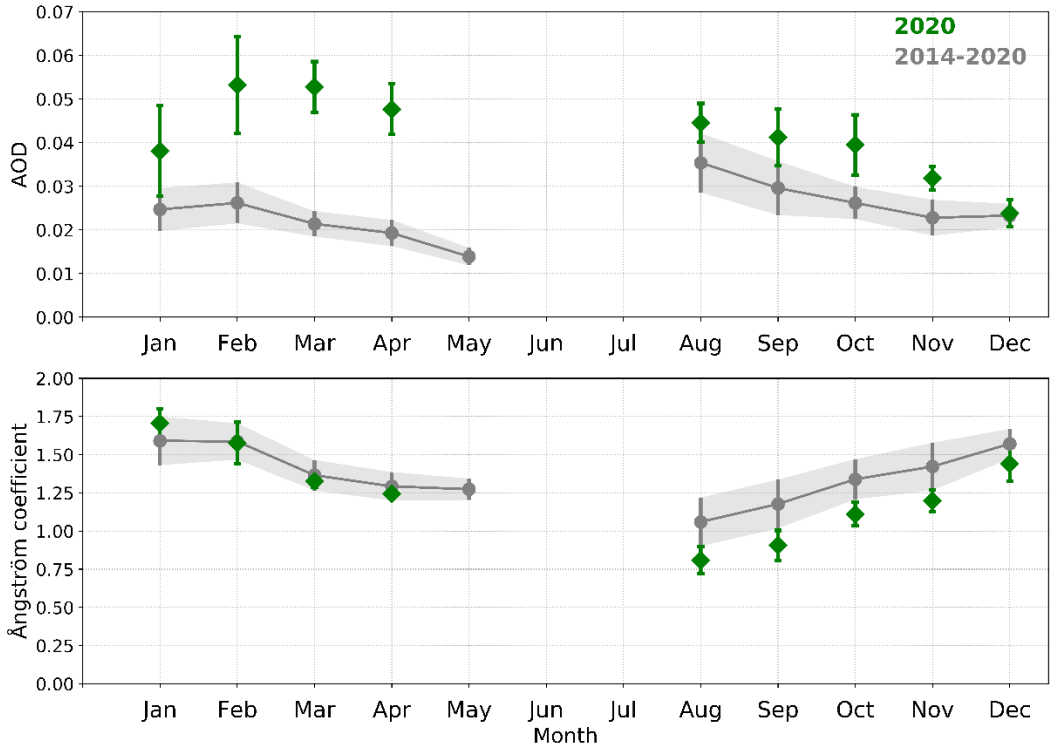

Figure 65: Seasonal variation of the aerosol optical depth (AOD) (upper panel) and Ångström coefficient (lower panel) observed at Troll Station, Antarctica. Values marked in grey are the mean and standard deviations for the time period 2009-2020; the 2020 monthly mean and standard deviations are shown in green.

Figure 65, which shows the seasonal variation of AOD and Ångström coefficient for 2020 and the average values over the 7-year series with standard deviations, further underlines the exceptional conditions in 2020, especially from February to April. In these months the AOD monthly means were far above the mean of previous years, while they gradually approached "normal" values after the austral winter break. Figure 66 showing the series with daily means and individual observations reveal a marked transition from low values in early January to large and highly variable values after January 20, with some daily means close to 0.08 and single measurements up to 0.1. The daily AOD variations remained large until November.

The Ångström exponents, on the other hand, were close to typical values of the 7-year period. The only reasonable explanation for the unique AOD values are the unprecedented biomass/forest fires in Australia in austral summer 2019/2020. These were observed occasionally on the Antarctic peninsula in January 2020, but obviously stayed in the area for a much longer period. It is plausible that part of the pollution was trapped in the stratospheric polar vortex and thus preserved over the winter. The extreme stability of the vortex until December obviously contributed to the signature of enhanced AOD to the end of the year.

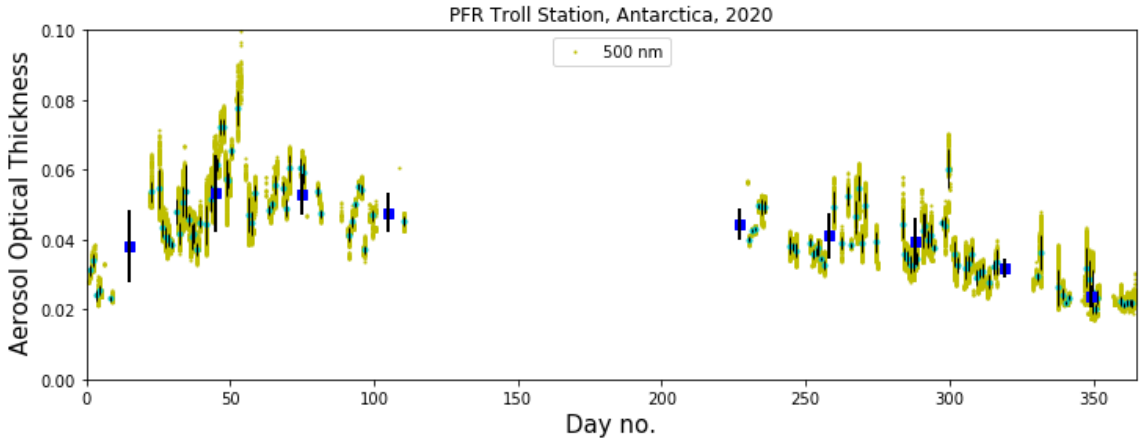

Figure 66: Aerosol optical depth (AOD) observations from Troll in 2020. The graph shows both monthly means (dark blue squares), daily means with variations (light blue marks with black "error" bars) and single measurements (yellow-green marks).

Table 11: Monthly mean values for 2020 and means for the time period 2014-2020 plus standard deviations, for aerosol optical depth (AOD) and Ångström coefficient observed at Trollhaugen Observatory. In addition, the number of days with cloud-free and quality-assured observations is given.

	Jan	Feb	Mar	Apr	May	Jun	Jul	Aug	Sep	Oct	Nov	Dec
Aerosol optical depth (AOD)												
2020	**0.038 ±0.01**	**0.053 ±0.01**	**0.053 ±0.01**	**0.048 ±0.01**				**0.045 ±0.004**	**0.041 ±0.007**	**0.040 ±0.007**	**0.032 ±0.003**	**0.024 ±0.003**
Mean 14-20	**0.025 ±0.005**	**0.026 ±0.005**	**0.021 ±0.003**	**0.019 ±0.003**	**0.014 ±0.002**			**0.035 ±0.007**	**0.030 ±0.006**	**0.026 ±0.004**	**0.023 ±0.004**	**0.023 ±0.003**
Ångström coefficient (Å)												
2020	**1.71 ± 0.10**	**1.58 ± 0.14**	**1.33 ± 0.04**	**1.24 ± 0.03**				**0.81 ± 0.09**	**0.91 ± 0.10**	**1.11 ± 0.08**	**1.20 ± 0.07**	**1.44 ± 0.11**
Mean 14-20	**1.59 ±0.16**	**1.59 ±0.12**	**1.37 ±0.10**	**1.29 ±0.09**	**1.27 ±0.07**			**1.06 ±0.16**	**1.18 ±0.16**	**1.34 ±0.13**	**1.42 ±0.16**	**1.57 ± 0.10**
Number of days with cloud-free and quality assured observations (AERONET level 2)												
2020	**12**	**21**	**11**	**7**				**7**	**17**	**17**	**10**	**15**
Total 14-20	**112**	**129**	**109**	**95**	**8**			**32**	**75**	**106**	**99**	**125**

3.7 Summary of aerosol column properties

As pointed out in the introduction, these type of measurements gives information about the total load of aerosols in the radiation path between the sun (or another external light source, like the moon and bright stars) and the instrument. This necessitates an extremely careful and frequent calibration of the instrument and regular updates on the respective external light source. The only solution to fulfil these criteria has been to have dual instruments at sites with continuous light (Birkenes) and very limited accessibility (Troll), and complementary instruments at sites with long periods without the main light source (the sun; Ny-Ålesund). From the end of 2018, this has been in place at all our sites.

With respect to Birkenes, there is no statistically significant trend in the eleven years of AOD observations, which is not surprising, taking into account the large variability both on an annual and monthly basis between 2009 and 2020. The most remarkable feature in the 2020 data is the high load of aerosols during parts of the summer and autumn. All of these coincide with severe forest fires in parts of Scandinavia and other areas in Eurasia. No signs of effects of the Covid-19 lockdown periods is evident at these sites.

Also in Ny-Ålesund, the 2019 monthly mean AOD values are characterized by very high values during summer, while in other months they are markedly below the long-term average. The high summer AOD values can be directly connected to very severe forest fires both in Northern Russia and the Northern regions of North America. In contrast to previous years the aerosol load persisted over a long time (more than 2 months).

AOD observations at the Trollhaugen Observatory in Antarctica in 2019 mostly fit into the picture of an extremely clean atmosphere at this site, with monthly average AOD values below 0.02. However, also here episodes with significantly enhanced AOD (up to 0.045) occurred in austral summer, and an influence of the increasing number and severity of forest fires in SH regions (South America, South Africa, Australia) cannot be excluded.

4 References

Aas, W., Eckhardt, S., Fiebig, M., Solberg, S., Platt, S.M., Yttri, K.E., Zwaaftink, C.G. (2021) Monitoring of long-range transported air pollutants in Norway. Annual Report 2020. (NILU report 13/2021; Norwegian Environment Agency M-2072|2021). Kjeller: NILU.

Asmi, A., Collaud Coen, M., Ogren, J. A., Andrews, E., Sheridan, P., Jefferson, A., Weingartner, E., Baltensperger, U., Bukowiecki, N., Lihavainen, H., Kivekäs, N., Asmi, E., Aalto, P. P., Kulmala, M., Wiedensohler, A., Birmili, W., Hamed, A., O'Dowd, C., G Jennings, S., Weller, R., Flentje, H., Fjaeraa, A. M., Fiebig, M., Myhre, C.E.L., Hallar, A. G., Swietlicki, E., Kristensson, A., Laj, P. (2013) Aerosol decadal trends - Part 2: In-situ aerosol particle number concentrations at GAW and ACTRIS stations. *Atmos. Chem. Phys.*, *13*, 895-916. doi:10.5194/acp-13-895-2013.

Baasandorj, M., Hall, B. D., Burkholder, J. B. (2012) Rate coefficients for the reaction of $O(^1D)$ with the atmospherically long-lived greenhouse gases NF_3, SF_5CF_3, CHF_3, C_2F_6, c-C_4F_8, *n*-C_5F_{12}, and *n*-C_6F_{14}. *Atmos. Chem. Phys., 12,* 11753-11764. doi:10.5194/acp-12-11753-2012.

Coen, M. Collaud., Andrews, E., Alastuey, A., Arsov, T. P., Backman, J., Brem, B. T., Bukowiecki, N., Couret, C., Eleftheriadis, K., Flentje, H., Fiebig, M., Gysel-Beer, M., Hand, J. L., Hoffer, A., Hooda, R., Hueglin, C., Joubert, W., Keywood, M., Kim, J. E., Kim, S.-W., Labuschagne, C., Lin, N.-H., Lin, Y., Lund Myhre, C., Luoma, K., Lyamani, H., Marinoni, A., Mayol-Bracero, O. L., Mihalopoulos, N., Pandolfi, M., Prats, N., Prenni, A. J., Putaud, J.-P., Ries, L., Reisen, F., Sellegri, K., Sharma, S., Sheridan, P., Sherman, J. P., Sun, J., Titos, G., Torres, E., Tuch, T., Weller, R., Wiedensohler, A., Zieger, P. and Laj, P. (2020) Multidecadal trend analysis of in situ aerosol radiative properties around the world. *Atmos. Chem. Phys., 20,* 8867-8908. doi: 10.5194/acp-20-8867-2020.

Coen, M. C., Andrews, E., Asmi, A., Baltensperger, U., Bukowiecki, N., Day, D., Fiebig, M., Fjaeraa, A. M., Flentje, H., Hyvärinen, A., Jefferson, A., Jennings, S. G., Kouvarakis, G., Lihavainen, H., Myhre, C. L, Malm, W. C., Mihapopoulos, N., Molenar, J. V., O'Dowd, C., Ogren, J. A., Schichtel, B. A., Sheridan, P., Virkkula, A., Weingartner, E., Weller, R., Laj, P. (2013) Aerosol decadal trends - Part 1: In-situ optical measurements at GAW and IMPROVE stations. *Atmos. Chem. Phys., 13,* 869-894. doi:10.5194/acp-13-869-2013.

Coen, M.C., Weingartner, E., Apituley, A., Ceburnis, D., Fierz-Schmidhauser, R., Flentje, H., Henzing, J. S. (2010) Minimizing light absorption measurement artifacts of the Aethalometer: evaluation of five correction algorithms. *Atmos. Meas. Tech, 3,* 457–474. doi: 10.5194/amt-3-457-2010.

Dalsøren, S. B., Myhre, C. L., Myhre, G., Gomez-Pelaez, A. J., Søvde, O. A., Isaksen, I. S. A., Weiss, R. F., Harth, C. M. (2016) Atmospheric methane evolution the last 40 years. *Atmos. Chem. Phys., 16,* 3099-3126. doi:10.5194/acp-16-3099-2016.

Dalsøren, S. D., Myhre, G., Hodnebrog, Ø., Myhre, C. L., Stohl, A., Pisso, I., Schwietzke, S., Höglund-Isaksson, L., Helmig, D., Reimann, S., Sauvage, S., Schmidbauer, N., Read, K. A., Carpenter, L. J., Lewis, A. C., Punjabi, S., Wallasch, M. (2018) Discrepancy between simulated and observed ethane and propane levels explained by underestimated fossil emissions. *Nature Geosci., 11,* 178-184. doi:10.1038/s41561-018-0073-0.

Delene, D.J., Ogren, J.A. (2002) Variability of aerosol optical properties at four North American surface monitoring sites. *J. Atmos. Sci., 59,* 1135-1150.

Dlugokencky, E.J., Hall, B. D., Montzka, S. A., Dutton, G., Mühle, J., Elkins, J. W. (2019) Long-lived greenhouse gases [in “State of the Climate in 2019”]. *Bull. Amer. Meteor. Soc.,* 101, No 8, S48–52. doi: 10.1175/2020BAMSStateoftheClimate.1.

Dlugokencky, E.J., Hall, B. D., Montzka, S. A., Dutton, G., Mühle, J., Elkins, J. W. (2018) Long-lived greenhouse gases [in “State of the Climate in 2017”]. *Bull. Amer. Meteor. Soc.,* 99, S46-49. doi:10.1175/2018BAMSStateoftheClimate.1.

Drinovec, L., Močnik, G., Zotter, P., Prévôt, A. S. H., Ruckstuhl, C., Coz, E., Rupakheti, M., Sciare, J., Müller, T., Wiedensohler, A., Hansen, A. D. A. (2015) The "dual-spot" Aethalometer: an improved measurement of aerosol black carbon with real-time loading compensation. *Atmos. Meas. Tech, 8,* 1965-1979. doi:10.5194/amt-8-1965-2015.

Etiope, G., Ciccioli, P. (2009) Earth's Degassing: A Missing Ethane and Propane Source. *Science 323,* 478. doi:10.1126/science.1165904.

Etminan, M.,Myhre, G., Highwood, E. J., Shine, K. P. (2016) Radiative forcing of carbon dioxide, methane, and nitrous oxide: A significant revision of the methane radiative forcing, *Geophys. Res. Lett*., 43, 12,614-12,623, doi:10.1002/ 2016GL071930.

Fiebig, M., Hirdman, D., Lunder, C. R., Ogren, J. A., Solberg, S., Stohl, A., Thompson, R. L. (2014) Annual cycle of Antarctic baseline aerosol: controlled by photooxidation-limited aerosol formation. *Atmos. Chem. Phys., 14,* 3083-3093. doi: 10.5194/acp-14-3083-2014

Fisher, R. E., France, J. L., Lowry, D., Lanoisellé, M., Brownlow, R., Pyle, J. A., Cain, M., Warwick, N., Skiba, U. M., Drewer, J., Dinsmore, K. J., Leeson, S. R., Bauguitte, S. J.-B., Wellpott, A., O'Shea, S. J., Allen, G., Gallagher, M. W., Pitt, J., Percival, C. J., Bower, K., George, C., Hayman, G. D., Aalto, T., Lohila, A., Aurela, M., Laurila, T., Crill, P. M., McCalley, C. K. and Nisbet, E. G. (2017) Measurement of the 13C isotopic signature of methane emissions from northern European wetlands. *Global Biogeochem. Cycles, 31,* 605-623, doi:10.1002/2016GB005504.

Forster, P., T. Storelvmo, K. Armour, W. Collins, J. L. Dufresne, D. Frame, D. J. Lunt, T. Mauritsen, M. D. Palmer, M. Watanabe, M. Wild, H. Zhang, 2021, The Earth's Energy Budget, Climate Feedbacks, and Climate Sensitivity. In: Climate Change 2021: The Physical Science Basis. Contribution of Working Group I to the Sixth Assessment Report of the Intergovernmental Panel on Climate Change [Masson-Delmotte, V., P. Zhai, A. Pirani, S. L. Connors, C. Péan, S. Berger, N. Caud, Y. Chen, L. Goldfarb, M. I. Gomis, M. Huang, K. Leitzell, E. Lonnoy, J.B.R. Matthews, T. K. Maycock, T. Waterfield, O. Yelekçi, R. Yu and B. Zhou (eds.)]. Cambridge University Press. In Press.

France, J. L., Cain, M., Fisher, R. E., Lowry, D., Allen, G., O'Shea, S. J., Illingworth, S., Pyle, J., Warwick, N., Jones, B. T., Gallagher, M. W., Bower, K., Le Breton, M., Percival, C., Muller, J., Welpott, A., Bauguitte, S., George, C., Hayman, G. D., Manning, A. J., Myhre, C. L., Lanoisellé, M., Nisbet, E. G. (2016) Measurements of δ 13C in CH4 and using particle dispersion modeling to characterize sources of Arctic methane within an air mass. *J. Geophys. Res. Atmos., 121,* 14,257-14,270, doi:10.1002/2016JD026006.

Gliß, J., Mortier, A., Schulz, M., Andrews, E., Balkanski, Y., Bauer, S. E., Benedictow, A. M. K., Bian, H., Checa-Garcia, R., Chin, M., Ginoux, P., Griesfeller, J. J., Heckel, A., Kipling, Z., Kirkevåg, A., Kokkola, H., Laj, P., Le Sager, P., Lund, M. T., Lund Myhre, C., Matsui, H., Myhre, G., Neubauer, D., van Noije, T., North, P., Olivié, D. J. L., Sogacheva, L., Takemura, T., Tsigaridis, K. and Tsyro, S. G. (2020) Multi-model evaluation of aerosol optical properties in the AeroCom phase III Control experiment, using ground and space based columnar observations from AERONET, MODIS, AATSR and a merged satellite product as well as surface in-situ observations from GAW sites. *Atmos. Chem. Phys*., doi: 10.5194/acp-2019-1214.

Groot Zwaaftink, C. D., Aas, W., Eckhardt, S., Evangeliou, N., Hamer, P., Johnsrud, M., Kylling, A., Platt, S. M., Stebel, K., Uggerud, H., and Yttri, K. E.: What caused a record high PM10 episode in northern Europe in October 2020?, Atmos. Chem. Phys. Discuss. [preprint], https://doi.org/10.5194/acp-2021-496, in review, 2021.

Gulev, S. K., P. W. Thorne, J. Ahn, F. J. Dentener, C. M. Domingues, S. Gerland, D. Gong, D. S. Kaufman, H. C. Nnamchi, J. Quaas, J. A. Rivera, S. Sathyendranath, S. L. Smith, B. Trewin, K. von Shuckmann, R. S. Vose, 2021, Changing State of the Climate System. In: Climate Change 2021: The Physical Science Basis. Contribution of Working Group I to the Sixth Assessment Report of the

Intergovernmental Panel on Climate Change [Masson-Delmotte, V., P. Zhai, A. Pirani, S. L. Connors, C. Péan, S. Berger, N. Caud, Y. Chen, L. Goldfarb, M. I. Gomis, M. Huang, K. Leitzell, E. Lonnoy, J. B. R. Matthews, T. K. Maycock, T. Waterfield, O. Yelekçi, R. Yu and B. Zhou (eds.)]. Cambridge University Press. In Press.

IPCC (2021a). *Climate Change 2021: The Physical Science Basis. Contribution of Working Group I to the Sixth Assessment Report of the Intergovernmental Panel on Climate Change* [Masson-Delmotte, V., P. Zhai, A. Pirani, S. L. Connors, C. Péan, S. Berger, N. Caud, Y. Chen, L. Goldfarb, M. I. Gomis, M. Huang, K. Leitzell, E. Lonnoy, J. B. R. Matthews, T. K. Maycock, T. Waterfield, O. Yelekçi, R. Yu and B. Zhou (eds.)]. Cambridge University Press. In Press

IPCC (2021b). *Summary for Policymakers. In: Climate Change 2021: The Physical Science Basis. Contribution of Working Group I to the Sixth Assessment Report of the Intergovernmental Panel on Climate Change* [Masson-Delmotte, V., P. Zhai, A. Pirani, S. L. Connors, C. Péan, S. Berger, N. Caud, Y. Chen, L. Goldfarb, M. I. Gomis, M. Huang, K. Leitzell, E. Lonnoy, J. B. R. Matthews, T. K. Maycock, T. Waterfield, O. Yelekçi, R. Yu and B. Zhou (eds.)]. Cambridge University Press. In Press.

Hall, B. D., Montzka, S. A., Dutton, G., Mühle, J., Elkins, J. W. (2017) Long-lived greenhouse gases [in "State of the Climate in 2016"]. *Bull. Amer. Meteor. Soc., 98* (8), S43-S46, doi:10.1175 /2017BAMSStateoftheClimate.1.

Hall, B. D., Montzka, S. A., Dutton, G., Miller, B. R., Elkins, J. W. (2020) Ozone-depleting substances [in "State of the Climate in 2019"]. *Bull. Amer. Meteor. Soc., 101* (8), S75-S76, https://doi.org/10.1175/BAMS-D-20-0104.1

Hansen, K. M., Christensen, J. H., Geels, C., Silver, J. D., and Brandt, J.: Modelling the impact of climate change on the atmospheric transport and the fate of persistent organic pollutants in the Arctic, Atmos. Chem. Phys., 15, 6549–6559, https://doi.org/10.5194/acp-15-6549-2015, 2015.

Hartmann, D.L., Klein Tank, A. M. G., Rusticucci, M., Alexander, L.V., Brönnimann, S., Charabi, Y., Dentener, F. J., Dlugokencky, E. J., Easterling, D. R., Kaplan, A., Soden, B. J., Thorne, P. W., Wild, M., Zhai, P. M. (2013) Observations: atmosphere and surface. In: *Climate Change 2013: The Physical Science Basis. Contribution of Working Group I to the Fifth Assessment Report of the Intergovernmental Panel on Climate Change*. Ed. by Stocker, T. F., Qin, D., Plattner, G.-K., Tignor, M., Allen, S. K., Boschung, J., Nauels, A., Xia, Y., Bex, V., Midgley, P.M. Cambridge, Cambridge University Press. pp. 159-254.

Heintzenberg, J. (1980) Particle size distribution and optical properties of Arctic haze. *Tellus, 32,* 251-260. doi: 10.3402/tellusa.v32i3.10580

Helmig, D., Rossabi, S., Hueber, J., Tans, P., Montzka, S. A., Masarie, K., Thoning, K., Plass-Duelmer, C., Claude, A., Carpenter, L. J., Lewis, A. C., Punjabi, S., Reimann, S., Vollmer, M. K., Steinbrecher, R., Hannigan, J. W., Emmons, L. K., Mahieu, E., Franco, B., Smale, D., Pozzer, A. (2016) Reversal of global atmospheric ethane and propane trends largely due to US oil and natural gas production. *Nature Geosci., 9,* 490-495. doi:10.1038/ngeo2721.

Hewitt, C. Nicholas (ed.) (1999) Reactive Hydrocarbons in the Atmosphere. San Diego, CA, Academic Press. p. 313.

Hodnebrog, Ø., M. Etminan J. S. Fuglestvedt G. Marston G. Myhre C. J. Nielsen K. P. Shine T. J. Wallington Global warming potentials and radiative efficiencies of halocarbons and related compounds: A comprehensive review, (2013) *Reviews of Geophysics*, *51,* 300-378. doi./10.1002/rog.20013

Hossaini, R., Chipperfield, M. P., Montzka, S. A., Leeson, A. A., Dhomse, S. and Pyle, J. A (2017) The increasing threat to stratospheric ozone from dichloromethane. *Nat. Commun., 8,* 15962, doi:10.1038/ncomms15962.

IPCC, 2021: Summary for Policymakers. In: Climate Change 2021: The Physical Science Basis. Contribution of Working Group I to the Sixth Assessment Report of the Intergovernmental Panel

on Climate Change [Masson-Delmotte, V., P. Zhai, A. Pirani, S. L. Connors, C. Péan, S. Berger, N. Caud, Y. Chen, L. Goldfarb, M. I. Gomis, M. Huang, K. Leitzell, E. Lonnoy, J.B.R. Matthews, T. K. Maycock, T. Waterfield, O. Yelekçi, R. Yu and B. Zhou (eds.)]. Cambridge University Press. In Press.

Isaksen, I. S. A., Hov, Ø. (1987) Calculation of trends in the tropospheric concentration of O_3, OH, CO, CH_4 and NO_x. *Tellus*, *39B*, 271-285.

Jackson, R.B., Saunois, M., Bousquet, P., Canadell, J.G., Poulter, B., Stavert, A.R., Bergamaschi, P., Niwa,Y., Segers, A., and Tsuruta, A. (2020) *Environ. Res. Lett., 15,* 071002. doi:10.1088/1748-9326/ab9ed2

Laj, P., Bigi, A., Rose, C. Andrews, E. Lund Myhre, C. Collaud Coen, M. Lin, Y. Wiedensohler, A. Schulz, M. Ogren, J. A. Fiebig, M. Gliß, J. Mortier, A. Pandolfi, M. Petäja, T. Kim, S.-W. Aas, W. Putaud, J.-P. Mayol-Bracero, O. Keywood, M., Labrador, L. Aalto, P. Ahlberg, E. Alados Arboledas, L. Alastuey, A. Andrade, M. Artíñano, B. Ausmeel, S. Arsov, T. Asmi, E. Backman, J. Baltensperger, U., Bastian, S., Bath, O., Beukes, J. P., Brem, B. T., Bukowiecki, N., Conil, S., Couret, C., Day, D., Dayantolis, W., Degorska, A., Eleftheriadis, K., Fetfatzis, P., Favez, O., Flentje, H., Gini, M. I., Gregorič, A., Gysel-Beer, M., Hallar, A. G., Hand, J., Hoffer, A., Hueglin, C., Hooda, R. K., Hyvärinen, A., Kalapov, I., Kalivitis, N., Kasper-Giebl, A., Kim, J. E., Kouvarakis, G., Kranjc, I., Krejci, R., Kulmala, M., Labuschagne, C., Lee, H.-J., Lihavainen, H., Lin, N.-H., Löschau, G., Luoma, K., Marinoni, A., Martins Dos Santos, S., Meinhardt, F., Merkel, M., Metzger, J.-M., Mihalopoulos, N., Nguyen, N. A., Ondracek, J., Pérez, N., Perrone, M. R., Petit, J.-E., Picard, D., Pichon, J.-M., Pont, V., Prats, N., Prenni, A., Reisen, F., Romano, S., Sellegri, K., Sharma, S., Schauer, G., Sheridan, P., Sherman, J. P., Schütze, M., Schwerin, A., Sohmer, R., Sorribas, M., Steinbacher, M., Sun, J., Titos, G., Toczko, B., Tuch, T., Tulet, P., Tunved, P., Vakkari, V., Velarde, F., Velasquez, P., Villani, P., Vratolis, S., Wang, S.-H., Weinhold, K., Weller, R., Yela, M., Yus-Diez, J., Zdimal, V., Zieger, P., and Zikova, N. (2020) A global analysis of climate-relevant aerosol properties retrieved from the network of Global Atmosphere Watch (GAW) near-surface observatories. *Atmos. Meas Tech., 13*, 4353-4392, doi: 10.5194/amt-13-4353-2020.

Lan, X., Tans, P., Hall, B. D., Dutton, G., Mühle, J., Elkins, J. W., Vimont, I., 2021: Long-lived greenhouse gases [in "State of the Climate in 2020"]. Bull. Amer. Meteor., 102 (8), S53–S87, https://doi.org/10.1175/BAMS-D-21-0098.1.

Montzka, S. A., Dutton, G. S., Yu, P., Ray, E., Portmann, R. W., Daniel, J. S., Kuijpers, L., Hall, B. D., Mondeel, D., Siso, Nance, J. D., Rigby, M., Manning, A. J., Hu, L., Moore, F., Miller, B. R., Elkins, J. W. (2018) An unexpected and persistent increase in global emissions of ozone-depleting CFC-11. *Nature, 557,* 413-417.

Mortier, A., Gliss, J., Schulz, M., Aas, W., Andrews, E., Bian, H., Chin, M., Ginoux, P., Hand, J., Holben, B., Hua, Z., Kipling, Z., Kirkevåg, A., Laj, P., Lurton, T., Myhre, G., Neubauer, D., Olivié, D., von Salzen, K., Takemura, T. and Tilmes, S. (2020) Evaluation of climate model aerosol trends with ground-based observations over the last two decades -- an AeroCom and CMIP6 analysis. *Atmos. Chem. Phys*. doi: 10.5194/acp-2019-1203.

Moskvitch, K. Mysterious Siberian crater attributed to methane. Nature (2014). https://doi.org/10.1038/nature.2014.15649

Myhre, C. L., Hermansen, O., Fiebig, M., Lunder, C., Fjæraa, A. M., Svendby, T., Platt, M., Hansen. G., Schmidbauer, N., Krognes, T. (2016) Monitoring of greenhouse gases and aerosols at Svalbard and Birkenes in 2015 - Annual report. Kjeller, NILU (Miljødirektoratet rapport, M-694/2016) (NILU report, 31/2016).

Myhre, C. L., Ferré, B., Platt, S. M., Silyakova, A., Hermansen, O., Allen, G., Pisso, I., Schmidbauer, N., Stohl, A., Pitt, J., Jansson, P., Greinert, J., Percival, C., Fjaeraa, A. M., O'Shea, S., Gallagher, M., Le Breton, M., Bower, K., Bauguitte, S., Dalsøren, S., Vadakkepuliyambatta, S., Fisher, R., Nisbet, E., Lowry, D., Myhre, G., Pyle, J., Cain, M., Mienert, J. (2016) Large methane release from the Arctic

seabed west of Svalbard, but small release to the atmosphere. *Geophys. Res. Lett*., *43,* 4624–4631. doi:10.1002/2016GL068999.

Myhre, G., Myhre C. L., Forster, P. M., Shine, K. P. (2017) Halfway to doubling of CO2 radiative forcing. *Nature Geosci., 10,* 710--711. doi:10.1038/ngeo3036.

Myhre, G., Myhre, C. L., Samset, B. H., Storelvmo, T. (2013a) Aerosols and their relation to global climate and climate sensitivity. *Nature Education Knowledge, 4,* 5,7. URL: http://www.nature.com/scitable/knowledge/library/aerosols-and-their-relation-to-global-climate-102215345

Myhre, G., Shindell, D., Bréon, F.-M., Collins, W., Fuglestvedt, J., Huang, J., Koch, D., Lamarque, J.-F., Lee, D., Mendoza, B., Nakajima, T., Robock, A., Stephens, G., Takemura, T., Zhang, H. (2013b) Anthropogenic and natural radiative forcing. In: *Climate Change 2013: The Physical Science Basis. Contribution of Working Group I to the Fifth Assessment Report of the Intergovernmental Panel on Climate Change*. Ed. by Stocker, T.F., Qin, D., Plattner, G.-K., Tignor, M., Allen, S.K., Boschung, J., Nauels, A., Xia, Y., Bex, V., Midgley, P.M. Cambridge, Cambridge University Press. pp. 659-740.

Mühle, J., Trudinger, C. M., Western, L. M., Rigby, M., Vollmer, M. K., Park, S., Manning, A. J., Say, D., Ganesan, A., Steele, L. P., Ivy, D. J., Arnold, T., Li, S., Stohl, A., Harth, C. M., Salameh, P. K., McCulloch, A., O'Doherty, S., Park, M.-K., Jo, C. O., Young, D., Stanley, K. M., Krummel, P. B., Mitrevski, B., Hermansen, O., Lunder, C., Evangeliou, N., Yao, B., Kim, J., Hmiel, B., Buizert, C., Petrenko, V. V., Arduini, J., Maione, M., Etheridge, D. M., Michalopoulou, E., Czerniak, M., Severinghaus, J. P., Reimann, S., Simmonds, P. G., Fraser, P. J., Prinn, R. G., and Weiss, R. F.: Perfluorocyclobutane (PFC-318, c-C4F8) in the global atmosphere, Atmos. Chem. Phys., 19, 10335–10359, https://doi.org/10.5194/acp-19-10335-2019, 2019.

Naik, V., S. Szopa, B. Adhikary, P. Artaxo, T. Berntsen, W. D. Collins, S. Fuzzi, L. Gallardo, A. Kiendler Scharr, Z. Klimont, H. Liao, N. Unger, P. Zanis, 2021, Short-Lived Climate Forcers. In: Climate Change 2021: The Physical Science Basis. Contribution of Working Group I to the Sixth Assessment Report of the Intergovernmental Panel on Climate Change [Masson-Delmotte, V., P. Zhai, A. Pirani, S. L. Connors, C. Péan, S. Berger, N. Caud, Y. Chen, L. Goldfarb, M. I. Gomis, M. Huang, K. Leitzell, E. Lonnoy, J. B. R. Matthews, T. K. Maycock, T. Waterfield, O. Yelekçi, R. Yu and B. Zhou (eds.)]. Cambridge University Press. In Press.

Ng, N. L., Kroll, J.H., Chan, A. W. H., Chhabra, P. S., Flagan, R. C., Seinfeld, J. H. (2007) Secondary organic aerosol formation from m-xylene, toluene, and benzene. *Atmos. Chem. Physics, 7,* 3909–3922.

Nicewonger, M. R., Verhulst, K. R., Aydin, M., Saltzman, E. S. (2016) Preindustrial atmospheric ethane levels inferred from polar ice cores: A constraint on the geologic sources of atmospheric ethane and methane. *Geophys. Res. Lett., 43,* 214-221. doi:10.1002/2015GL066854.

Oram, D. E., Mani, F. S., Laube, J. C., Newland, M. J., Reeves, C. E., Sturges, W. T., Penkett, S. A., Brenninkmeijer, C. A. M., Röckmann, T., and Fraser, P. J. (2012) Long-term tropospheric trend of octafluorocyclobutane (c-C_4F_8 or PFC-318), *Atmos. Chem. Phys., 12,* 261-269. doi:10.5194/acp-12-261-2012.

Pandolfi, M. et al., 2018: A European aerosol phenomenology – 6: scattering properties of atmospheric aerosol particles from 28 ACTRIS sites. Atmospheric Chemistry and Physics, 18(11), 7877–7911, doi:10.5194/acp-18-7877-2018.

Park, S., Western, L. M., Saito, T., Redington, A., Henne, S., Fang, X., Prinn, R. G., Manning, A. J., Montzka, S. A., Fraser, P. J., Ganesan, A. L., Harth, C. M., Kim, J., Krummel, P. B., Liang, Q., Mühle, J., O'Doherty, S., Park, H., Park, M-K., Reimann, S., Salameh, P. K., Weiss, R. F., Rigby, M. (2021) A decline in emissions of CFC-11 and related chemicals from eastern China. Nature, 590(7846), 433-437. https://doi.org/10.1038/s41586-021-03277-w

Platt, S. M., Eckhardt, S., Ferré, B., Fisher, R. E., Hermansen, O., Jansson, P., Lowry, D., Nisbet, E. G., Pisso, I., Schmidbauer, N., Silyakova, A., Stohl, A., Svendby, T. M., Vadakkepuliyambatta, S., Mienert, J., and Lund Myhre, C. (2018) Methane at Svalbard and over the European Arctic Ocean. *Atmos. Chem. Phys., 18,* 17207--17224. 10.5194/acp-18-17207-2018

Platt, S. M., Hov, Ø., Berg, T., Breivik, K., Eckhardt, S., Eleftheriadis, K., Evangeliou, N., Fiebig, M., Fisher, R., Hansen, G., Hansson, H.-C., Heintzenberg, J., Hermansen, O., Heslin-Rees, D., Holmén, K., Hudson, S., Kallenborn, R., Krejci, R., Krognes, T., Larssen, S., Lowry, D., Lund Myhre, C., Lunder, C., Nisbet, E., Nizetto, P. B., Park, K.-T., Pedersen, C. A., Aspmo Pfaffhuber, K., Röckmann, T., Schmidbauer, N., Solberg, S., Stohl, A., Ström, J., Svendby, T., Tunved, P., Tørnkvist, K., van der Veen, C., Vratolis, S., Yoon, Y. J., Yttri, K. E., Zieger, P., Aas, W., and Tørseth, K.: Atmospheric composition in the European Arctic and 30 years of the Zeppelin Observatory, Ny-Ålesund, Atmos. Chem. Phys. Discuss. [preprint], https://doi.org/10.5194/acp-2021-505, in review, 2021.

Prather, M., Ehhalt, D., Dentener, F., Derwent, R. G., Dlugokencky, E., Holland, E., Isaksen, I. S. A., Katima, J., Kirchhoff, V., Matson, P., Midgley, P. M., Wang, M. (2001) Atmospheric chemistry and greenhouse gases. In: *Climate Change 2001: The Scientific Basis, Contribution of Working Group I to the Third Assessment Report of the Intergovernmental Panel on Climate Change.* Ed. by: Houghton, J. T., Ding, Y., Griggs, D. J., Noguer, M., van der Linden, P. J., Dai, X., Maskell, K., Johnson, C. A. Cambridge, Cambridge University Press. pp. 239-287.

Pisso, I., Myhre, C. L., Platt, S. M., Eckhardt, S., Hermansen, O., Schmidbauer, N., Mienert, J., Vadakkepuliyambatta, S., Bauguitte, S., Pitt, J., Allen, G., Bower, K.N., O'Shea, S., Gallagher, M. W., Percival, C.J., Pyle, J., Cain, M., Stohl, A. (2016) Constraints on oceanic methane emissions west of Svalbard from atmospheric in situ measurements and Lagrangian transport modelling. *J. Geophys. Res., 121,* 14188-14200. doi:10.1002/2016JD025590.

Putaud, J.-P. et al., 2010: A European aerosol phenomenology – 3: Physical and chemical characteristics of particulate matter from 60 rural, urban, and kerbside sites across Europe. Atmospheric Environment, 44(10), 1308–1320, doi:10.1016/j.atmosenv.2009.12.011.

R Core Team (2018) R: A language and environment for statistical computing. Vienna, Austria, R Foundation for Statistical Computing. URL: https://www.R-project.org/.

Ramonet, M. , P. Ciais, F. Apadula, J. Bartyzal, Bartyzel, , A. Bastos, , P. Bergamaschi, P.E. Blanc, D. Brunner, L. C. di Torchiarolo, F. Calzolari, H. Chen, L. Chmura, A. Colomb, S. Conil, P. Cristofanelli, E. Cuevas, R. Curcoll, M. Delmotte1, A. di Sarra, L. Emmenegger, G. Forster, A. Frumau, C. Gerbig, F. Gheusi, S. Hammer, L. Haszpra12, J. Hatakka, L. Hazan, M. Heliasz, S. Henne, A. Hensen, O. Hermansen, P. Keronen, R.Kivi, K. Komínková, D. Kubistin, O. Laurent, T. Laurila, J.V. Lavric, I. Lehner, K.E.J. Lehtinen, A. Leskinen, M. Leuenberger, I. Levin, M. Lindauer, M. Lopez, C. LundMyhre, I. Mammarella, G. Manca, A. Manning, M.V. Marek, P. Marklund, D. Martin, F. Meinhardt, N. Mihalopoulos, M. Mölder, J.A. Morgui, J. Necki, S. O'Doherty, C. O'Dowd, M. Ottosson, C. Philippon, S. Piacentino, J.M. Pichon, C. Plass-Duelmer, A. Resovsky, L.Rivier, X. Rodó, M.K. Sha, H.A. Scheeren, D. Sferlazzo, T.G. Spain, K.M. Stanley, M. Steinbacher, P. Trisolino, A. Vermeulen, G. Vítková, D. Weyrauch, I. Xueref-Remy, K. Yala, C. Yver Kwok. The fingerprint of the summer 2018 drought in Europe on ground-based atmospheric CO2 measurements. *Phil.l Trans. R. Soc. B, 375,* 20190513. doi:10.1098/rstb.2019.0513

Repo, M. E., Susiluoto, S., Lind, S. E., Jokinen, S., Elsakov, V., Biasi, C., Virtanen, T., Pertti, J., Martikainen, P. J. (2009) Large N_2O emissions from cryoturbated peat soil in tundra. *Nature Geosci., 2*, 189-192. doi: 10.1038/ngeo434.

Rigby, M., Park, S., Saito, T., Western, L. M., Redington, A. L., Fang, X. , Henne, S., Manning, A. J., Prinn, R. G., Dutton, G. S., Fraser, P. J., Ganesan, A. L., Hall, B. D., Harth, C. M., Kim, J., Kim, K.-R., Krummel, P. B., Lee, T., Li, S., Liang, Q., Lunt, M. F., Montzka, S. A., Mühle, J., O'Doherty, S., Park, M.-K., Reimann, S., Salameh, P. K., Simmonds, P., Tunnicliffe, R. L., Weiss, R. F., Yokouchi, Y. ,

Young, D. (2019) Increase in CFC-11 emissions from eastern China based on atmospheric observations. *Nature*, *569*, 546-550. doi: 10.1038/s41586-019-1193-4 .

Saunois, M., Stavert, A. R., Poulter, B., Bousquet, P., Canadell, J. G., Jackson, R. B., Raymond, P. A., Dlugokencky, E. J., Houweling, S., Patra, P. K., Ciais, P., Arora, V. K., Bastviken, D., Bergamaschi, P., Blake, D. R., Brailsford, G., Bruhwiler, L., Carlson, K. M., Carrol, M., Castaldi, S., Chandra, N., Crevoisier, C., Crill, P. M., Covey, K., Curry, C. L., Etiope, G., Frankenberg, C., Gedney, N., Hegglin, M. I., Höglund-Isaksson, L., Hugelius, G., Ishizawa, M., Ito, A., Janssens-Maenhout, G., Jensen, K. M., Joos, F., Kleinen, T., Krummel, P. B., Langenfelds, R. L., Laruelle, G. G., Liu, L., Machida, T., Maksyutov, S., McDonald, K. C., McNorton, J., Miller, P. A., Melton, J. R., Morino, I., Müller, J., Murguia-Flores, F., Naik, V., Niwa, Y., Noce, S., O'Doherty, S., Parker, R. J., Peng, C., Peng, S., Peters, G. P., Prigent, C., Prinn, R., Ramonet, M., Regnier, P., Riley, W. J., Rosentreter, J. A., Segers, A., Simpson, I. J., Shi, H., Smith, S. J., Steele, L. P., Thornton, B. F., Tian, H., Tohjima, Y., Tubiello, F. N., Tsuruta, A., Viovy, N., Voulgarakis, A., Weber, T. S., van Weele, M., van der Werf, G. R., Weiss, R. F., Worthy, D., Wunch, D., Yin, Y., Yoshida, Y., Zhang, W., Zhang, Z., Zhao, Y., Zheng, B., Zhu, Q., Zhu, Q., and Zhuang, Q. (2020), The Global Methane Budget 2000–2017. *Earth Syst. Sci. Data, 12,* 1561-1623. doi:10.5194/essd-12-1561-2020.

Simmonds, P. G., Manning, A. J., Cunnold, D. M., Fraser, P. J., McCulloch, A., O'Doherty, S., Krummel, P. B., Wang, R. H. J., Porter, L. W., Derwent, R. G., Greally, B., Salameh, P., Miller, B. R., Prinn, R. G., Weiss, R. F. (2006) Observations of dichloromethane, trichloroethene and tetrachloroethene from the AGAGE stations at Cape Grim, Tasmania, and Mace Head, Ireland. J. Geophys. Res., 111, D18304. doi:10.1029/2006JD007082.

Stohl, A., Klimont, Z., Eckhardt, S., Kupiainen, K., Shevchenko, V. P., Kopeikin, V. M., and Novigatsky, A. N.: Black carbon in the Arctic: the underestimated role of gas flaring and residential combustion emissions, Atmos. Chem. Phys., 13, 8833–8855, https://doi.org/10.5194/acp-13-8833-2013, 2013.

Svendby, T.M., Hansen, G.H., Bäcklund, A., Nilsen, A.C., Schulze, D., Johnsen, B. (2021). Monitoring of the atmospheric ozone layer and natural ultraviolet radiation. Annual Report 2020. (NILU report 18/2021; Norwegian Environment Agency, M-2091|2021). Kjeller: NILU.

Thompson R.L. G. Broquet, C. Gerbig, T. Koch, M. Lang, G. Monteil, S. Munassar, A. Nickless, M. Scholze, M. Ramonet, U. Karstens, E. van Schaik, Z. Wu and C. Rödenbeck, (2020) Changes in net ecosystem exchange over Europe during the 2018 drought based on atmospheric observations. *Phil. Trans. R. Soc*. *B, 375,* 20190512. doi:10.1098/rstb.2019.0512

Thompson, R. L., Sasakawa, M., Machida, T., Aalto, T., Worthy, D., Lavric, J. V., Myhre, C. L., Stohl, A. (2017) Methane fluxes in the high northern latitudes for 2005–2013 estimated using a Bayesian atmospheric inversion. *Atmos. Chem. Phys.*, 17, 3553-3572. doi:10.5194/acp-2016-660.

Thompson, R. L., Dlugockenky, E., Chevallier, F., Ciais, P., Dutton, G., Elkins, J. W., Langenfelds, R. L., Prinn, R. G., Weiss, R. F., Tohjima, Y., Krummel, P. B., Fraser, P., Steele, L. P. (2013) Interannual variability in tropospheric nitrous oxide. *Geophys. Res. Lett, 40*, 4426-4431. doi:10.1002/grl.50721.

Tørseth, K., Aas, W., Breivik, K., Fjæraa, A. M., Fiebig, M., Hjellbrekke, A. G., Myhre, C. L., Solberg, S., Yttri, K. E. (2012) Introduction to the European Monitoring and Evaluation Programme (EMEP) and observed atmospheric composition change during 1972–200. *Atmos. Chem. Phys., 12,* 5447-5481. doi:10.5194/acp-12-5447-2012.

Umezawa, T., Baker, A. K., Oram, D., Sauvage, C., O'Sullivan, D., Rauthe-Schöch, A., Montzka, S. A., Zahn, A., Brenninkmeijer, C. A. M. (2014) Chloromethane in the upper troposphere observed by the CARIBIC passenger aircraft bservatory: Large-scale distributions and Asian summer monsoon outflow. *J. Geophys. Res. Atmos., 119,* 5542-5558, doi:10.1002/2013JD021396.

Vollmer, M. K., Young, D., Trudinger, C. M., Muhle, J., Henne, S., Rigby, M., Park, S., Li, S., Guillevic, M., Mitrevski, B., Harth, C. M., Miller, B. R., Reimann, S., Yao, B., Steele, L. P., Wyss, S. A., Lunder,

C. R., Arduini, J., McCulloch, A., Wu, S., Rhee, T. S., Wang, R. H. J., Salameh, P. K., Hermansen, O., Hill, M., Langenfelds, R. L., Ivy, D., O'Doherty, S., Krummel, P. B., Maione, M., Etheridge, D. M., Zhou, L., Fraser, P. J., Prinn, R. G.; Weiss, R. F., Simmonds, P. G. (2018) Atmospheric histories and emissions of chlorofluorocarbons CFC-13 (CClF3), ΣCFC-114 (C2Cl2F4), and CFC-115 (C2ClF5). *Atmos. Chem. Phys.*, *18*, 979-1002, doi:10.5194/acp-18-979-2018

Wiedensohler, A., Birmili, W., Nowak, A., Sonntag, A., Weinhold, K., Merkel, M., Wehner, B., Tuch, T., Pfeifer, S., Fiebig, M., Fjäraa, A. M., Asmi, E., Sellegri, K., Depuy, R., Venzac, H., Villani, P., Laj, P., Aalto, P., Ogren, J. A., Swietlicki, E., Williams, P., Roldin, P., Quincey, P., Hüglin, C., Fierz-Schmidhauser, R., Gysel, M., Weingartner, E., Riccobono, F., Santos, S., Grüning, C., Faloon, F., Beddows, D., Harrison, R., Monahan, C., Jennings, S. G., O'Dowd, C. D., Marinoni, A., Horn, H.-G., Keck, L., Jiang, J., Scheckman, J., McMurry, P.H., Deng, Z., Zhao, C. S., Moerman, M., Henzing, B., de Leeuw, G., Löschau, G., Bastian, S. (2012) Mobility particle size spectrometers: harmonization of technical standards and data structure to facilitate high quality long-term observations of atmospheric particle number size distributions. *Atmos. Meas. Tech.*, *5,* 657-685. doi:10.5194/amt-5-657-2012.

Wilkinson, M. D., Dumontier, M., Aalbersberg, I. J., Appleton, G., Axton, M., Baak, A., Blomberg, N., Boiten, J. W., Santos, L. B. D., Bourne, P. E., Bouwman, J., Brookes, A. J., Clark, T., Crosas, M., Dillo, I., Dumon, O., Edmunds, S., Evelo, C. T., Finkers, R., Gonzalez-Beltran, A., Gray, A. J. G., Groth, P., Goble, C., Grethe, J. S., Heringa, J., Hoen, P. A. C., Hooft, R., Kuhn, T., Kok, R., Kok, J., Lusher, S. J., Martone, M. E., Mons, A., Packer, A. L., Persson, B., Rocca-Serra, P., Roos, M., van Schaik, R., Sansone, S. A., Schultes, E., Sengstag, T., Slater, T., Strawn, G., Swertz, M. A., Thompson, M., van der Lei, J., van Mulligen, E., Velterop, J., Waagmeester, A., Wittenburg, P., Wolstencroft, K., Zhao, J., and Mons, B. (2016)The FAIR Guiding Principles for scientific data management and stewardship*. Sci. Data, 3,* 160018.doi: /10.1038/sdata.2016.18.

WMO (2020) Greenhouse Gas Bulletin. The state of greenhouse gases in the atmosphere using global observations through 2019. Geneva, World Meteorological Organization (GHG Bulletin No. 16, 23 November 2020). URL: https://library.wmo.int/doc_num.php?explnum_id=10437

WMO (2019) Greenhouse Gas Bulletin. The state of greenhouse gases in the atmosphere using global observations through 2018. Geneva, World Meteorological Organization (GHG Bulletin No. 15, 25 November 2019). URL: https://library.wmo.int/index.php?lvl=notice_display&id=21620#.X1i3NN7VI2w

WMO (2018) Scientific assessment of ozone depletion: 2018. Geneva, World Meteorological Organization (Global Ozone Research and Monitoring Project-Report No. 58). URL: https://www.esrl.noaa.gov/csd/assessments/ozone/2018/

WMO (2017) Greenhouse Gas Bulletin. The state of greenhouse gases in the atmosphere using global observations through 2016. Geneva, World Meteorological Organization (GHG Bulletin No. 13, 30 October 2017). URL: https://library.wmo.int/opac/doc_num.php?explnum_id=4022

WMO (2016) Greenhouse Gas Bulletin. The state of greenhouse gases in the atmosphere using global observations through 2015. Geneva, World Meteorological Organization (GHG Bulletin No. 12, 24 October 2016). URL: http://library.wmo.int/pmb_ged/ghg-bulletin_12_en.pdf

WMO (2015) Greenhouse Gas Bulletin. The state of greenhouse gases in the atmosphere using global observations through 2014. Geneva, World Meteorological Organization (GHG Bulletin No. 11, 9 November 2015). URL: http://library.wmo.int/pmb_ged/ghg-bulletin_11_en.pdf

WMO (2014) Greenhouse Gas Bulletin. The state of greenhouse gases in the atmosphere using global observations through 2013. Geneva, World Meteorological Organization (GHG Bulletin No. 10, 9th September 2014). URL: http://library.wmo.int/opac/index.php?lvl=notice_display&id=16396#.VGHPz5-gQtK

WMO (2014b) Scientific assessment of ozone depletion: 2014. Geneva, World Meteorological Organization (Global ozone research and monitoring project, Report No. 55). **URL:** https://www.esrl.noaa.gov/csd/assessments/ozone/2014/chapters/2014OzoneAssessment.pdf

WMO (2013) Greenhouse Gas Bulletin. The state of greenhouse gases in the atmosphere using global observations through 2012. Geneva, World Meteorological Organization (GHG Bulletin No. 9, 6 November 2013). URL: http://www.wmo.int/pages/prog/arep/gaw/ghg/documents/GHG_Bulletin_No.9_en.pdf

WMO (2012) Greenhouse Gas Bulletin. The state of greenhouse gases in the atmosphere using global observations through 2011. Geneva, World Meteorological Organization (GHG Bulletin No. 8, 19 November 2012). URL: http://www.wmo.int/pages/prog/arep/gaw/ghg/documents/GHG_Bulletin_No.8_en.pdf

WMO (2011) Scientific assessment of ozone depletion: 2010. Geneva, World Meteorological Organization (Global ozone research and monitoring project, Report No. 52).

Xu, Y., Zaelke, D., Velders, G.J.M., Ramanathan, V. (2013) The role of HFCs in mitigating 21st century climate change. *Atmos. Chem. Phys., 13,* 6083-6089. doi:10.5194/acp-13-6083-2013.

Zanatta, M. et al., 2016: A European aerosol phenomenology-5: Climatology of black carbon optical properties at 9 regional background sites across Europe. Atmospheric Environment, 145, 346–364, doi:10.1016/j.atmosenv.2016.09.035.

Zeileis A. (2004) Econometric Computing with HC and HAC Covariance Matrix Estimators. *J. Stat. Software*, *11,* 1-17. doi: 10.18637/jss.v011.i10.

Zeileis, A. (2006) Object-oriented computation of sandwich estimators. *J. Stat. Software*, *16,* 1-16. doi:10.18637/jss.v016.i09.

Appendix I

Data Tables

Table A 1: Annual mean concentration for all greenhouse gases included in the programme at Zeppelin and Birkenes. All concentrations are mixing ratios in ppt, except for methane and carbon monoxide (ppb) and carbon dioxide (ppm). The annual means are based on a combination of the measurements and the fitted values; during periods with lacking observations we have used the fitted mixing ratios in the calculation of the annual mean. All underlying measurement data are open and accessible and can be downloaded directly from the database: http://ebas.nilu.no/

Component	2001	2002	2003	2004	2005	2006	2007	2008	2009	2010	2011	2012	2013	2014	2015	2016	2017	2018	2019	2020
Carbon dioxide - Zeppelin												394.8	397.4	399.6	401.4	404.4	408.0	409.3	411.9	414.2
Carbon dioxide - Birkenes									391.5	394.0	396.6	397.9	400.7	402.8	405.2	409.8	411.2	415.2	416.1	418.8
Methane - Zeppelin	1844.0	1842.9	1855.5	1852.9	1852.2	1853.3	1863.4	1873.3	1888.7	1881.2	1880.0	1892.0	1898.1	1910.0	1920.2	1931.8	1938.9	1938.5	1953.0	1968.7
Methane - Birkenes									1880.5	1887.1	1895.6	1900.5	1902.6	1917.3	1926.1	1941.9	1945.3	1953.0	1961.2	1975.2
Carbon monoxide	129.7	126.1	140.2	130.5	128.6	126.3	120.2	120.1	117.9	128.9	115.8	120.7	113.1	113.4	112.9	112.4	114.3	113.6	115.5	120.3
Nitrous oxide										323.6	324.2	325.1	326.1	327.2	328.0	329.0	330.0	331.3	332.1	333.4
Chlorofluorocarbons																				
CFC-11	259.1	257.2	255.0	253.4	251.1	249.3	246.6	244.7	242.7	240.8	238.5	237.1	235.5	234.1	232.6	231.3	230.1	229.2	227.7	225.5
CFC-12	547.3	547.5	547.6	545.7	546.8	546.2	542.3	541.5	537.7	534.5	531.6	528.8	525.8	522.4	519.0	516.0	512.4	509.1	505.7	501.9
CFC-113	81.5	80.8	80.0	79.4	78.8	77.9	77.4	76.8	76.2	75.5	74.7	74.1	73.5	73.0	72.3	71.7	71.1	70.6	70.0	69.5
CFC-115	8.22	8.18	8.22	8.28	8.41	8.39	8.38	8.40	8.43	8.42	8.42	8.44	8.43	8.45	8.51	8.53	8.59	8.66	8.74	8.77
Hydrochlorofluorocarbons																				
HCFC-22	158.6	164.2	170.7	175.7	181.4	189.1	196.3	204.6	212.5	219.7	225.9	231.1	236.5	241.2	245.4	248.8	252.2	254.1	256.0	257.1
HCFC-141b	16.8	17.9	18.7	19.2	19.5	19.9	20.5	21.2	21.6	22.2	23.1	24.0	24.7	25.4	25.6	25.9	25.8	25.6	25.8	26.1
HCFC-142b	14.3	15.0	15.9	16.6	17.3	18.2	19.3	20.3	21.3	22.0	22.7	23.0	23.2	23.4	23.5	23.5	23.5	23.3	23.1	22.8
Hydrofluorocarbons																				
HFC-125	2.2	2.6	2.9	3.3	4.0	4.9	5.8	6.9	8.0	9.6	11.8	13.5	15.6	17.9	20.3	22.9	25.8	28.9	32.3	35.6
HFC-134a	21.0	26.0	30.7	35.4	39.9	44.1	48.6	53.5	57.8	63.6	68.6	73.6	78.9	84.5	90.1	96.5	103.1	108.5	114.7	120.2
HFC-152a	2.6	3.4	4.3	5.1	5.8	6.8	7.8	8.6	9.0	9.5	10.0	10.2	10.2	10.2	10.1	10.3	10.3	10.3	10.6	10.5
HFC-23										23.6	24.7	25.6	26.7	27.7	28.7	29.6	30.7	31.9	33.2	34.5
HFC-365mfc										0.74	0.79	0.87	0.92	1.02	1.10	1.19	1.24	1.29	1.32	1.32

Component	2001	2002	2003	2004	2005	2006	2007	2008	2009	2010	2011	2012	2013	2014	2015	2016	2017	2018	2019	2020
HFC-227ea										0.71	0.79	0.88	0.99	1.10	1.21	1.34	1.47	1.59	1.75	1.90
HFC-236fa										0.09	0.10	0.11	0.13	0.14	0.15	0.16	0.17	0.19	0.21	0.22
HFC-245fa										1.61	1.80	1.98	2.19	2.39	2.58	2.80	3.04	3.26	3.53	3.73
HFC-32										5.70	6.57	7.67	9.28	10.92	12.87	15.22	18.26	21.54	25.22	28.73
HFC-4310mee										0.21	0.22	0.24	0.25	0.26	0.27	0.28	0.29	0.29	0.30	0.31
HFC-143a										11.95	13.18	14.56	16.03	17.63	19.10	20.75	22.51	23.93	25.57	27.08
Perfluorinated compounds																				
PFC-14															82.43	83.30	84.28	85.26	86.12	86.91
PFC-116										4.12	4.20	4.27	4.37	4.45	4.55	4.64	4.74	4.82	4.91	4.99
PFC-218										0.56	0.57	0.59	0.60	0.61	0.63	0.64	0.66	0.67	0.69	0.71
PFC-318										1.29	1.33	1.38	1.43	1.47	1.53	1.59	1.66	1.73	1.80	1.87
Sulphurhexafluoride	4.96	5.14	5.37	5.61	5.82	6.09	6.31	6.64	6.93	7.19	7.50	7.79	8.11	8.43	8.75	9.09	9.46	9.80	10.14	10.44
Nitrogen trifluoride																1.61	1.76	1.98	2.21	2.48
Sulfuryl fluoride										1.72	1.81	1.91	2.03	2.12	2.22	2.33	2.45	2.53	2.63	2.74
Halons																				
H-1211	4.39	4.43	4.48	4.53	4.52	4.48	4.43	4.39	4.33	4.26	4.18	4.09	3.97	3.87	3.77	3.65	3.55	3.45	3.37	3.27
H-1301	2.99	3.07	3.13	3.17	3.21	3.22	3.24	3.28	3.29	3.32	3.33	3.35	3.36	3.37	3.39	3.38	3.39	3.38	3.39	3.39
H-2402										0.47	0.46	0.45	0.44	0.43	0.43	0.42	0.41	0.41	0.41	0.40
Other halocarbons																				
Chloromethane	506.7	521.2	526.4	522.6	519.1	520.7	523.1	525.1	526.3	520.7	509.6	515.4	519.2	514.4	512.6	521.5	516.7	514.2	507.7	508.6
Bromomethane	9.10	9.12	8.88	8.87	8.54	8.58	8.32	7.77	7.37	7.29	7.20	7.05	6.98	6.87	6.67	6.73	6.55	6.54	6.73	6.71
Dichloromethane	31.64	31.54	32.36	32.20	31.91	33.36	35.38	37.51	38.58	42.18	42.13	45.19	53.69	54.41	54.10	56.63	61.23	60.63	58.82	62.46
Trichloromethane	11.17	10.70	10.67	10.32	10.33	10.41	10.59	10.42	10.87	11.53	11.99	12.23	12.77	13.50	13.70	14.25	15.32	14.79	12.28	13.05
Carbon tetrachloride										86.61	85.27	84.46	83.51	82.52	81.71	80.60	79.44	78.77	78.01	77.26
Trichloroethane	37.86	31.99	27.29	22.89	19.19	15.96	13.35	11.08	9.23	7.74	6.48	5.36	4.50	3.78	3.32	2.82	2.34	2.00	1.70	1.47

Component	2001	2002	2003	2004	2005	2006	2007	2008	2009	2010	2011	2012	2013	2014	2015	2016	2017	2018	2019	2020
Trichloroethene	0.72	0.67	0.57	0.52	0.51	0.48	0.34	0.37	0.53	0.54	0.55	0.49	0.55	0.49	0.45	0.42	0.40	0.37	0.30	0.24
Tetrachloroethene	4.68	4.22	4.07	3.88	3.37	2.91	3.13	2.71	2.97	3.13	2.83	2.68	2.55	2.58	2.59	2.56	2.48	2.31	2.28	2.09
Volatile Organic Compounds (VOC)																				
Ethane										1472.2	1472.2	1583.2	1568.7	1647.2	1638.6	1581.4	1576.9	1525.2	1602.4	1512.9
Propane										485.6	527.2	569.8	580.1	573.2	545.8	565.1	583.4	497.2	453.8	337.0
Butane										178.1	187.0	200.1	204.4	193.3	181.4	167.6	193.2	143.5	140.0	119.0
Pentane										60.9	61.5	63.3	67.7	64.2	61.3	57.7	60.9	39.1	43.8	41.0
Benzene										84.4	72.7	74.3	69.5	71.4	68.3	67.5	62.3	61.9	59.7	59.2
Toluene										33.4	29.3	28.7	26.7	28.7	26.1	25.6	17.3	18.3	16.1	14.4

*Trichloroethene: Larger uncertainties in the numbers due to low concentrations, memory effects and blanks in the instrument. The reference numbers (scale UB-98) have also larger uncertainties for the same reasons.
**Tetrachloroethene: Larger uncertainties in the 2001-2010 numbers due to larger variability in the measurements with the ADS-GCMS instrument.

Table A 2: All calculated trends per year, error and regression coefficient for the fit. The trends are all in ppt per year, except for CH_4, N_2O, and CO which are in ppb and CO_2 is in ppm. The negative trends are in blue, and the positive trends are shown in red. Generally, the period is from 2001 to 2020, but for some compounds the measurements started after September 2010. For these compounds the trends are in general more uncertain.

Component	Formula	Trend /yr	Error	R^2
Carbon dioxide - Zeppelin	CO_2	2.44	0.04	0.97
Carbon dioxide - Birkenes		2.54	0.06	0.75
Methane - Zeppelin	CH_4	6.42	0.10	0.91
Methane - Birkenes		8.38	0.24	0.65
Carbon monoxide	CO	-1.06	0.21	0.79
Nitrous oxide	N_2O	0.99	0.01	0.99
Chlorofluorocarbons				
CFC-11	CCl_3F	-1.77	0.013	0.99
CFC-12	CF_2Cl_2	-2.57	0.022	0.98
CFC-113	CF2ClCFCl2	-0.63	0.002	0.99
CFC-115	CF_3CF_2Cl	0.03	0.001	0.75
Hydrochlorofluorocarbons				
HCFC-22	$CHClF_2$	5.61	0.031	0.997
HCFC-141b	$C_2H_3FCl_2$	0.51	0.018	0.972
HCFC-142b	CH_3CF_2Cl	0.50	0.011	0.985
Hydrofluorocarbons				
HFC-125	CHF_2CF_3	1.74	0.006	0.999
HFC-134a	CH_2FCF_3	5.19	0.012	0.999
HFC-152a	CH_3CHF_2	0.40	0.010	0.965
HFC-23	CHF_3	1.07	0.005	0.998
HFC-365mfc	$CH_3CF_2CH_2CF_3$	0.06	0.000	0.983
HFC-227ea	CF_3CHFCF_3	0.12	0.000	0.998
HFC-236fa	$CF_3CH_2CF_3$	0.01	0.000	0.986
HFC-245fa	$CHF_2CH_2CF_3$	0.21	0.001	0.997
HFC-32	CH_2F_2	2.31	0.010	0.998
HFC-4310mee	$C_5H_2F_{10}$	0.01	0.000	0.949
HFC-143a	CH_3CF_3	1.54	0.003	0.998
Perfluorinated compounds				
PFC-14	CF_4	0.897	0.0575	0.996
PFC-116	C_2F_6	0.089	0.0002	0.997
PFC-218	C_3F_8	0.015	0.0001	0.981
PFC-318	c-C_4F_8	0.058	0.0002	0.995
Sulphurhexafluoride	SF_6	0.294	0.0004	0.999
Nitrogen trifluoride	NF_3	0.218	0.0409	0.995
Sulfuryl fluoride	SO_2F_2	0.103	0.0008	0.993

Halons				
H-1211	$CBrClF_2$	-0.068	0.0003	0.996
H-1301	$CBrF_3$	0.018	0.0004	0.780
H-2402	$CBrF_2CBrF_2$	-0.007	0.0001	0.964
Halogenated compounds				
Chloromethane	CH_3Cl	-0.459	0.1979	0.868
Bromomethane	CH_3Br	-0.153	0.0055	0.885
Dichloromethane	CH_2Cl_2	1.914	0.0546	0.939
Trichloromethane	$CHCl_3$	0.225	0.0172	0.693
Carbon tetrachloride	CCl_4	-0.935	0.0133	0.952
Trichloroethane	CH_3CCl_3	-1.700	0.0087	0.999
Trichloroethene	$CHClCCl_2$	-0.015	0.0036	0.396
Tetrachloroethene	CCl_2CCl_2	-0.109	0.0071	0.525
Volatile Organic Compounds (VOC)				
Ethane*	C_2H_6	4.84	3.39	0.88
Propane*	C_3H_8	-11.66	2.93	0.81
Butane*	C_4H_{10}	-6.63	1.35	0.74
Pentane*	C_5H_{12}	-2.44	0.48	0.68
Benzene*	C_6H_6	-	-	-
Toluene*	$C_6H_5CH_3$	-	-	-

**Trichloroethene: Larger uncertainties in the numbers due to low concentrations, memory effects and blanks in the instrument. The reference numbers (scale UB-98) have also larger uncertainties for the same reasons.*

***Tetrachloroethene: Larger uncertainties in the 2001-2010 numbers due to larger variability in the measurements with the ADS-GCMS instrument.*

**** Larger uncertainty for VOC due to shorter timeseries*

Table A 3: 2010 - 2019 seasonal and annual means of integral particle concentrations in the ultrafine, fine and coarse particle size range for Birkenes, Trollhaugen, and Zeppelin stations, as far as available.

		Birkenes				Trollhaugen[1]		Zeppelin	
Year	Season	N_{ait} / cm^{-3}	N_{acc} / cm^{-3}	N_{coa} / cm^{-3}	N_{tot} / cm^{-3}	N_{ait} / cm^{-3}	$^{2}N_{acc}$ / cm^{-3}	N_{ait} / cm^{-3}	$^{2}N_{acc}$ / cm^{-3}
2009/10	Winter	467	433	0.296	967				
2010	Spring	1249	372	0.704	1633				
2010	Summer	1807	555	0.643	2381				
2010	Autumn	912	343	0.562	1358				
2010	Whole Year	1101	412	0.575	1593				
2010/11	Winter	544	320	0.974	863				
2011	Spring	1341	422	1.620	1765				
2011	Summer	1661	497	1.250	2161				
2011	Autumn	1908	560	1.844	2470				
2011	Whole Year	1215	417	1.427	1644				
2011/12	Winter	433	217	0.927	664				
2012	Spring	1179	303	0.982	1523				
2012	Summer	1447	435	1.041	1892				
2012	Autumn	722	169	0.918	898				
2012	Whole Year	951	288	0.912	1258				
2012/13	Winter	421	203	0.550	626				
2013	Spring	1314	392	1.012	1711				
2013	Summer	1680	497	0.951	2182				
2013	Autumn	785	183	0.952	968				
2013	Whole Year	1107	335	0.951	1454				
2013/14	Winter	737	342	1.246	1079				
2014	Spring	1569	429	0.823	1998	183	32		
2014	Summer	1717	642	0.757	2358	43	19		
2014	Autumn	1286	532	0.950	1818	207	28		
2014	Whole Year	1333	488	0.859	1821	183	34		
2014/15	Winter	567	203	1.038	770	368	67		
2015	Spring	1571	360	1.030	1931	134	25		
2015	Summer	2198	614	0.866	2812	38	23		
2015	Autumn	1081	378	0.766	1459	221	28		
2015	Whole Year	1363	395	0.963	1758	171	32		
2015/16	Winter	594	245	0.867	839				
2016	Spring	1471	483	0.848	1954	170	26		
2016	Summer	1608	535	0.876	2143	47	18	156	64
2016	Autumn	983	319	0.707	1302	262	35	47	31
2016	Whole Year	1167	391	0.804	1558	231	37	---	---
2016/17	Winter	585	219	0.717	804	473	74	---	---
2017	Spring	1474	476	0.564	1950	157	31	96	126
2017	Summer	1599	537	1.013	2136	51	20	282	70
2017	Autumn	1291	440	0.734	1731	265	27	56	63
2017	Whole Year	1256	424	0.721	1679	238	38	---	---
2017/18	Winter	517	275	0.399	792	482	78	27	44
2018	Spring	1511	649	---	2159	170	24	107	85
2018	Summer	1948	617	---	2565	45	18	225	66
2018	Autumn	986	300	---	1286	273	28	30	25
2018	Whole Year	1255	460	---	1715	233	35	92	55
2018/19	Winter	578	229	---	806	427	64	18	60
2019	Spring	1406	500	---	1906	183	25	78	95
2019	Summer	1867	509	---	2376	34	14	224	68
2019	Autumn	805	185	---	990	233	29	29	28
2019	Whole Year	1163	356	---	1519	202	31	87	64
2019/20	Winter	567	133	---	700	398	78	25	78
2020	Spring	1480	291	---	1770	187	27	90	88
2020	Summer	1570	554	---	2125	36	13	148	96
2020	Autumn	907	251	---	1158	237	28	34	38
2020	Whole Year	1133	306	---	1439	219	37	77	75

[1] Cells shaded in grey mark values obtained with an older instrument version that can't be compared directly with later values. Numbers given for the time when the respective season is present in the Northern hemisphere. Actual seasons in Southern hemisphere are shifted by 6 months. In 2020, numbers for Birkenes have been reprocessed for all years since 2010 taking into account recent intercalibrations.

[2] The accumulation mode integral particle concentration N_{acc} at Trollhaugen and Zeppelin extends only up to 0.8 µm particle diameter due to lack of an instrument covering larger particles. For Birkenes, N_{acc} includes particles up to 1 µm diameter

Table A 4: 2010 - 2020 seasonal and annual means of optical aerosol properties scattering coefficient, absorption coefficient, and single scattering albedo for Birkenes, Trollhaugen, and Zeppelin stations, as far as available.

		Birkenes			Trollhaugen[1]			Zeppelin		
Year	Season	σ_{sp} (550 nm) / Mm^{-1}	σ_{ap} (550 nm) / Mm^{-1}	ϖ_0 (550 nm)	σ_{sp} (550 nm) / Mm^{-1}	σ_{ap} (550 nm) / Mm^{-1}	ϖ_0 (550 nm)	σ_{sp} (550 nm) / Mm^{-1}	σ_{ap} (550 nm) / Mm^{-1}	ϖ_0 (550 nm)
2009/10	Winter	16.82	3.09	0.88						
2010	Spring	12.33	0.78	0.93						
2010	Summer	11.30	0.70	0.94						
2010	Autumn	7.26	0.71	0.90						
2010	Whole Year	11.52	1.24	0.91						
2010/11	Winter	16.96	2.18	0.89						
2011	Spring	18.67	1.26	0.93						
2011	Summer	15.43	0.74	0.95						
2011	Autumn	29.74	2.87	0.92						
2011	Whole Year	20.26	1.69	0.93						
2011/12	Winter	11.29	1.00	0.91						
2012	Spring	15.10	0.86	0.93						
2012	Summer	12.62	0.67	0.95						
2012	Autumn	9.80	0.65	0.92						
2012	Whole Year	12.22	0.83	0.92						
2012/13	Winter	12.48	1.84	0.84						
2013	Spring	17.03	1.48	0.90						
2013	Summer	13.81	1.15	0.92						
2013	Autumn	8.89	1.25	0.85						
2013	Whole Year	13.73	1.40	0.88						
2013/14	Winter	22.89	2.64	0.87						
2014	Spring	12.95	2.09	0.87	0.74	-0.05	0.95			
2014	Summer	15.85	1.26	0.92	1.39	0.04	0.98			
2014	Autumn	18.76	3.41	0.82	1.02	0.15	0.93			
2014	Whole Year	16.99	2.30	0.87	1.01	0.09	0.95			
2014/15	Winter	13.98	1.30	0.89	0.74	0.04	0.94			
2015	Spring	12.72	1.48	0.89	0.65	0.02	0.97			
2015	Summer	12.45	1.46	0.90	2.44	0.02	0.98		0.30	
2015	Autumn	15.69	2.45	0.95	1.32	0.07	0.94		0.14	
2015	Whole Year	14.36	1.56	0.90	1.32	0.04	0.96			
2015/16	Winter	13.59	1.24	0.88	0.87	0.05	0.94		0.38	
2016	Spring	14.86	1.10	0.91	0.78	0.17	0.97		0.39	
2016	Summer	11.93	0.77	0.94	2.01	0.00	0.99		0.09	
2016	Autumn	11.47	1.46	0.85	1.54	0.04	0.95		0.12	
2016	Whole Year	12.26	1.12	0.89	1.31	0.06	0.97		0.24	
2016/17	Winter	12.27	2.24	0.81	0.82	0.05	0.94		0.40	
2017	Spring	8.71			0.76	0.02	0.97		0.48	
2017	Summer	8.58			1.57	0.01	0.99		0.10	
2017	Autumn	8.09	1.21	0.85	1.22	0.05	0.94		0.29	
2017	Whole Year	9.07			1.10	0.03	0.96		0.33	
2017/18	Winter	13.56	1.66	0.83	0.72	0.04	0.95		0.34	
2018	Spring	17.10	2.45	0.87	0.60	0.03	0.97		0.32	
2018	Summer	13.62	1.23	0.91	1.78	0.06	0.98		0.12	
2018	Autumn	14.08	2.04	0.86	1.31	0.04	0.95		0.10	
2018	Whole Year	14.54	1.90	0.86	1.10	0.04	0.96		0.21	
2018/19	Winter	---	---	---	0.73	0.04	0.94		0.45	
2019	Spring	---	---	---	0.81	0.03	0.97		0.46	
2019	Summer	---	---	---	1.81	0.01	0.99		0.19	
2019	Autumn	6.26	0.93	0.85	1.61	0.04	0.96		0.13	
2019	Whole Year	---	---	---	1.26	0.03	0.97		0.33	
2019/20	Winter	10.15	0.96	0.87	0.88	0.04	0.95		0.73	
2020	Spring	10.84	1.03	0.90	0.89	0.02	0.98		0.36	
2020	Summer	11.28	1.07	0.91	1.43	0.01	0.99		0.24	
2020	Autumn	12.63	1.53	0.88	1.60	0.04	0.97		0.13	
2020	Whole Year	11.62	1.21	0.89	1.19	0.03	0.97		0.36	

[1]*Numbers given for the time when the respective season is present in the Northern hemisphere. Actual seasons in Southern hemisphere are shifted by 6 months.*

Table A 5: Monthly means and standard deviation of aerosol optical depth (AOD) at 500 nm at Ny-Ålesund.

Month/ Year	Jan	Feb	Mar	Apr	May	Jun	Jul	Aug	Sep	Oct	Nov	Dec
Aerosol optical depth (AOD)												
2002				0.06 ±0.01	0.08 ±0.03	0.06 ±0.02	0.07 ±0.12	0.07 ±0.08	0.06 ±0.05			
2003			0.15 ±0.12	0.11 ±0.05	0.15 ±0.06	0.10 ±0.03	0.04 ±0.01	0.05 ±0.02	0.06 ±0.03			
2004			0.06 ±0.00	0.12 ±0.08	0.13 ±0.09	0.06 ±0.01	0.10 ±0.07	0.05 ±0.02	0.04 ±0.02			
2005			0.08 ±0.03	0.12 ±0.07	0.10 ±0.03	0.05 ±0.02	0.05 ±0.02	0.04 ±0.03	0.03 ±0.01			
2006			0.12 ±0.03	0.16 ±0.07		0.04 ±0.00	0.05 ±0.02	0.05 ±0.04	0.04 ±0.03			
2007				0.10 ±0.05	0.10 ±0.12	0.07 ±0.03	0.05 ±0.01	0.05 ±0.02	0.04 ±0.03			
2008			0.13 ±0.05	0.14 ±0.06	0.14 ±0.04	0.06 ±0.02	0.06 ±0.02	0.09 ±0.03	0.16 ±0.03			
2009					0.11 ±0.03	0.08 ±0.02	0.11 ±0.04	0.10 ±0.02	0.09 ±0.01			
2010			0.11±0. 03	0.08 ±0.03	0.08 ±0.01	0.06 ±0.01	0.05 ±0.01	0.05 ±0.01				
2011					0.08 ±0.02	0.08 ±0.01	0.05 ±0.01	0.06 ±0.02	0.05 ±0.01			
2012			0.10 ±0.03	0.10 ±0.02	0.10 ±0.03	0.06 ±0.02	0.06 ±0.02	0.07 ±0.03	0.07 ±0.03			
2013			0.11 ±0.04	0.09 ±0.04	0.06 ±0.02	0.05 ±0.01	0.06 ±0.02	0.05 ±0.01	0.04 ±0.02			
2014				0.07 ±0.01	0.10 ±0.02	0.06 ±0.02	0.06 ±0.03	0.08 ±0.01	0.11 ±0.05			
2015			0.05 ±0.02	0.10 ±0.03	0.07 ±0.02	0.05 ±0.01	0.15 ±0.20	0.05 ±0.02	0.05 ±0.01			
2016			0.08 ±0.03	0.06 ±0.02	0.08 ±0.03	0.07 ±0.02	0.04 ±0.01	0.05 ±0.04	0.03 ±0.01			
2017				0.07 ±0.03	0.07 ±0.03	0.04 ±0.01	0.04 ±0.01	0.05 ±0.01	0.07 ±0.01			
2018	0.05 ±0.01		0.05 ±0.01	0.08 ±0.02	0.07 ±0.02	0.04 ±0.01	0.03 ±0.01	0.08 ±0.07	0.05 ±0.02	0.10 ±0.01	0.04 ±0.00	0.05 ±0.01
2019	0.10 ±0.01	0.07 ±0.02		0.06 ±0.02	0.07 ±0.02	0.05 ±0.01	0.20 ±0.09	0.19 ±0.04	0.10 ±0.01	0.08 ±0.00		
2020		**0.08 ±0.02**	**0.07 ±0.04**	**0.07 ±0.01**	**0.08 ±0.01**							
Mean (2002-2020)	**0.08 0.01**	**0.08 ±0.02**	**0.10 ±0.04**	**0.10 ±0.04**	**0.10 ±0.04**	**0.06 ±0.02**	**0.07 ±0.04**	**0.07 ±0.03**	**0.06 ±0.02**	**0.10 ±0.01**	**0.04 ±0.00**	**0.05 ±0.01**

Table A 6: Monthly means and standard deviation of the Ångström coefficient (Å) at Ny-Ålesund. There are no observations of this parameter during the winter months due to polar night.

Month/ Year	Jan	Feb	Mar	Apr	May	Jun	Jul	Aug	Sep	Oct	Nov	Dec
Aerosol optical depth (AOD)												
2002				0.9 ±0.1	1.4 ±0.1	1.2 ±0.3	1.2 ±0.2	1.3 ±0.4	1.2 ±0.5			
2003			0.9 ±0.5	1.3 ±0.3	1.3 ±0.2	1.5 ±0.1	1.5 ±0.3	1.4 ±0.5	1.4 ±0.3			
2004			1.3 ±0.1	1.2 ±0.3	1.4 ±0.5	1.7 ±0.2	1.6 ±0.4	1.5 ±0.3	1.3 ±0.3			
2005			1.1 ±0.3	1.4 ±0.4	1.0 ±0.2	1.6 ±0.3	1.7 ±0.2	1.4 ±0.7	1.5 ±0.4			

2006			0.9 ±0.1	0.9 ±0.3		1.7 ±0.2	1.4 ±0.3	1.3 ±0.6	1.4 ±0.3			
2007				1.4 ±0.4	1.4 ±0.6	1.7 ±0.2	1.6 ±0.2	1.7 ±0.3	1.5 ±0.4			
2008			1.4 ±0.2	1.3 ±0.2	1.4 ±0.2	1.4 ±0.4	1.2 ±0.2	1.3 ±0.3	1.4 ±0.3			
2009					1.3 ±0.4	1.4 ±0.2	1.3 ±0.3	1.2 ±0.1	1.1 ±0.1			
2010			1.0 ±0.3	1.4 ±0.2	1.3 ±0.2	1.3 ±0.3	1.4 ±0.2	1.0 ±0.1				
2011					1.7 ±0.3	1.8 ±0.1	1.5 ±0.1	1.4 ±0.3	1.6 ±0.2			
2012			1.1 ±0.2	1.3 ±0.2	1.2 ±0.2	1.1 ±0.1	1.3 ±0.2	1.4 ±0.2	1.5 ±0.2			
2013			1.3 ±0.2	1.2 ±0.3	1.4 ±0.2	1.6 ±0.3	1.3 ±0.2	1.4 ±0.2	1.2 ±0.5			
2014				1.4 ±0.1	1.4 ±0.1	1.3 ±0.3	1.5 ±0.1	1.5 ±0.1	1.5 ±0.2			
2015			1.32 ±0.17	1.23 ±0.26	1.47 ±0.14	1.50 ±0.20	1.47 ±0.16	1.56 ±0.16	1.18 ±0.52			
2016			1.30 ±0.21	1.56 ±0.12	1.57 ±0.06	1.49 ±0.19	1.45 ±0.28	1.52 ±0.18	1.43 ±0.22			
2017				1.46 ±0.20	1.46 ±0.21	1.38 ±0.09	1.57 ±0.11	1.54 ±0.09	1.36 ±0.06			
2018	1.34 ±0.12		1.41 ±0.08	1.35 ±0.15	1.22 ±0.31	1.47 ±0.17	1.43 ±0.08	1.41 ±0.10	1.16 ±0.12	1.03 ±0.03	1.02 ±0.03	1.11 ±0.07
2019	1.59 ± 0.16	1.35 ± 0.23		1.25 ± 0.27	1.47 ± 0.23	1.35 ± 0.23	1.38± 0.18	1.30 ± 0.10	1.28 ± 0.06	1.19 ± 0.12		
2020		**1.10 ± 0.39**	**1.14 ±0.19**	**1.45 ± 0.06**	**1.49 ± 0.09**							
Mean (2002-2020)	**1.48 ±0.14**	**1.15 ±0.35**	**1.19 ±0.22**	**1.33 ±0.24**	**1.36 ±0.23**	**1.43 ±0.24**	**1.43 ±0.21**	**1.42 ±0.24**	**1.35 ±0.30**	**1.10 ±0.04**	**1.02 ±0.03**	**1.11 ± 0.07**

Table A 7: Number of days with AOD observations at Ny-Ålesund made within the months.

Month/Year	Jan	Feb	Mar	Apr	May	Jun	Jul	Aug	Sep	Oct	Nov	Dec
Number of days with cloud-free and quality assured observations												
2002				4	15	11	6	9	14			
2003			3	12	16	8	15	17	12			
2004			2	8	13	9	5	12	12			
2005			12	17	24	15	10		11			
2006			6	12		5	12	4	13			
2007				16	9	12	17	10	9			
2008			15	12	14	20	16	13	2			
2009					7	10	17	8	8			
2010			7	18	7	10	12	3	1			
2011					2	2	7	4	6			
2012			6	18	12	15	16	11	4			
2013			5	13	10	10	8	7	9			
2014				13	9	9	9	14	4			

2015			5	17	15	9	17	13	6			
2016			6	14	8	7	12	10	7			
2017				13	19	11	12	6	3			
2018	7		3	10	5	12	9	11	5	2	2	2
2019	9	3		10	19	18	9	16	7	1		
2020		**11**	**5**	**6**	**7**							
Total (2002-2020)	**16**	**14**	**75**	**213**	**211**	**193**	**209**	**168**	**133**	**3**	**2**	**2**

Table A 8: Monthly means and standard deviation of aerosol optical depth (AOD) at 500 nm at Birkenes.

Month/Year	Jan	Feb	Mar	Apr	May	Jun	Jul	Aug	Sep	Oct	Nov	Dec
Aerosol optical depth (AOD)												
2009				0.29 ±0.00	0.09 ±0.05	0.09 ±0.05	0.18 ±0.06	0.17 ±0.07	0.10 ±0.04	0.08 ±0.03		
2010					0.10 ±0.04	0.09 ±0.04	0.10 ±0.07	0.10 ±0.05	0.05 ±0.02	0.07 ±0.03	0.04 ±0.01	
2011	0.02 ±0.01	0.03 ±0.01	0.07 ±0.02	0.21 ±0.19	0.13 ±0.07	0.10 ±0.04	0.13 ±0.06	0.09 ±0.05				
2012			0.07 ±0.05	0.05 ±0.02	0.08 ±0.04	0.09 ±0.04	0.07 ±0.03	0.08 ±0.03	0.07 ±0.01	0.06 ±0.03	0.04 ±0.00	
2013							0.17 ±0.17	0.12 ±0.09	0.05 ±0.03	0.05 ±0.03		
2014			0.15 ±0.14	0.11 ±0.06	0.10 ±0.03	0.08 ±0.03	0.13 ±0.06	0.15 ±0.07	0.14 ±0.06			
2015			0.04 ±0.02	0.07 ±0.02	0.07 ±0.03	0.06 ±0.02	0.10 ±0.07	0.09 ±0.06	0.04 ±0.02	0.03 ±0.03	0.04 ±0.01	
2016	0.01 ±0.00	0.03 ±0.01	0.03 ±0.02	0.05 ±0.03							0.02 ±0.00	
2017*				0.08 ±0.01	0.06 ±0.03	0.04 ±0.03	0.06 ±0.03	0.09 ±0.07	0.09 ±0.03	0.06 ±0.03		
2018*				0.09 ±0.07	0.11 ±0.05	0.07 ±0.06	0.08 ±0.06	0.10 ±0.08	0.06 ±0.04			
2019	0.03 ±0.01	0.07 ±0.09	0.04 ±0.02	0.11 ±0.08	0.06 ±0.03	0.12 ±0.11	0.19 ±0.06	0.16 ±0.04			0.07 ±0.03	0.05 ±0.00
2020	**0.06 ±0.02**	**0.08 ±0.07**	**0.07 ±0.02**	**0.08 ±0.01**	**0.07 ±0.02**	**0.10 ±0.07**	**0.06 ±0.02**	**0.11 ±0.06**	**0.14 ±0.10**	**0.08 ±0.04**	**0.04 ±0.02**	**0.03 ±0.01**
Mean 2009 -2020	**0.03 0.01**	**0.05 ±0.03**	**0.07 ±0.04**	**0.09 ±0.06**	**0.09 ±0.04**	**0.08 ±0.05**	**0.12 ±0.06**	**0.11 ±0.06**	**0.08 ±0.04**	**0.06 ±0.03**	**0.04 ±0.01**	**0.04 ±0.01**

* version 3 data analysis (Aeronet)

Table A 9: Monthly means and standard deviation of the Ångström coefficient (Å) at Birkenes

Month/Year	Jan	Feb	Mar	Apr	May	Jun	Jul	Aug	Sep	Oct	Nov	Dec
Ångström coefficient (Å)												
2009				1.5 ±0.0	1.2 ±0.3	1.4 ±0.3	1.4 ±0.4	1.1 ±0.2	1.0 ±0.2	1.1 ±0.2		
2010					1.3 ±0.3	1.4 ±0.3	1.4 ±0.2	1.4 ±0.2	1.3 ±0.3	1.3 ±0.3	1.3 ±0.23	
2011	1.0 ±0.2	1.0 ±0.1	1.0 ±0.3	1.2 ±0.5	1.3 ±0.3	1.5 ±0.3	1.6 ±0.3	1.6 ± 0.1				
2012			1.1 ±0.4	1.6 ±0.3	1.4 ±0.4	1.7 ±0.1	1.6 ±0.3	1.5 ±0.3	1.1 ±0.3	1.4 ±0.4	0.8 ±0.3	
2013							1.3 ± 0.2	1.2 ±0.3	0.8 ±0.2	0.8 ±0.3		
2014			0.87 ±0.48	1.04 ±0.33	1.07 ±0.27	1.02 ±0.24	1.38 ±0.33	1.14 ±0.25	1.19 ±0.16			
2015			0.93 ±0.16	1.06 ±0.13	1.11 ±0.20	1.30 ±0.20	1.49 ±0.20	1.37 ±0.26	1.30 ±0.23	1.23 ±0.25	0.84 ±0.33	
2016	0.68 ±0.07	1.00 ±0.2	0.90 ±0.3	1.13 ±0.2							1.11 ±0.08	
2017*				1.77 ±0.07	1.39 ±0.35	1.39 ±0.37	1.73 ±0.34	1.48 ±0.37	0.93 ±0.18	0.78 ±0.20		
2018				1.02 ± 0.24	1.31 ± 0.25	1.23 ± 0.31	1.54 ± 0.28	1.36 ± 0.23	1.11 ±0.25			
2019	0.83 ±0.23	0.96 ±0.45	1.01 ±0.31	1.47 ± 0.28	1.29 ± 0.23	1.43 ± 0.17	1.60 ± 0.16	1.41 ± 0.15			1.04 ±0.29	1.08 ±0.14
2020	**0.88 ±0.29**	**0.80 ±0.28**	**1.10 ±0.25**	**1.17 ± 0.18**	**1.18 ± 0.24**	**1.39 ± 0.28**	**1.41 ± 0.21**	**1.51 ± 0.21**	**1.16 ±0.35**	**1.24 ±0.38**	**1.05 ±0.18**	**0.94 ±0.22**
Mean 2009-2020	**0.84 ±0.15**	**0.95 ±0.24**	**0.98 ±0.33**	**1.27 ±0.24**	**1.26 ±0.26**	**1.37 ±0.24**	**1.50 ±0.27**	**1.38 ±0.23**	**1.10 ±0.24**	**1.12 ±0.28**	**1.02 ±0.23**	**1.01 ±0.18**

* version 3 data analysis (Aeronet)

Table A 10: Number of days with AOD observations at Birkenes made within the months.

Month/Year	Jan	Feb	Mar	Apr	May	Jun	Jul	Aug	Sep	Oct	Nov	Dec
Number of days with cloud-free and quality assured observations (lev 2; lev 1.5 for 2013)												
2009				1	22	25	11	13	15	12		
2010					13	16	18	15	16	10	6	
2011	7	2	20	23	18	20	15	13				
2012			11	12	10	7	16	18	9	12	2	
2013							26	18	13	7		
2014			12	17	16	25	20	13	7			
2015			6	1	14	21	21	16	9	11	3	
2016	1	9	11	8							1	
2017*				2	17	15	17	11	6	8		
2018*				8	27	20	22	15	10			
2019	6	9	14	23	23	11	5	10			3	3
2020	**8**	**10**	**7**	**3**	**11**	**21**	**22**	**22**	**16**	**11**	**8**	**3**
Total	**22**	**30**	**81**	**98**	**171**	**181**	**193**	**165**	**101**	**71**	**23**	**6**

* version 3 data analysis (Aeronet)

Table A 11: Monthly means and standard deviation of aerosol optical depth (AOD) at 500 nm at Trollhaugen Observatory.

Month/Year	Jan	Feb	Mar	Apr	May	Jun	Jul	Aug	Sep	Oct	Nov	Dec
Aerosol optical depth (AOD)												
2014	0.016 ±0.002	0.015 ±0.002	0.014 ±0.002	0.014 ±0.005					0.022 ±0.003	0.017 ±0.002	0.021 1±0.002	0.020 ±0.002
2015	0.029 ±0.003	0.018 ±0.003	0.018 ±0.002	0.017 ±0.001				0.048 ±0.009	0.034 ±0.010	0.040 ±0.007	0.035 ±0.009	0.031 ±0.005
2016	0.035 ±0.006	0.033 ±0.004	0.026 ±0.003	0.027 ±0.004				0.039 ±0.010	0.026 ±0.005	0.024 ±0.005	0.019 ±0.005	0.019 ±0.001
2017	0.020 ±0.003	0.020 ±0.003	0.016 ±0.003	0.015 ±0.002				0.022 ±0.006	0.021 ±0.006	0.019 ±0.002	0.020 ±0.004	0.016 ±0.003
2018	0.016 ±0.004	0.016 ±0.002	0.013 ±0.002	0.014 ±0.001	0.013 ±0.003				0.027 ±0.006	0.022 ±0.002	0.020 ±0.003	0.021 ±0.002
2019	0.027 ±0.006	0.026 ±0.006	0.020 ±0.003	0.019 ±0.002	0.015 ±0.001			0.029 ±0.002	0.019 ±0.001	0.022 ±0.001	0.022 ±0.003	0.026 ±0.002
2020	**0.038 ±0.01**	**0.053 ±0.01**	**0.053 ±0.01**	**0.048 ±0.01**				**0.045 ±0.004**	**0.041 ±0.007**	**0.040 ±0.007**	**0.032 ±0.003**	**0.024 ±0.003**
Mean 2014-2020	**0.025 ±0.005**	**0.026 ±0.005**	**0.021 ±0.003**	**0.019 ±0.003**	**0.014 ±0.002**			**0.035 ±0.007**	**0.030 ±0.006**	**0.026 ±0.004**	**0.023 ±0.004**	**0.023 ±0.003**

Table A 12: Monthly means and standard deviation of the Ångström coefficient (Å) at Trollhaugen.

Month/Year	Jan	Feb	Mar	Apr	May	Jun	Jul	Aug	Sep	Oct	Nov	Dec
Ångström coefficient (Å)												
2014	1.59 ±0.18	1.54 ±0.14	1.29 ±0.09	1.22 ±0.08					1.29 ±0.15	1.52 ±0.17	1.37 ±0.15	1.76 ±0.06
2015	1.69 ±0.61	1.60 ±0.12	1.43 ±0.10	1.34 ±0.09				0.97 ±0.15	1.03 ±0.18	1.26 ±0.14	1.22 ±0.34	1.47 ±0.15
2016	1.53 ±0.12	1.63 ±0.14	1.41 ±0.09	1.42 ±0.05				1.32 ±0.21	1.25 ±0.18	1.34 ±0.22	1.53 ±0.13	1.48 ±0.09
2017	1.61 ±0.16	1.68 ±0.10	1.23 ±0.14	1.21 ±0.08				1.08 ±0.18	1.18 ±0.24	1.28 ±0.13	1.35 ±0.19	1.53 ±0.10
2018	1.51 ±0.10	1.45 ±0.09	1.29 ±0.08	1.32 ± 0.17	1.30 ± 0.06				1.47 ±0.16	1.47 ±0.11	1.56 ±0.12	1.73 ±0.08
2019	1.63 ±0.11	1.63 ±0.10	1.56 ±0.08	1.34 ± 0.08	1.26 ± 0.08			0.92 ±0.07	1.51 ±0.12	1.44 ±0.09	1.53 ±0.14	1.61 ±0.10
2020	**1.71 ± 0.10**	**1.58 ± 0.14**	**1.33 ± 0.04**	**1.24 ± 0.03**				**0.81 ± 0.09**	**0.91 ± 0.10**	**1.11 ± 0.08**	**1.20 ± 0.07**	**1.44 ± 0.11**
Mean 2014-2019	**1.59 ±0.16**	**1.59 ±0.12**	**1.37 ±0.10**	**1.29 ±0.09**	**1.27 ±0.07**			**1.06 ±0.16**	**1.18 ±0.16**	**1.34 ±0.13**	**1.42 ±0.16**	**1.57 ± 0.10**

Table A 13: Number of days with AOD observations at Trollhaugen made per month

Month/Year	Jan	Feb	Mar	Apr	May	Jun	Jul	Aug	Sep	Oct	Nov	Dec
Number of days with cloud-free and quality assured observations (lev 2; lev 1.5 for 2013)												
2014	15	22	13	21					4	10	**13**	**11**
2015	7	21	11	12				5	14	12	10	25
2016	20	15	15	13				8	10	15	21	21
2017	24	15	24	9				11	11	15	15	10
2018	22	14	14	22	3				12	20	21	13
2019	12	21	21	11	5			1	7	17	9	20
2020	**12**	**21**	**11**	**7**				**7**	**17**	**17**	**10**	**15**
Total	**112**	**129**	**109**	**95**	**8**			**32**	**75**	**106**	**99**	**125**

Appendix II

Description of instruments and methodologies

ON THE INSTRUMENTAL METHODS USED FOR THE MEASUREMENTS OF THE VARIOUS GREENHOUSE GASES AT BIRKENES AND ZEPPELIN OBSERVATORIES

In this section of the appendix, the instrumental methods used for the measurements of the various greenhouse gases are presented, see also Platt et al, 2021 for more details and historical development of Zeppelin. Additionally, we explain the theoretical methods used in calculation of the trends.

The next table provides details about greenhouse gas measurements and recent improvement and extensions.

Table A 14: Instrumental details for greenhouse gas measurements at Zeppelin and Birkenes.

Component		Instrument and method	Time res.	Calibration procedures	Start - End	Comment
Methane (Birkenes)	CH_4	Picarro CRDS G1301 CO2/CH4/H2O	1 h 5 s	Working std. calibrated against GAW stds at EMPA	19th May 2009 – Jan 2018	
Methane (Birkenes)	CH_4	Picarro CRDS G2401 CO2/CH4/CO	1 h 5 s	ICOS reference standards	1st Jan 2018 ->	Data coverage in 2020: 96%
Methane (Zeppelin)	CH_4	GC-FID	1h	NOAA reference standards	Aug 2001-Apr 2012	
Methane (Zeppelin)	CH_4	Picarro CRDS	1 h 5 sec	ICOS reference standards	20th Apr. 2012 ->	Data coverage 2020: 94%
Nitrous oxide (Zeppelin)	N_2O	GC-ECD	30 min	NOAA reference standards	27th Mar 2010 – 31st Dec 2015	
Nitrous oxide (Zeppelin)	N_2O	Picarro CRDS	1 h 5 sec	ICOS reference standards	1st Jan 2016 ->	Data coverage 2020 95%
Carbon monoxide (Zeppelin)	CO	GC-HgO/UV	20 min	Every 20 min, working std. calibrated vs. GAW std.	Sep. 2001 - 2012	Data coverage 2020: 94%
Carbon monoxide (Zeppelin)	CO	Picarro CRDS	1 h 5 sec	ICOS reference standards.	20th Apr 2012 ->	Data coverage 2019: 95%
Carbon monoxide (Birkenes)	CO	Picarro CRDS G2401 CO2/CH4/CO	1 h 5 sec	ICOS reference standards.	1st Jan 2018 ->	Data coverage in 2020: 96%
Carbon dioxide (Zeppelin)	CO_2	Li-Cor	1 h	NOAA reference standards	1989 - 2012	CO_2 measured by ITM Stockholm University (SU) until 2012
Carbon dioxide (Zeppelin)	CO_2	Picarro CRDS	1 h 5 sec	ICOS reference standards	20th Apr. 2012 ->	Data coverage 2020: 94%
Carbon dioxide (Birkenes)	CO_2	Picarro CRDS G1301 CO2/CH4/H2O	1 h 5 s	Working std. calibrated against GAW stds at EMPA	19th May 2009 –– Jan 2018>	Data coverage in 2019: 95%
Carbon dioxide (Birkenes)	CO_2	Picarro CRDS G2401 CO2/CH4/CO	1 h 5 s	ICOS reference standards	1st Jan 2018 ->	Data coverage in 2020: 96%
CFC-11 CFC-12 CFC-113 CFC-115 HFC-125 HFC-134a HFC-152a HFC-365mfc HCFC-22 HCFC-141b HCFC-142b H-1301 H-1211 H-2402	$CFCl_3$ CF_2Cl_2 $CF_2ClCFCl_2$ CF_3CF_2Cl CHF_2CF_3 CH_2FCF_3 CH_3CHF_2 $CF_3CH_2CHF_2CH_3$ CHF_2Cl CH_3CFCl_2 CH_3CF_2Cl CF_3Br CF_2ClBr	ADS-GCMS	4 h	Every 4 hours, working std. calibrated vs. AGAGE std.	4th Jan 2001-2010	The measurements of the CFCs, TCE and PCE have higher uncertainty and are not within the required precision of AGAGE. See next section for details.

Component		Instrument and method	Time res.	Calibration procedures	Start - End	Comment
Chloromethane	CH_3Cl	ADS-GCMS	4h	Every 4 hours, working std. calibrated vs. AGAGE std.	4th Jan 2001-2010	
Bromomethane	CH_3Br					
Dichloromethane	CH_2Cl_2					
Trichloromethane	$CHCl_3$					
Trichloroethane	CH_3CCl_3					
Trichloroethene	$CHClCCl_2$					
Tetrachloroethene	CCl_2CCl_2					
Sulphurhexafluoride	SF_6					
Nitrogen trifluoride	NF_3	Medusa-GCMS No. 19	2 h	Every 2 hours, working std. calibrated vs. AGAGE std	1st September 2010	Data coverage 2020: 80% (except for CFC-11, CFC-12, CFC-113, H-1211 (65%). Benzene and Toluene data were not released for 2020
PFC-14	CF_4					
PFC-116	C_2F_6					
PFC-218	C_3F_8					
PFC-318	$c\text{-}C_4F_8$					
Sulphurhexafluoride	SF_6					
Sulfuryl fluoride	SO_2F_2					
HFC-23	CHF_3					
HFC-32	CH_2F_2					
HFC-125	CHF_2CF_3					
HFC-134a	CH_2FCF_3					
HFC-143a	CH_3CF_3					
HFC-152a	CH_3CHF_2					
HFC-227ea	CF_3CHFCF_3					
HFC-236fa	$CF_3CH_2CF_3$					
HFC-245fa	$CF_3CH_2CHF_2$					
HFC-365mfc	$CH_3CF_2CH_2CF_3$					
HFC-43-10mee	$CF_3(CHF)_2CF_2CF_3$					
HCFC-22	$CHClF_2$					
HCFC-141b	CH_3CCl_2F					
HCFC-142b	CH_3CClF_2					
CFC-11	CCl_3F					
CFC-12	CCl_2F_2					
CFC-113	CCl_2FCClF_2					
CFC-115	$CClF_2CF_3$					
H-1211	$CBrClF_2$					
H-1301	$CBrF_3$					
H-2402	$C_2Br_2F_4$					
Chloromethane	CH_3Cl					
Bromomethane	CH_3Br					
Dichloromethane	CH_2Cl_2					
Trichloromethane	$CHCl_3$					
Trichloroethane	CH_3CCl_3					
Dibromomethane	CH_2Br_2					
Trichloroethene	$CHClCCl_2$					
Tetrachloroethene	CCl_2CCl_2					
Carbon tetrachloride	CCl_4					
Ethane	C_2H_6					
Propane	C_3H_8					
Butane	C_4H_{10}					
Pentane	C_5H_{12}					
Benzene	C_6H_6					
Toluene	$C_6H_5CH_3$					
Ozone	O_3		5 min			

The overall data coverage for 2020 was 80 %. But for CFC-11, CFC-12 and CFC-113 there were issues with the instrument up to March 2020, so these data had to be rejected. The lower overall data coverage is due to a malfunctioning air conditioning at Zeppelin Observatory combined with higher summer temperatures at Ny-Ålesund. This caused several instrumental stops throughout the summer

months. This affected the quality of the instrument performance and most of the components had to be rejected. An ongoing unsolved issue in the trapping Benzene and Toluene was partly solved in November 2019 after maintenance of the sample pump. But after comparing Benzene and Toluene values with other stations in the Northern Hemisphere (e.g. Mace Head and Trinidad Head) throughout 2020, we are not confident about the results, especially the last months The first months of 2020 data might be released at a later stage when we can compare with 2021/2022 data. A new sample pump was installed in February 2021 and so far it seems to have solved the issues for Benzene and Toluene.

DATA QUALITY AND UNCERTAINTIES

HALOCARBONS

In 2001 – 2010 measurements of a wide range of hydrochlorofluorocarbons, hydrofluorocarbons (HCFC-141b, HCFC-142b, HFC-134a etc.), methyl halides (CH_3Cl, CH_3Br, CH_3I) and the halons (e.g. H-1211, H-1301) were measured with good scientific quality by using ADS-GCMS. The system also measured other compounds like the chlorofluorocarbons (CFCs), but the quality and the precision of these measurements were not at the same level. Table A 15 shows a list over those species measured with the ADS-GCMS at Zeppelin Observatory from 2001 - 2010. The species that are in blue are of acceptable scientific quality and in accordance with recommendations and criteria of the AGAGE network for measurements of halogenated greenhouse gases in the atmosphere. Those listed in red have higher uncertainties and are not within the required precision of AGAGE. There are various reasons for these increased uncertainties; unsolved instrumental problems e.g. possible electron overload in detector (for the CFC's), influence from other species, detection limits (CH_3I, $CHClCCl_2$) and unsolved calibration problems ($CHBr_3$) or instrumental issues (CCl_2CCl_2). On 1st September 2010, the ADS-GCMS was replaced by a Medusa-GCMS system. The uncertainties improved for almost all species (Table A 11 for details), but there are periods where measurements of the CFC's were still not satisfactory due to a failure in the detector and still high blank values and memory effects in the instruments leads to higher uncertainties in the CHClCCl2 (TCE) measurements.

Table A 15: ADS-GCMS measured species at Zeppelin from 4th January 2001 to 1st September 2010. Good scientific quality data in Blue; Data with reduced quality data in Red. The data are available through http://ebas.nilu.no. Please read and follow the stated data policy upon use.

Compound	Typical precision (%)	Compound	Typical precision (%)
SF_6	1.5	H1301	1.5
HFC134a	0.4	H1211	0.4
HFC152a	0.6	CH_3Cl	0.6
HFC125	0.8	CH_3Br	0.8
HFC365mfc	1.7	CH_3I	5.1
HCFC22	0.2	CH_2Cl_2	0.4
HCFC141b	0.5	$CHCl_3$	0.3
HCFC142b	0.5	$CHBr_3$	15
HCFC124	2.3	CCl_4	0.5
CFC11	0.3	CH_3CCl_3	0.6
CFC12	0.3	$CHClCCl_2$	1.2
CFC113	0.2	CCl_2CCl_2	0.7
CFC115	0.8		

Table below gives an overview over the species measured with the Medusa-GCMS systems at the AGAGE stations and the typical precision with the different instruments. The Medusa-GCMS instrument at the Zeppelin Observatory has the same precision as shown in the Table A 16.

Table A 16: AGAGE measured species.

Compound	Typical precision (%)	Compound	Typical precision (%)
NF_3	1	CFC-11	0.15
CF_4	0.15	CFC-12	0.05
C_2F_6	1	CFC-113	0.2
C_3F_8	3	CFC-115	0.8
c-C4F8	1.5	H-1301	1.7
SF_6	0.6	H-1211	0.4
SO_2F_2	2	H-2402	2
HFC-23	0.7	CH_3Cl	0.2
HFC-32	3	CH_3Br	0.6
HFC-134a	0.5	CH_2Cl_2	0.5
HFC-152a	1.4	CH_2Br_2	1.5
HFC-125	0.7	CCl_4	1
HFC-143a	1	CH_3CCl_3	0.7
HFC-227ea	2.2	$CHClCCl_2$	3
HFC-236fa	10	CCl_2CCl_2	0.5
HFC-245fa	3	C_2H_6	0.3
HFC-365mfc	5	C_3H_8	0.6
HFC-43-10mee	3	C_4H_{10}	0.6
HCFC-22	0.3	C_6H_6	0.3
HCFC-141b	0.5	C_7H_8	0.6
HCFC-142b	0.4		

METHANE

Methane is measured at both Birkenes and Zeppelin using a Picarro CRDS (Cavity Ring-Down Spectrometer) monitor which is calibrated against ICOS reference standards (NOAA scale). The instrument participates in ring tests and applies to the ICOS system for calibration and measurement control. The continuous data are also compared to weekly flask samples sent to NOAA CMDL, Boulder Colorado. All data are available for download from EBAS database http://ebas.nilu.no.

$\delta^{13}C_{CH4}$

Air samples from Zeppelin are collected in 1 L steel or aluminium canisters at the same air inlet as CH_4. Two samples per week are sent to the Greenhouse Gas Laboratory at Royal Holloway University of London. Methane mole fraction was measured using a Picarro 1301 cavity ring down spectrometer (CRDS). δ13C analysis is carried out using a modified gas chromatography isotope ratio mass spectrometry system for all samples (Trace Gas and Isoprime mass spectrometer, Isoprime Ltd.) with 0.05‰ repeatability. All measurements for the canisters are made in triplicate. See Fischer et al, 2017 and Myhre et al, 2016 for more details.

N_2O MEASUREMENTS

N_2O at Zeppelin is measured using a mid-IR Cavity Ring Down instrument (since December2017) which is calibrated against ICOS reference standards (NOAA scale). The instrument participates in ring tests and applies to the ICOS system for calibration and measurement control. The continuous data are also compared to weekly flask samples sent to NOAA CMDL, Boulder Colorado. This instrument is doing continuous measurements with improved precision and higher measurement frequency (< 1 min).

CO_2 MEASUREMENTS Carbon dioxide (CO_2) at Birkenes and Zeppelin is monitored using a Picarro Cavity Ring-Down Spectrometer for continuous measurements, calibrated against a set of ICOS reference standards (NOAA scale). The instrument participates in ring tests and applies to the ICOS system for calibration and measurement control. The continuous data are also compared to weekly flask samples sent to NOAA CMDL, Boulder Colorado. All data will be available for download from the EBAS database http://ebas.nilu.no.

CO MEASUREMENTS

Carbon monoxide (CO) at Birkenes and Zeppelin is monitored using a Picarro Cavity Ring-Down Spectrometer for continuous measurements, calibrated against a set of ICOS reference standards (NOAA scale). The instrument participates in yearly ring tests and applies to the ICOS system for calibration and measurement control. The continuous data are also compared to weekly flask samples sent to NOAA CMDL, Boulder Colorado. All data will be available for download from the EBAS database http://ebas.nilu.no.

^{14}C IN CO2 MEASUREMENTS

As part of the ICOS program, isotope ^{14}C in CO2 is sampled every 2-weeks. CO2 is absorbed by sodium hydroxide solution (NaOH 4mol/l) in a rotating Raschig-tube. The liquid sodium hydroxide samples are transferred into glass bottles and sent to the ICOS Central Radiocarbon Laboratory for analysis of the 14C/C ratio in the absorbed CO2. Sampling started in 2017.

IMPLEMENTATION OF MEASUREMENTS FROM BIRKENES AND ZEPPELIN INTO ICOS RESEARCH INFRASTRUCTURE

The Integrated Carbon Observation System (ICOS) is a European research infrastructure forming an observation system that will measure and assess the global carbon budget, including atmospheric CO_2, CH_4 and CO concentrations, while ensuring independent and reliable measurements. ICOS-Norway (https://no.icos-cp.eu) contributes to the network of atmospheric measurements with two observatories, Birkenes and Zeppelin.

ICOS has divided their sites into two labels Class 1 and Class 2, dependent on instrumental setup. At Class 1 sites a wider range of measurements of different species are required. Whilst for Class 2 fewer parameters are mandatory. The labelling process evaluates the site set up, the instrumentation with its calibration set-up and data handling, as a quality certificate of the data output from the ICOS site (Figure 58). The labelling process is time consuming as the instrument (Picarro) needs to be evaluated for minimum 1 month at the central ICOS lab, ICOS Atmospheric Thematic Centre (ATC) in France. Another central ICOS lab, ICOS Central Analytical Laboratories (CAL) in Germany, provides calibration cylinders and it takes 4 months to produce them. The same lab provides calibration cylinders and it takes 4 months to produce them. After having the instrument and calibration routines established at the site, the measurements will have to go through a 6 months evaluation period before approval as an ICOS site. In total it typically takes about 1.5 years to get an ICOS certificate.

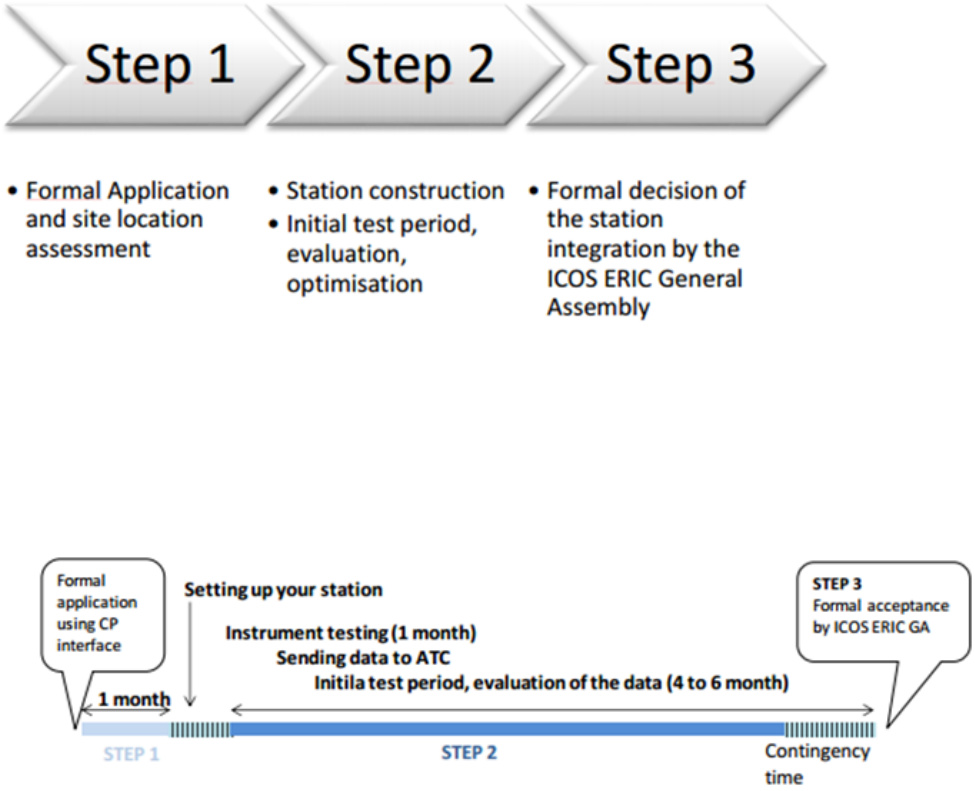

Figure 58: Outline of the labelling process for ICOS stations according to the atmosphere thematic centre (ATC).

The ATC has established the following recommended parameters for ICOS Class 1 and Class 2 sites:

Category	Gases, continuous	Gases, periodical	Meteorology, continuous	Eddy Fluxes
Class 1 Mandatory parameters	• **CO_2, CH_4, CO** : at each sampling height	• **CO_2, CH_4, N_2O, SF_6, CO, H_2, ^{13}C and ^{18}O in CO_2**: weekly sampled at highest sampling height† • **^{14}C** (radiocarbon integrated samples): at highest sampling height	• **Air temperature, relative humidity, wind direction, wind speed**: at highest and lowest sampling height* • **Atmospheric Pressure** • **Planetary Boundary Layer Height**** †	
Class 2 Mandatory parameters	• **CO_2, CH_4** : at each sampling height		• **Air temperature, relative humidity, wind direction, wind speed**: at highest and lowest sampling height* • **Atmospheric Pressure**	
Recommended parameters***	• **^{222}Rn, N_2O, O_2/N_2 ratio** • **CO** for Class 2 stations	• **CH_4 stable isotopes, O_2/N_2 ratio** for Class 1 stations: weekly sampled at highest sampling height		• **CO_2** : at one sampling height

* Atmospheric temperature and relative humidity recommended at all sampling heights

** Only required for continental stations.

*** Recommended for its scientific value but support from ATC in terms of protocols, data base, spare analyzer will not be ensured as long as the parameters are not mandatory.

The Zeppelin Observatory was labelled as an ICOS Class 1 site in 2018. Meanwhile, for sites such as Birkenes, classed as a 'continental site' by ICOS, the ATC requires that measurements are from air sampled at 100 m above ground or higher, typically using sampling inlets installed on a mast, with additional sampling at 10 m, and between 40-70 m. The purpose of this is to minimise the influence of vegetation (i.e. photosynthesis) on CO_2 measurements. For Zeppelin, a mountain top site, the only requirement was that sampling is 'sufficiently high to avoid contamination e.g. by local sources'.

Due to the location of the Birkenes Observatory on a small hill at 40 m, construction of foundations for a 100 m would be challenging and expensive. Thus, NILU initiated negotiations with ATC to lower the required sampling height on the basis that the Observatory is already elevated by 40 m. The ATC agreed to lower the required sampling height to 75 m, a more feasible mast height requiring less extensive foundations, stating in writing: "The Birkenes Observatory location and site infrastructure fulfil the ICOS requirements and recommendations specified in the latest ICOS Atmospheric Station Specifications document (version 1.3, November 2017) when the tower will be installed."

As of 28th August 2020 construction of the 75 m mast was complete (Figure 3 and Figure 59) and the installation of equipment on the mast (meteorological equipment, sample inlets etc.) were mostly done by the second week of September. The very first measurements from the 75-meter mast were performed on 14th September. The finalization of the installation is scheduled to the beginning of October. Note that the new mast has also required changes to the station infrastructure i.e. changing the location of the station entrance, upgraded protection from lightning strikes and falling ice, as well as changes in health and safety procedures (the station may no longer be accessed if there is a risk of thunder storms).

Figure 59: Birkenes Observatory with the new 75 m mast installed August-September 2020 to comply with the ICOS requirements.

Status of the labelling process for Birkenes and Zeppelin Observatories:

- The Zeppelin Observatory has achieved Class 1 status and is fully integrated in the network
- The Birkenes Observatory has achieved class 2 status as of May 2021

At class 1 sites an automatic flask sampler is mandatory and has been installed at the Zeppelin station. The flask sampling program is developed by ICOS but there are some issues with the automatic flask sampler. Work in progress for fixing this.

On 25th May 2021, The ICOS General Assembly unanimously accepted labelling of Birkenes Observatory as a Class 2 Atmosphere Station.

AIR INLET AT ZEPPELIN

In 2011 the air inlet for the GHG measurements at Zeppelin were improved to reduce possible influence from the station and visitors at the station. The inlet was moved away from the station and installed in a 15 m tower nearby for the following components:

- N_2O
- CH_4
- CO_2
- CO
- Halogenated compounds
- NOAA flasks sampling program
- Isotope flask sampling of CO_2 and CH_4

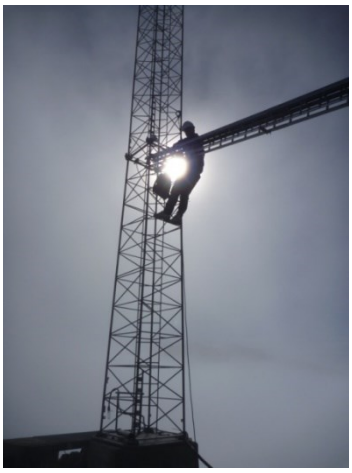

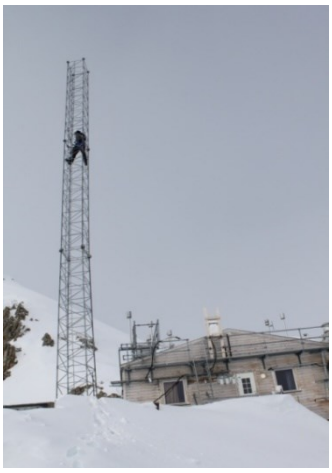

DETERMINATION OF BACKGROUND DATA

Based on the daily mean concentrations an algorithm is selected to find the values assumed as clean background air. If at least 75% of the trajectories within +/- 12 hours of the sampling day are arriving from a so-called clean sector, defined below, one can assume the air for that specific day to be non-polluted. The remaining 25% of the trajectories from European, Russian or North American sector are removed before calculating the background.

CALCULATION OF TRENDS FOR GREENHOUSE GASES AND VOCS

To calculate the annual trends the observations have been fitted as described in Simmonds et al. (2006) by an empirical equation of Legendre polynomials and harmonic functions with linear, quadratic, and annual and semi-annual harmonic terms:

$$f(t) = a + b\left(\frac{N}{12}\right)\cdot P_1\left(\frac{t}{N}-1\right) + \frac{1}{3}\cdot d\left(\frac{N}{12}\right)^2 \cdot P_2\left(\frac{t}{N}-1\right) + c_1\cdot\cos\left(\frac{2\pi t}{12}\right) + s_1\sin\left(\frac{2\pi t}{12}\right) + c_2\cos\left(\frac{4\pi t}{12}\right) + s_2\sin\left(\frac{4\pi t}{12}\right)$$

The observed *f* can be expressed as functions of time measures from the 2N-months interval of interest. The coefficient *a* defines the average mole fraction, *b* defines the trend in the mole fraction and *d* defines the acceleration in the trend. The *c* and *s* define the annual and inter-annual cycles in mole fraction. N is the mid-point of the period of investigation. P_i are the Legendre polynomials of order *i*.

This equation is used for all GHGs except for the halocarbons, where the fit between the empirical equation and observations improves if the semi-annual harmonic terms are replaced by an additional Legendre polynomial.

We are applying a new and improved method for estimating the *uncertainties* in the estimated annual trends from the time series regression modelling. In previous years, these uncertainties were estimated using a standard method from ordinary linear regression, where it was implicitly assumed that the residuals of the fitted regression models were uncorrelated. However, the use of such standard methods is known to often underestimate the true uncertainties in the estimated parameters if these assumptions are not true, i.e. if the residuals are autocorrelated, which to a large extent is the case for the regression models being fitted here.

In the current report we have replaced the standard method with a new method for estimation of uncertainties in the estimated annual trend that takes into account the presence of autocorrelated errors in the fitted model residuals. The new method also takes into account possible presence of heteroscedasticity, which means that the variances of the residuals might vary with the level of the time series, which also affects the uncertainties of the estimated trend. To this end we use the routine vcovHAC in the sandwich package in R (R Core Team, 2018) as described in Zeileis (2006; 2004), to estimate standard deviation of all estimated parameters of the time series regression models. Here HAC is short for Heteroscedastic and Autocorrelation Consistent.

It is important to emphasize that the new method only alters the estimated *uncertainties* of the annual trend estimates. The annual trend estimates themselves are not influenced by this update and have been correctly estimated using standard linear regression also in previous year's reports.

ON THE SURFACE IN SITU OBSERVATIONS OF AEROSOL MICROPHYSICAL AND OPTICAL PROPERTIES AT BIRKENES, ZEPPELIN AND TROLLHAUGEN OBSERVATORY

Table A 17: Overview of atmospheric aerosol parameters measured by surface in situ observations operated at which station

	Birkenes	Trollhaugen	Zeppelin
Particle Number Size Distribution (fine size range D_p < 0.8 µm)	X	X	X
Particle Number Size Distribution (coarse size range D_p > 0.8 µm)	X (OPS)		X (APS)
Particle Number Size Distribution, refractory particle fraction (fine size range D_p < 0.8 µm)			X
Aerosol Scattering Coefficient (spectral)	X	X	
Aerosol Absorption Coefficient (spectral)	X	X	X

Concerning surface in situ observations of microphysical and optical properties of atmospheric aerosol, the table on the left gives an overview over the parameters observed at Birkenes, Trollhaugen, and Zeppelin stations and operated by NILU.

To achieve high quality data with appropriate uncertainty and precision, this requires networked instruments to participate in inter-comparisons at ACTRIS aerosol calibration centre in Leipzig, Germany, in regular intervals. This activity has proven to be necessary in order to ensure comparable measurements within the distributed infrastructure. The frequency of these inter-comparisons, once every 2-3 years, is balanced with minimising the downtime associated with these quality assurance measures. In 2016, instruments targeting the direct aerosol climate effect were in the focus of inter-comparisons. Both the integrating nephelometer and the newer filter absorption photometer, measuring the spectral aerosol particle scattering and absorption coefficients respectively, were scheduled for being inter-compared, with satisfactory outcome in both cases. Between inter-comparisons, instruments are field calibrated regularly to ensure internal consistency of the time series.

With respect to microphysical aerosol properties, the particle number size distribution (PNSD) at surface-level is observed at all 3 stations covered in this report, at least over parts of the relevant range in particle size. The relevant particle sizes cover a range of 0.01 µm – 10 µm in particle diameter. The diameter range of 1.0 µm – 10 µm is commonly referred to as coarse mode, the range D_p < 1.0 µm as fine mode. The fine mode is separated further into Aitken-mode (0.01 µm < D_p < 0.1 µm) and accumulation mode (0.1 µm < D_p < 1 µm). The distinction of these modes is justified by different predominant physical processes as function of particle size. In the Aitken-mode, particles grow by condensation of precursor gases from the gas-phase, and coagulate among themselves or with accumulation mode particles. Accumulation mode particles grow by taking up Aitken-mode particles or by mass uptake while being activated as cloud droplets, and they are removed by precipitation. Coarse mode particles in turn are formed by break-up of biological or crustal material, including pollen, bacteria, and fungus spores, and removed by gravitational settling and wet removal. The PNSD of an aerosol is needed for quantifying any interaction or effect of the aerosol since all of them depend strongly on particle size.

To measure the PNSD over the full relevant size range, several measurement principles need to be combined. A Differential Mobilty Particle Spectrometer (DMPS) measures the particle number size distribution, now in the range of 0.01 – 0.8 µm particle diameter after several improvements of the instruments at all three stations, i.e. almost the full fine mode. In a DMPS, the particles in the sample air stream are put into a defined state of charge by exposing them to an ionised atmosphere in thermal equilibrium. The DMPS uses a cylindrical capacitor to select a narrow size fraction of the particle phase. The particle size of the selected size fraction is determined by the voltage applied to the capacitor. The

particle number concentration in the selected size fraction is then counted by a Condensation Particle Counter (CPC). A mathematical inversion that considers charge probability, diffusional losses of particles in the system, transfer function of the capacitor, and counting efficiency of the CPC is then used to calculate the particle number size distribution.

The PNSD of particles with diameters 0.25 µm < D_p < 30 µm can be measured with 2 device types: 1) an Optical Particle Spectrometer (OPS); 2) an Aerodynamic Particle Spectrometer (APS). In the OPS, the particles in the sample stream are focussed through a laser beam. The instrument registers number and amplitude of the pulses of light scattered by the particles. The particle pulses are sorted into a histogram by their amplitude, where the pulse amplitude yields the particle diameter and the pulse number the particle concentration, i.e. together the PNSD. Particle sizing in an OPS depends on the particle refractive index, particularly its imaginary part which determines particle absorption. In an APS, particles are exposed to an air flow passage where the particles are accelerated. The time needed for the particle to pass the passage depends on the amount of acceleration, and thus its aerodynamic diameter. The time needed to pass the passage is measured by laser beams at start and end of the passage. Together with counting the number of particles per time, this yields the particle number size distribution.

Both, the DMPS, the OPS, and the APS, yield method specific measures of the particle diameter, the electrical mobility, the optical, and the aerodynamic particle diameter, respectively. When related to the spherical equivalent geometric particle diameter commonly referred to, all particle size measures depend on particle shape (causing a 5% systematic uncertainty in particle diameter), the optical particle diameter in addition on particle refractive index (causing a 20% systematic uncertainty in particle diameter), and the aerodynamic particle diameter on particle density (causing a 15% systematic uncertainty in particle diameter). Where possible, the PNSDs provided by DMPS and OPS / APS are joined into a common PNSD, in this report. To quality assure this process, PNSDs are accepted only if DMPS and OPS/APS PNSD agree within 25% in particle diameter in their overlap size range. Together, both instruments provide a PNSD that spans over 3 orders of magnitude in particle diameter, and over 6 orders of magnitude in particle concentration.

Optical aerosol parameters quantify the direct aerosol climate effect. The observation programme at Birkenes includes the spectral particle scattering coefficient $\sigma_{sp}(\lambda)$ and the spectral particle absorption coefficient $\sigma_{ap}(\lambda)$. The scattering coefficient quantifies the amount of light scattered by the aerosol particle population in a sample per distance a light beam travels through the sample. The absorption coefficient is the corresponding property quantifying the amount of light absorbed by the particle population in the sample. An integrating nephelometer is used for measuring $\sigma_{sp}(\lambda)$ at 450, 550, and 700 nm wavelength. In this instrument, the optical sensors look down a blackened tube that is filled with aerosol sample. The tube is illuminated by a light source with a perfect cosine intensity characteristic perpendicularly to the viewing direction. It can be shown mathematically that this setup integrates the scattered light seen by the optical sensors over all scattering angles. The nephelometer at Birkenes has successfully undergone quality assurance by intercomparison within the EU research infrastructure ACTRIS in 2015. In 2017 we detected drift in the older filter absorption photometer operated at Birkenes since 2009 through carefully implemented quality control within ACTRIS. The drift was detected by operating the older filter absorption photometer in parallel with a newer, more stable make and model in order to ensure a continuous, rupture-free aerosol absorption time series at Birkenes. In addition, the newer instrument was sent to an inter-comparison within the European research infrastructure for short-lived climate forcers ACTRIS. These exercises connect individual instruments to a network-wide primary standard, ensuring traceability and comparability of observations at stations in the network. The old instrument exhibiting the drift has since been decommissioned.

For the nephelometer at Trollhaugen, such intercomparisons are impossible because of the remote Antarctic location and associated logistical challenges. However, the Trollhaugen instrument undergoes the same regular on-site quality assurance as the Birkenes instrument, including regular

calibration verification traceable to physical first principles (calibration with high-purity carbon dioxide, where scattering coefficient of carbon dioxide can be calculated from fundamental quantum mechanics).

The spectral particle absorption coefficient $\sigma_{ap}(\lambda)$ is measured by filter absorption photometers. A filter absorption photometer infers $\sigma_{ap}(\lambda)$ by measuring the decrease in optical transmissivity of a filter while the filter is loaded with the aerosol sample. The transmissivity time series is subsequently translated into an absorption coefficient time series by using Lambert-Beer's law, the same law also used in optical spectroscopy. The filter absorption photometers deployed at Birkenes have been a custom-built 1 wavelength Particle Soot Absorption Photometer (PSAP), a commercial 3-wavelength PSAP, and a modern AE33 aethalometer. The 1-wavelength PSAP received quality assurance by intercomparison within ACTRIS in 2013 discovering calibration stability issues. The 3-wavelength PSAP has undergone ACTRIS intercalibration successfully in 2015, i.e. without discovering any issues. Thus, both instruments are interpreted in combination to benefit from both, quality assurance in a research network and spectral capabilities. For 2013 and later, the data of the 3-wavelength PSAP are used, for 2010-2012, the data of the older 1-wavelength are used after being corrected by comparison with the newer instrument during the overlap period. For comparison with the nephelometer, the PSAP data has been transferred to a wavelength of 550 nm using the measured spectral dependence (3-wavelength PSAP), or by assuming an absorption Ångström coefficient $å_{ap}$ of -1 (1-wavelength PSAP, adding 2% systematic uncertainty to the data). The AE33 aethalometer has been deployed at Birkenes in late 2017. It extends the spectral range of the $\sigma_{ap}(\lambda)$ measurements to 370 – 950 nm (UV to near IR) with a resolution of 7 wavelengths. Previous aethalometer models suffered from high systematic uncertainties due to uncorrected dependencies on filter loading (e.g. Collaud Coen et al.,2010). Comparisons and calibrations within ACTRIS have shown that this systematic uncertainty has been reduced significantly in the AE33 model by an internal loading compensation (Drinovec et al., 2015).

The same AE33 aethalometer instrument type has been operated at Zeppelin since 2015.

Figure 60 compares the particle absorption coefficient between the Particle Absorption Photometer (PSAP) deployed at Birkenes in 2012, and the AE33 aethalometer deployed there in 2017 with a scatter plot including regression line. The analysis shows a correlation coefficient R^2 of 0.97 for the whole range of values, i.e. 97% of the variation in the data of one instrument is explained by the respective variation of the other instrument. This result ensures that the new instrument will continue the time series consistently. The slope of the regression line deviates from 1. Corresponding calibration factors are currently being established by the ACTRIS Research Infrastructure.

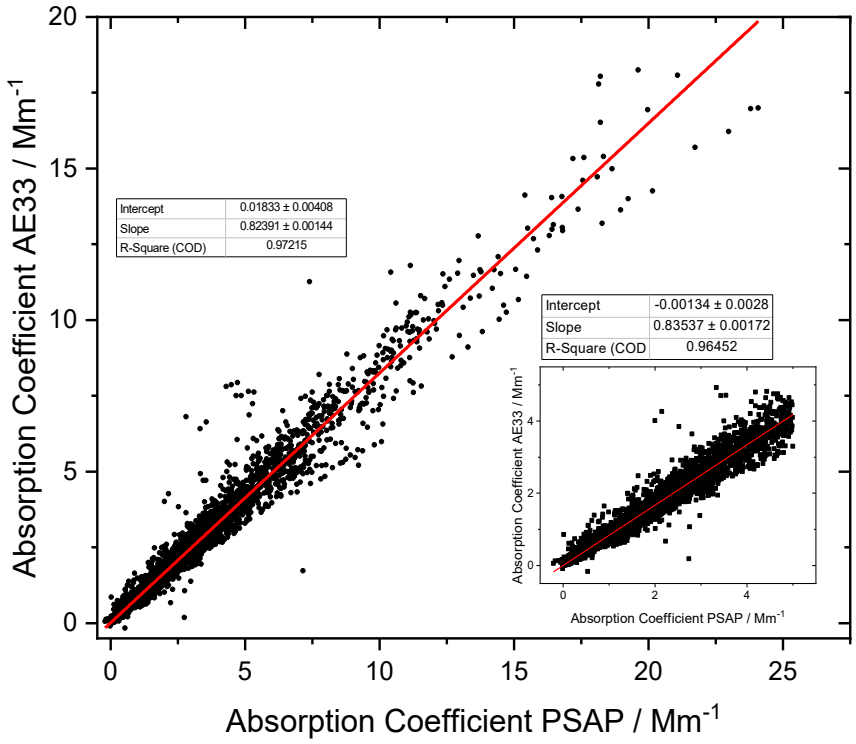

Figure 60: Comparison of particle absorption coefficient data measured the Particle Absorption Photometer (PSAP) deployed at Birkenes in 2012, and the AE33 aethalometer deployed there in 2017. The wavelength of the absorption coefficient has been interpolated to 550 nm for both instruments. The data are compared as scatter plot with regression line (red), large panel for the total range of values, small panel for values ≤ 5 Mm^{-1}.

Even though the oldest filter absorption photometer in operation at Birkenes underwent quality assurance by off-site intercomparison within ACTRIS in 2013, a drift of the reading of the older compared to the newer instrument can be observed between 2013 – 2015. These stability issues of the older filter absorption photometer were discovered already during the 2013 intercomparison. Consequently, also the newer filter absorption photometer was subjected to an ACTRIS intercomparison in 2015. The intercomparison discovered no issues with the newer instrument and confirmed stability of calibration. As a result, the whole σ_{ap} time series obtained with the old filter absorption photometer has been corrected with the 2012 instrument as reference, yielding a consistent aerosol absorption time series for Birkenes for the years since 2010. In 2017, the 2012 absorption photometer experienced problems related to an unstable measurement of the sample flow, leading to low data coverage in summer 2017. Due to the importance of the aerosol absorption measurement in relation to emissions from biomass combustion for domestic heating, it was decided to install the new 7-wavelength version in parallel, and keep both instruments running as mutual backup.

All in situ observations of aerosol properties representing the ground-level are conducted for the aerosol at dry-state (RH < 40%) for obtaining inter-comparability across the network.

DETAILS ABOUT AEROSOL OPTICAL DEPTH MEASUREMENTS

The amount of particles in the air during sunlit conditions is continuously monitored by means of Precision-Filter-Radiometer (PFR) sun photometers, located at the Sverdrup station in Ny-Ålesund and at Trollhaugen Atmospheric Observatory, Troll Station, Antarctica, and a Cimel instrument at Birkenes.

The observations in Ny-Ålesund and at Troll Station are performed in collaboration with PMOD/WRC (N. Kouremeti, S. Kazadzis), Davos, Switzerland. The main instrument characteristics are given below.

AERONET - Cimel C-318

- Sun (9 channels) and sky radiances
- Wavelength range: 340-1640 nm
- 15 min sampling
- No temperature stabilization
- AOD uncertainty: 0.01-0.02

PFR-GAW- Precision Filter Radiometer

- Direct sun measurements (4 channels)
- Wavelength range: 368 - 862 nm
- 1 min averages
- Temperature stabilized
- AOD uncertainty: 0.01

Figure 61: Photos and typical features of the standard instrument of the AERONET (left panel) and GAW PFR network instruments (right panel)

In 2002, Physikalisch-Meteorologisches Observatorium Davos/World Radiation Center (PMOD/WRC), in collaboration with NILU, started AOD observations in Ny-Ålesund (at the Sverdrup station, 46 m a.s.l.) as part of the global AOD network on behalf of the WMO GAW program. A precision filter radiometer (PFR) measures the extinction in four narrow spectral bands at 368 nm, 415 nm, 500 nm and 862 nm. Data quality control includes instrumental control like detector temperature and solar pointing control as well as objective cloud screening. Ångström coefficients are derived for each set of measurements using all four PFR channels. Calibration is performed annually at PMOD/WRC. Quality assured data are available at the World Data Centre of Aerosols (WDCA), hosted at NILU (see https://ebas.nilu.no). In order to calculate a daily average, at least 50 single measurements are required.

The sun-photometer measurements in Ny-Ålesund are part of the global network of aerosol optical depth (AOD) observations, which started in 1999 on behalf of the WMO GAW program. The instrument is located on the roof of the Sverdrup station, Ny-Ålesund, close to the EMEP station on the Zeppelin Mountain (78.9°N, 11.9°E, 474 m a.s.l.). The Precision Filter Radiometer (PFR) has been in operation since May 2002. In Ny-Ålesund, the sun is below 5° of elevation from 10th October to 4th March, limiting the period with sufficient sunlight to the spring-early autumn season. However, during the summer months it is possible to measure day and night if the weather conditions are satisfactory. The instrument measures direct solar radiation in four narrow spectral bands centred at 862 nm, 501 nm, 411 nm, and 368 nm. Data quality control includes instrumental control like detector temperature and solar pointing control as well as objective cloud screening. Measurements made at full minutes are averages of 10 samples for each channel made over a total duration of 1.25 seconds. SCIAMACHY TOMSOMI and OMI ozone columns as well as meteorological data from Ny-Ålesund are used for the retrieval of aerosol optical depth (AOD).

At Birkenes Observatory, aerosol optical depth measurements started in spring 2009, utilizing an automatic sun and sky radiometer (CIMEL type CE-318) of the global Aerosol Robotic Network (AERONET) at NASA-GSFC, with spectral interference filters centred at selected wavelengths: 340 nm, 380 nm, 440 nm, 500 nm, 675 nm, 870 nm, 1020 nm, and 1640 nm. The measurement frequency is approximately 15 minutes (this depends on the air-mass and time of day). Calibration is performed about once per year, at the Atmospheric Optics Group at the University of Valladolid (GOA-UVa), Spain. GOA manages the calibration for the AERONET sun photometers of the European sub-network of AERONET. Raw data are processed and quality assured centrally by AERONET. Data reported for 2009 - 2017 are quality-assured AERONET level 2.0 data, which means they have been pre- and post-field-calibrated, automatically cloud cleared and have been manually inspected by AERONET.

From 2017, only the new analysis algorithm (version 3) is used at the central AERONET analysis unit at NASA GSFC. In this version, the data quality control, including cloud screening, has been improved and a temperature correction has been applied to all wavelength channels. A comparison between the data from all years of operations at Birkenes (2019 – 2016) analysed with version 3 and version 2 revealed an increase of 25% in number of usable data, especially in the winter half-year. While during the summer months, the agreement between the two versions is better than 2% for both AOD and (470, 870nm) Ångström coefficient, there are significant deviations (>10%) in the months with less than 1000 observations over the whole period (November – February). A comprehensive analysis of the differences between the two versions and possible effects on trend studies is in progress; a paper by the NASA GSFC team will be published in the near future.

Due to the large gaps in data acquisition caused by the obligatory annual calibrations at the University of Valladolid combined with technical problems and occasionally unfavourable weather conditions at Birkenes, NILU decided to purchase a second Cimel instrument which will be operated alternately with the current instrument. It will be taken into operation in fall 2018.

OUTLOOK ON OBSERVATIONS OF AEROSOL OPTICAL DEPTH IN NY-ÅLESUND BEYOND 2019

A major obstacle to obtaining a year-round AOD climatology in the Arctic arises from the long polar night. To fill gaps in the aerosol climatology at Ny-Ålesund, a lunar photometer will be operated on a quasi-permanent basis in the frame of the SIOS infrastructure project. This is a collaborative initiative between NILU, PMOD/WRC and ISAC-CNR. Seasonal deployments of a lunar photometer owned by PMOD/WRC were already made in the winters of 2014/15 and 2016/17. The multiple-season deployment started in autumn 2018.

Figure 62: Moon PFR on the Kipp & Zonen tracker during the day (left, parking position) and during night-time measurements (right).

The PFR instrument modified by PMOD-WRC was installed on a tracker model Kipp & Zonen provided usually hosting a sun photometer. Figure 62 shows the instrument on the tracker during day-time and night-time. Six lunar cycles were monitored: the first during February 2014, while the other 5 during winter 2014-2015. We collected data on 66 measurement periods, from Moon-rise to Moon-set or from minimum-to-minimum elevation as in Polar Regions no set-rise events are possible. Among these, we obtained 17 distinct good measurement periods, due to the frequent occurrence of clouds. For further details see e.g. Mazzola at al., 2015.

Appendix III

Abbreviations

Abbreviation	Full name
ACSM-ToF	Aerosol Chemical Speciation Monitor
ACTRIS	Aerosols, Clouds, and Trace gases Research InfraStructure Network
ADS-GCMS	Adsorption-Desorption System – Gas Chromatograph Mass Spectrometer
AeroCom	Aerosol Comparisons between Observations and Models
AERONET	Aerosol Robotic Network
AGAGE	Advanced Global Atmospheric Gases Experiment
AIRS	Atmospheric Infrared Sounder
AMAP	Arctic Monitoring and Assessment
AOD	Aerosol optical depth
AWI	Alfred Wegener Institute
BC	Black carbon
CAMP	Comprehensive Atmospheric Monitoring Programme
CCN	Cloud Condensation Nuclei
CCNC	Cloud Condensation Nucleus Counter
CFC	Chlorofluorocarbons
CICERO	Center for International Climate and Environmental Research – Oslo
CIENS	Oslo Centre for Interdisciplinary Environmental and Social Research
CLTRAP	Convention on Long-range Transboundary Air Pollution
CO	Carbon monoxide
CPC	Condensation Particle Counter
DMPS	Differential Mobility Particle
EMEP	European Monitoring and Evaluation Programme
ENVRI^{plus}	Environmental Research Infrastructures Providing Shared Solutions for Science and Society
EOS	Earth Observing System
ERF	Effective radiative forcing ERF
ERFaci	ERF due to aerosol–cloud interaction
EU	European Union
EUSAAR	European Supersites for Atmospheric Aerosol Research
FLEXPART	FLEXible PARTicle dispersion model
GAW	Global Atmosphere Watch
GB	Ground based
GHG	Greenhouse gas
GOA-UVA	Atmospheric Optics Group of Valladolid University

Abbreviation	Full name
GOSAT	Greenhouse Gases Observing Satellite
GOSAT-IBUKI	Greenhouse Gases Observing Satellite "IBUKI"
GWP	Global Warming Potential
HCFC	Hydrochlorofluorocarbons
HFC	Hydrofluorocarbons
ICOS	*Integrated Carbon Observation System*
InGOS	Integrated non-CO2 Greenhouse gas Observing System
IPCC	Intergovernmental Panel on Climate Change
ISAC-CNR	Institute of Atmospheric Sciences and Climate (ISAC) of the Italian National Research Council
ITM	Stockholm University - Department of Applied Environmental Science
JAXA	Japan Aerospace Exploration Agency
LLGHG	Well-mixed greenhouse gases
MOCA	Methane Emissions from the Arctic OCean to the Atmosphere: Present and Future Climate Effects
MOE	Ministry of the Environment
NARE	Norwegian Antarctic Research Expeditions
NASA	National Aeronautics and Space Administration
NEOS-ACCM	Norwegian Earth Observation Support for Atmospheric Composition and Climate Monitoring
NIES	National Institute for Environmental Studies
NOAA	National Oceanic and Atmospheric Administration
NRS	Norsk Romsenter
OC	Organic Carbon
ODS	Ozone-depleting substances
OH	Hydroxyl radical
OPS	Optical Particle Spectrometer
OSPAR	Convention for the Protection of the marine Environment of the North-East Atlantic
PFR	Precision filter radiometer
PMOD/WRC	Physikalisch-Meteorologisches Observatorium Davos/World Radiation Center
PNSD	Particle number size distribution
ppb	Parts per billion
ppm	Parts per million
ppt	Parts per trillion
PSAP	Particle Soot Absorption Photometers

Abbreviation	Full name
RF	Radiative forcing
RI	Research Infrastructure
RIMA	Red Ibérica de Medida fotométrica de Aerosoles
SACC	Strategic Aerosol Observation and Modelling Capacities for Northern and Polar Climate and Pollution
SCIAMACHY	SCanning Imaging Absorption spectroMeter for Atmospheric CHartographY
SIS	Strategisk instituttsatsing
SMPS	Scanning Mobility Particle
TES	Tropospheric Emission Spectrometer
TOA	Top Of Atmosphere
TOMS OMI	Total Ozone Mapping Spectrometer Ozone Monitoring instrument
UN	United Nations
UNFCCC	United Nations Framework Convention on Climate Change
VOC	Volatile organic compounds
WDCA	World Data Centre for Aerosol
WDCS	World Data Centre of Aerosols
WMGHG	Well-mixed greenhouse gases
WMO	World Meteorological Organization

NILU – Norwegian Institute for Air Research

NILU – Norwegian Institute for Air Research is an independent, non-profit institution established in 1969. Through its research NILU increases the understanding of climate change, of the composition of the atmosphere, of air quality and of hazardous substances. Based on its research, NILU markets integrated services and products within analysing, monitoring and consulting. NILU is concerned with increasing public awareness about climate change and environmental pollution.

NILU's values: *Integrity - Competence - Benefit to society*
NILU's vision: *Research for a clean atmosphere*

NILU – Norwegian Institute for Air Research
P.O. Box 100, NO-2027 KJELLER, Norway

E-mail: nilu@nilu.no
http://www.nilu.no

ISBN: 978-82-425-3060-8
ISSN: 2464-3327

Norsk institutt for luftforskning
Norwegian Institute for Air Research